UNIVERSITY OF SOUTHAMPTON

Faculty of Engineering and Physical Sciences

Optoelectronic Research Center

Fundamentals and limitations of XUV ptychography with high harmonic sources

DOI: ????

by

Rhys Jacob William Donovan

[MPhys]

ORCiD: 0000-0001-5673-2081

A thesis for the degree of

Doctor of Philosophy

May 2025

University of Southampton

Abstract

Faculty of Engineering and Physical Sciences
Optoelectronic Research Center

Doctor of Philosophy

Fundamentals and limitations of XUV ptychography with high harmonic sources

by Rhys Jacob William Donovan

XUV ptychography provides an excellent technique for studying small structures in thin biological samples. Using XUV ptychography to image neurons is potentially very important given the current interest in neurodegenerative diseases, such as Alzheimer's or tauopathies, which are linked to the neuron's structure.

This thesis addresses the overlooked nuances in the fundamental understanding of XUV ptychography, shedding light on neglected aspects within the field. Employing a combination of real and simulated data, the research shows how ptychographic reconstruction can be optimised for a given XUV source. Focusing on optimising the illuminating probe, we show an improvement in resolution and signal-to-noise. The directional nature of resolution is considered, introducing a novel measurement technique to account for this aspect. These changes lead to a potential threefold resolution improvement by using a new design for the beam-shaping aperture and faster and lower-dose imaging.

While XUV ptychography offers inherent advantages, its synergy with complementary fluorescence-based imaging techniques is important in understanding neuron structure. Correlative imaging using three fluorescence-based techniques is explored to see how these can aid in attaining a more profound understanding of the sample composition and structure.

Furthermore, this thesis delves into the limits of damage in lab-based XUV ptychography, discussing the mechanism behind the damage, and showcasing the repeatability of experiments with XUV ptychography.

Contents

List of Figures **ix**

Declaration of Authorship **xix**

Acknowledgements **xxi**

Definitions and Abbreviations **xxiii**

COVID Impact Statement **xxv**

1 Introduction **1**
1.1 Motivation . . . 1
1.2 Contents of the Thesis . . . 2

2 Imaging **5**
2.1 Imaging Theory . . . 5
2.2 Classical Imaging . . . 7
2.3 Coherent Diffractive Imaging . . . 7
2.3.1 Image Reconstruction . . . 9
2.3.1.1 Gerchburg Saxton/Error Reduction . . . 9
2.3.1.2 Hybrid Input Output . . . 13
2.4 Ptychography . . . 16
2.4.1 The Difference Map . . . 17
2.4.2 Extended Ptychography Iterative Engine . . . 19
2.4.3 Maximum likelihood . . . 20
2.4.4 Algorithm comparison . . . 21
2.5 High-Resolution Imaging Techniques . . . 23
2.5.1 X-ray-based Techniques . . . 23
2.5.1.1 HHG Ptychography . . . 23
2.5.1.2 X-ray Holography . . . 24
2.5.1.3 Conventional X-ray Imaging . . . 24
2.5.2 Synchrotrons . . . 24
2.5.2.1 Synchrotron Microscopy . . . 25
2.5.2.2 Synchrotron X-ray Tomography . . . 25
2.5.3 X-ray Free Electron Laser . . . 26
2.5.4 Fluorescence-Based Techniques . . . 26
2.5.4.1 Confocal Microscopy . . . 26
2.5.4.2 Structured Illumination Microscopy . . . 26

2.5.4.3 Stochastic Optical Reconstruction Microscopy 27
2.5.4.4 Stimulated Emission Depletion 28
2.5.4.5 Minimal Photon Fluxes 28
2.5.5 Electron Microscopy 28
2.5.5.1 Transmission Election Microscopy 28
2.5.5.2 Scanning Electron Microscopy 29
2.5.6 Ion Beam Microscopy 29
2.5.6.1 Helium Ion Microscopy 29
2.5.7 Scanning Probe Microscopy 29
2.5.7.1 Scanning Tunneling Microscopy 29
2.5.7.2 Atomic Force Microscopy 30
2.5.8 Superlens-based 30
2.5.8.1 Far-Field Superoscillatory Metamaterial Superlens . . . 30
2.5.9 Comparison 31

3 Introduction to High Harmonic Generation 33
3.1 Theory of High Harmonic Generation 33
3.1.1 High Harmonic Generation 33
3.1.1.1 Three-Step Model 34
3.1.1.2 Cutoff Energy 35
3.1.1.3 Quantum Mechanical Model 43
3.1.1.4 Odd Harmonics 45
3.1.1.5 Phase Matching 46
3.1.1.6 Coherence 51
3.1.2 Summary 51
3.2 System for High Harmonic Generation and Ptychography 51
3.2.1 Experimental Setup 52
3.2.1.1 Mode-Locked Seed Laser 52
3.2.1.2 Millennia 53
3.2.1.3 Tsunami 53
3.2.1.4 Chirped Pulse Amplification 54
3.2.1.5 Evolution 55
3.2.1.6 Spitfire 55
3.2.1.7 Frequency-Resolved Optical Gating 56
3.2.1.8 Beam Stabilisation 58
3.2.1.9 Gas Cell 59
3.2.1.10 Beam Filters 61
3.2.1.11 Vacuum Chamber 63
3.2.1.12 SmarAct Stages 63
3.2.1.13 Aperture 64
3.2.1.14 Detector 66
3.2.2 Summary 68

4 Experimental Procedure 69
4.1 Preparation 69
4.2 Mode-locking 70
4.3 Evolution 71

4.4 Spitfire . . . 71
4.5 Beam Stabilisation . . . 71
4.6 Beam Quality . . . 72
4.7 Aperture to Object Distance . . . 72
4.8 Locating Apertures and Samples . . . 73
4.9 Data acquisition . . . 73
4.10 Changing Samples and Apertures . . . 74

5 What Makes a Good Probe? 75
5.1 Introduction . . . 76
5.2 Fourier Ring Correlation . . . 84
5.2.1 Two-axis Fourier Line Correlation . . . 86
5.2.2 Complete Fourier Line Correlation . . . 88
5.3 Methodology . . . 90
5.4 Simulation . . . 90
5.4.1 Initialisation . . . 91
5.4.2 The Gaussian Beam . . . 92
5.4.3 The Aperture and Probe . . . 93
5.4.4 The Object and Scanning Pattern . . . 94
5.4.5 The Scatter Pattern . . . 95
5.4.6 Reconstruction . . . 96
5.4.7 The Error Calculation . . . 97
5.5 Variation of Simulation . . . 97
5.6 Flux . . . 98
5.7 CCD Distance . . . 100
5.8 Probe Complexity . . . 105
5.9 Probe Overlap . . . 108
5.10 Binning . . . 117
5.11 Beam Instability Effects . . . 121
5.12 Ice Formation . . . 125
5.13 Super Resolution . . . 129
5.14 Angular Spread . . . 135
5.15 Best aperture . . . 141
5.16 Summary . . . 148

6 Correlative Imaging 149
6.1 Sample preparation . . . 150
6.2 Resolution of Techniques . . . 151
6.3 Structured Illumination Microscopy . . . 152
6.4 Lightning . . . 156
6.5 STORM . . . 159
6.6 Comparison . . . 161
6.7 Summary . . . 164

7 XUV damage 167
7.1 Radiation dose unit: Gray . . . 167
7.2 Damage mechanism . . . 168

7.3 Attempted XUV damage of Neurons 169
7.4 Summary 172

8 Conclusion and Future Work **175**
8.1 Conclusions 175
8.1.1 What Makes a Good Probe? 175
8.1.2 Correlative Imaging 176
8.1.3 XUV Damage 176
8.2 Future Work 177
8.2.1 Ring Aperture 177
8.2.2 Super Resolution 177
8.2.3 Correlative Imaging 177
8.2.4 Sample in Water Vapour 178

References **179**

List of Figures

1 Timeline of the impact of Covid upon my PhD, where the duration of lockdowns and post-Covid effect of the laser being broken have been compared to the total duration of my PhD. xxvi

2.1 ER algorithm (blue line) applied to y=$\frac{2}{3}$x (black line) and y=4x-2 (red line) starting at the point (4,4), calculating the closest point alternating between lines. 12
2.2 ER algorithm (blue line) applied to y=$\frac{2}{3}$x (black line) and y=cos(2x)-2 (red line) starting at the point (4,4), calculating the closest point alternating between lines. 13
2.3 HIO algorithm (blue line) applied to y=$\frac{2}{3}$x (black line) and y=4x-2 (red line) starting at the point (4,4), calculating the next point using equation (2.12) with $\beta = \frac{2}{3}$. 14
2.4 HIO algorithm (blue line) applied to y=$\frac{2}{3}$x (black line) and y=cos(2x)-2 (red line) starting at the point (4,4), calculating the next point using equation (2.12) with $\beta = \frac{2}{3}$. 15
2.5 Diagram of how ptychography is implemented within our setup. Firstly, the beam is reflected towards an aperture; secondly, multiple probe locations will be separately illuminated with overlap; finally a scatter pattern is measured on the CCD. 17
2.6 Comparison of reconstructive algorithms on real data on 1 μm polystyrene spheres with a double slit aperture (5x1 μm slits spaced 4 μm from centres). (A) reconstructed data using 100 iterations of DM, (B) reconstructed data using 100 iterations of MLs, (C) reconstructed data using initially 50 iterations of DM followed 50 iterations of MLs. 22

3.1 This figure shows the position and wave function of the electron (black line 'A' side) in a varying potential, which is the Coulomb potential plus the laser potential at three different points of the laser cycle, (blue line 'A' side) due to different phases (black cross 'B' side) of an electric field (blue line 'B' side). 34
3.2 Electron trajectories for the classical three-step model with differing t_0, (multiple colour lines, left axis), as described by (3.7) due to the acceleration induced by the electric field (solid orange line, right axis) against time (black line, both axes). The initial time of emittance, t_0 (red star points) are followed by times of recombination with a gradient of displacement, if applicable(red lines). The key shows the return energy of the different ejection times. 37

3.3 Energy for electrons emitted at different times (orange line) are separated into short and long trajectories, to the left and right respectively (black line) with $3.17U_p$ marked (red line). The key shows the return energy of the different ejection times. The coloured points correspond to lines of figure 3.2. 41
3.4 The probability density of the total wave function (black line) is the coherent sum of the ground state wave function (blue line) and the returning wave packet's wave function (orange line). Point of zero potential (red line) and the expectation value of the total wave function (vertical black line). 43
3.5 Position of expectation values of the probability density of the total wave function (blue line) over 1.6ps plotted over the position of a mean of zero (red line). 44
3.6 Graph of the fundamental (thick black line), second harmonic (thick red line), and third harmonic (thick blue line) for an arbitrary beam. The vertical lines note offset half periods of the fundamental. 46
3.7 Time in which electrons spend in the continuum (orange line) are separated by the point of greatest kinetic energy (dark green point, vertical black line). To the left of the line are long trajectories and short trajectories to the right of the line, and are aptly named for relation to time in the continuum. The key shows the return energy of the different ejection times. Coloured points correspond to lines of identical colour on figure 3.2. 48
3.8 The calculated coherence length for the long and short HHG trajectories for the 27^{th} harmonic of an 800 nm beam, with a pulse energy of 1.5 mJ with a 40 fs pulse length focused to a beam waist of 60 μm in argon gas. This data was calculated and the diagram was created by Doctor Charles Pooley. 50
3.9 Diagram of the experimental setup. Section A is where the Millennia(1) pumps the Tsunami (2) to generate modelocked pulses. Section B is where the Evolution(3) pumps the Spitfire CPA system(4). Power is selected by a polariser(5). Section C is the beam stabilisation that occurs with a mirror(7), lens(8), and cameras(9). Section D is the FROG(6) to measure the pulse duration and chirp. Section E is where the XUV beam is generated from the gas cell(10), passes through the aluminium filters(11), and into the vacuum chamber(12). 52
3.10 Graph of the emission spectrum from the Ti:Sapphire, showing intensity versus wavelength. 54
3.11 Image of the FROG trace of the pulse after the CPA, showing wavelength against delay. 57
3.12 Graph of the movement of the beam on the CCD with and without the stabilisation system turned on. Times before roughly 150 s the stabilisation system is off and times after the stabilisation system is on. The graph shows the stabilisation of the x-axis (green line) and y-axis (blue line), where 1 pixel is 20 nm. This data was taken by Doctor Michal Odstrčil 59
3.13 Diagram of high harmonic generation using a high intensity pulsed beam focused onto a gas cell contained by openings in copper tape, created by the laser to be the minimal size; then the parent beam is filtered out, leaving only the generated beam. 60

3.14 The transmission values of four materials from 10 eV to 100 eV (blue line), with the photon energy of the HHG beam (red line). (A) shows the transmission values of Ar with a density of $1.78\times10^3 g/cm^3$. (B) shows the transmission values of Au with a density of 19.32 g/cm^3. (C) shows the transmission values of Al with a density of 2.7 g/cm^3. (D) shows the transmission values of Al_2O_3 with a density of 3.97 g/cm^3. The transmission data were from the CXRO database (1). 62
3.15 Diagram of the beam path, spherical mirror, the aperture, the sample, and CCD within the vacuum chamber of the system 63
3.16 Diagram of the SmarAct stages used to position the aperture and the sample. Where A is used for the aperture, and B is used for the sample. . 64
3.17 The theoretical log-base-10 diffraction patterns for a Gaussian beam passing through a 10 μm diameter aperture after off-axis reflection, the aperture is positioned at (A) the horizontal focus, giving a vertical line at the centre; (B) the vertical focus, giving a horizontal line at the centre; (C) circle of least confusion, giving a cross-shaped pattern at the centre. . . . 65
3.18 The theorectical horizontal (blue line) and vertical beam waists (orange line) for the reflected beam from the XUV mirror. This figure shows the CLC at the point where the two lines intersect. 66
3.19 Recorded measurements of the diffraction pattern of a 10 μm aperture, with a maximum exposure of 10 s, binning of 2, cropping of 1, at a temperature of -40 °C and taking 18 s. 67

5.1 Images of the beam at the aperture and corresponding probes, after the beam at the aperture has propagated to the object plane, with a Hue Saturation Value (HSV) display in the top right-hand corner of (A). (A) is the beam at a 7 μm diameter circular aperture recovered by the backpropagation of (B) using ASM to backpropagate 141 μm to the aperture plane, (B) is the reconstructed probe from a reconstruction of ptychographic data using a circular aperture (7 μm diameter). (C) is the beam at a double slit aperture (5x1 μm slits spaced 4 μm from centres) recovered by the backpropagation of (D) using ASM to backpropagate 141 μm, (D) is the reconstructed probe from a reconstruction of ptychographic data using a double slit aperture (5x1 μm slits spaced 4 μm from centres). (E) is the beam at a double slit aperture (5x1 μm slits spaced 4 μm from centres) recovered by the backpropagation of (F) using ASM to backpropagate 89 μm, (F) is the reconstructed probe from a reconstruction of ptychographic data using a double slit aperture (5x1 μm slits spaced 4 μm from centres) with 1 μm diameter polystyrene spheres on the aperture. 77
5.2 Images comparing a coherent and incoherent beam at the CLC for a double slit aperture (5x1 μm slits spaced 4 μm from centres) using simulated data. (A) is the amplitude and phase of a propagated beam from the double slit aperture 141 μm away using a coherent beam. (B) is the intensity of a propagated beam from the double slit aperture 3.69 cm away using a coherent beam. (C) is the amplitude and phase of a propagated beam from the double slit aperture 141 μm away using an incoherent beam. (D) is the intensity of a propagated beam from the double slit aperture 3.69 cm away using an incoherent beam. 80

5.3 Images comparing the beam at the aperture for two different M^2 values using simulated data. (A) is the beam at the aperture with an M^2 value of 3, the value used for all other simulated data throughout this thesis. (B) is the beam at the aperture with an M^2 value of 10. 81
5.4 The cross-sections of the power spectrums of the Fourier transform of a Gaussian object, two probes, the convolution of object and individual probes, (A) the low angular spread probe, and (B) the high angular spread probe, with the power spectrum of the object's Fourier transform (blue line), the Fourier transform of the probe (black line), the convolution of the object and the probe (yellow dashed line), the noise level (purple line), and the intercept of a noise threshold and the convolution of the object and the probe (red circles). 82
5.5 FRC calculation of experimental datathat I took. (A) and (C) are cropped images of reconstructions from unique data of 945 nm polystyrene spheres using a double slit (5x1 μm slits spaced 4 μm from centres) positioned 140 μm before the object at the CLC of 29 nm soft X-ray beam. (B) and (D) are the Fourier transforms of (A) and (C) respectively. (E) is the FRC against the ratio of spatial frequency and Nyquist frequency (blue) with the one-bit criterion (yellow) and the half-bit criterion (orange). 85
5.6 FLC calculations of experimental data. (A) is the FLC for reconstructed data from a 7 μm circular aperture, (B) is the FLC for the data used in figure 5.5, reconstructed data from a double slit aperture (5x1 μm slits spaced 4 μm from centres, with the slit diffraction along the x-axis), to compare FLC_x (orange) and FLC_y (blue), and containing the one-bit criterion (purple) and the half-bit criterion (yellow). 87
5.7 A diagram showing how the Fourier correlations for FLCs are calculated for an angle θ at a distance u where the red lines without arrows are the regions being compared between the two Fourier transforms of the two reconstructions of the same object. 88
5.8 FLC calculations of experimental data that I took. (A) is the FLC for reconstructed data from a 7 μm circular aperture, (B) is the FLC for the data used in figure 5.5, reconstructed data from a double slit aperture (5x1 μm slits spaced 4 μm from centres). 89
5.9 The electric field of the beam just before the aperture and at the CLC used in the simulations. 93
5.10 (A) the beam at a circular aperture (8 μm diameter), and (B) the probe after the beam propagated 141 μm from the aperture to the plane of the object. 94
5.11 (A) The scanning positions and order of a 30 μm by 30 μm scan area with a step size of 2 μm, resulting in 251 scanning positions, and (B) the object used in the simulation, where it has been created from an actual experimental reconstruction of neurons, then reduced in size and tiled. . 95
5.12 A histogram and scatter plot 24 runs of the simulation with same initialisation values. The histogram shows groups of FRC values in 0.1 ranges (blue bars). The scatter plot shows the exact FRC values for the 24 simulation runs (black crosses). 98

5.13 FRC half-bit intercept of simulated data with varying levels of flux. The FRC half-bit intercept (blue line) for simulated data using a circular aperture (8 μm diameter) with a reconstructed object of neurons for flux counts from 1% to $1 \cdot 10^8$% of a flux count measured from a circular aperture (7 μm diameter). 99
5.14 FRC half-bit intercept of simulated data with varying object to CCD distances. The average FRC half-bit intercept compared to the Nyquist of the CCD (blue line) against the object to CCD distance, and error bars are the maximum and minimum of the three FRC half-bit intercept values. 101
5.15 FRC half-bit intercept of simulated data with varying object to CCD distances. The average FRC half-bit intercept as the smallest resolvable feature (blue line) against the object to CCD distance, and error bars are the maximum and minimum of the three FRC half-bit intercept values. Where reconstructions at distances equal to and lower than object to CCD distances at the red line are not valid due to approximations. . . . 102
5.16 FRC half-bit intercept of simulated data with varying object to CCD distances. The average FRC half-bit intercept as the smallest resolvable feature (blue line) against the numerical aperture, and error bars are the maximum and minimum of the three FRC half-bit intercept values. . . . 103
5.17 The beam widths (black crosses) of a circular aperture (8 μm diameter) for multiple object to CCD propagation distances. 104
5.18 The probe complexity of a circular aperture (8 μm diameter) for multiple aperture to object propagation distances. 106
5.19 The FRC first intercept of the half-bit criterion of a circular aperture (8 μm diameter) for multiple aperture to object propagation distances. . . . 107
5.20 Radial integrals of probes for (A) a double slit aperture (5x1 μm slits spaced 4 μm from centres), and (B) a circular aperture (8μm diameter). Both with an aperture to object propagation distance of 141 μm. 109
5.21 The total intensity distribution for simulated data of all probes over an object over a scan area of 30 μm by 30 μm with 251 scans for (A) a double slit aperture (5x1 μm slits spaced 4 μm from centres), and (B) a circular aperture (8 μm diameter). Both with an aperture to object propagation distance of 141 μm. 110
5.22 (A) The multiples of intensity at the beam width of all probes over an object over a scan area of 30 μm by 30 μm with 251 scans for a circular aperture (8 μm diameter), and (B) the reconstructed object. The black square of (A) is the same region as the red square of (B). 111
5.23 (A) The multiples of intensity at the beam width of all probes over an object over a scan area of 30 μm by 30 μm with 251 scans for a double slit aperture (5x1 μm slits spaced 4 μm from centres), and (B) the reconstructed object. The black square of (A) is the same region as the red square of (B). 112
5.24 (A) Beam at the star aperture, (B) beam after propagating 141 μm from the star aperture, and (C) the radial integral of the beam after propagating 141 μm from the non-uniform star aperture. (D) shows a scanning electron microscope image of the star aperture. 113

5.25 (A) Reconstructed object of a non-uniform star aperture, with an aperture to object propagation distance of 141 μm and object to CCD distance of 3.69 cm, using 100 iterations of DM and then 500 iterations of MLs for reconstruction, and a binning of 2. The resolution at the Nyquist limit is 82 nm. The linear overlap is 50%. (B) is the FLC of the reconstructed object. 114
5.26 (A) Reconstructed object of a non-uniform star aperture, with an aperture to object propagation distance of 141 μm and object to CCD distance of 3.69 cm, using 100 iterations of DM and then 500 iterations of MLs for reconstruction, and a binning of 2. The resolution at the Nyquist limit is 82 nm. The linear overlap is 75%. (B) is the FLC of the reconstructed object. 115
5.27 (A) Reconstructed object of a non-uniform star aperture, with an aperture to object propagation distance of 700 μm and object to CCD distance of 3.69 cm, using 100 iterations of DM and then 500 iterations of MLs for reconstruction, and a binning of 2. The resolution at the Nyquist limit is 82 nm. The linear overlap is 75%. (B) is the FLC of the reconstructed object. 116
5.28 The cross-section of two overlapping probes with a binning of 2. The Probe at position 1 (blue line), and the probe at position 2 (red line), the extent of the probe array 1 (grey vertical line). The region of overlap between the two probes within the extent of the probe array (blue area), and the region of overlap missed due to binning (red area). 117
5.29 The cross-section of two overlapping probes with no binning. The Probe at position 1 (blue line), and the probe at position 2 (red line), the extent of the probe array 1 (grey vertical line). The region of overlap between the two probes within the extent of the probe array (blue area), and the region of overlap missed due to binning (red area). 118
5.30 log10 of the amplitude a reconstructed probe of an 8 μm diameter circular aperture that has propagated 141 μm with a binning of 2. This image was reconstructed by PtychoShelves from data that I took. 119
5.31 log10 of the amplitude a reconstructed probe of a double slit aperture (5x1 μm slits spaced 4 μm from centres) that has propagated 141 μm with a binning of 2. This image was reconstructed by PtychoShelves from data that I took. 120
5.32 The FRC for different amounts of binning for an 8 μm circular aperture using 100 iterations of DM followed by 100 iterations of MLs with an aperture to object distance of 141 μm and an object to detector distance of 3.69 cm, where a not binned reconstruction (orange line) and binning of 2 reconstruction (blue line) are compared against the one-bit criterion (purple line) and the half-bit criterion (yellow line). 121
5.33 The first FRC intercepts of the half-bit criterion for varying levels of normal distribution of the position error for an 8 μm circular aperture using 100 iterations of DM followed by 100 iterations of MLs with an aperture to object distance of 141 μm and an object to detector distance of 3.69 cm, with the average FRC intercepts of the half-bit criterion (blue line), the maximum and minimum FRC intercepts of the half-bit criterion (error bars). 122

5.34 The first FRC intercepts of the half-bit criterion for varying levels of power oscillations of the position error for an 8 μm circular aperture using 100 iterations of DM followed by 100 iterations of MLs with an aperture to object distance of 141 μm and an object to detector distance of 3.69 cm, with the average FRC intercepts of the half-bit criterion (blue line), the maximum and minimum FRC intercepts of the half-bit criterion (error bars). 124
5.35 The first FRC intercepts of the half-bit criterion for varying levels of power oscillations of the position error for an 8 μm circular aperture using 100 iterations of DM followed by 100 iterations of MLs with an aperture to object distance of 141 μm and an object to detector distance of 3.69 cm, with the average FRC intercepts of the half-bit criterion (blue line), the maximum and minimum FRC intercepts of the half-bit criterion (error bars). 125
5.36 The reconstructed objects for varying levels of rate of ice formation on the detector at different regions of the reconstructed object for an 8 μm circular aperture using 100 iterations of DM followed by 100 iterations of MLs with an aperture to object distance of 141 μm and an object to detector distance of 3.69 cm, (A) 0 intensity lost to ice for final scatter pattern, (B) 20% intensity lost to ice for final scatter pattern, (C) 90% intensity lost to ice for final scatter pattern, (D) 95% intensity lost to ice for final scatter pattern. 127
5.37 The first FRC intercept of the half-bit criterion for varying levels of rate of ice formation on the detector at different regions of the reconstructed object for an 8 μm circular aperture using 100 iterations of DM followed by 100 iterations of MLs with an aperture to object distance of 141 μm and an object to detector distance of 3.69 cm, (A) 0 intensity lost to ice for final scatter pattern, (B) 20% intensity lost to ice for final scatter pattern, (C) 90% intensity lost to ice for final scatter pattern, (D) 95% intensity lost to ice for final scatter pattern. 128
5.38 The contribution of the Fourier transform of a probe on the convolution for two positions, at the centre of the detector (black line) and outside the detector (blue line). Within the detector (grey verticals) is the area of the Fourier transform of the probe at the centre of the detector (black area) and the area of the Fourier transform of the probe outside the detector (blue). The amount of contribution to the convolution of the Fourier transform of the probe at the outside position is shown under the Fourier transform of the object and the Fourier transform of the probe (red area). 129
5.39 Reconstructed 945 nm diameter polystyrene spheres where no mask (A) and a 32-pixel inward mask (B) has been applied on the data, using a double slit aperture (5x1 μm slits spaced 4 μm from centres) 141 μm before the object and detector 3.69 cm away from the object, using 100 iterations of DM and 500 iterations of MLs. Where (A) and (B) are two different data sets of the same object. (C) and (D) are the masks for what data were used in the reconstruction of (A) and (B) respectively, where 1 is the data are used and 0 is the data were not used. (C) is the mask where all the data are used, and (D) is the 32-pixel inward mask where the black border is where the data were not used. 130

5.40 (A) and (B) are the Fourier transforms of a central region from figure 5.39 respectively, (C) is the FRC of (A) and (B), and (D) is the FLC of (A) and (B). The resolution at the Nyquist limit for this is 82 nm. 131
5.41 Reconstructed 945 nm diameter polystyrene spheres where a 32-pixel outward mask has been applied on the data, using a double slit aperture (5x1 μm slits spaced 4 μm from centres) 141 μm before the object and detector 3.69 cm away from the object, using 100 iterations of DM and 500 iterations of MLs. Where (A) and (B) are two different data sets of the same object. 132
5.42 (A) and (B) are the Fourier transforms of a central region from figure 5.41 respectively, (C) is the FRC of (A) and (B), and (D) is the FLC of (A) and (B). The resolution at the Nyquist limit for this is 74 nm. 133
5.43 The contribution of the Fourier transform of a probe on the convolution for two positions, at the centre of the detector (black line) and outside the detector (blue line). Within the detector (grey verticals) is the area of the Fourier transform of the probe at the centre of the detector (black area) and the area of the Fourier transform of the probe outside the detector (blue). The amount of contribution to the convolution of the Fourier transform of the probe at the outside position is shown under the Fourier transform of the object and the Fourier transform of the probe (red area). 134
5.44 The beam at the aperture (A) and probe after propagating 141 μm (B) of the circular aperture (8 μm diameter). (C) will be the symbol for the circular aperture (8 μm diameter). 136
5.45 The beam at the aperture (A) and probe after propagating 141 μm (B) of the double-double slit aperture (5 μm square outside height and width and 4 μm inside height and width). (C) will be the symbol for the double-double slit aperture (5 μm square outside height and width and 4 μm inside height and width). 136
5.46 The beam at the aperture (A) and probe after propagating 141 μm (B) of the double slit aperture (5x1 μm slits spaced 4 μm from centres). (C) will be the symbol for the double slit aperture (5x1 μm slits spaced 4 μm from centres). 137
5.47 The beam at the aperture (A) and probe after propagating 141 μm (B) of the ring aperture (10 μm outside diameter and 9 μm inside diameter). (C) will be the symbol for the ring aperture (10 μm outside diameter and 9 μm inside diameter). 137
5.48 The beam at the aperture (A) and probe after propagating 141 μm (B) of the deformed spiral (10 μm outside diameter and 0.5 μm thickness). (C) will be the symbol for the deformed spiral (10 μm outside diameter and 0.5 μm thickness). 138
5.49 The average FRC first intercept of the half-bit criterion of three runs for a circular aperture (8 μm diameter), double-double slit aperture (5 μm square outside height and width and 4 μm inside height and width), double slit aperture (5x1 μm slits spaced 4 μm from centres), ring aperture (10 μm outside diameter and 9 μm inside diameter), deformed spiral (10 μm outside diameter and 0.5 μm thickness) respectively (blue line), with lowest resolution FRC first intercept of the half-bit criterion (top error bar), and highest resolution FRC first intercept of the half-bit criterion (bottom error bar). 139

5.50 On the right axis, the flux of the first scatter pattern for a circular aperture (8 μm diameter), double-double slit aperture (5 μm square outside height and width and 4 μm inside height and width), double slit aperture (5x1 μm slits spaced 4 μm from centres), ring aperture (10 μm outside diameter and 9 μm inside diameter), deformed spiral (10 μm outside diameter and 0.5 μm thickness) respectively (orange crosses). This figure also contains figure 5.49 on the left axis. 140
5.51 The average FRC first intercept of the half-bit criterion of three runs for a double-double slit aperture (5 μm square outside height and width and 4 μm inside height and width), ring aperture (10 μm outside diameter and 9 μm inside diameter), deformed spiral (10 μm outside diameter and 0.5 μm thickness) respectively (blue line), with lowest resolution FRC first intercept of the half-bit criterion (top error bar), and highest resolution FRC first intercept of the half-bit criterion (bottom error bar). 141
5.52 (A) Beam at the ring aperture, (B) beam after propagating 141 μm from the ring aperture, and (C) the radial integral of the beam after propagating 141 μm from the ring aperture. 142
5.53 Fourier correlations for the ring aperture (10 μm outside diameter and 9 μm inside diameter), with an aperture to object propagation distance of 141 μm and object to CCD distance of 3.69 cm, using 100 iterations of DM and then 100 iterations of MLs for reconstruction, and a binning of 2. The resolution at the Nyquist limit is 82 nm. 143
5.54 Fourier correlations for the ring aperture (10 μm outside diameter and 9 μm inside diameter), with an aperture to object propagation distance of 141 μm and object to CCD distance of 1.35 cm, using 100 iterations of DM and then 100 iterations of MLs for reconstruction, and a binning of 1. The resolution at the Nyquist limit is 33 nm. 144
5.55 A simulated reconstruction of neurons, using a ring aperture (10 μm outside diameter and 9 μm inside diameter) 141 μm before the object and detector. (A) had an object to CCD distance of 3.69 cm, and (B) had an object to CCD distance of 1.35 cm, using 100 iterations of DM and 100 iterations of MLs. (A) had a resolution at the Nyqusit limit of 82 nm, and (B) had a resolution at the Nyquist limit of 33 nm. (C) and (D) are the same zoomed-in region of (A) and (B) respectively. 145
5.56 (A) The total intensity distribution of all probes over an object over a scan area of 30 μm by 30 μm with 62 scans for ring aperture (10 μm outside diameter and 9 μm inside diameter). (B) The multiples of intensity at the beam width of all probes over an object. With an aperture to object propagation distance of 141 μm. 146
5.57 (A) The FRC and (B) one of the corresponding simulated reconstruction of neurons. (B) was using a ring aperture (10 μm outside diameter and 9 μm inside diameter), with an aperture to object propagation distance of 141 μm and object to CCD distance of 3.69 cm, using 100 iterations of DM and then 100 iterations of MLs for reconstruction, and a binning of 2. The resolution at the Nyquist limit is 82 nm. This reconstruction used 62 scan positions with a step size between scan positions of 4 μm. 146

5.58 (A) The FRC and (B) one of the corresponding simulated reconstruction of polystyrene spheres. (B) was using a ring aperture (10 μm outside diameter and 9 μm inside diameter), with an aperture to object propagation distance of 141 μm and object to CCD distance of 3.69 cm, using 100 iterations of DM and then 100 iterations of MLs for reconstruction, and a binning of 2. The resolution at the Nyquist limit is 82 nm. This reconstruction used 62 scan positions with a step size between scan positions of 4 μm. 147

6.1 Comparison of raw data collected for SIM (A), and the reconstructed image of the mouse neurons (B), with tubulin stained with Alexa-488 (green) and actin stained with Alexa-647 (red). 153
6.2 Heat map of modulation contrast-to-noise ratio for the reconstructed image (B) from figure 6.1. 154
6.3 The mean intensity of each data slice taken used in the reconstruction of the image (B) in figure 6.1 155
6.4 The Fourier transforms of the reconstructed image (B) from figure 6.1, with concentric rings denoting the spatial frequency in mm. 156
6.5 The deconvolved image of mouse neurons (B), with tubulin stained with Alexa-488 (green) and actin stained with Alexa-647 (red). The white square indicates the area used for figure 6.6. 157
6.6 A zoomed-in region of figure 6.5, a deconvolved image of mouse neurons (B), with tubulin stained with Alexa-488 (green) and actin stained with Alexa-647 (red). The yellow line indicates the cross-section used for figure 6.7. 158
6.7 The full-width half-maximum of the smallest feature from figure 6.6. . . 158
6.8 The STORM image of mouse neurons (B), with tubulin stained with Alexa-488 (green) and actin stained with Alexa-647 (red). 160
6.9 The full-with half-maximum of the smallest feature in figure 6.8. 161
6.10 A comparison of images from the four techniques: (A) is the reconstructed SIM object from figure 6.1, (B) is the reconstructed Lightning object from figure 6.5, (C) is the reconstructed STORM object from figure 2.26, (D) is the reconstructed object of mouse neurons using a double slit aperture (5x1 μm slits spaced 4 μm from centres). 163

7.1 Reconstructed objects of a 40 μm by 40 μm region using a circular aperture (10 μm diameter) with 197 scan positions with a step size of 3 μm, (A) reconstructed object of the sample before attempted damage, (B) reconstructed object of the sample after attempted damage, and region of attempted damage (black box). (C) and (D) show the regions in the black boxes from (A) and (B) respectively. 171
7.2 (A) the FRC of the two reconstructed objects in figure 7.1, and (B) the FLC of the two reconstructed objects in figure 7.1. 172

Declaration of Authorship

I declare that this thesis and the work presented in it is my own and has been generated by me as the result of my own original research.

I confirm that:

1. This work was done wholly or mainly while in candidature for a research degree at this University;
2. Where any part of this thesis has previously been submitted for a degree or any other qualification at this University or any other institution, this has been clearly stated;
3. Where I have consulted the published work of others, this is always clearly attributed;
4. Where I have quoted from the work of others, the source is always given. With the exception of such quotations, this thesis is entirely my own work;
5. I have acknowledged all main sources of help;
6. Where the thesis is based on work done by myself jointly with others, I have made clear exactly what was done by others and what I have contributed myself;
7. Parts of this work have been published as:

Signed:..... Date:.....

Acknowledgements

During my fourth year of university, my depression was at its worst, and I believed I was a failure and worthless. It was the darkest time of my life, but I had one lecturer who made me believe in myself. Dr Bill Brocklesby was one of the most important pillars in regaining my happiness. Therefore, I thank my main supervisor not only for their incredible advice throughout my PhD, but also for giving me my life back.

I would like to thank Prof. Russell Minns for giving me excellent explanations of Chemistry concepts, and supervisor Prof. Jeremy Frey for bringing endless enthusiasm to every group meeting.

An enormous thank you goes to supervisor Prof. Katrin Deinhardt and Dr Dianne Lopez for showing me through sample preparation, preparing the samples of mouse neurons, and explaining neurons and biological concepts.

This PhD would not have been possible without Dr Joanne Woodhouse, Dr Charles Pooley, and Dr Haoyan Lyu who were instrumental in teaching me all aspects of the lab and how to use the system.

Chapter 5 would not have been possible without Dr Mark Willett's expertise in other forms of imaging.

A thank you to the rest of the X-ray group and my peers for making this a great experience.

A tremendous thank you to my fiancée, Chloe Langford, for all her support throughout this PhD, being the absolute best, and her invaluable grammar and vocabulary checking.

A special thank you to Vikki Langford, Kevin Walters, and Elliott Campbell for their diligent proofreading and sacrificing parts of their holidays.

Finally, a thank you to the rest of my friends, family, and Chloe's family for always being there and getting me to the finish line.

Definitions and Abbreviations

AFM	Atomic Force Microscopy
AOM	Acousto-Optic Modulator
ASM	Angular Spectrum Method
Au	Gold
CCD	Charged-Coupled Device
CDI	Coherent Diffractive Imaging
CLC	Circle of Least Confusion
CMOS	Complementary Metal-Oxide-Semiconductor
CPA	Chirped Pulse Amplification
DM	Difference Map
ePIE	Extended Ptychography Iterative Engine
ER	Error Reduction
FIB	Focused Ion Beam
FLC	Fourier Line Correlation
FRC	Fourier Ring Correlation
FROG	Frequency-Resolved Optical Gating
FZP	Fresnel Zone Plate
HHG	High Harmonic Generation
HIM	Helium Ion Microscopy
HIO	Hybrid Input-Output
HSV	Hue Value Saturation
LINAC	Linear Accelerator
MINFLUX	Minimal Photon Fluxes
ML	Maximum Likelihood
MLc	Maximum Likelihood cluster

MLs	Maximum Likelihood stochastic
$MOPA$	Master Oscillator Power Amplifier
NA	Numerical Aperture
$Nd:YLF$	Neodymium-Doped Yttrium Lithium Fluoride
$Nd:YVO_4$	Neodymium-Doped Yttrium Orthovanadate
OTF	Optical Transfer Function
PBS	Phosphate Buffer Solution
PID	Proportional–Integral–Derivative
PIE	Ptychography Iterative Engine
PSF	Point Spread Function
$RAAR$	Relaxed Averaged Alternating Reflections
$RASP$	Relaxed Averaged Successive Projections
SEM	Scanning Electron Microscopy
SHG	Second Harmonic Generation
SIM	Structured Illumination Microscopy
SiN	Silicon Nitride
$STED$	Stimulated Emission Depletion
STM	Scanning Tunnelling Microscopy
$STORM$	Stochastic Optical Reconstruction Microscopy
SXT	Synchrotron X-ray Tomography
TEM	Transmission Electron Microscopy
Ti	Titanium
Ti^{3+}	Titanium Ions
$XFEL$	X-ray Free-Electron Laser
XUV	Extreme Ultraviolet

COVID Impact Statement

This PhD has been heavily influenced by the impact of the COVID pandemic, resulting in significant setbacks from loss of samples, invaluable time, and collaborative interactions. Despite many efforts to mitigate these effects, these challenges could not be completely overcome.

The onset of COVID restrictions coincided with the completion of imaging samples at the Rutherford Appleton Laboratories. The samples meant for correlative imaging could not be imaged or appropriately stored and became damaged during the first lockdown.

With this project initially being an experimentally based PhD, the unavailability of laboratory facilities had the largest impact, as the laboratory was inaccessible for over a year. Consequently, opportunities to engage with senior PhD students in the laboratory were lost, hindering the acquisition of valuable insights about systems and imaging methods. This all had to be learnt via the much less effective method of messaging with PhD candidates who were now on the other side of the world. Lost time in the laboratory also meant less time to collect data that would be used for the thesis. The prolonged hiatus from laboratory access had cascading effects while access was unavailable as maintenance could not be performed, causing essential equipment to break. This required a year to fix the equipment due to ongoing COVID precautions; otherwise, data would not be able to be collected.

Because of the pandemic, office spaces were unavailable for two years. During the closure of the offices, many impromptu discussions and conversations about each other's fields were missed, resulting in an absence of exchange of ideas. The resumption of activities within office spaces after two years did not fully alleviate the issues of the pandemic, as working from home had become the norm for many.

Even post-lockdown COVID disruptions continued to impact this thesis, where cases with housemates postponed work within the laboratory and preparation of samples.

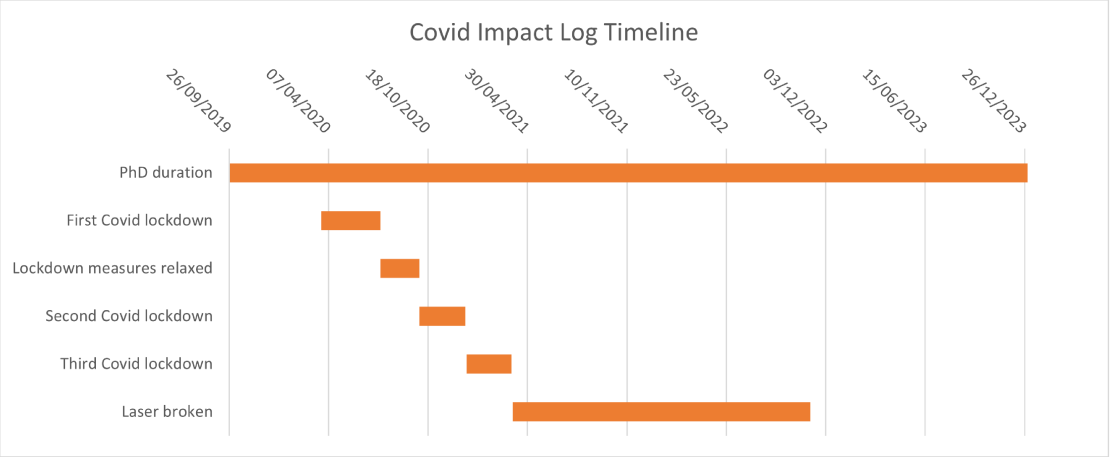

FIGURE 1: Timeline of the impact of Covid upon my PhD, where the duration of lockdowns and post-Covid effect of the laser being broken have been compared to the total duration of my PhD.

Chapter 1

Introduction

1.1 Motivation

In today's ageing society, neurodegenerative diseases, such as Alzheimer's disease, are becoming evermore present. Techniques to image neurons are therefore becoming more essential to assist in this field. Imaging neurons is not a simple task; neurons have features on the nanoscale and the smallest features of neurons have been shown to be sensitive to high-energy photons. With the linkage errors involved when using fluorophores being comparable to the size of some features of neurons, fluorescence-based techniques are, therefore, limited.

A simple way to resolve smaller features has always been to use a shorter wavelength. This is described by Abbe's limit, where the smallest resolvable feature is defined by:

$$R = \frac{\lambda}{2\mathrm{NA}} \tag{1.1}$$

where λ is the wavelength of the light, and NA is the Numerical Aperture (NA) of the imaging system. From this, it is clear that reducing λ reduces the size of the smallest resolvable feature.

High-Harmonic Generation (HHG) can be used as a lab-based and high-spatial-coherence XUV source, making it a short wavelength and accessible source. Harmonic generation has been used for decades (2), beginning with the non-linear generation of harmonics and the discovery of second-harmonic generation (SHG) in 1961 (3), and progressed

with the third to eleventh harmonic orders being generated in 1977 (4). HHG has now been shown to reach energies over 3keV, allowing for generation of radiation with sub-nanometer wavelengths (5)(6). Due to the characteristics of refractive lenses in the XUV regime, conventional lens-based imaging is not feasible. Mirrors can also focus a beam, but with the difficulties of polishing a spherical mirror to the precision required to prevent mirror aberrations affecting short wavelengths, spherical mirrors are very difficult to make. The precision a mirror needs to be smooth to can be explained by the phase shift induced by the different heights of a rough mirror,

$$\Delta\phi = \frac{4\pi h cos(i)}{\lambda} \tag{1.2}$$

where $\Delta\phi$ is the phase difference between beams reflected at the peak height of the mirror and the lowest trough of the mirror, h is the distance from the trough to the peak height of the mirror, i is the incident angle of the beam on the mirror, and λ is the wavelength of the beam. For $\Delta\phi \leq \frac{\pi}{2}$ the previous equation can be rearranged to:

$$h \leq \frac{\lambda}{8cos(i)}. \tag{1.3}$$

Therefore the surface aberrations for the 29.6 nm wavelength laser used throughout this thesis would need to be less than 3.7 nm .

Coherent Diffractive Imaging (CDI) is a technique that can image objects without lenses or mirrors; however, CDI has many limitations. Ptychography is a form of CDI that can overcome these limitations. This thesis will demonstrate the power of ptychography for high-resolution imaging and the developments to improve this further.

1.2 Contents of the Thesis

In Chapter 2, the fundamentals of imaging will be introduced along with the basics of conventional lens-based imaging. This will lead on to how it is possible to image without a lens and what CDI does to facilitate this will be discussed. Following this, how ptychography can recover the lost phase and the reconstructive algorithms used to facilitate this. Finally, similar resolution techniques will be compared, with the advantages and disadvantages that affect each being discussed.

In Chapter 3, the process of HHG will be explained initially from the simple three-step model to the more accurate quantum mechanical model, and the characteristics and properties required from the HHG to perform successful imaging will be discussed. This is followed by a detailed explanation of the system used to generate the high-harmonics and the equipment which performs ptychography using the Extreme Ultraviolet (XUV) beam.

Chapter 4 will demonstrate a more detailed understanding of the probes used with ptychography. This will also include methods used to quantitatively measure the resolution of reconstructions, from the Fourier ring correlation (FRC), to a more detailed Fourier line correlation (FLC) that considers direction when calculating the resolution. Then follows an explanation of the simulation used to gather data and investigate the effects of multiple parameters on the resolution of the reconstructed objects. Multiple parameters will then be investigated using this simulation, giving a greater insight into the fundamentals of ptychography and what improves the resolution of reconstructed objects. Developing from previous research, an attempt at building upon super-resolution will be reported. Finally, the best aperture for the best probe will be explored when imaging with XUV ptychography.

In Chapter 5, correlative imaging of Structured Illumination Microscopy (SIM), Stochastic Optical Reconstruction Microscopy (STORM), Lightning, and XUV ptychography will be performed with a more detailed explanation of the requirements to perform the first three techniques and methods to determine their resolution. The chapter ends by comparing the four techniques and proposing suggestions for improving the correlative imaging performed in this chapter.

Chapter 6 sets out the mechanism behind the damage caused by hard X-ray imaging and why XUV imaging doesn't appear to cause damage. The chapter ends with an in-depth attempt to damage a sample using XUV ptychography and define the damage threshold when imaging with XUV ptychography.

Chapter 7 outlines the pertinent results of chapters 4, 5, and 6. It ends with the potential avenues for future work and further progression of how to improve XUV ptychography imaging.

Chapter 8 contains the titles of planned papers from the research within this thesis.

Chapter 2

Imaging

This chapter aims to explain the theory of imaging and why the use of XUV needs a lensless technique. This chapter will begin with an introduction to the theory of lensless techniques and how they can be taken further to improve the problems found with CDI by using ptychography. Then, the reconstructive algorithms used by ptychography will be explored in greater detail to understand how ptychography overcomes the underconstrained problem. Finally, this chapter will compare other techniques with a similar resolution to XUV ptychography.

2.1 Imaging Theory

Microscopes have been around since circa 1600, with Hans Janssen and his son Zacharias being credited for inventing the compound microscope (7). Conventional lens-based microscopes, such as the compound microscope, work by a wave illuminating the object; the light will then propagate through an objective lens that forms a real image on the other side of the lens compared to the object, and then an eyepiece can be used to further magnify the image to form a virtual image. When determining the smallest resolvable feature using (1.1), the numerical aperture is required and is defined as:

$$\mathrm{NA} = n(\lambda) sin(\theta) \tag{2.1}$$

where n is the wavelength-dependent refractive index of the medium surrounding the entrance to the objective and θ is the maximum half-angle of acceptance of the cone of the incoming beam into the objective. Modern optical systems have achieved NAs of 1.9 (8), allowing for resolutions of a quarter of the wavelength used. This is compared to a typical XUV ptychography system with a numerical aperture of 0.18, leading to three times the wavelength for resolvable features. To calculate the NA for ptychography or CDI the following equation is used:

$$\text{NA} = sin^{-1}(\frac{r}{\sqrt{d^2 + r^2}}) \tag{2.2}$$

where r is the distance from the centre of the detector to the closest edge of the detector, and d is the distance from the sample to the detector.

A more accurate measure of resolution is the point spread function (PSF); the PSF is how a pattern of light emitted from an infinitely small point in the object plane is transformed when it reaches the image plane. Images are comprised of many features that are composed of individual spatial frequencies. A wide PSF corresponds to a blurred image of low resolution and a narrow PSF corresponds to a sharp image of higher resolution. Taking the Fourier transform of the PSF results in the Optical Transfer Function (OTF); the OTF describes how the spatial frequencies will be transformed (9).

In the XUV regime, refractive lenses are difficult to produce due to the properties and characteristics of materials in this regime. In the XUV regime, materials have a short attenuation length, so the beam is heavily absorbed by the material it is propagating through. The phase shift caused by materials is not great enough for the rate of attenuation incurred to make a feasible lens. The complex refraction index of a material is defined by:

$$n = 1 - \delta - i\beta \tag{2.3}$$

where δ is the refractive index decrement, also known as the phase retardation index, and β is the absorption coefficient, also known as the extinction coefficient. δ corresponds to effects of phase and β corresponds with the attenuation of the beam. The ratio of $\frac{\delta}{\beta}$ determines the ability to create a refractive lens. It is possible for $n < 1$ as this is the phase velocity of the wave is greater than the speed of light; in this situation

the group velocity of the wave, which is the speed at which information travels in the wave, is less than the speed of light.

Fresnel zone plates (FZP) are an alternative to refractive lenses that work in the XUV regime, and they do not rely on the ratio of $\frac{\delta}{\beta}$. FZPs will be discussed later, but they have different issues that cause them not to be used.

2.2 Classical Imaging

A 4f imaging system can be used when performing classical imaging. This system uses four separate focal lengths between the input and the output plane, hence its name.

A collimated light source, such as a laser, first illuminates the object in the input plane. The light source being collimated is important as a planar wavefront is required for accurate Fourier transforms. One focal length after the input plane a lens L_1 is placed to focus the wave, producing a Fourier transform of the wave in the Fourier plane. One focal length after L_1 a filter is placed to control the spectrum of the wave; as the wave is currently represented by its frequency components a high-pass filter can be used to block low frequencies improving smaller details. One focal length after the filter another lens L_2 is placed to focus the wave one focal length away, this performs an inverse Fourier transform on the wave, returning the wave back to the spatial domain and this forms an image at the output plane (10).

2.3 Coherent Diffractive Imaging

Due to the inability to use lenses with wavelengths in the XUV regime, coherent diffractive imaging (CDI) can be used to image an object with an XUV beam. Initially, the idea of using diffraction patterns to recover the image of an object began in 1912 with father William Henry Bragg and son William Lawrence Bragg, and was for periodic crystalline structures (11). Two years later, William Lawrence Bragg published a paper proving that Laue's measurements showed diffraction patterns and how to interpret the diffraction patterns (12). In 1952 Sayre proved that the object's structure could be recovered from the diffraction patterns (13). When not using a lens the intensity of a

scatter pattern is measured and the phase information of the scatter pattern is lost. In 1972, Gerchburg and Saxton proposed an algorithm, originally for electron microscopy, to recover the lost phase from an intensity measurement, now commonly known as Error Reduction (ER). In 1982, Fienup then proved that only the Fourier modulus was required to reconstruct the object and improved upon the ER phase reconstruction algorithm with Hybrid Input-Output (HIO), which overcame the 'local minimum' problem (14), where the 'local minimum' is the lowest point in phase space for a region but not the lowest point in the whole of phase space. In 1982, Bates proved that unique solutions to the phase retrieval problem existed for objects with enough Fourier modulus sampling (15). However, isolated objects that have been uniformly shifted in position and the Hermitian complex conjugate of the objects would also be valid solutions for these phase reconstruction algorithms. In 1988, Miao, Sayre, and Chapman proved that a solution could be found as long as the total number of intensity measurements in the image plane exceeded the number of unknown points in the object plane (16). CDI requires the spatial coherence of the beam to be twice the width of the object being imaged (17):

$$X_c = 2W \tag{2.4}$$

where X_c is the lateral coherence width, and W is the width of the object. Now considering the Nyquist-Sharron sampling theorem, to capture all the information of a signal it must be sampled at least twice per period, as shown by the following equation:

$$\Delta x = \frac{\lambda z}{N \Delta q} \tag{2.5}$$

where Δx is the sampling interval in the object plane, λ is the wavelength of the beam, z is the distance between the sample and detector, N is the number of pixels in a row or column, and Δq is the pixel size.

With these developments, it was possible to perform lensless imaging by recovering the lost phase by just measuring the intensity of the scatter pattern from an object, where recovering the phase is the process of calculating the phase for phaseless intensity measurements of scatter patterns. Two constraints and how the planes are connected are

needed to perform CDI: the constraint in the object plane, usually a border around the object to reduce the number of unknown points, and a constraint in the image plane, which is the measured intensity. The connection between the image and object plane is a transform function, such as a Fourier transform.

2.3.1 Image Reconstruction

You cannot directly get the phase from the intensity measurement of the scatter pattern as you only have N data points but have 2N unknowns, the amplitude and the phase of each pixel in the diffraction pattern. Iterative algorithms are used to recover the phase of measured scatter patterns. To recover the phase, these algorithms initially estimate the phase of the image to form a prediction of the image. Then, the algorithm transforms the image into the object plane and the constraints are applied. Then, the algorithm transforms the object into the image plane and constrains the image prediction. Over many iterations, the algorithms reduce the error of the image's phase and the error of the object.

2.3.1.1 Gerchburg Saxton/Error Reduction

ER is the simplest of the algorithms described. ER entails repeating the following four steps (18):

1. Fourier transform an estimate of the object exit wave function into the Fourier plane.
2. Apply the Fourier constraint; this is replacing the modulus of the Fourier plane wave function with the measured modulus of the Fourier plane wave function.
3. Inverse Fourier transform the Fourier plane wave function back to the object plane.
4. Apply the object constraint; this is replacing the object exit wave function's modulus with the constraint's modulus, such as a border or the autocorrelation.

The requirements to perform ER are an intensity measurement of the scatter pattern, the object constraint, and the transfer function. The intensity measurement is the Fourier

plane constraint, and the object plane constraint is usually an opaque border. With these constraints, ER begins by calculating the amplitude of the diffraction pattern for the intensity measurements and multiplying this image estimate with random phases for each pixel. This gives the wave function of the scatter pattern in the detector plane:

$$\psi' = |\sqrt{I'(r')}|e^{i\phi(r')} \tag{2.6}$$

where $'$ denotes the detector plane, $I'(r')$ is the measured intensity of the scatter pattern at position r', $\phi(r')$ is the phase of the wave function at position r'. With an estimate of the wave function of the scatter pattern, it is now possible to calculate the exit wave function of the object in the object plane by taking the Fourier transform of the estimate of the wave function of the scatter pattern:

$$\psi = \mathcal{F}[\psi']. \tag{2.7}$$

The object constraint is applied to the object exit wave function estimate. The commonly used object constraint, the border, involves setting the amplitude of the object exit wave function to zero where the border constraint is and leaving the non-constrained pixels, inside the border, to be the same value:

$$\psi(r) = \begin{cases} 0, & \text{if } r \in A \\ \psi(r), & \text{if r} \notin A \end{cases} \tag{2.8}$$

where r is a position of the object wave function, and A denotes the area in which the constraint applies. Afterwards, the object wave function is then inverse Fourier transformed back to the image plane:

$$\psi'(r') = \mathcal{F}^{-1}[\psi(r)] \tag{2.9}$$

and this completes an iteration of ER. Future iterations of ER follow the previous steps, except for applying a random phase during the first step, as future iterations use the previously calculated phase. The constraints in the detector and object plane drive the changes of the wave function towards the correct solution of the phase of the scatter pattern and exit wave function of the object.

It is useful to calculate the error of the reconstructed image and object to ensure that

the algorithm is progressing or to stop the code once the desired error is reached. The Fourier error is defined by:

$$\epsilon' = \frac{\sum_{r'} |\psi'(r')|^2 - I'(r')}{\sum_{r'} I'(r')} \tag{2.10}$$

this calculates the error between the reconstructed and the measured scatter patterns to ensure the reconstructive algorithm has not caused the reconstructed scatter pattern to diverge from the measured scatter pattern. The object error calculates the convergence of the algorithm and is defined by:

$$\epsilon = \sum_{r} |\psi(r)_n|^2 - |\psi(r)_{n-1}|^2 \tag{2.11}$$

which calculates the difference between the current and the previous iteration of the object to ensure that the reconstructive algorithm is converging on a solution. These errors are used together to make sure the algorithm converges to the correct solution.

To understand how ER works, it is helpful to visualise how ER solves a simple two-constraint problem. By reducing the problem to a simple two-constraint problem, it can be shown how the algorithm uses the two constraints to arrive at the solution. Two lines will represent all the valid solutions for the two constraints. The transform between the two constraints will be the projection, the closest point on the other line. The solution to the problem is where both constraints are satisfied, where the two lines intercept.

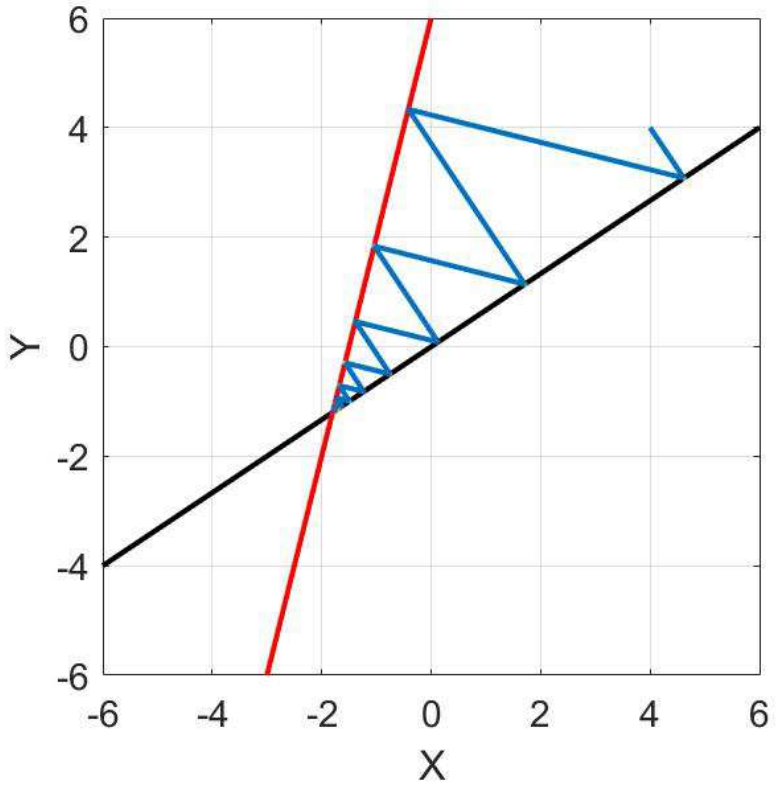

FIGURE 2.1: ER algorithm (blue line) applied to y=$\frac{2}{3}$x (black line) and y=4x-2 (red line) starting at the point (4,4), calculating the closest point alternating between lines.

From figure 2.1, it is shown that ER is applying the transform and the constraints, and over multiple iterations, it converges to the point where the lines cross. This point is the minimum distance between lines, known as the minimum, or global minimum. ER works well for problems of a single defined minimum, as it converges directly to the minimum. ER, however, struggles where the constraints result in multiple 'local minima', such as in the following example where one of the lines has multiple curves.

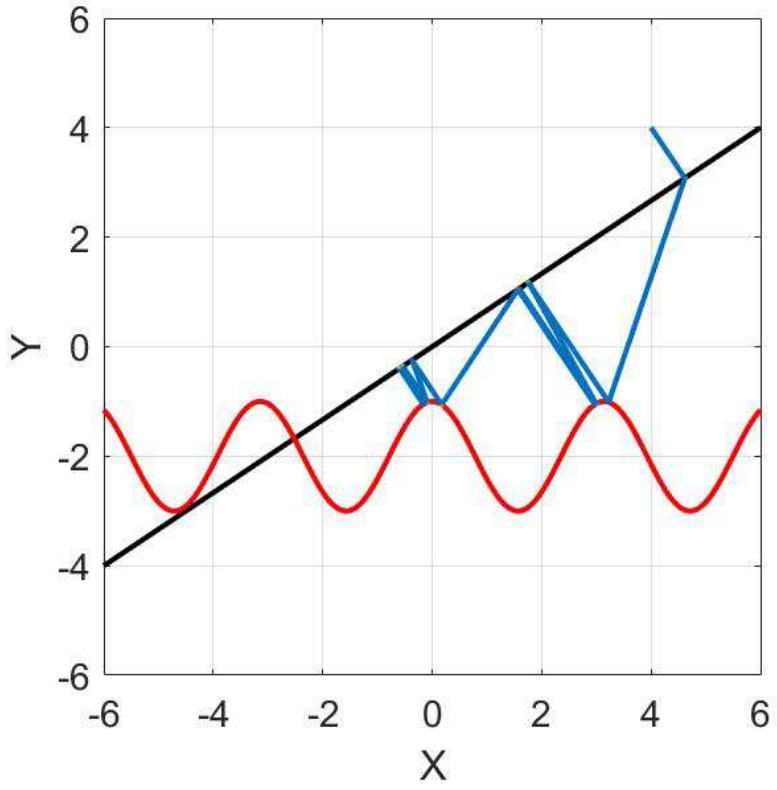

FIGURE 2.2: ER algorithm (blue line) applied to y=$\frac{2}{3}$x (black line) and y=cos(2x)-2 (red line) starting at the point (4,4), calculating the closest point alternating between lines.

Figure 2.2 has the situation of multiple 'local minima'. A 'local minimum' is where the two constraints are closest for a region but is not the global minimum. Here, the algorithm gets trapped in a local minimum. ER just about escapes the first local minimum of this problem but is trapped by the second; however, if the initial guess had been closer to the global minimum than a local minimum, ER would have converged to the global minimum and arrived at the correct solution.

2.3.1.2 Hybrid Input Output

HIO is an algorithm that can overcome the 'local minimum' problem by using information from previous iterations to influence the current iteration. HIO is similar to ER, following the same steps as ER, but updating the constraint in the fourth step using information from the previous iteration to prevent stagnation within local minima. (18).

$$\psi(r)_{n+1} = \begin{cases} \psi(r)_n, & \text{if } r \in A \\ \psi(r)_n - \beta\psi(r)_{n-1}, & \text{if r} \notin A \end{cases} \tag{2.12}$$

where β is the fraction of the previous iteration used in calculating the current iteration. It is typical to use values between 0.5 and 1, and if a value of 1 is used then HIO is reduced to ER as the algorithm no longer uses information from previous iterations.

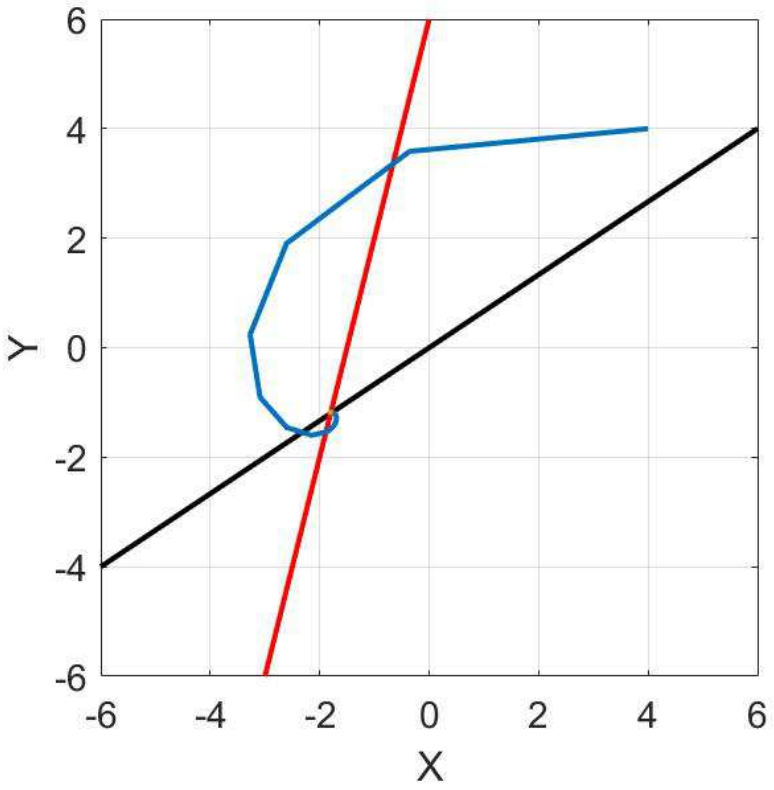

FIGURE 2.3: HIO algorithm (blue line) applied to y=$\frac{2}{3}$x (black line) and y=4x-2 (red line) starting at the point (4,4), calculating the next point using equation (2.12) with $\beta = \frac{2}{3}$.

From figure 2.3 is it clearly shown that HIO can find the solution to the simple one minimum problem. The advantage of HIO is that it can overcome local minima.

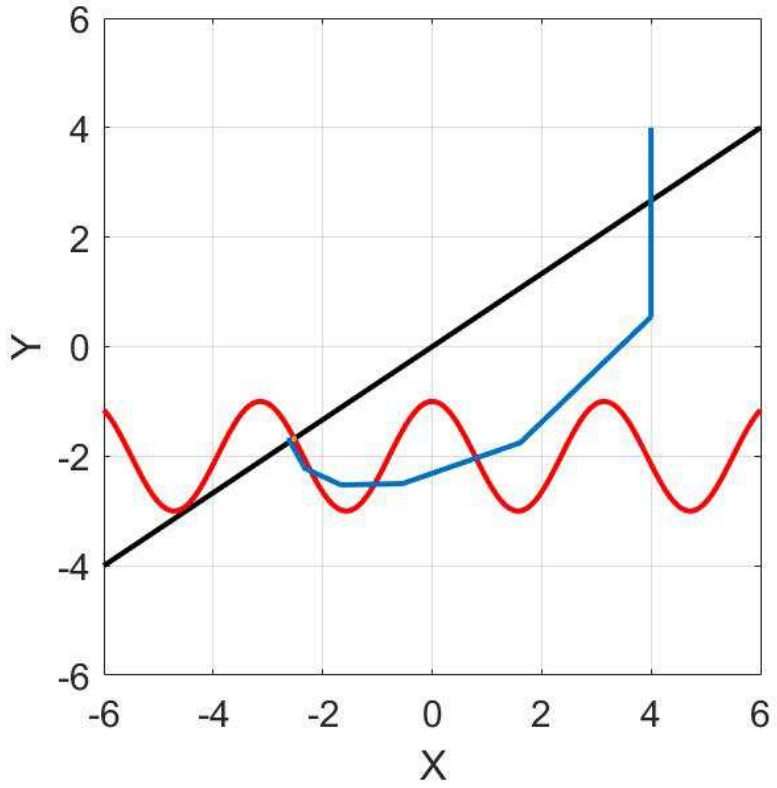

FIGURE 2.4: HIO algorithm (blue line) applied to y=$\frac{2}{3}$x (black line) and y=cos(2x)-2 (red line) starting at the point (4,4), calculating the next point using equation (2.12) with $\beta = \frac{2}{3}$.

From figure 2.4 it is shown that HIO was able to pass the local minimum and converge on the global minimum of this constraint problem. This technique of using the information of past iterations in calculating the current iteration is a useful tool that will be used later to improve the reconstructions by avoiding 'local minima'. A problem of HIO, however, is that HIO does not converge directly to the solution but circles towards it. This can be solved by increasing β towards 1 once the solution is the closest minima, as ER converges to the nearest minima.

ER and HIO suffer from a degeneracy problem. When reconstructing an image, the true solution is identical to its Hermitian complex conjugate. ER and HIO are unable to distinguish between the two, and the reconstruction will only solve one at random. This is true because the Fourier transform of an exit wave function $\psi(r)$ is equal to the Fourier transform of an image rotated by $180^\circ \psi(-r)$. To overcome this degeneracy, Fienup proposed reduced support method as a solution (19). This new object constraint, or mask,

would use a subset of the correct mask that have at least one edge, wasn't centrosymmetric, and used for a few iterations. This worked because after a few iterations the algorithm would converge on one of the two solutions, and once this had occurred the correct mask could be used once again to converge on to the correct solution.

In 2003, Marchesini proposed a new method of solving the degeneracy problem by introducing the 'shrink wrap' method, so named because the constraint appears as if you are shrink-wrapping the constraint around the reconstructed object (20). This method involves taking a Gaussian blur of the object, the convolution of the object, and a 2-D Gaussian to which a threshold is applied. As the iteration progresses, the Gaussian blur is retaken to reduce the size of the object constraint to prevent convergence to the wrong solution and reduce the error of the reconstruction.

Though these solutions to the degeneracy problem improved the reconstructions, they were not entirely robust, and the issue of requiring the spatial coherence of the beam to be greater than the width of the sample being imaged remains. This issue also constrains the size of the sample being imaged. Both of these were solved with a new technique that had been proposed to improve reconstructions.

2.4 Ptychography

The original idea of ptychography was proposed over 50 years ago by Hoppe and Strube (21)(22)(23). The first experimental use of ptychography in two dimensions was in 1996 by Chapman using the Wigner-distribution deconvolution method (24). Later in 2007 the uptake on the use of hard X-rays to perform ptychography was begun by Rodenburg (25). Finally, in 2014 the use of XUV in ptychography happened by using HHG to generate XUV of 30 nm by Seaberg (26).

Ptychography uses a probe, the beam profile illuminating the sample, to create a scatter pattern that will be measured. The sample is moved, and another scatter pattern is measured; an overlap on the object between the current and the previous probe is required. This process is repeated until all of the scatter patterns of the scan area have been measured. A reconstruction algorithm is then used to recover the lost phase. The image constraints of ptychography are the scatter pattern's measured intensity and the object constraint is that the object in the overlapping regions of the probes must

be equal. The overlapping object regions collapse the degeneracy of two solutions, as only one solution is correct for both regions in the overlap, and this doesn't allow the hermitian complex conjugate to exist as a solution. (27)

Ptychography is a relatively new technique, and reconstruction algorithms are rapidly developing. The two new reconstruction algorithms used in this thesis are Maximum-Likelihood (ML) and Difference Map (DM). Newer techniques have and are being developed, such as Relaxed Averaged Alternating Reflections (RAAR), and Relaxed Averaged Successive Projections (RASP) (28).

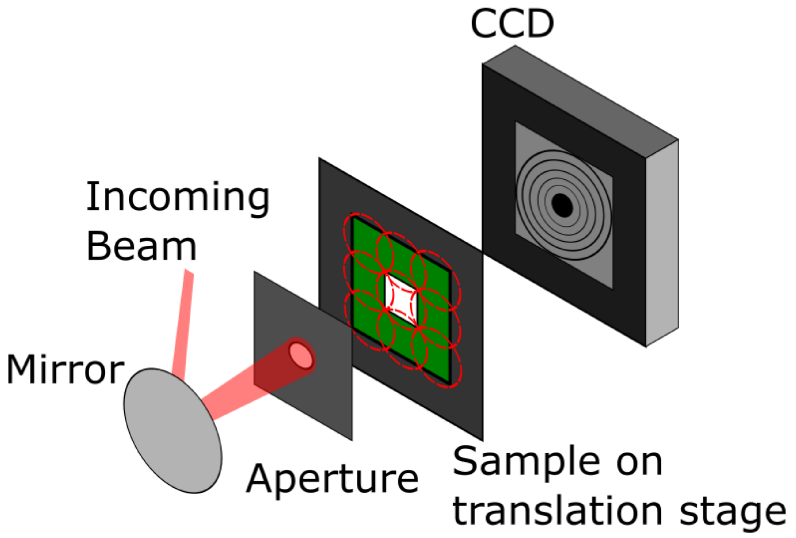

FIGURE 2.5: Diagram of how ptychography is implemented within our setup. Firstly, the beam is reflected towards an aperture; secondly, multiple probe locations will be separately illuminated with overlap; finally a scatter pattern is measured on the CCD.

The following sections give the basic explanations of the techniques used for reconstruction throughout this thesis, and the techniques that they are built upon.

2.4.1 The Difference Map

The difference map was first proposed by Elser (29) and later improved by Thibault (30). DM applies the constraints to both sets of solutions at the same time and then uses the difference between the constraints to calculate the next iteration. DM is a batch method of a reconstructive algorithm where it is applying both constraints at the same time. Batch methods can run in parallel so that the data reconstruction can be faster. DM is the reconstructive algorithm initially used in our reconstruction process

as it is more robust to noise than sequential techniques and will converge faster to the solution. HIO, as described before, is a particular case of DM. DM still retains the feature of avoiding local minima and still converges towards the global minimum. The DM is defined by (29):

$$D = 1 + \beta\Delta \tag{2.13}$$

and

$$\Delta = \pi_1(f_2) - \pi_2(f_1) \tag{2.14}$$

where π_i are the two projections between constraints, f_i are the maps for real and Fourier space that π_i are composed on, and Δ is the difference of the two projection operators. A fixed point of D, p^* is defined by $\Delta(p^*) = 0$, where applying the difference map to p^* does not change it, also expressed as:

$$(\pi_1(f_2)) = p_1 \cap p_2 = (\pi_2(f_1)). \tag{2.15}$$

When using DM to reconstruct an object, the following equation is used:

$$p_{n+1} = p_n + \beta D(p_n) \tag{2.16}$$

where p_n are the values of p for the current iteration, and p_{n+1} are the values of p for the next iteration. Starting from an initial point $p(0)$ the DM from (2.13) is applied repeatedly until a fixed point is found (30). The convergence of p can be monitored by calculating the norm of the differences:

$$\epsilon_i = ||\Delta(p(i))||. \tag{2.17}$$

2.4.2 Extended Ptychography Iterative Engine

Ptychography Iterative Engine (PIE) is a sequential method of reconstruction algorithms. PIE applies one constraint at a time to calculate the next iteration (31). Sequential methods cannot be run in parallel but are more memory efficient and will converge faster to the solution when converging on the correct solution, giving a better reconstruction. PIE is another reconstruction algorithm that can be used in phase retrieval. PIE and ER are linked in a way that is similar to the link between DM and HIO. PIE starts with an estimate of the object exit wave function, then transforms this wave function into the Fourier plane. The Fourier constraint is then applied to the Fourier plane wave function, after which the updated Fourier plane wave function is transformed back to the object plane. The object constraint is then applied, and this process is repeated.

Extended Ptychography Iterative Engine (ePIE) is an improvement on PIE. PIE does not update the probe when reconstructing, and ePIE updates the probe estimate between iterations to improve the reconstruction. ePIE consists of the following six steps (32)(33):

1. An initial estimate of the object and probe exit wave function at each probe position ψ_j is created by multiplying the object function $O(\mathbf{r})$ with the shifted probe function $P(\mathbf{r} - \mathbf{R}_j)$.

$$\psi_j(\mathbf{r}) = O(\mathbf{r})P(\mathbf{r} - \mathbf{R}_j) \tag{2.18}$$

   where $\mathbf{r}$ is the real space coordinate vector, and $\mathbf{R}_j$ is the relative position of the probe to the object for the j^{th} probe position.

2. The object and probe exit wave function is then propagated to the Fourier plane using a Fourier transform

$$\psi'_j = \mathcal{F}[\psi_j] \tag{2.19}$$

   Then the modulus constraint is applied to the Fourier plane wave function by replacing the modulus using the measured intensity at the j^{th} probe position.

$$\psi'_j = \sqrt{I_j}\frac{\psi'_j}{|\psi'_j|} \tag{2.20}$$

3. The updated Fourier plane wave function is then propagated back to the object plane using an inverse Fourier transform.

$$\psi_j^u = \mathcal{F}^{-1}[\psi'_j] \quad [1] \tag{2.21}$$

4. The updated object and probe exit wave function is used to update the object and probe functions using:

$$O_{j+1}(\mathbf{r}) = O_j(\mathbf{r}) + \alpha \frac{P_j^*(\mathbf{r} - \mathbf{R}_j)}{|P_j(\mathbf{r} - \mathbf{R}_j)^2_{max}|}(\psi_j^u(\mathbf{r}) - \psi_j(\mathbf{r})) \tag{2.22}$$

$$P_{j+1}(\mathbf{r}) = P_j(\mathbf{r}) + \beta \frac{O_j^*(\mathbf{r} - \mathbf{R}_j)}{|O_j(\mathbf{r} - \mathbf{R}_j)^2_{max}|}(\psi_j^u(\mathbf{r}) - \psi_j(\mathbf{r})) \tag{2.23}$$

where α and β are coefficients that alter the step size of the update.

5. Steps 1-5 are repeated for all probe positions j to update all the estimates of the object and probe exit wave functions.

Updating the probe provides an accurate amplitude and phase of the probe as well as leading to faster convergence (32).

2.4.3 Maximum likelihood

Maximum likelihood (ML) improves upon ePIE by using gradient descent to find the minima with a grouping of scan positions (34). ePIE updates the object and probe wave function at one probe position at a time, ensuring the next object and probe wave function is more accurate; however, this is slow. ML selects a group of probe positions to update the object and probe wave function simultaneously. This results in a less accurate update for the group of probe positions but is much faster. There are two types of ML, Maximum Likelihood stochastic (MLs) and Maximum Likelihood cluster (MLc). The stochastic grouping uses random probe positions, and the cluster grouping uses nearby probe positions. This technique is slower to converge per iteration but is faster to converge in real time.

[1] In the original paper ψ' was used to denote the updated object and probe exit wave function; however, this convention conflicted elsewhere in this thesis and has been replaced by ψ^u to denote the updated exit wave function

2.4.4 Algorithm comparison

When discussing these algorithms, comparing the error of the reconstructions and the speed at which they reconstruct data is useful. This will be conducted by running 100 iterations for purely DM, purely MLs, and an equal split of DM and MLs. The Fourier error of the reconstructions will be used to calculate the quality of the reconstructions by using:

$$\epsilon_{Fourier} = \frac{(A_{reconstructed,n} - A_{measured,n})^2}{0.5^2} \tag{2.24}$$

where $A_{reconstructed,n}$ is the modulus of the reconstructed wave function of the scatter pattern at the n^{th} scan position, $A_{measured,n}$ is the modulus of the measured wave function of the scatter pattern at the n^{th} scan position, and 0.5^2 is the correction for Poisson noise if single photon precision is expected. (2.24) calculates the difference between the measured wave function and the reconstructed wave function at the detector.

Using real data with a double slit aperture (5x1 μm slits spaced 4 μm from centres) to image 1 μm polystyrene spheres, it is possible to compare the effect of different reconstructive algorithms.

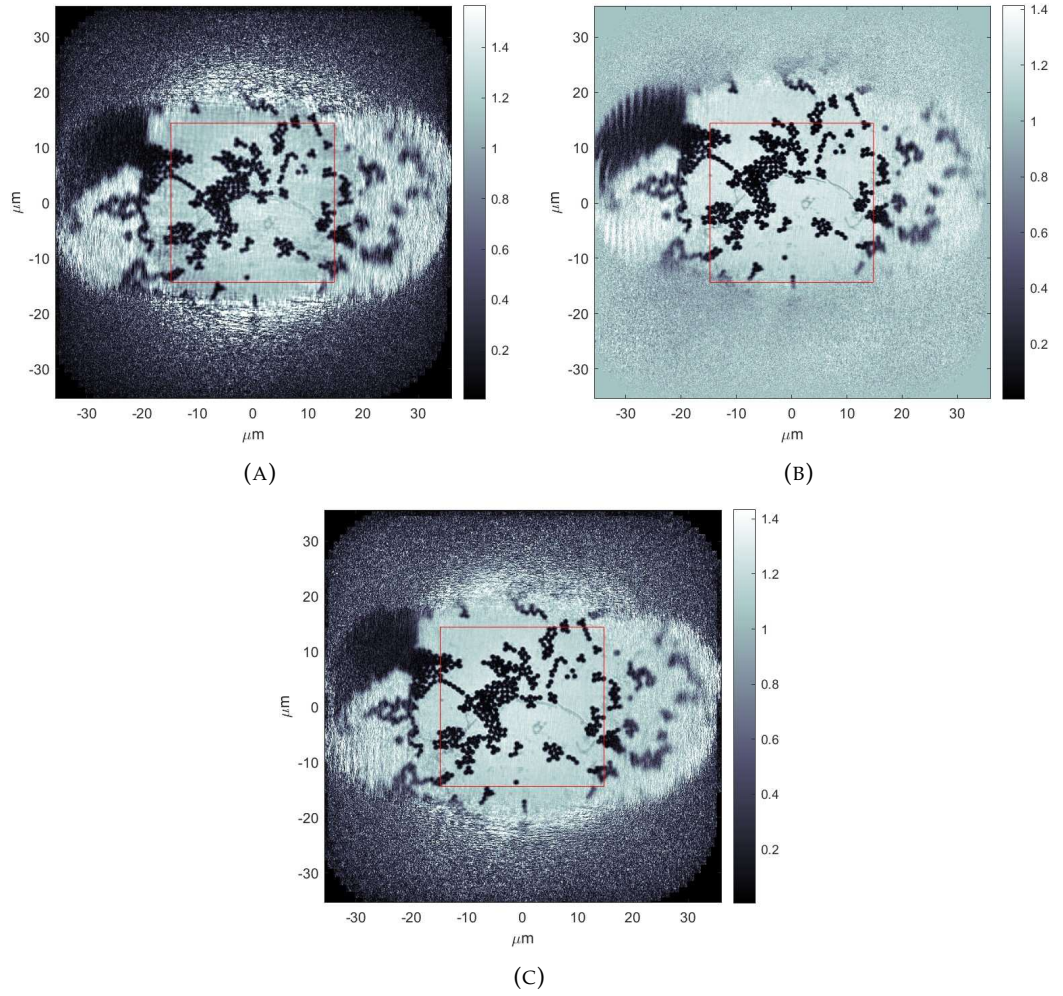

FIGURE 2.6: Comparison of reconstructive algorithms on real data on 1 μm polystyrene spheres with a double slit aperture (5x1 μm slits spaced 4 μm from centres). (A) reconstructed data using 100 iterations of DM, (B) reconstructed data using 100 iterations of MLs, (C) reconstructed data using initially 50 iterations of DM followed 50 iterations of MLs.

The images from figure 2.6 are reconstructions from data I took using an HHG source. These data were taken using my system to image two sets of data of 1 μm polystyrene spheres with a double slit aperture (5x1 μm slits spaced 4 μm from centres). One of the data sets was then reconstructed with different ratios of reconstructive alogthrims to compare the speed and effectiveness of the different ratios of DM and MLs.

From figure 2.6 it can be seen without error metrics that the reconstructions using MLs are better, which is corroborated by the Fourier error, where the Fourier errors are (A) is 6.43, (B) is 1.61, and (C) is 1.60; though the difference between (B) and (C) is not statistically different enough for (C) to be better error-wise. Using no MLs is therefore detrimental to the quality of the reconstruction, and why the reconstruction speed

needs to be accounted for. The total time for the entire code to run for (A) is 20 s, (B) is 38 s, and (C) is 29 s. When removing the time used by the code not on the reconstructive algorithms, the new times are (A) is 13 s, (B) is 31 s, and (C) is 22 s. DM, therefore, is over twice as fast as MLs, which is why the combination of the two algorithms is used.

Using a combination gives the benefits of both methods; DM converges quickly near the global minimum and the code being fast to run, and MLs converging towards the local minimum.

The code used here, PtychoShelves, was written by researchers at the Paul Scherrer Institute to reconstruct ptychography data (35). The reconstructive algorithm DM can be completely parallelised leading to faster reconstruction times. MLs can parallelise groups of scan positions, therefore, reconstruction times depend on the group sizes, but group sizes of 20-40 tend to give the best reconstructions.

2.5 High-Resolution Imaging Techniques

Many other techniques can resolve features to a similar resolution as XUV ptychography, currently around a maximum resolution of 50 nm using our system at a wavelength of 29 nm, found by previous group member Dr Peter Baksh and Dr Michal Odstrčil (36). This section will explore these other techniques while explaining their advantages and disadvantages. These other techniques can be categorised as X-ray-based, synchrotrons, fluorescence-based, electron microscopy, ion beam, scanning probe microscopy, and superlens-based.

2.5.1 X-ray-based Techniques

2.5.1.1 HHG Ptychography

Ptychography has been described in greater detail earlier in this chapter, and this section will explore the state of the art of HHG ptychography. Briefly, HHG uses a driving laser to excite atoms to generate higher harmonics of the driving laser to achieve lower wavelengths, HHG will be explained in greater detail later in the thesis. Using a 13.5 nm HHG source the Kapteyn-Murnane group achieved resolutions of sub 20 nm (37).

2.5.1.2 X-ray Holography

Holography was first proposed by Gabor in 1948 (38). The technique of holography relies on the interference pattern created between the wavefront from scattered light from an object and a reference wave. The interference between the scattered light and reference beam creates a hologram (39). The hologram is then measured by a detector, and this pattern encodes the amplitude and phase of the scattered wave from the object. The hologram can then be multiplied by the reference wave in the hologram plane to retrieve the diffraction pattern in the image plane; the diffraction pattern can then be backpropagated to retrieve the reconstructed image of the object at multiple distances (40). Holography has been able to achieve sub 1 nm spatial resolution (41).

2.5.1.3 Conventional X-ray Imaging

Attenuation X-ray imaging measures the transmitted intensity of the beam after being absorbed by the object, and the intensity pattern gives an image of the object. The resolution of attenuation-based X-ray imaging is determined by the pixel size of the detector being used to image the transmission. A resolution of less than 25μm has been recorded (42).

Phase-contrast imaging measures the phase variations caused when passing through the object, where the different refractive indices will change the direction of propagation of the X-rays (43). For objects that attenuate the beam weakly, measuring the phase contrast provides higher resolution. This improved sensitivity of phase-contrast imaging allows the imaging of samples that absorption-based X-ray imaging cannot, such as tissue, since the tissue is weakly absorbing. A disadvantage of phase-contrast imaging is that it requires thin samples, as low attenuation is required (44). Phase-contrast imaging can resolve features of around 50nm (45).

2.5.2 Synchrotrons

Synchrotrons are large facilities that generate tunable x-rays. To generate the X-rays the synchrotrons first accelerate electrons around a circular track, the electrons are guided and contained by the magnets. The electrons pass through an undulator, wiggler or

electron bender, which accelerate the electrons to produce x-ray radiation. The wavelength of the beam is dependent on the acceleration of the electron (46). Since synchrotrons are large and expensive, they have low availability. The high flux of X-rays generated by synchrotrons can also damage thin samples, such as biological samples, therefore repeated imaging would result in a different image.

2.5.2.1 Synchrotron Microscopy

When the synchrotron beam is monochromatic a Fresnel Zone Plate (FZP) can be used to focus the beam. FZPs are a type of lens that can focus monochromatic beams and can work in the X-ray regime. FZPs consist of concentric circular rings of increasing size, the distance between rings decreases as the distance from the centre increases. For an FZP to produce constructive interference at a certain distance with a certain wavelength the circular rings need to have radii defined by the following equation:

$$r_n = (fn\lambda)^{1/2}(1 + \frac{n\lambda}{4f})^{1/2} \tag{2.25}$$

where n is an integer defining which ring, f is the distance from the centre of the FZP to the focus of the FZP, and λ is the wavelength of light the FZP is designed for (47). Typical binary FZPs have efficiencies around 10%, but using more advanced fabrication techniques they can reach 95% efficiency (48).

With FZPs synchrotron X-rays can be used as a source for scanning microscopy (49). FZPs have low efficiency, so the measured flux is reduced; FZPs are also expensive. Synchrotron microscopy can resolve features of 15nm, where the photon energies used ranged from 250eV to 1.8keV (50).

2.5.2.2 Synchrotron X-ray Tomography

Synchrotron X-ray Tomography (SXT) can measure the three-dimensional structure of a sample. In SXT the sample is measured in multiple orientations. The transmitted beam passes onto a scintillator before being measured by a CCD. These results are reconstructed into a set of 2-D layers which form a 3-D image (51). Synchrotron microscopy can resolve features of sub 50nm (52).

2.5.3 X-ray Free Electron Laser

An X-ray Free-Electron Laser (XFEL) generates X-rays similarly to synchrotrons. XFELs generate x-rays via an undulator, which can be over 100m long. Undulators have higher coherence but lower flux beams compared to wigglers. Most XFELs do not accelerate electrons in a recycling ring; instead, XFELs accelerate electrons with a Linear Accelerator (LINAC). LINACs bunch the electrons more than a synchrotron (53). XFELs can reach a brilliance of over $1 \times 10^{33} photons/s/mm^2/mrad^2/0.1\%BW$, which is 1×10^{10} greater than a typical synchrotron. XFELs can also generate sub-femtosecond pulses (54). These pulses can image extremely quick processes such as the formation of molecules. XFELs suffer from spatial, spectral and temporal instability, as they rely on self-amplified spontaneous emission. New systems are being developed which use a seed to initiate generation, though they are at lower fluxes at the moment (55). XFELs mostly image using single-shot CDI as the brilliance of the beam damages the sample too much for more measurements.

2.5.4 Fluorescence-Based Techniques

2.5.4.1 Confocal Microscopy

Confocal microscopy is a more specialised version of wide-field fluorescence microscopy. Where wide-field fluorescence microscopy allows all light from the sample to reach the camera, confocal microscopy uses a pinhole aperture to filter out light from different focal planes. By filtering out the light from different focal planes the resolution of the image can be improved; however, reducing the pinhole's size reduces the incoming amount of photons, this is why a photomultiplier is used to increase the signal-to-noise ratio. A confocal microscope can then image the object by scanning over the object(56). Confocal microscopy has a typical resolution of 180nm.

2.5.4.2 Structured Illumination Microscopy

Structured Illumination Microscopy (SIM) is a fluorescence-based imaging technique. A beam is split, and the two parts of the beam interfere at the focal plane of an objective to form striped illumination patterns. This striped illumination is superimposed with

the sample to produce a Moiré pattern. A Moiré pattern is the apparent lines formed when similar gratings overlap. Multiple Moiré patterns are measured from multiple rotations and translations of the sample. Using the multiple Moiré patterns, a reconstruction algorithm recreates an image of the sample (57). The main disadvantage of SIM is that it images the fluorescent material attached to the sample instead of the sample directly. This issue becomes more apparent the smaller the feature that is resolved. SIM can resolve features at $\lambda/4$ (58). A fluorophore's emission also diminishes over time, resulting in increasingly noisy images.

2.5.4.3 Stochastic Optical Reconstruction Microscopy

Stochastic Optical Reconstruction Microscopy (STORM) images by activating and deactivating fluorophores. Measuring the Point Spread Function (PSF) of the emission from the fluorophores, it is possible to calculate the centre position of the PSF (59). The calculated centre position of the PSF has a standard deviation of:

$$\sigma = \frac{R}{\sqrt{N}} \tag{2.26}$$

where σ is the standard deviation, R as defined in equation (1.1) as Abbe's limit, and N is the number of photons measured. Initially, all fluorophores are deactivated by a strong pulse of wavelength A, to induce the fluorophores into the triplet state, to ensure no fluorophores are in the singlet state. In the triplet state, the fluorophores will randomly switch between the fluorescent and nonfluorescent states. Wavelength B is then used to cause the fluorophores in the fluorescent state to fluoresce. STORM requires a small amount of the fluorophores to be in the fluorescent state at a given moment so that the individual fluorophores' PSFs do not overlap (60). Over multiple images, the individual PSF locations can be reconstructed. Using STORM it is possible to resolve features at a 20nm resolution (61). STORM can beat the diffraction limit by calculating the PSFs centres. As STORM uses fluorophores, it has the same disadvantages as SIM, with increasingly noisy images from fluorophore degradation.

2.5.4.4 Stimulated Emission Depletion

Stimulated Emission Depletion (STED) is a dual-beam system where there is a depletion beam and an excitation beam. The excitation beam is to induce fluorescence; the depletion beam is doughnut-shaped, overlapping the outermost region of the excitation beam. This overlap is to induce depletion of the excited state by stimulated emission before fluorescence is possible. This causes only the innermost region to fluoresce, effectively reducing the point spread function. STED can overcome the diffraction limit and resolve features as small as 20nm. This technique uses fluorescence, so has the same disadvantages as SIM and STORM. The intensity of the depletion beam can also damage the outermost region when imaging. (62)

2.5.4.5 Minimal Photon Fluxes

Minimal Photon Fluxes (MINFLUX) is an improvement on STED. MINFLUX is a single-beam system that only has a doughnut-shaped beam. The fluorophores will fluoresce proportional to the strength of the beam on the fluorophore. To find the location of a fluorophore, measurements of the flux count are collected, where the minimum flux will be collected when the centre of the beam is at the fluorophore. Multiple measurements are collected for a single fluorophore to determine the location of the fluorophore. The size of the doughnut-shaped beam can be large to quickly find the approximate location of the fluorophore, and then the size of the beam can be reduced to improve the resolution. MINFLUX is both faster and causes much less photobleaching compared to STED (63). The resolution of MINFLUX is 1nm for fixed structures and 3nm for living cells.

2.5.5 Electron Microscopy

2.5.5.1 Transmission Election Microscopy

Transmission Electron Microscopy (TEM) uses the transmission of electrons through a sample to image. Since electrons have such a short wavelength a TEM can resolve fine detail while being limited by Abbe's limit. Samples being imaged by TEMs need to be

transparent to electrons, usually with thicknesses of less than 100nm; thicker samples require higher electron energies. TEMs can resolve features of 0.2nm. (64)

2.5.5.2 Scanning Electron Microscopy

Scanning Electron Microscopy (SEM) scans a sample with a focused beam of electrons and the scattered electrons are used to image the sample. A magnetic lens is used to focus a beam of electrons onto the sample, and the current of re-emitted secondary electrons is collected. The current is dependent on the material and structure of the sample. After accounting for the material, the current can be used to produce an image of the sample. SEM requires the sample to be conductive for the electron current to pass and insulating materials often need to be coated by a conductive material (65). SEM can resolve features of 10nm (66).

2.5.6 Ion Beam Microscopy

2.5.6.1 Helium Ion Microscopy

Helium Ion Microscopy (HIM) uses a focused beam of helium, which is similar to SEM, where the most common signal to form the image is from secondary electrons re-emitted after the helium beam. HIM can use higher energies than SEM, as there is less interaction with the sample when imaging with a helium atom compared to an electron. The best spot size is predicted to be 0.25nm resulting in a resolution of 0.25nm (67).

2.5.7 Scanning Probe Microscopy

2.5.7.1 Scanning Tunneling Microscopy

Scanning Tunnelling Microscopy (STM) uses electron tunnelling as a measure to determine the surface of a structure. Holding a sharp tip close to a conductive surface, electrons can tunnel from the tip to the surface. This tunnelling can be measured as a current. By moving the tip laterally and maintaining a constant current the height of a surface can be measured. STM can measure samples at a lateral resolution of 0.1nm and

depth resolution of 0.01nm. STM is fragile and the tip can break, which is more likely when scanning faster. STM also requires a conductive surface otherwise tunnelling will not occur, reducing viable samples to be imaged. (68)

2.5.7.2 Atomic Force Microscopy

Much like STM, Atomic Force Microscopy (AFM) uses a tip for scanning the surface of a material. AFM places a conical tip on the end of a cantilever, which is brought close to the surface. The tip experiences a van der Waals force, which is dependent on the distance between the surface and the tip. The force on the cantilever is inversely proportional to the distance from the atom. A laser is reflected from the cantilever, and the deflection of the laser is measured. This deflection is converted into the height of the cantilever and, therefore, the surface of the sample. AFM has a lateral resolution of 0.1nm and a depth resolution of 0.1nm. AFM can be a relatively slow technique compared to STM but doesn't require a conductive surface. (69)

2.5.8 Superlens-based

2.5.8.1 Far-Field Superoscillatory Metamaterial Superlens

By diffracting light with specific masks it is possible to form superoscillations, rapid local variations of the electromagnetic field, in the far-field. These superoscillations can beat Abbe's limit since they can oscillate much faster than the highest Fourier component in their spectra.

Most masks are static and cannot be modified after fabrication; a mask using subwavelength plasmonic metamolecules can alter the scattered waves. This control allows for the forming of superoscillatory hotspots that can be shaped as desired. This then can beat Abbe's limit as a superlens can achieve an effective numerical aperture of 1.52 and focus of 0.33λ, usually, they are conventionally limited to 1 and 0.5λ respectively. Surrounding these hotspots is a region of low intensity, or halo, which defines the field of view. These superlenses can image samples without damaging them and do not require the use of fluorescent materials. The limitations of this technique are that only samples smaller than the field of view can be imaged, as the halo will interfere with

any samples larger. Superlenses can resolve features of 264nm, beating Abbe's limit for an 800nm wavelength beam (70). Superoscillatory illumination has recently achieved 12.6nm pixel sizes for 466nm (71). Superlenses have a reported focusing efficiency of up to 10% (72).

2.5.9 Comparison

Here is a table summary of the previously mentioned techniques for easy comparison.

Technique	Advantages	Disadvantages	Resolution	Imaging time
X-Ray-Based				
XUV Ptychography	• Material differentiation • No Sample damage	• Thin samples	20 nm	Requires lots of long exposure scans
Holography	• High resolution • 3 dimensional images	• Sensitivity of equipment	< 1nm	Limited by reconstruction time
Phase-Contrast Imaging	• High resolution • Material differentiation	• Thin samples	30 nm	Limited by the refresh rate of the camera
Synchrotron Microscopy	• High brilliance • Viable lenses	• Large facility • Sample damage	15 nm	Limited by time for each scans and number of scans
Synchrotron X-ray Tomography	• High brilliance • Three dimensional image	• Large facility • Sample damage	50 nm	Limited by time to image each rotation
Fluorescence-Based				
Structured Illumination Microscopy	• Fast • Fluorophores tag specific parts of the sample	• Measures fluorescent materials	50 nm	Up to real time
Stochastic Optical Reconstruction Microscopy	• High resolution • Fluorophores tag specific parts of the sample	• Measures fluorescent materials	20 nm	Up to real time
Stimulated Emission Depletion	• High resolution • Fluorophores tag specific parts of the sample	• Measures fluorescent materials • Damaging to samples	20 nm	Up to real time
MINFLUX	• Extremely high resolution • Fluorophores tag specific parts of the sample	• Measures fluorescent materials	1-3 nm	Up to real time
Confocal Microscopy	• Fluorophores tag specific parts of the sample	• Measures fluorescent materials • Lower resolution compared to the other techniques	180 nm	Up to real time
Electron Microscopy				
Transmission Election Microscopy	• Extremely high resolution	• Thin samples	0.2 nm	Up to real time
Scanning Electron Microscopy	• High resolution	• Conductive samples	10 nm	Up to real time
Ion Beam Microscopy				
Helium Ion Microscopy	• Extremely high resolution	• Thin samples	0.25 nm	Up to real time
Scanning Probe Microscopy				
Scanning Tunneling Microscopy	• Extremely high resolution • Three dimesional profile scan	• Equipment is fragile • Requiers a conductive sample surface	0.1 nm	As fast as the probe moves
Atomic Force Microscopy	• Extremely high resolution • Three dimesional profile scan • High depth resolution	• Slow • Image scan size	0.1 nm	As fast as the probe moves
Superlens Techniques				
Far-Field Superoscillatory Metamaterial Superlens	• Doesn't require fluorescent materials • Doesn't damage samples	• Lower resolution compared to the other techniques	264 nm	Limited by speed of scans

TABLE 2.1: A table of the techniques discussed at the end of Chapter 2

Chapter 3

Introduction to High Harmonic Generation

3.1 Theory of High Harmonic Generation

In this chapter, the generation of high harmonics will be explained. Initially explained is the three-step model, a simplified model of HHG, used to give a basic understanding of the process of HHG. Next is the quantum mechanical model, a more detailed approach to HHG that gives a greater understanding of the true process of HHG, and how ionising an atom can generate short wavelengths. Afterwards, the important effects of phase matching and coherence will be discussed, as well as how they are relevant to imaging with HHG.

The later part of this chapter is dedicated to the detailed description of my experimental setup, where the components are described, and the processes that each component performs are explained to give a deeper understanding of what is required for HHG. This section will explain the laser involved and the auxiliary components to generate high harmonics and perform ptychography successfully.

3.1.1 High Harmonic Generation

High harmonic generation is the generation of odd harmonic frequencies from a non-linear optical effect caused by the interaction of a high-intensity laser pulse with an

atomic field, typically of a gas (73). This causes the atoms to ionise and generate a shorter wavelength than the parent beam.

3.1.1.1 Three-Step Model

The three-step model is a basic model for understanding the mechanisms of HHG; the model is a description of the behaviour of electrons during the HHG process, also providing quantitative information on some HHG processes, such as the cutoff energy. Explained by Corkum in 1993 (74), the three-step model is semi-classical and hence misses crucial details of the electron's behaviour contained in the quantum model; nevertheless, the three-step model is useful for visualising HHG and granting a fundamental understanding of some aspects of the process.

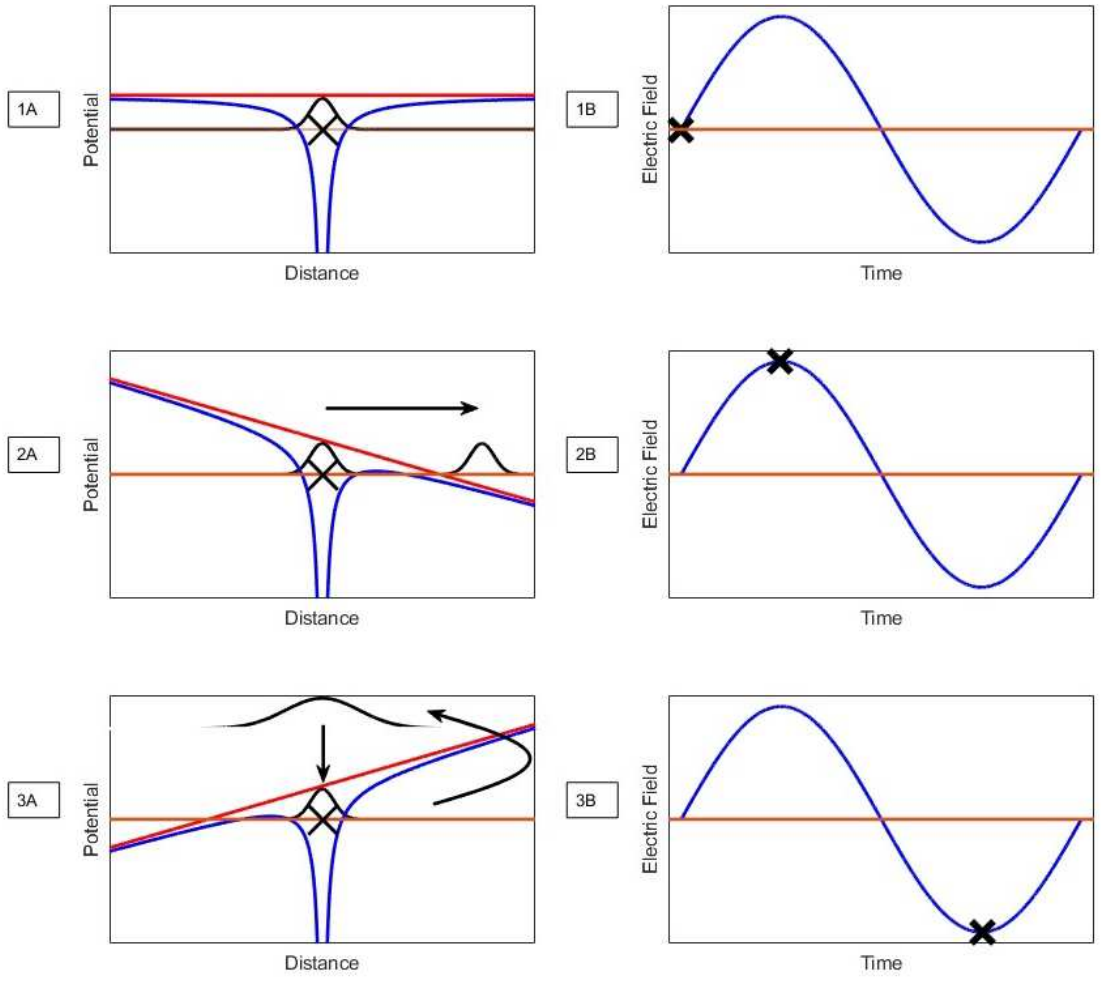

FIGURE 3.1: This figure shows the position and wave function of the electron (black line 'A' side) in a varying potential, which is the Coulomb potential plus the laser potential at three different points of the laser cycle, (blue line 'A' side) due to different phases (black cross 'B' side) of an electric field (blue line 'B' side).

The three steps as shown in the figure 3.1 are (75):

1. Initially, the electron is in the ground state; when an oscillating electric field large enough to significantly distort the Coulomb potential of the atom interacts with the atom's potential field, the electron then tunnels out of the atom's potential field.

2. After tunnelling, the electron begins to accelerate away from the nucleus as it effectively has become a free particle; this is due to the external field dominating the electron over the atom's Coulomb potential since the electron is now far from the nucleus.

3. As the oscillating external field's direction begins to reverse, the electron begins to accelerate back towards the nucleus, and it may recombine. Upon recombination, a photon is released. The photon's energy equals the ionisation energy plus the kinetic energy of the electron gained from this acceleration.

This model is a semi-classical approach as the behaviour of the interaction of the electric field and the electron is classical; the effect of tunnelling is a quantum effect. Though it misses the detail of the quantum approach, the three-step model can still predict the highest harmonic that can be generated as described by the cutoff energy.

3.1.1.2 Cutoff Energy

The cutoff energy is the maximum possible energy of the harmonics produced in the three-step model. This maximum energy is acquired by an electron ionising at the time that leads to the maximum induced velocity at recombination. To calculate the cutoff energy, the assumption that the distance travelled by the electron is large compared to the atomic radius of the atom is used. From this assumption, the Coulomb potential can be ignored, and only the Lorentz force due to the laser needs to be considered. For intensities below 1×10^{17} Wcm^{-2} the Lorentz force can to simplified from

$$\bar{F} = e[\bar{E} + \bar{v} \times \bar{B}] \tag{3.1}$$

to

$$\bar{F} = e[\bar{E}]. \tag{3.2}$$

Then applying this to Newton's 2^{nd} law we get:

$$eE_0 \cos(\omega t) = m\ddot{x}. \tag{3.3}$$

Rearranging and integrating for velocity, we get:

$$\dot{x} = \frac{eE_0}{m\omega} \sin(\omega t) + c'. \tag{3.4}$$

We can assume that the electron initially has zero velocity at the moment of tunnelling, $t = t_0$. With this we can apply $\dot{x}(t_0) = 0$ to (3.4) and we get:

$$-c' = \frac{eE_0}{m\omega} \sin(\omega t_0). \tag{3.5}$$

Then combining (3.4) and (3.5) we get:

$$\dot{x} = \frac{eE_0}{m\omega}[\sin(\omega t) - \sin(\omega t_0)]. \tag{3.6}$$

Another assumption we can use is that the electron's initial position is zero, such that $x(t_0) = 0$. With this assumption after integration of (3.6) we get:

$$x = \frac{eE_0}{m\omega^2}[\cos(\omega t_0) - \cos(\omega t) + \omega(t_0 - t)\sin(\omega t_0)]. \tag{3.7}$$

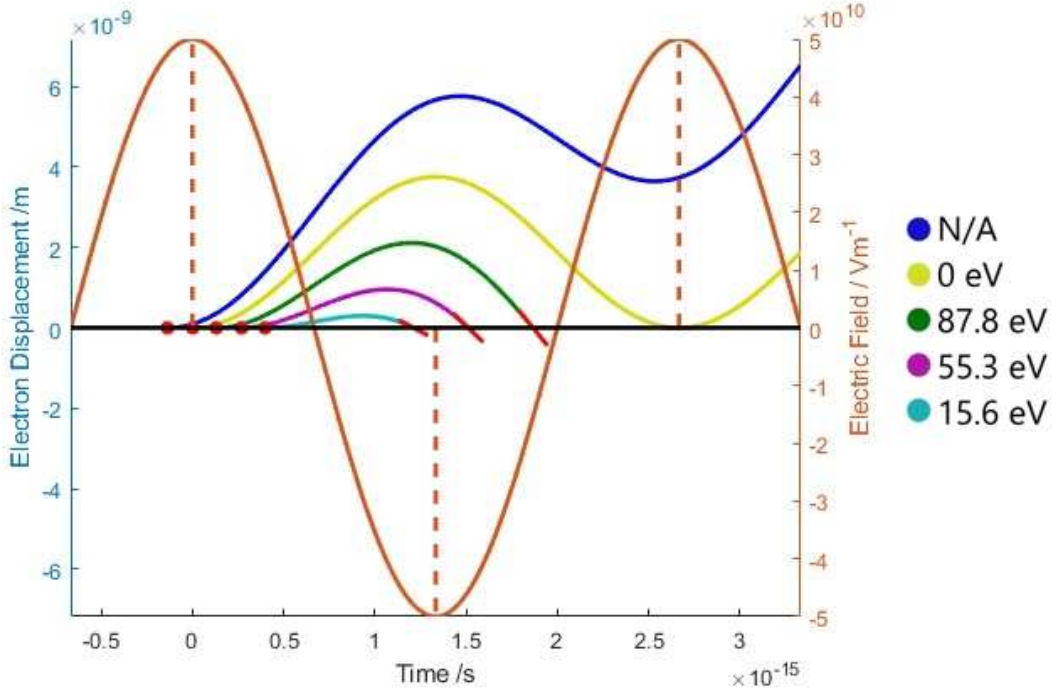

FIGURE 3.2: Electron trajectories for the classical three-step model with differing t_0, (multiple colour lines, left axis), as described by (3.7) due to the acceleration induced by the electric field (solid orange line, right axis) against time (black line, both axes). The initial time of emittance, t_0 (red star points) are followed by times of recombination with a gradient of displacement, if applicable(red lines). The key shows the return energy of the different ejection times.

As shown in figure 3.2, only electrons emitted for a quarter period after a maximum of the electric field will recombine with the atom. Electrons emitted within a quarter period before the maximum will accelerate away for the atom and will not recombine within the timescale of the laser pulse; if and when the electron were to recombine with the atom, it would no longer be coherent with the atom, not contributing to HHG. The gradients of displacement at recombination are important as this is the kinetic energy of the returning electron. Electrons emitted exactly at the maximum of the electric field will recombine with a kinetic energy of zero and emit a photon with an energy equal to the ionisation potential, so they also don't contribute to HHG. Electrons emitted with a phase difference of half the period of the electric field will propagate along a path equal but opposite to an electron emitted half a period before.

An issue that can arise when performing HHG is that the average separation of atoms in the generation medium is less than electron displacement. If the separation is below the electron displacement, then ejected electrons could recombine with neighbouring atoms. Calculating this distance can be done by first using the ideal gas law equation:

$$PV = nRT \tag{3.8}$$

where P is the pressure of the gas, V is the volume of the gas, n is the number of moles, R is the ideal gas constant, and T is the temperature of the gas. This equation can then be rearranged to find the number of moles per volume:

$$\frac{n}{V} = \frac{P}{RT}. \tag{3.9}$$

Then multiplying equation 3.9 by Avogadro's constant the number of molecules per volume can be found, with the following equation:

$$\frac{N}{V} = \frac{nN_A}{V} \tag{3.10}$$

where N is the number of molecules, and N_A is Avogadro's constant. The following equation can be used to find the volume occupied by one molecule:

$$V_{molecule} = \frac{V}{N} \tag{3.11}$$

where $V_{molecule}$ is the volume occupied by one molecule. Finally, to find the separation between atoms the cube root of equation 3.11 is taken:

$$d = (V_{molecule})^{\frac{1}{3}} \tag{3.12}$$

where d is the separation between atoms. For argon at 0.1 bar at 18°C, the same values as I have when performing HHG, the separation between atoms is 7.4 nm. This separation is quite close to the electron displacement, and since this is an average some electrons may combine with different atoms, but it is large enough that it will not significantly affect HHG. Due to the timescale of this process the recombination happens instantaneously compared the movement of the atoms, so only the atomic separation and electron displacement need to be considered.

To produce an XUV beam of high flux from HHG, a high probability of ionisation in the quarter period after the maximum of the electric field is mandatory. The Keldysh parameter is a measure of ionisation probability given by:

$$\gamma = \frac{I_p}{2U_p} \tag{3.13}$$

where I_p is the ionisation potential, and U_p is the ponderomotive potential. The ponderomotive potential is the cycle averaged kinetic energy of an electron in an electric field. For HHG with my system 32.5% of the argon experiences first degree ionisation. The ponderomotive energy can be derived by starting with the force on an electron in an electric field:

$$F = qE\cos(\omega t) \tag{3.14}$$

where q is the charge of an electron, E is the amplitude of the electric field, ω is the angular frequency of the electric field, and t is time. The acceleration of the electron is then:

$$a = \frac{F}{m} = \frac{qE}{m}\cos(\omega t) \tag{3.15}$$

where m is the mass of an electron. Since the electron is experiencing harmonic motion the electron's position is:

$$x = \frac{-a}{\omega^2} = -\frac{qE}{m\omega^2}\cos(\omega t). \tag{3.16}$$

To find the time-averaged energy, x^2 is required and is:

$$x^2 = (-\frac{qE}{m\omega^2}\cos(\omega t))^2 = \frac{q^2E^2}{m^2\omega^4}\cos^2(\omega t). \tag{3.17}$$

Time-averaging for $\langle x^2\rangle \cos^2(\omega t)$ becomes $\frac{1}{2}$ and therefore $\langle x^2\rangle$ becomes:

$$\langle x^2\rangle = \frac{q^2E^2}{2m^2\omega^4}. \tag{3.18}$$

The time-averaged potential energy for harmonic motion is given by:

$$U_p = \frac{1}{2}m\omega^2\langle x^2\rangle. \tag{3.19}$$

Ponderomotive energy is then given by substituting equation 3.18 into equation 3.19.

$$U_p = \frac{e^2 E_0^2}{4m\omega^2} = \frac{e^2 E_0^2 \lambda^2}{16\pi^2 mc^2} \tag{3.20}$$

where e is the charge of the electron, E_0 is the peak electric field strength of the driving pulse, m is the mass of the electron, ω is the angular frequency of the driving pulse, λ is the wavelength of the driving pulse, and c is the speed of light.

When $\gamma > 1$, the atomic potential dominates the electron's motion, but when $\gamma < 1$, the external field's potential dominates the electron's motion. Therefore, for HHG $\gamma < 1$ is required. However, as γ decreases and ionisation probability increases, early depletion leads to fewer electrons emitting in the quarter period after the maximum of the electric field. Electrons that tunnel in this quarter period will not return to the electron, within the timescale of the HHG process, and therefore will not produce any high harmonics . This depletion is caused by the external field's intensity being large compared to the atomic potential, increasing the probability of tunnelling and over-the-barrier ionisation. With fewer electrons available to emit in the quarter period after, this leads to less recombination, and the HHG emission is reduced. , though the less ionisation that occurs the fewer electrons there will be to tunnel to produce high harmonics. There is a balancing act not to ionise so much that the medium being used to generate high harmonics still has electrons available to ionise after the quarter period after the maximum of the electric field, while not ionising too little that the medium has electrons available when the electric field has zero amplitude.

The Keldysh parameter can also be explained in terms of timescales, where the Keldysh parameter is the ratio of the Keldysh tunnel time and the laser oscillation period (76). When the laser oscillation period is much lower than the Keldysh tunnel time the combined Coulomb field and laser field can be considered static or quasi-static. If the combined fields have a potential that allows the electron to tunnel, the electron can then tunnel in this stable quasi-static state. If the laser oscillation period is too fast, tunnelling will be restricted.

Using equation (3.6) the potential energy of the ejected electrons at recombination can be calculated.

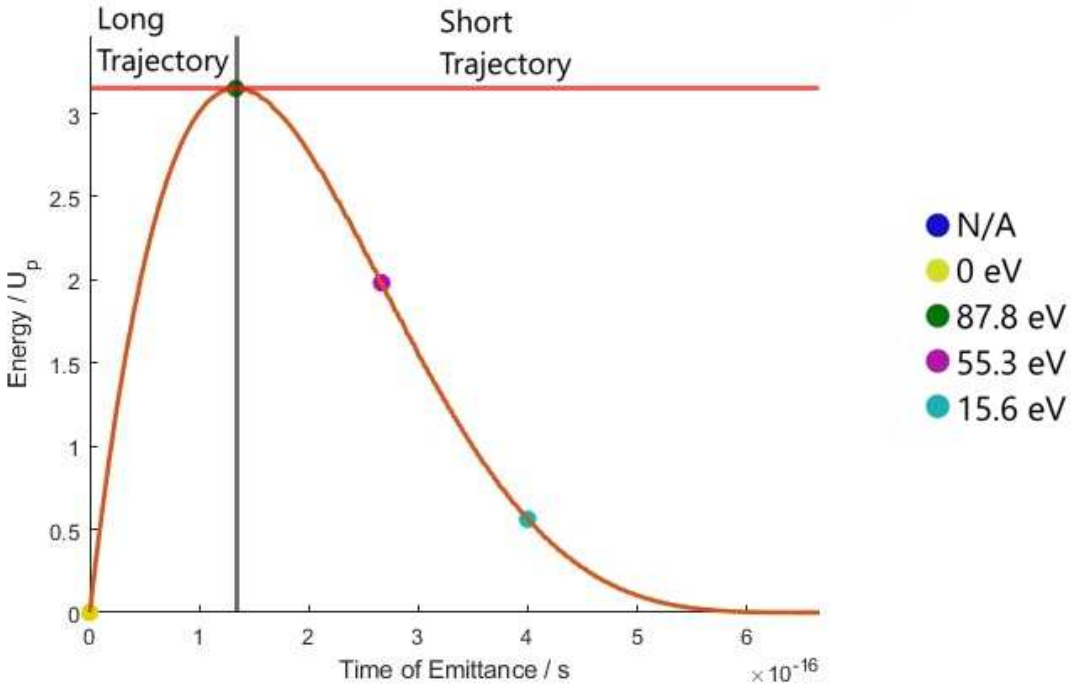

FIGURE 3.3: Energy for electrons emitted at different times (orange line) are separated into short and long trajectories, to the left and right respectively (black line) with $3.17U_p$ marked (red line). The key shows the return energy of the different ejection times. The coloured points correspond to lines of figure 3.2.

From figure 3.3, the kinetic energies for different tunnelling times are shown; the maximum energy is the cutoff energy. The photon energies are not discrete, and equal photon energies can be produced from two different times of emission, the long and short trajectories. The short trajectory refers to the electrons that spend a shorter time in the continuum and are ejected after the time that would result in the maximum kinetic energy. The long trajectory refers to the electrons that spend a longer time in the continuum and are ejected before the time that would result in the maximum kinetic energy. Where photons of the same energy can be released, this leads to interference. This interference is affected by the relative phase between the two times of emission. The effect of this quantum path interference can be adjusted with the driving laser's intensity (77). The long and short trajectories merge at the cutoff energy. Electrons with a long trajectory spend more time in continuum than electrons with a short trajectory, and the harmonics they produce have a broader angular spectrum and are less likely to propagate in the direction of the driving beam. Long trajectories are therefore less likely to contribute to the desired HHG beam.

Given the maximum kinetic energy gained by the electron, it is possible to calculate the maximum energy of the released photon. The maximum energy of a photon that can be generated is given by (75):

$$h\nu_{max} = 3.17U_p + I_p \tag{3.21}$$

where I_p is the ionisation energy of the atom. Using the equation for the ponderomotive energy (3.20), this then leads to:

$$h\nu_{max} \propto I\lambda^2. \tag{3.22}$$

where I is the intensity of the driving pulse and λ is the wavelength of the driving pulse. With equation (3.22) it is shown a longer driving wavelength gives a larger maximum photon energy. The larger the photon energy, the shorter the HHG wavelength. A shorter wavelength would allow smaller features to be resolved in an imaging experiment following equation (1.1); however, HHG flux varies proportionally from λ^{-5} to λ^{-6} (78); this means the intensity of the driving beam must be increased, or the flux would be diminished. Though intensity cannot be indefinitely increased even though this would increase the ponderomotive potential, as the pondermotive potential is proportional to the intensity of the beam, and this would lead to over-ionisation as described by the Keldysh parameter. To further increase the flux of the HHG other approaches are required such as phase-matching or quasi-phase-matching of the generated photons, or increasing the repetition rate of the driving beam.

For the HHG system used for the thesis, a driving beam of 1.4 W with a 50 fs pulse was used. The beam was focused to a spot of 50 μm, where spot size is the diameter of the beam's intensity at $1/e^2$, giving a peak intensity of $8\times10^{14}Wcm^{-2}$. Using (3.20), with the beam's electric field equaling 6×10^{10} with a wavelength of 800 nm, a ponderomotive potential of 30 eV is calculated, and this result is used in (3.21) to calculate a maximum photon energy of 94 eV. These results will be used in the next section to provide realistic values.

3.1.1.3 Quantum Mechanical Model

The three-step model describes an electron's behaviour during the HHG process; however, it does not fully explain the electron's behaviour and the process of HHG. The quantum model explains the interaction between the returning wave packet wave function and the ground state wave function. A fraction of the electron's wave function tunnels from the ground state dependent on the intensity of the electric field. Once tunnelling has occurred, the fraction of the wave packet that tunnelled will gain energy dependent on the time of tunnelling described as such by figure 3.3, though not with the semi-classical nature as before. When the wave packet returns, it interferes with the ground state wave function of the atom. The probability density of the resultant total wave function is:

$$\Psi_{\text{Total}} = |\Psi_{\text{GS}} + \Psi_{\text{WP}}|^2 \tag{3.23}$$

where Ψ_{GS} is the wave function of the ground state of the atom; Ψ_{WP} is the wave function of the returning wave packet.

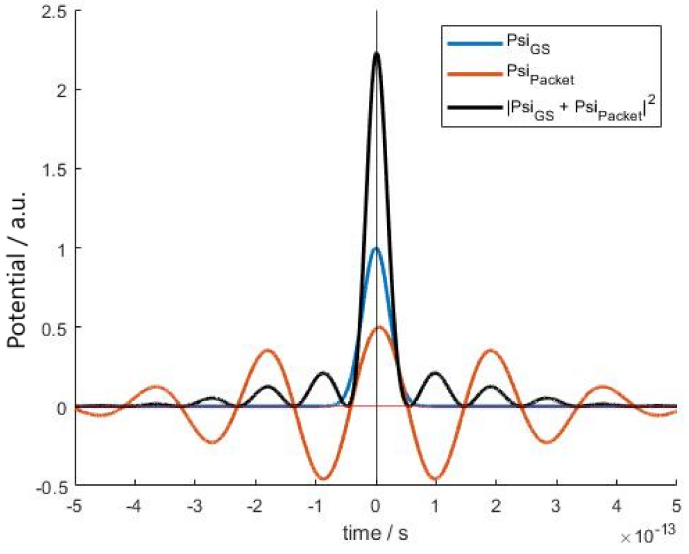

FIGURE 3.4: The probability density of the total wave function (black line) is the coherent sum of the ground state wave function (blue line) and the returning wave packet's wave function (orange line). Point of zero potential (red line) and the expectation value of the total wave function (vertical black line).

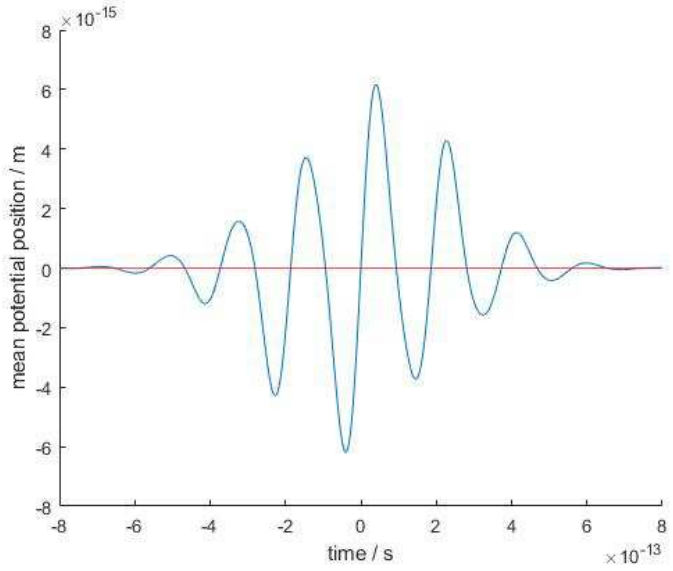

FIGURE 3.5: Position of expectation values of the probability density of the total wave function (blue line) over 1.6ps plotted over the position of a mean of zero (red line).

The oscillations shown in figure 3.5 correspond to the oscillations of the mean position of the electron density of the atom; this causes dipole moments to be formed. These dipole moments radiate an electric field proportional to their acceleration (79). This acceleration can be derived from the Ehrenfest theorem:

$$\frac{d}{dt}\langle A\rangle = \frac{1}{i\hbar}\langle [A,H]\rangle + \langle \frac{\partial A}{\partial t}\rangle \tag{3.24}$$

where A is a quantum mechanical operator, and H is the Hamiltonian. Rewriting the previous equation for x gives:

$$\frac{d}{dt}\langle x(t)\rangle = \frac{1}{i\hbar}\langle [x,H]\rangle \tag{3.25}$$

where $\langle \frac{\partial x}{\partial t}\rangle = 0$ since x is not explicitly dependent on time. Then taking the derivative with respect to time gives:

$$\frac{d^2}{dt^2}\langle x(t)\rangle = \frac{d}{dt}\frac{1}{i\hbar}\langle [x,H]\rangle \tag{3.26}$$

Then applying the Ehrenfest theorem again the following equation is given:

$$\frac{d}{dt}\langle [x,H]\rangle = \frac{1}{i\hbar}\langle [[x,H],H]\rangle \tag{3.27}$$

Substituting (3.27) into (3.26):

$$\frac{d^2}{dt^2}\langle x(t)\rangle = \frac{1}{i\hbar}(\frac{1}{i\hbar}\langle[[x,H],H]\rangle) \tag{3.28}$$

This can then be simplified to give acceleration:

$$a(t) = \frac{d^2}{dt^2}\langle x(t)\rangle = -\frac{1}{\hbar^2}\langle[H,[H,x]]\rangle \tag{3.29}$$

where a is the acceleration, $\langle x\rangle$ is the expectation value of electron position, the expectation value of the wave function, and H is the Hamiltonian.

3.1.1.4 Odd Harmonics

In high harmonic generation, only odd harmonics are present, and it is possible to explain this by the argument of symmetry. The polarisation for a wave can be described by:

$$P(\omega) = \epsilon_0[\chi^{(1)}E(t) + \chi^{(2)}E^2(t) + \chi^{(3)}E^3(t) + ...] \tag{3.30}$$

Due to the electron being in free space, there is spherical symmetry, meaning P(ω) = -P(-ω). This is only true for odd harmonics as there is no sign change for even harmonics, leading to χ for even orders to be 0.

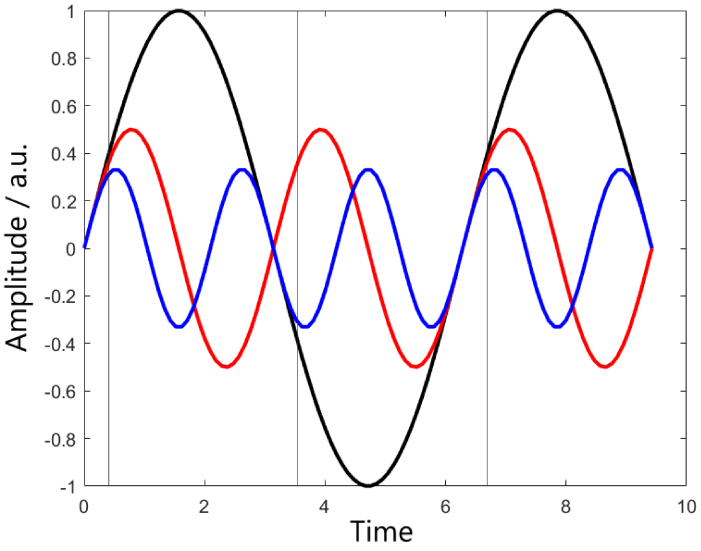

FIGURE 3.6: Graph of the fundamental (thick black line), second harmonic (thick red line), and third harmonic (thick blue line) for an arbitrary beam. The vertical lines note offset half periods of the fundamental.

From figure 3.6, it is possible to see the effect of the sign changes, where the second harmonics generated at the first vertical line would destructively interfere with the second harmonics generated at the second vertical line.

3.1.1.5 Phase Matching

Phase matching is vital, as it is required for increasing the flux. The increased flux increases the intensity of measured scatter patterns, this improves the contrast between the high-frequency components and the noise of the scatter pattern. This improved intensity of the measured scatter leads to better image reconstructions. To achieve phase matching, all forms of phase contributions must be balanced within the system given by the equation (80):

$$\Delta\vec{k} = \Delta\vec{k}_{gas} + \Delta\vec{k}_{plasma} + \Delta\vec{k}_{delay} + \Delta\vec{k}_{geo} \tag{3.31}$$

where $\Delta\vec{k}$ is the total phase shift, $\Delta\vec{k}_{gas}$ is the neutral gas phase shift gained from the dispersion from neutral atoms, $\Delta\vec{k}_{plasma}$ is the plasma phase shift gained from the free-electron plasma, $\Delta\vec{k}_{delay}$ is the atomic phase shift gained from the recombination

delay of the electron, and $\Delta\vec{k}_{geo}$ is the geometric phase shift gained from the geometric dispersion (81)(82)(83).

The neutral phase shift gained is from when a wave travels through a medium; it is affected by the refractive index of the medium. The refractive index of a medium is wavelength-dependent. The refractive index causes the driving laser and emitted HHG photons to experience optical paths of different lengths. Therefore, the phase of photons generated later will be shifted, causing a phase shift. The phase shift induced is given by the equation (84):

$$\Delta\vec{k}_{gas} = \frac{2\pi}{\lambda} n(\lambda) d \tag{3.32}$$

where λ is the wavelength of the beam, n is wavelength- and intensity-dependant refractive index, and d is the distance propagated through the neutral gas.

Due to the intensities involved in HHG, plasma is formed in the gas—the plasma forms when the electrons are excited to become free. It is possible to balance the neutral gas and plasma phase shifts to produce phase matching. The phase shift induced due to free electrons of the plasma is defined as (85):

$$\Delta\vec{k}_{plasma} = \frac{\pi q \omega_p^2}{\lambda_0 \omega_0^2} \tag{3.33}$$

Where q is the harmonic order generated, λ_0 is the fundamental wavelength of the driving beam, ω_0 is the angular frequency of the driving laser, and ω_p is the plasma frequency as defined by:

$$\omega_p = \sqrt{\frac{n_e e^2}{m_e \epsilon_0}} \tag{3.34}$$

where n_e is the electron density, e is the electron charge, m_e is the mass of an electron, and ϵ_0 is the permittivity of free space.

The atomic phase is determined by the electron's time within the continuum.

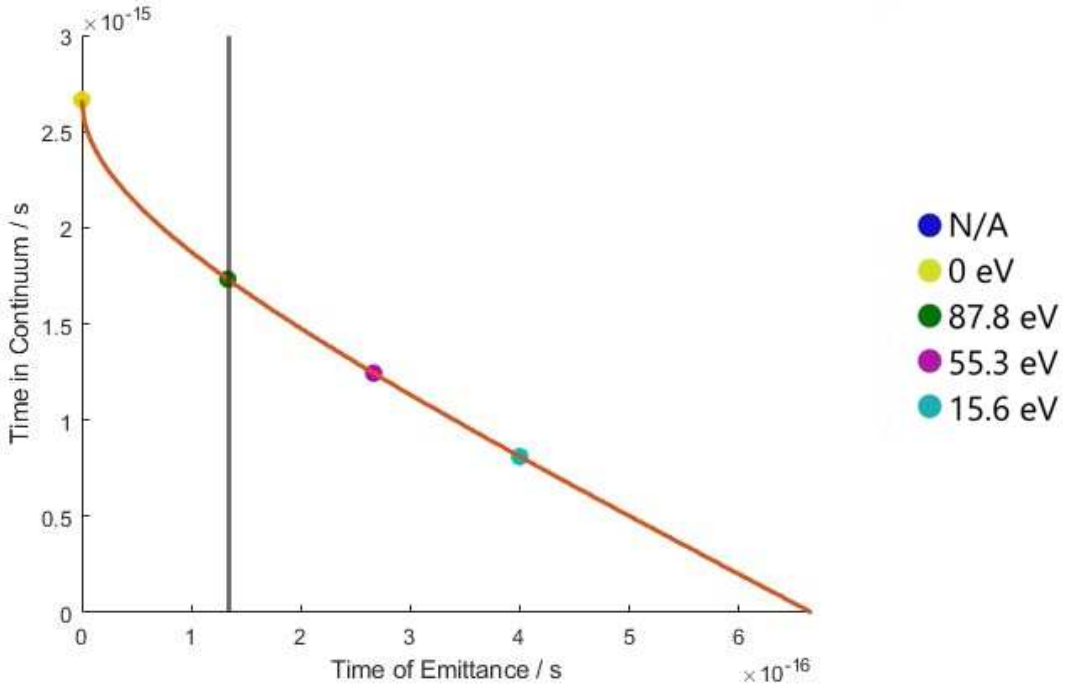

FIGURE 3.7: Time in which electrons spend in the continuum (orange line) are separated by the point of greatest kinetic energy (dark green point, vertical black line). To the left of the line are long trajectories and short trajectories to the right of the line, and are aptly named for relation to time in the continuum. The key shows the return energy of the different ejection times. Coloured points correspond to lines of identical colour on figure 3.2.

From figure 3.7 it can be seen that different times of tunnelling lead to varying time spent in the continuum. The emission of XUV is delayed while the electron is in the continuum, and this delay causes a phase shift in the emitted radiation.

The geometric phase is the phase shift acquired by a Gaussian beam propagating through a focus. This contribution is also known as the Gouy phase and is given by;

$$\Delta \vec{k}_{geo} = \Psi_{\text{Gouy}} = -tan^{-1}\frac{z}{z_R} \tag{3.35}$$

where z_R is the Rayleigh length and z is the position within the beam—z = 0 corresponds with the position of the beam waist. The Rayleigh length is given by:

$$z_R = \frac{\pi\omega_0^2}{\lambda} \tag{3.36}$$

where ω_0 is the beam waist, and λ is the wavelength of the beam.

It is difficult to achieve $\Delta\vec{k} = 0$, where there would be perfect phase matching throughout the entire gas. The coherence length of the region where waves will be π out of phase is defined by (85):

$$L = \frac{\pi}{\Delta\vec{k}} \tag{3.37}$$

and this shows that minimising $\Delta\vec{k}$ will increase the region in which phase matching is possible. Within this region, there will be HHG that is coherent and can increase in intensity. There are two regions where phase matching is possible, corresponding to HHG due to the short and long trajectory electrons.

The terms for the atomic phase shift and the geometric phase shift are the most important terms for phase matching for HHG. The plasma phase shift and the neutral gas phase have less of an impact on phase matching for HHG.

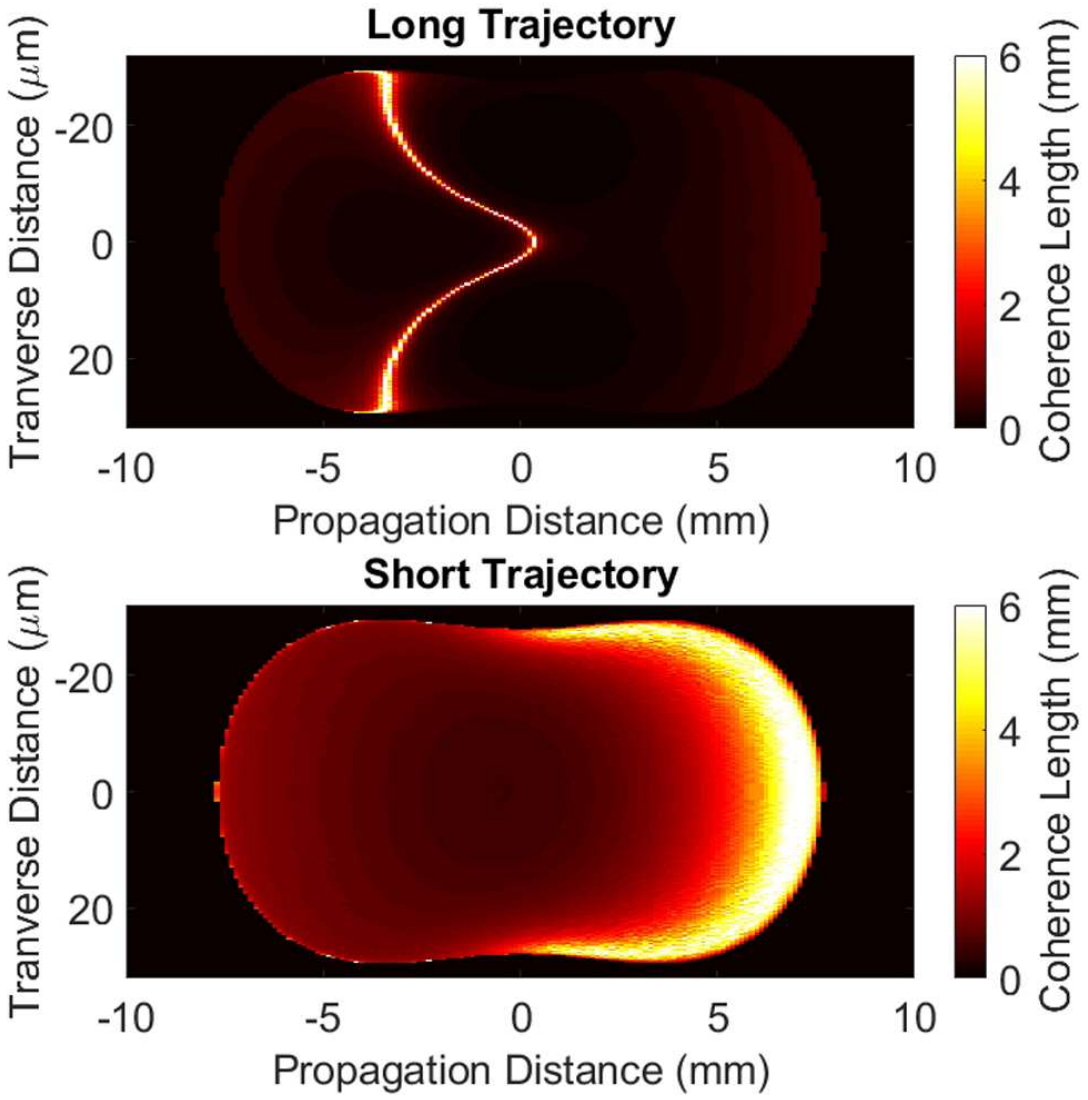

FIGURE 3.8: The calculated coherence length for the long and short HHG trajectories for the 27th harmonic of an 800 nm beam, with a pulse energy of 1.5 mJ with a 40 fs pulse length focused to a beam waist of 60 μm in argon gas. This data was calculated and the diagram was created by Doctor Charles Pooley.

Figure 3.8 shows the coherence length of the long and short trajectories generated at different distances relative to the beam's focus. Positioning the focal point of the beam so that the gas jet is 6 mm after results in the optimal point to generate high harmonics as the coherence length of the short trajectories is high and the coherence length of the long trajectories is low. More flux can be generated at 7 mm, but the coherence of the high harmonics will be lower as the coherence length of the long trajectories is higher there than at 6 mm.

3.1.1.6 Coherence

Coherence is a characteristic of a beam relating to the predictability of the phase within the beam. Coherence consists of two parts, temporal and spatial.

Temporal coherence is defined by the phase relationship of the electric field between the same point of the beam profile at different times.

Spatial coherence is defined by the phase relationship of the electric field between two different points on the beam profile at the same time.

Coherence is required for our imaging technique, as it is required for stable interference patterns. The spatial coherence condition for diffractive imaging is(17):

$$X_s = 2W \tag{3.38}$$

where X_s is the spatial coherence length, and W is the beamwidth of the probe. When performing HHG in a gas cell, both long and short trajectories are produced in different proportions. The focus of the driving laser is positioned towards the short trajectory region. The short trajectory is preferable as radiation is generated with a greater coherence length than the region corresponding to the long trajectory(82).

3.1.2 Summary

The three-step model is a simple model of the behaviour of the electron in HHG. The quantum model explains the interaction of the wave functions in HHG. The argument of symmetry explained the existence of only odd harmonics. The sources of phase contribute to phase matching with HHG were discussed. Finally, coherence consists of two types, spatial and temporal, and a spatial coherence length of twice the probe's beamwidth is ideally required for ptychography.

3.2 System for High Harmonic Generation and Ptychography

High harmonic generation is not a simple process; it is complex, and a system to generate high-harmonics contains many elements. The system for HHG is not just a tool

that can be turned on, but something that takes time to understand. Input power needs to be optimised into the gas cell to generate the highest flux while not causing saturation of the ionisation process; this is important as too high ionisation will lead to early depletion and reduce the high harmonics generated. A region of phase matching must be selected to balance the flux and spatial coherence of the XUV beam. The location of the Circle of Least Confusion (CLC) is required as this region gives the maximum flux through the aperture. Selecting the sample region to image with the SmarAct stages is also crucial as the region must be thin due to attenuation of the XUV beam in the sample and contain many interesting features to image, which become more sparse in thinner regions. This complexity has led to only a few groups being able to perform ptychographic imaging with HHG successfully. The remainder of this chapter contains the details of the elements that make up the system.

3.2.1 Experimental Setup

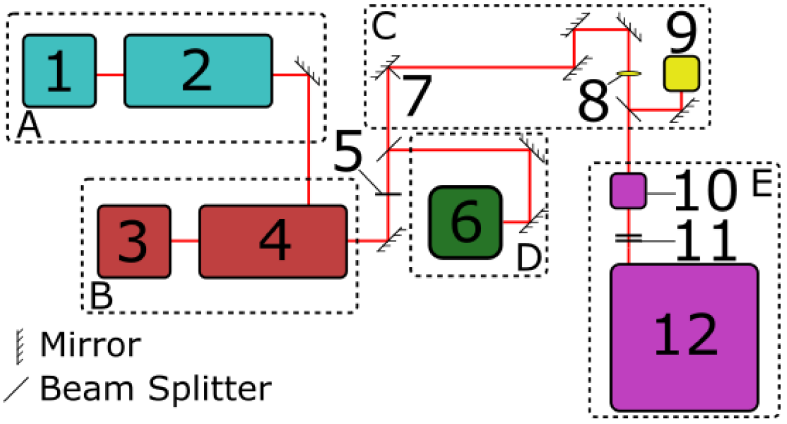

FIGURE 3.9: Diagram of the experimental setup. Section A is where the Millennia(1) pumps the Tsunami (2) to generate modelocked pulses. Section B is where the Evolution(3) pumps the Spitfire CPA system(4). Power is selected by a polariser(5). Section C is the beam stabilisation that occurs with a mirror(7), lens(8), and cameras(9). Section D is the FROG(6) to measure the pulse duration and chirp. Section E is where the XUV beam is generated from the gas cell(10), passes through the aluminium filters(11), and into the vacuum chamber(12).

3.2.1.1 Mode-Locked Seed Laser

This system uses a Master Oscillator Power Amplifier (MOPA) system. MOPAs give great control over the pulse shape and generate pulses of high energy. This is due to the pulse being generated in a low-power laser with high stability to give the great control

required to generate the pulse with the desired characteristics sans power. The desired power can then be acquired through the use of an amplifier.

3.2.1.2 Millennia

For the Ti:Sapphire laser to lase, a pump laser is required. The pump laser used in this system is a Millennia, which is a diode-pumped continuous wave laser with a Neodymium-doped yttrium orthovanadate (Nd:YVO_4 gain medium. This generates a 1064 nm wavelength that is then frequency doubled to a wavelength of 532 nm, the wavelength which matches the peak absorption of Ti:Sapphire to pump to the Tsunami. The Millennia pumps at a power in this system of 3.8 W.

3.2.1.3 Tsunami

The Tsunami is used to generate the ultrashort pulses, which are required later in the system to perform HHG. The Tsunami is a mode-locked ultrashort pulse Ti:Sapphire laser, which in this system generates approximately 30 fs pulses at a repetition rate of 80 MHz, with a central wavelength of 800 nm, a bandwidth of 50 nm, and an output power of 0.33 W.

The Titanium ions (Ti^{+3}) doped within the gain medium have a large bandwidth; this is required for mode-locking. Mode-locking is important for high intensities, which is crucial for HHG. Within the laser cavity, there are a large number of longitudinal modes. Mode-locking is the process of forcing coherence between these modes so that they are in phase; this causes destructive interference for most of the wave, but with a few regions of constructive interference where pulses form. The Tsunami initially uses an Acousto-Optic Modulator (AOM) to force all the longitudinal modes of the cavity to become in phase. The Tsunami is then kept mode-locked due to the Kerr effect, where the more intense parts of the pulse causes a stronger change in the refractive index causing intensity-dependent focusing within the crystal (86)(87).

Vibronic transitions are electronic transitions where there is a simultaneous change in the vibrational state of the molecule. The Franck-Cordon principle states that electronic transitions occur almost instantaneously compared to nuclear motion, where transitions between vibronic states happen vertically on potential energy diagrams. Where

the vibrational wave functions of the excited states and ground states do not perfectly overlap, the intensity of the vibronic transition is proportional to the square of the overlap integral between the vibrational wave functions of the initial and final states in a vibrational transition. Ti:Sapphire crystals have a large overlap integral between vibronic states resulting in a large bandwidth (88).

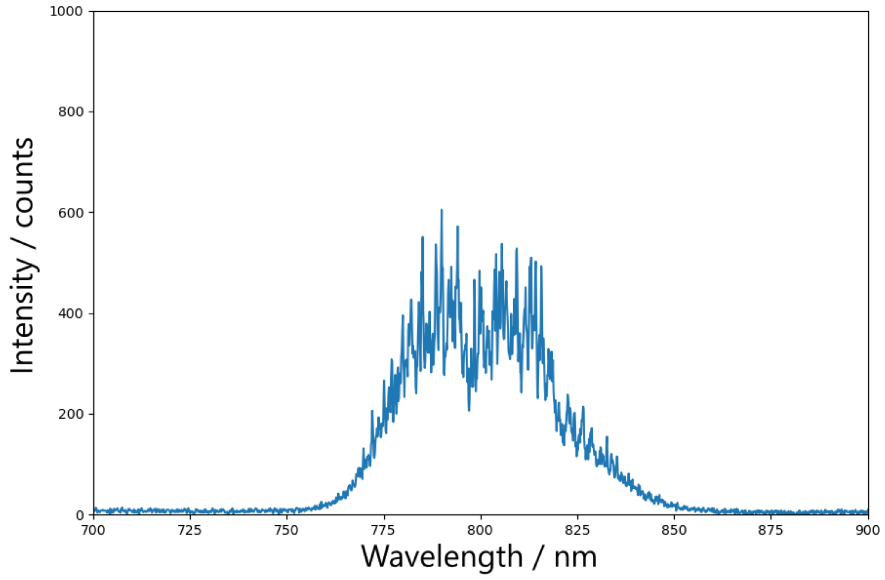

FIGURE 3.10: Graph of the emission spectrum from the Ti:Sapphire, showing intensity versus wavelength.

Figure 3.10 shows the spectrum generated by the Tsunami. The noise in figure 3.10 is real, but is not a true representation of the spectrum, and is due to the optical fibre used to measure the spectrum. Since the optical fibre has multiple modes and there are many different wavelengths entering, the noise is an effect of the interference between them.

3.2.1.4 Chirped Pulse Amplification

Chirped Pulse Amplification (CPA) was first demonstrated by Strickland in 1985 (89), which later won the Nobel Prize in Physics in 2018. The intensity of the Ti:Sapphire pulses initially is too low for HHG; therefore, the pulses need to be amplified. Directly amplifying the pulse results in non-linear effects, such as irregular amplification of the pulse, distortion of the pulse and damage to the amplifier. To avoid this, CPA is used.

CPA achieves this by using positive dispersion to increase the temporal length of the pulse, so that when the pulse is amplified the peak intensity remains low. Once the pulse has been amplified negative dispersion can then reduce the temporal length of the pulse to return the pulse to a short length.

3.2.1.5 Evolution

To increase the gain within the amplifier, a pump laser is required for population inversion to occur. This pump laser is the Evolution, a Q-switched laser with a Neodymium-doped yttrium lithium fluoride (Nd:YLF) gain medium. In this system, the Evolution generates a wave with a wavelength of 1053 nm that is then frequency doubled to a wavelength of 527 nm with a repetition rate of 1 kHz.

Q-switching is a technique of generating highly energetic pulses. To cause Q-switching in the Evolution, the laser cavity is blocked by an AOM being turned on to stop lasing, and this causes the population of the gain medium to increase. When the gain medium is saturated, the AOM is turned off, causing the cavity loss to decrease suddenly and allowing the Evolution to lase. This causes a short, highly energetic pulse to be released. The process is then repeated by turning the AOM on again.

3.2.1.6 Spitfire

The Spitfire is the regenerative amplifier used for CPA in this system, with the seed pulse provided by the Tsunami. The Spitfire in this system generates 800 nm wavelength 50fs pulses with a repetition rate of 1kHz and an output power of 2.8W.

Directly amplifying the pulse is not viable as the intensities within the amplifier would be too high and could lead to unwanted nonlinear effects or permanent damage to the amplifier. CPA is a way to amplify the pulse without direct amplification.

CPA is performed by the pulse temporally being broadened via chirping, chirp is the time variation of frequencies; this results in a lower peak intensity of the pulse. Positive dispersion is used to chirp the pulse; a grating stretcher is an example source of positive dispersion. Once chirped, the pulse is safe to be amplified with this lower peak intensity. The broadened pulse is temporally shortened to increase the intensity of the pulse

by using a source of negative dispersion; a grating compressor is an example source of negative dispersion. The resultant temporally-altered amplified pulse is equivalent to the theoretical directly amplified pulse(90).

While CPA produces pulses of high intensity the average power of the system can be low, this can be improved by increasing the repetition rate of the CPA system. The Spitfire is limited by the Evolution's repetition rate of 1 kHz. The Evolution is limited by the time it takes for the population inversion needed for Q-switching. In the future, a fibre system could be used for higher average power, as a fibre system's average power is limited by thermal distortions when the average power is too high. The fibre system would also need to have a bandwidth as high as the Ti:Sapphire to ensure short pulse lengths.

3.2.1.7 Frequency-Resolved Optical Gating

Ultrashort pulses are difficult to measure due to the response time required. Autocorrelators are devices that have the time resolution to measure an ultrashort pulse. Autocorrelators record a signal that depends on the time-delay between a pulse and its replica. However, since the detector response is slow in comparison with the oscillation period of light, the phase information is lost, and the autocorrelation of a pulse is not unique; therefore, multiple pulse shapes of identical autocorrelation cannot be distinguished. The Frequency-Resolved Optical Gating (FROG) system used was a Grenouille. A Grenouille uses a Fresnel biprism to separate the beam by delay along the x-axis, and by wavelength along the y-axis. A FROG system using SHG (second harmonic generation) can use the same method as autocorrelation but with the addition of a spectrometer. SHG is required to be used here as it is a combination of the reference wave and the delayed wave that is measured. The spectrometer measures the gated frequency spectrum, which is a function of the delay and the wavelength. The phase can be recovered from the frequency spectrum from a gated pulse and intensity measurement. With the phase, it is possible to distinguish pulse shapes.

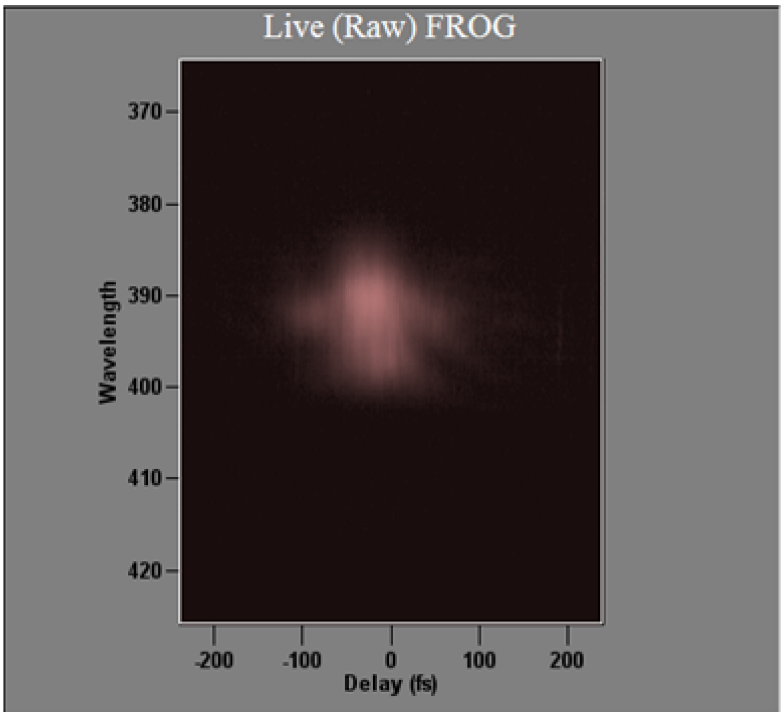

FIGURE 3.11: Image of the FROG trace of the pulse after the CPA, showing wavelength against delay.

Figure 3.11 shows an example FROG trace that I took from the system used throughout this thesis. A FROG trace shows the different orders of dispersion of the pulse, where 1^{st} order is a linear tilt in the trace, 2^{nd} order is a symmetrical broadening of the trace, 3^{rd} order is an asymmetric skew of the trace, and 4^{th} is finer modulations in the trace. Typically the pulse length is 50 fs, but the trace also shows that not all 3^{rd} and 4^{th} order dispersion is compensated for as the pulse should be an ellipse stretched in the vertical direction. Not compensating for all 3^{rd} and 4^{th} order dispersion is shown by the stretched corners, dots to the sides, and waves of intensity across the trace.

The Grenouille has a temporal resolution of 0.5 fs and a spectral resolution of 0.3 nm. The Grenouille system used an algorithm to recover the pulse where the algorithm solves two constraints. The first constraint is the gated signal field:

$$E_{sig}(t,\tau) = E(t)|E(t-\tau)| \tag{3.39}$$

where t is time, τ is the time delay, and E is the electric field of the pulse. The second constraint is the spectrally resolved intensity:

$$I_{FROG}(\omega, \tau) = \left| \int_{-\infty}^{\infty} E_{sig}(t, \tau) e^{-i\omega t} dt \right|^2 \tag{3.40}$$

where ω is the angular frequency.

3.2.1.8 Beam Stabilisation

The beam stabilisation system was created by a previous user of the laser system, Dr Michal Odstrčil. Positional instability of the beam can cause image reconstruction to fail because beam movement shifts the illuminated region of the object, resulting in a scatter pattern of a different region than what the code is expecting. A motorised mirror and a motorised lens are used to maintain the beam's position on two cameras to stabilise the beam. The mirror's orientation and the position of the lens are controlled by a proportional–integral–derivative (PID) error minimisation code. PID controllers use the equation:

$$u(t) = K_p e(t) + K_i \int e(t) dt + K_p \frac{de}{dt} \tag{3.41}$$

where u is the PID control variable, K_p is the proportional gain, e is the error value, K_i is the integral gain, and t is the time. The proportional section of the equation, $K_p e(t)$, creates an output proportional to the magnitude error signal to maintain a constant offset from the set point. The integral section of the equation, $K_i \int e(t) dt$, creates an output proportion to the duration and magnitude of the error signal to reduce the offset from the set point. The derivative section of the equation, $K_p \frac{de}{dt}$, creates an output proportional to the rate of change of the error signal to reduce the induced oscillations from the integral section. This results in the beam not drifting more than 20 nm at the detector. The distance between the mirror and the lens was over 1 m, 30 cm from the lens to the gas cell, 1.2 m from the gas cell to the mirror in the vacuum chamber, and 0.3 m from the mirror in the vacuum chamber to the CCD. A variation of beam position of 0.1 μm at the lens leads to a variation of beam position at the CCD of 20 nm; by using the ratio of the distance between the stabilisation lens and the mirror, and the mirror

and the CCD, to calculate the beam position variation at the CCD from the variation at the stabilisation lens. My input into this part of the system was calibrating the system before use and maintaining its quality.

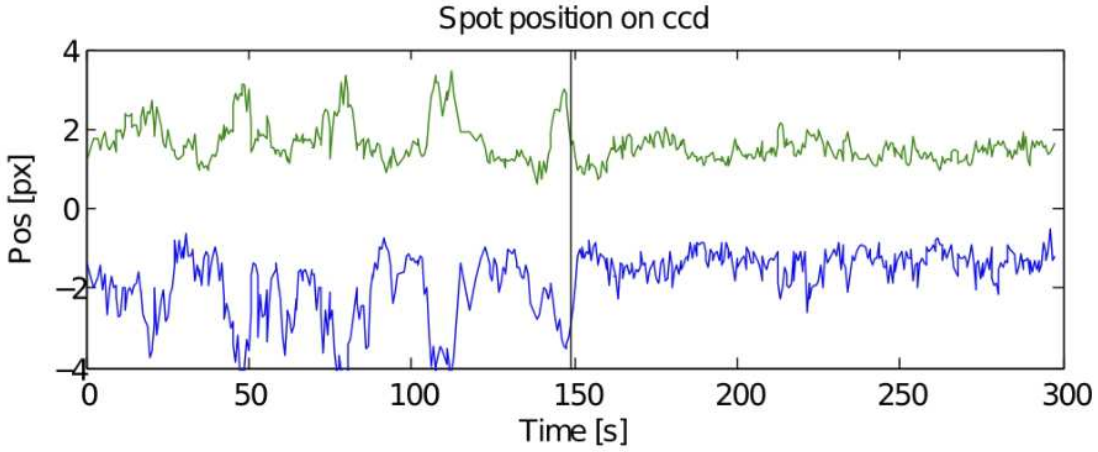

FIGURE 3.12: Graph of the movement of the beam on the CCD with and without the stabilisation system turned on. Times before roughly 150 s the stabilisation system is off and times after the stabilisation system is on. The graph shows the stabilisation of the x-axis (green line) and y-axis (blue line), where 1 pixel is 20 nm. This data was taken by Doctor Michal Odstrčil

From figure 3.12 it can be seen that when not being stabilised the x-axis varies by about 60 nm and the y-axis varies by about 80 nm. When the stabilisation system is on both axes vary by 20 nm.

3.2.1.9 Gas Cell

Argon is used as the HHG medium for the system used throughout this thesis. Argon is a gas at room temperature; gases are used here for transmission HHG as the attenuation of liquids and solids are too high. Argon is a noble gas, and the noble gas group has the highest first ionisation energy of their periods. The first ionisation energy of argon is 15.76 eV. This high ionisation energy prevents the early depletion of electrons, as discussed earlier, and allowing higher energy HHG to be performed. Helium and neon have higher first ionisation energies, however, HHG with these gases results in a lower flux of the XUV produced. The gas still attenuates the beam, so generation efficiency is limited by the absorption length of the XUV beam in the gas. A cell containing the argon with windows would be preferred; however, materials such as silicon and

diamond ablate at intensities of $2.4 \times 10^6 Wcm^{-2}$ (91). Our beam reaches intensities of $1 \times 10^{15} Wcm^{-2}$, so windows are not viable. To contain the argon, copper tape is applied on either side of a cell through which argon is pumped. The beam will form one hole in each piece of copper tape, the size of the beam waist at the tape. This is the minimum hole size achievable and, therefore, causes the least argon leakage.

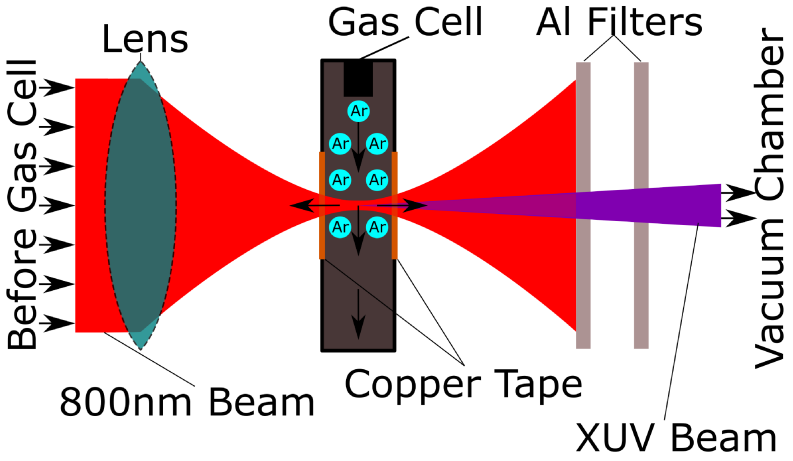

FIGURE 3.13: Diagram of high harmonic generation using a high intensity pulsed beam focused onto a gas cell contained by openings in copper tape, created by the laser to be the minimal size; then the parent beam is filtered out, leaving only the generated beam.

Figure 3.13 is a diagram of the gas cell used in the system used throughout this thesis. The size of the gas cell tube is approximately 3 mm with a 500 μm hole machined through the tube.

argon has higher flux when generating high harmonics compared to Helium and Neon since they are smaller and therefore there is less overlap between Helium and Neon's wave functions and the returning electron's wave function; a lower overlap reduces the flux generated.

Gaseous argon was not only used as the medium for HHG compared to a solid because the system was setup to only accept gases, but due to complications such as high attenuation which arise when generating high harmonics through a solid. High harmonics can be generated at an angle from solids but this also adds complexity to refitting the current experimental setup.

3.2.1.10 Beam Filters

The high intensity of the IR pulses used to generate HHG would overwhelm measurements from the XUV and cause damage to the Charge-Coupled Device (CCD) used for measurements if allowed to reach the detector. Two 100 nm thick free-standing aluminium filters are used to block the driving beam's wavelength. Aluminium is well suited for this purpose as it has high transmission at our HHG's 29.2 nm wavelength and relatively high reflectance at the driving beam's 800 nm wavelength. The XUV still attenuates within the aluminium, and Aluminium oxide forms a layer 4nm thick on aluminium, which attenuates the XUV beam even more. Aluminium of 184 nm thickness has a transmission of 0.640; Aluminium oxide of 16 nm thickness has a transmission of 0.364, therefore, the overall transmission is 0.233 (1).

The combination of aluminium and aluminium oxide has an optimal transmission around 29 nm, leading to the 27^{th} harmonic (29.2 nm) being chosen for the wavelength used in this system.

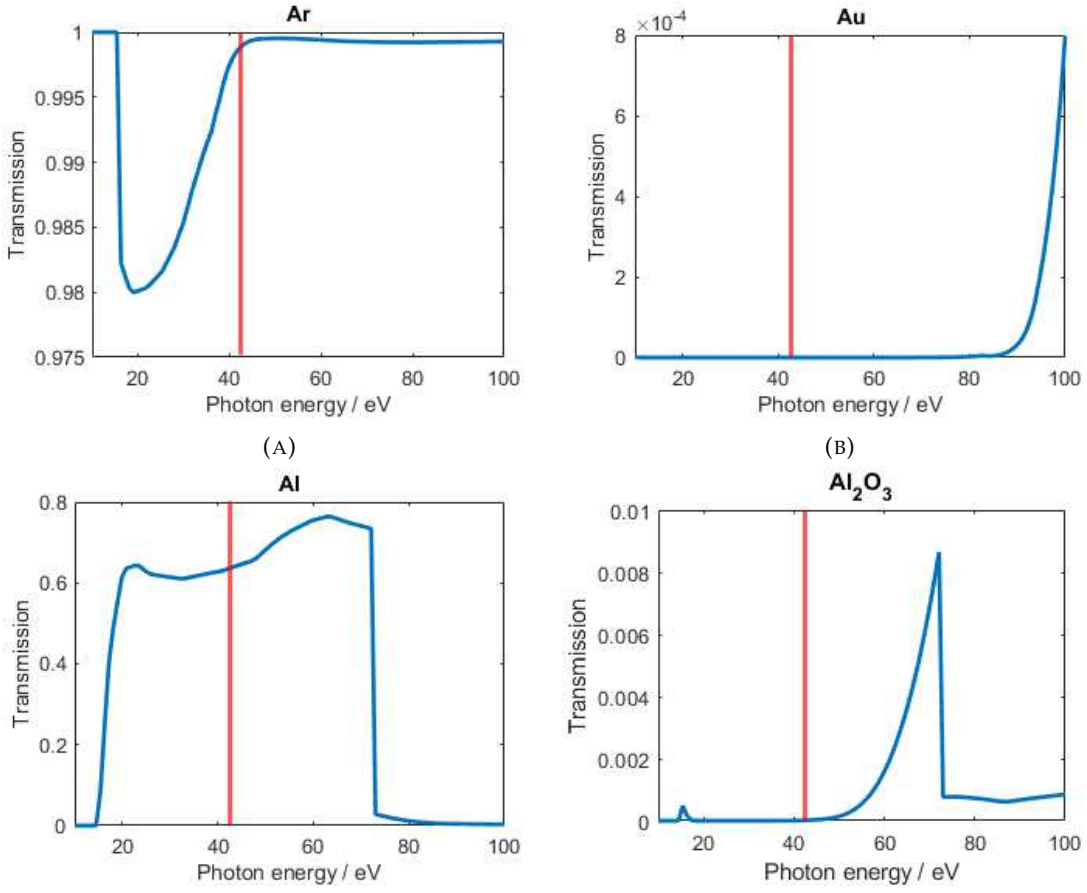

FIGURE 3.14: The transmission values of four materials from 10 eV to 100 eV (blue line), with the photon energy of the HHG beam (red line). (A) shows the transmission values of Ar with a density of $1.78\times10^3 g/cm^3$. (B) shows the transmission values of Au with a density of 19.32 g/cm^3. (C) shows the transmission values of Al with a density of 2.7 g/cm^3. (D) shows the transmission values of Al_2O_3 with a density of 3.97 g/cm^3. The transmission data were from the CXRO database (1).

3.2.1.11 Vacuum Chamber

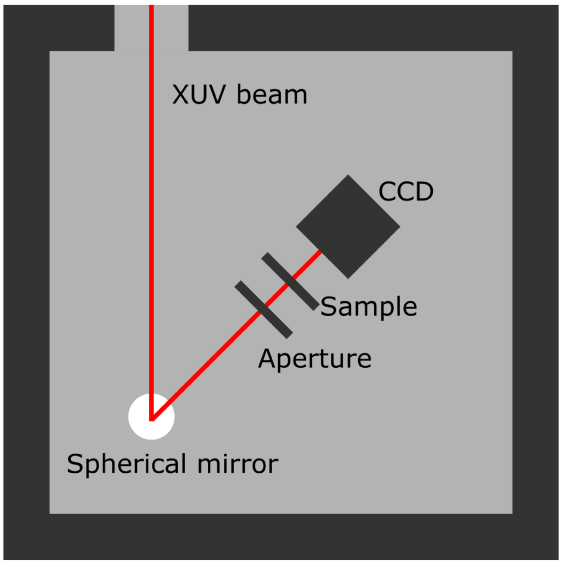

FIGURE 3.15: Diagram of the beam path, spherical mirror, the aperture, the sample, and CCD within the vacuum chamber of the system

The final stage of our setup is contained within a vacuum chamber. Air at 1bar has a transmission of 2×10^{-23} over 1mm, for a wavelength of 29 nm. The pressure in our vacuum is 7×10^{-6}mbar, which has an absorption of 4×10^{-4} over 1m (1). The reduced attenuation increases the flux of the XUV available for scattering. While in the vacuum chamber, the XUV beam is reflected by a spherical mirror to focus the beam. The Radius of curvature of the mirror is 0.5 m, the angle of incidence is 7°, and the coating is presumed to be scandium silicon, though this cannot be precisely known as the mirror is proprietary technology. The beam then passes through an aperture to define the probe. The beam is then scattered by the object. Finally, the scatter pattern is measured by a detector.

3.2.1.12 SmarAct Stages

The sample and aperture are positioned by a pair of SmarAct stages. These stages can perform 1 nm movement with a repeatability of 25 nm. Ptychography requires accuracy and precision on the samples since it uses the aperture and sample position to reconstruct the sample correctly. While used for ptychography within this thesis, this equipment could be used for other imaging techniques such as single-shot CDI.

There are also specially designed mounts fitted to the SmarAct stages that have been machined to allow nanometer precision in positioning the aperture and sample, and also the ability to fit four samples or aperture selections on each.

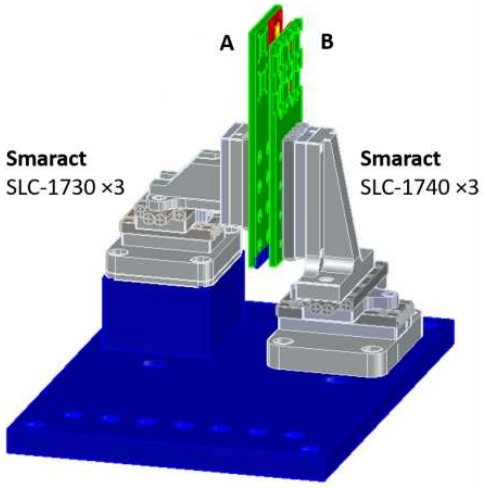

FIGURE 3.16: Diagram of the SmarAct stages used to position the aperture and the sample. Where A is used for the aperture, and B is used for the sample.

3.2.1.13 Aperture

The aperture is used to define the probe before the sample; usually, a 10μm diameter circular aperture 100μm before the sample. A well-defined probe is required for ptychography. A multi-stage process is used to create the apertures used in this system. Firstly, a 5 nm thick layer of Titanium (Ti) is evaporated onto a 50 nm thick membrane of Silicon Nitride (SiN); Ti is used as a binding layer to allow Gold (Au) to attach to the membrane, as Au alone would not hold onto the SiN. Afterwards, a 100 nm thick layer of Au is evaporated onto the membrane, as Au has a low transmission for a 29.2 nm wavelength beam. Finally, a Focused Ion Beam (FIB) is used to cut the apertures, as FIB is a highly precise method to cut shapes.

To achieve maximum flux through the aperture, the beam must be focused at the aperture. A spherical mirror is used to focus the beam, though the mirror cannot focus the beam enough for scan-based imaging. When reflecting with a spherical mirror at a non-zero angle, the beam becomes asymmetrical, and the horizontal and vertical foci shift. The CLC is the position between the horizontal and vertical foci. The two foci are defined by the ray transfer matrices:

$$M_x = \begin{bmatrix} 1 & 0 \\ \frac{-2}{R\cos(\theta)} & 1 \end{bmatrix} \tag{3.42}$$

and

$$M_y = \begin{bmatrix} 1 & 0 \\ \frac{-2}{R/\cos(\theta)} & 1 \end{bmatrix} \tag{3.43}$$

where M_x is the ray transfer matrix for the horizontal focus, M_y is the ray transfer matrix for the vertical focus, R is the mirror radius, and θ is the angle between the beam incident on the mirror and the off-axis beam. The horizontal focus is affected by $R * cos(\theta)$ and the vertical focus is shifted by $R/cos(\theta)$ (92)(93).

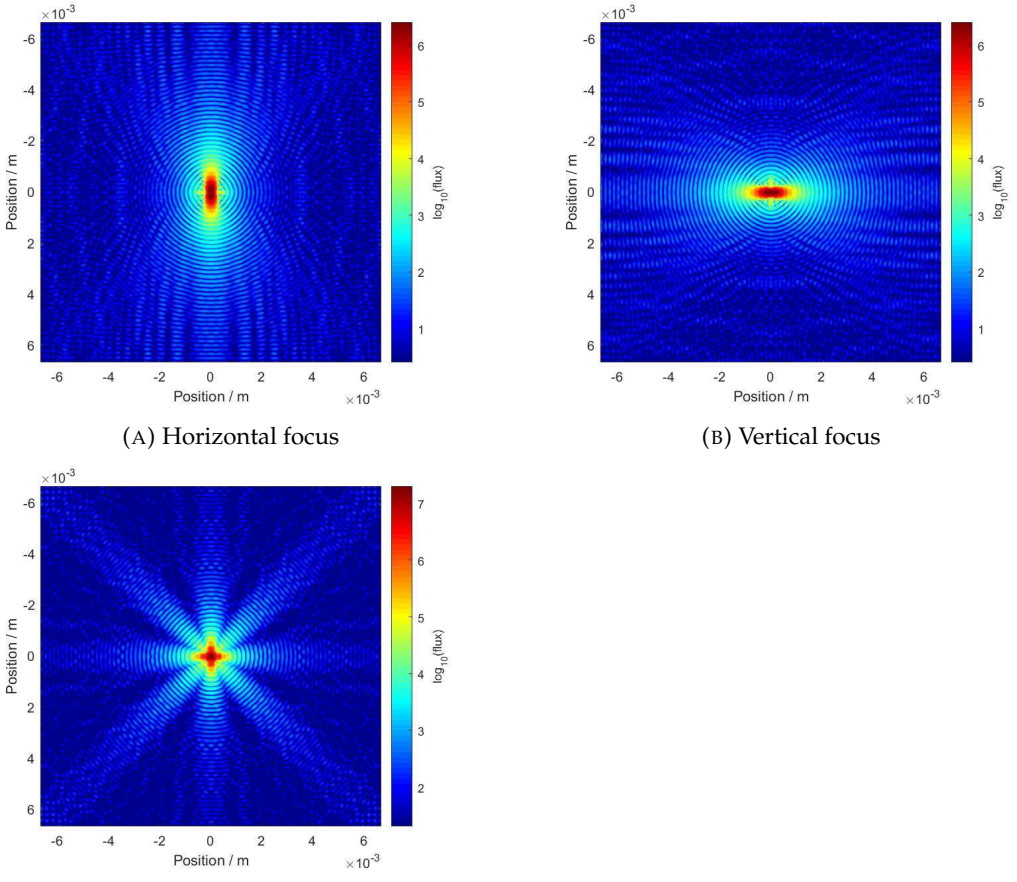

(A) Horizontal focus

(B) Vertical focus

(C) Circle of least confusion

FIGURE 3.17: The theoretical log-base-10 diffraction patterns for a Gaussian beam passing through a 10 μm diameter aperture after off-axis reflection, the aperture is positioned at (A) the horizontal focus, giving a vertical line at the centre; (B) the vertical focus, giving a horizontal line at the centre; (C) circle of least confusion, giving a cross-shaped pattern at the centre.

The diffraction patterns of figure 3.17 were calculated using Fraunhofer propagation, as the distance from the aperture to the detector is 3.57 cm, which is in the far-field regime. The aperture shape was the same for the three diffraction patterns; later in the thesis the shape of the aperture and the effects on the diffraction pattern will be discussed.

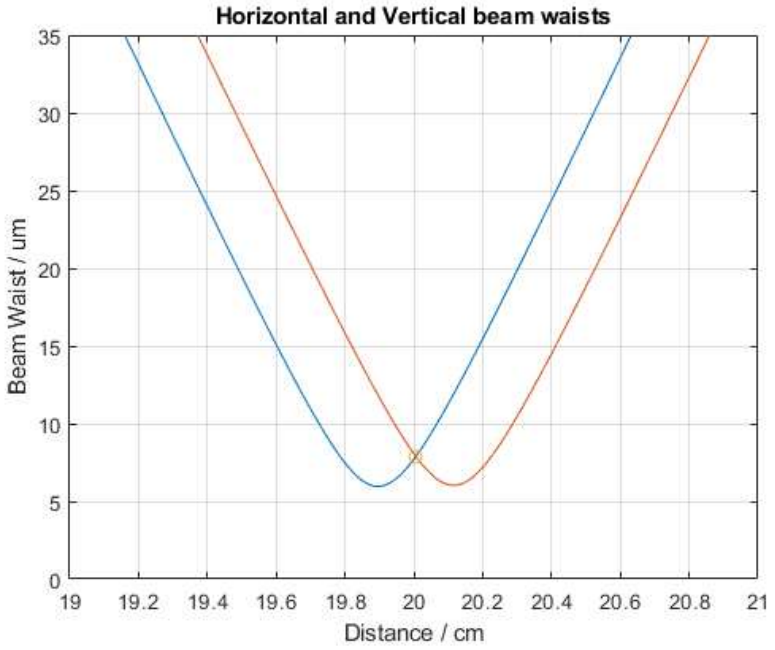

FIGURE 3.18: The theorectical horizontal (blue line) and vertical beam waists (orange line) for the reflected beam from the XUV mirror. This figure shows the CLC at the point where the two lines intersect.

From figure 3.18 the calculated beam waist at the CLC is 7.58 μm, which is larger than the largest aperture used that has a radius of 5 μm.

3.2.1.14 Detector

The type of detector used to measure the XUV scatter pattern is a CCD. To reduce noise, the CCD is cooled to -40 °C. The CCD uses two thermoelectric cooling chips; these Peltier modules can each cool a differential of 20 °C each, allowing for the -40 °C total to be reached, and reducing the dark noise. A CCD is used to measure the scatter patterns over a Complementary Metal-Oxide-Semiconductor (CMOS) due to high dark noise, as CMOS typically cannot reach -40 °C. However, CCDs are slower at reading out than CMOS. A CCD measures pixels charged by incident photons and then reads these pixels off pixel by pixel. CMOS measure the pixels line by line, which is much

faster than a CCD (94). A new CMOS has been developed, which can operate at lower temperatures and with lower dark noise; this CMOS is being considered for future applications.

Using the diffraction pattern from an aperture, the position of the aperture relative to the CLC can be discovered, and the centre of the diffraction pattern reveals the position of the aperture. From figure 3.17a a vertical line at the centre of the diffraction pattern is observed, from figure 3.17b a horizontal line at the centre of the diffraction pattern is observed, and from figure 3.17c a cross-shaped pattern is at the centre of the diffraction pattern is observed. The aperture can be positioned at the CLC for maximum flux from these patterns.

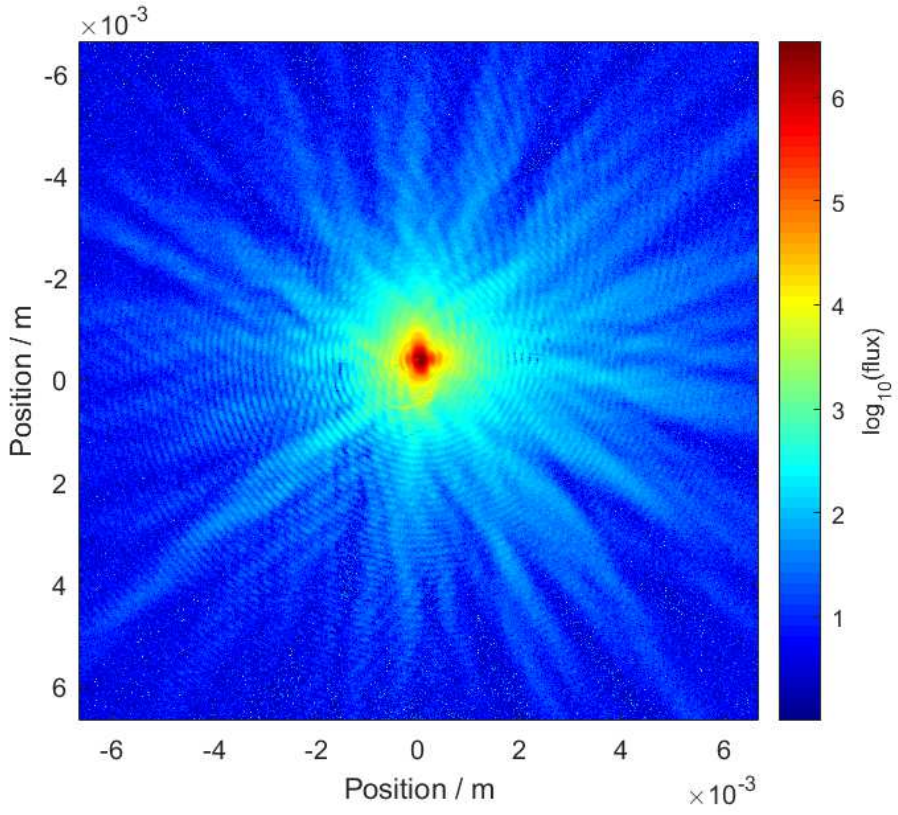

FIGURE 3.19: Recorded measurements of the diffraction pattern of a 10 μm aperture, with a maximum exposure of 10 s, binning of 2, cropping of 1, at a temperature of -40 °C and taking 18 s.

This image was taken by myself using the experimental setup. From figure 3.19 it is seen that the aperture's position is within the CLC due to the cross at the centre of the scatter pattern; it can also be seen that the beam is spatially coherent due to the ring pattern existing across figure 3.19 towards the edge. Figure 3.19 doesn't exactly

resemble figure 3.17c, where the cross in the middle is not the same and the rings decay towards the edge. This can be due to not being exactly at the CLC, the aperture not being at the centre of the beam, or due to higher flux being chosen at the expense of the coherence of the beam.

3.2.2 Summary

The system for HHG and ptychography consists of many different elements. This section discussed the components of the system that generate a high-intensity short-pulse beam, followed by an explanation of the peripherals that measure and stabilise the beam. The equipment used for HHG was discussed. Finally, the vacuum chamber and the components within were explained.

Chapter 4

Experimental Procedure

This chapter is a detailed outline of how to use the system explained in the previous chapter to acquire data for later reconstruction. This section will first explain the process I used to generate high harmonics, then how the high harmonics are optimised for imaging, and finally the process of acquiring the data.

4.1 Preparation

The first thing to do is turn on and get all the equipment ready for use. First, the chillers for the lasers are turned on to bring them to the desired temperature. The Millennia, Tsunami, and Evolution need to be turned on and warmed up for around an hour to reach thermal stability.

The Spitfire needs to be dehumidified to below 10% before it can be cooled to -14 °C, otherwise ice will form on the gain crystal.

The turbo for the vacuum chamber can be turned on if the chamber is less than $5{\cdot}10^{-2}$ mbar from the rotary pump being on, this will bring the chamber down to $7{\cdot}10^{-6}$ mbar. This should take around an hour. Initialise the CCD and SmarAct stages with the MATLAB commands 'cam = Andor()' and 'motor = Smaract()'. Once the chamber pressure is low, begin cooling the CCD now to save time, otherwise it will need to be cooled before the ptychography scan. This is to reduce the dark noise when collecting data. The

CCD should not be cooled before the chamber's pressure has been lowered, otherwise too much ice will form on the CCD's chip.

The turbo for the gas cell and the chamber it's attached to can be turned on, and this will bring the pressure down to $3{\cdot}10^{-2}$ mbar. This is quick, and should only take minutes since the volume of these parts is much smaller than the vacuum chamber. Once the pressure has lowered, the software controlling the flow of argon into the system should be turned on. Then, open the final valve connecting the argon to the gas cell, this will cause a spike in the pressure measured by the software, but is nothing of concern. Next, open the valve of the manifold. Then, open the valve on the argon canister, and increase the pressure to 5 bar. The reason for opening the valves in this order is to allow the argon to have somewhere to go. Then, adjust the valve of the manifold to 2 bar. Afterwards, adjust the valve before the gas cell to 1 bar. When the pressure of the vacuum chamber is $7{\cdot}10^{-6}$ mbar pull the filter to the 'out of the beam path' position. Slowly open the gate closest to the vacuum chamber attached to the gas cell, once the pressure has stabilised put the filter back into the 'in the beam' position. Finally, in increments of 20 mbar increase the pressure of the argon flow on the software, waiting for the pressure to stabilise each time; this is to prevent the filter from being damaged.

4.2 Mode-locking

Once the Tsunami has warmed up it can be mode-locked. The output power of the Tsunami should be 330 mW. Mode-locking the Tsunami is achieved by turning the acousto-optic modulator on and moving the prism out of the beam. When moving the prism out of the beam the central wavelength of the beam measured by the spectrometer will increase. When the central wavelength is greater than 850 nm, begin moving the prism back into the beam and the central wavelength will decrease; continue until the pulse width suddenly increases. If you reach a central wavelength of 800 nm, try again but move the prism out to a higher central wavelength. If the Tsunami is still not mode-locking it is most likely that the Tsunami has not warmed up enough. Continue moving the prism into the beam until the central wavelength has decreased by 10 nm, then turn the AOM off. Keep moving the prism in until the pulse width is 50 nm. If it does not reach 50 nm the Tsunami has most likely not warmed up enough, but if that

is not the case the slits of the Tsunami need to be adjusted, and in a worst-case scenario the prism needs to be realigned.

4.3 Evolution

On the Evolution software press and hold the run button until the current of the Evolution begins to increase. The Evolution current will increase to 22.5 A, and then it is ready for the Spitfire to begin amplifying the beam.

4.4 Spitfire

Once the Tsunami has been mode-locked the safety measures preventing the beam from entering the Spitfire will now allow the mode-locked beam to enter. The Spitfire has been set for the mode-locked pulse to use all the gain in the crystal, but this can be checked with an oscilloscope where increasing the number of round trips through the Spitfire crystal will increase the power of the mode-locked pulse to a point after which the power will begin to drop. The time the pulse spends in the Spitfire should be adjusted to just before the power drops. The distance between the compressor grating and mirror should be adjusted until the pulse length is 50 fs, this will need to be adjusted around every half an hour to an hour as the Spitfire warms up. Rotate the quarter wave plate after the Spitfire so that the power after the quarter wave plate is 1.4 W.

4.5 Beam Stabilisation

Once the pulse has been amplified and the beam is exiting the Spitfire make sure the mirror to change the beam line is down so the beam goes the ptychography setup. The beam will then appear on two cameras. Adjust the rotation of the stabilisation mirror to centre the beam on camera 1, then adjust the rotation of the stabilisation lens to centre the beam on camera 2, and repeat until the beam is centred on both cameras. After, press 'find optimal exposure', and then press 'lock beam position' on the beam stabilisation software. Then, run the stabilisation routine. If the stabilisation is not good, run the calibration routine, then rerun the stabilisation routine.

4.6 Beam Quality

With no aperture or sample in the beam path, images of the beam's flux count can quickly be taken to see the shape of the beam at the CCD, with the MATLAB command 'While cam.GetData'. The stabilisation lens can be moved along the beam path to change the total flux and shape of the beam by changing the focal point of the beam in the gas cell. Move the lens to a position where the beam's shape is close to a circle but is still an ellipse, as this balances flux and coherence. If no beam is showing it could be that the compressor distance needs adjusting, the gate to the gas cell is not opening, or no argon is reaching the gas cell.

To perform ptychography the HHG beam needs to be spatially coherent. This can be measured by collecting the diffraction pattern of the beam passing through a double slit mask. The visibility can be calculated by finding the ratio of the height of the central peak and its nearest trough. A visibility of lower than 0.85 should not be used, as the spatial coherence of the beam will be too low. If the visibility is too low adjust the position of the stabilisation mirror along the beam path until a high enough visibility has been achieved.

4.7 Aperture to Object Distance

The two SmarAct stages have position values that are independent of each other. To calibrate the z distance between the aperture and the object mounts align the two SmarAct stages along the x-axis using the camera in the chamber. There is a series of steps at the bottom of the aperture mount, change the y position to match the z distance you desire between the aperture and sample. While observing the mounts from the camera in the vacuum chamber move one mount closer to the other mount along the z direction until the mount can no longer move. This can then be used to know the offset of the two mounts.

When attempting to find the offset of the two SmarAct stages I missed the steps and pushed the aperture into a sample of polystyrene spheres. Afterwards, the apertures were permanently altered with some of the polystyrene spheres attached to the apertures. When reconstructing data afterwards the probe did not appear to be the same,

and back-propagating the probe to the position of the aperture, the polystyrene spheres could be seen on the aperture. This prompted the investigations of chapter 5.

4.8 Locating Apertures and Samples

Locating the apertures is achieved by performing an intensity scan of an area, with the sample mount set to a position where it does not interfere with the beam. If imaging has been done recently a small area can be used if imaging has not been done recently the beam's position may have drifted too far away for a small area. If new apertures or samples have been added to the mount a larger area might also be needed. A small area is between 10-100 μm^2 and a large area is greater than 1 mm^2. For a large area, more scanning positions might be needed. Once the rough location has been found, an appropriately sized area for the aperture should be used with 25 or more scanning positions to find the centre of the aperture.

To find the sample use a previously known location, or if not known perform an intensity scan with a large area, with the aperture mount in a position that will not interfere with the beam. Have the sample and aperture mounts 1 mm apart, and move the aperture mount so the aperture is in the beam, then move the aperture mount to a distance 100 μm away from the sample mount. Then perform an intensity scan of an area the size of the sample. This will show the rough structure of the sample, and the sample can be moved to an area of interest, based on a visible microscope image of the sample before it was in the chamber.

4.9 Data acquisition

Position the desired aperture into the beam path, and the sample at the region that is to be imaged. This is so the mounts don't move too much before imaging, and potentially damage the aperture or the sample. In the MATLAB code that performs the ptychography scan, select the scan area, the aperture position, the sample position, and distance between scan positions. Every half an hour adjust the compressor grating in the Spitfire to maintain a 50 fs pulse length.

4.10 Changing Samples and Apertures

When changing the apertures and/or the samples on the mounts the vacuum chamber must be at atmosphere. Before changing either make sure to acquire a microscope image to be able to refer to, to locate apertures or regions of interest on the sample. Use acetone on the corners of the aperture or the sample to remove the glue. Then carefully remove the aperture or sample, add the new aperture or sample to the mount, and use glue to hold it in place on the mount.

To image at atmosphere the vacuum chamber would need to still be low pressure, but by encasing the sample between membranes containing water vapour and spaced by 50 μm it would be possible. The membranes can withstand the pressure difference without breaking, the water vapour allows the sample to not be fixed, and the 50 μm spacing minimises the distance the beam propagates through the water vapour while not complicating the fabrication process too much. The 50 μm spacer can be 3D printed as a hollow square and then the two membranes can be glued together with the spacer in between. This fabrication technique for combining the membranes with a spacer has been proven to work, but has never been tested for imaging with the experimental setup. Another complication of imaging at atmosphere is the cells will only survive 24 hours without additional nutrients, so this needs to be done quickly, and the time it takes to bring the pressure down in the current vacuum chamber is too long as the chamber is large, so a smaller chamber that can be depressurised quickly would be needed.

Chapter 5

What Makes a Good Probe?

When performing ptychography, the probe is the beam at the object and should be constant when collecting the scatter pattern data. The probe is translated along the x and y-axes around the object, such that there is an area of overlap between areas illuminated by the probe. A scatter pattern is formed for each probe position as a result of the interaction between the probe and the object. It is important that the beam is spatially coherent for the size of the probe, however, the beam does not need to be spatially coherent for the size of the final reconstructed image as that is made up of multiple smaller scans.

Within this chapter, the factors that make a good probe will be discussed throughout, with the aim to improve the overall resolution of reconstructions by changing the aperture used. What the probe is, its characteristics, and the current research into the effect of different probes on reconstructions will be discussed. Following will be an explanation of methods of measuring reconstruction resolution to compare the impact of different probes. This chapter contains both experimental and simulated data, as the experimental data offers authenticity, but the simulated data are more abundant. The code used for generating and analysing the simulated data was written by myself, except for the initial code to generate the Gaussian beam at the CLC, which was written by Dr Bill Brocklesby. PtychoShelves was used to reconstruct experimental data and the simulated data (35). Finally, an aperture and probe that results in a greatly improved resolution will be discussed.

5.1 Introduction

The probe's characteristics are controlled by the beam and an aperture. A probe can be characterised by its beam width, profile, flux count, degree of coherence and angular spread.

If the beam width of the probe is increased and the scanning positions are unchanged, the overlap of the probes on the sample increases. The optimal overlap of circular probes is reported to be around 70% to 90%(95); an overlap value less than this region will have a lower resolution as there is not enough overlap for current ptychographic reconstruction methods to work optimally, and above this region it tends towards single-shot CDI and loses the benefits of ptychography. As the size of the probe is varied, changing the scan positions to scan a larger area or using fewer positions is necessary to keep a fixed overlap. Scanning a larger area will increase the speed of imaging per unit area; fewer scanning positions can lead to a lower resolution of the reconstructed object, as there will then be less overlap of the probes on the sample. This will be explored further in section 4.8.

The probe profile is the shape of the 2-D cross-section of the probe. Its effects on the resolution of reconstruction are less well understood. The effect of the profile of the probe's field is investigated later by defining the complexity of the probe as a measure of the predicted resolution of reconstruction. This will be explored in section 4.7.

If a different aperture is used to shape the probe, the amount of flux transmitted can also change, where higher amounts of flux result in a greater signal-to-noise ratio. The amount of flux is important because certain objects, such as biological samples, may be sensitive to too much flux. This will be explored in section 4.5.

The angular spread of the probe is linked to the spatial frequencies measured by the detector. Increasing the angular spread, the higher spatial frequencies will be raised above the noise fluctuation threshold, leading to a higher resolution of the reconstructed object. This will be discussed further in section 4.1 and explored in section 4.13.

Below in figure 5.1 are experimental examples of probes that are the results of an off-axis focused HHG beam (15.6 μm spot size, and 29.3 nm) passing through a circular aperture (7 μm diameter) and a double slit aperture (5x1 μm slits spaced 4 μm from

centres), and propagating for 141 μm, the typical aperture to sample distance in our system.

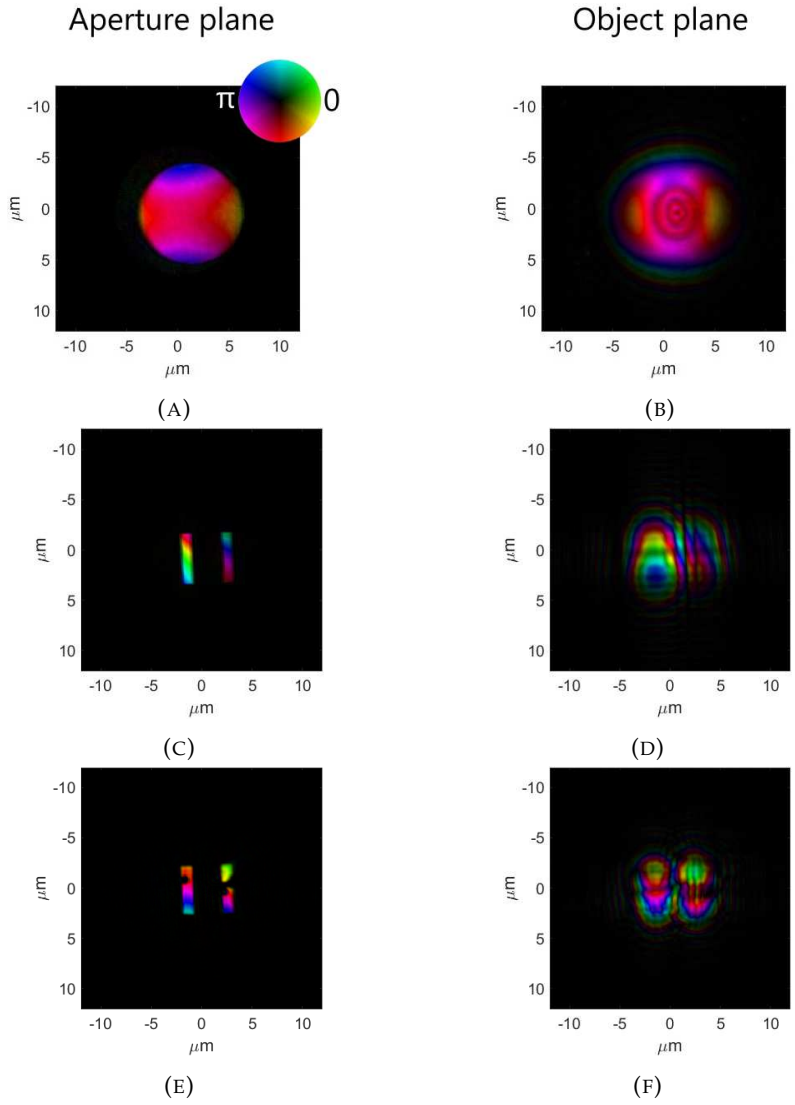

FIGURE 5.1: Images of the beam at the aperture and corresponding probes, after the beam at the aperture has propagated to the object plane, with a Hue Saturation Value (HSV) display in the top right-hand corner of (A). (A) is the beam at a 7 μm diameter circular aperture recovered by the backpropagation of (B) using ASM to backpropagate 141 μm to the aperture plane, (B) is the reconstructed probe from a reconstruction of ptychographic data using a circular aperture (7 μm diameter). (C) is the beam at a double slit aperture (5x1 μm slits spaced 4 μm from centres) recovered by the backpropagation of (D) using ASM to backpropagate 141 μm, (D) is the reconstructed probe from a reconstruction of ptychographic data using a double slit aperture (5x1 μm slits spaced 4 μm from centres). (E) is the beam at a double slit aperture (5x1 μm slits spaced 4 μm from centres) recovered by the backpropagation of (F) using ASM to backpropagate 89 μm, (F) is the reconstructed probe from a reconstruction of ptychographic data using a double slit aperture (5x1 μm slits spaced 4 μm from centres) with 1 μm diameter polystyrene spheres on the aperture.

HSV is an intuitive method of displaying the phase information and the amplitude of the electric field of ptychographic reconstructions of objects. The hue represents the phase of the reconstructed object, and the value and saturation, the brightness, represent the amplitude of the reconstructed object. The hue corresponds to a phase shift from 0 to 2π. The brightness corresponds to the converted intensity of a grayscale image. This HSV wheel is not present on all ptychographic reconstructions as this would interrupt the images, but the concept applies to all coloured ptychographic reconstructions.

From figure 5.1, it is shown that the aperture used is very influential on the characteristics of the probe, where all four of the characteristics have been changed. The dark spot in the middle of (B) is due to the diffraction of the beam by the aperture, and would be a bright spot if the propagation distance had been 10 μm closer or further away. It is possible to transform between the object and the aperture plane using a near-field propagation technique. The near-field propagation was performed with the Angular Spectrum Method (ASM); ASM involves Fourier transforming the beam into its angular spectrum, then propagating the probe in the frequency domain by multiplying by the wave vector, and finally, an inverse Fourier transform is performed to calculate the propagated beam. ASM is limited in how far the wave can be propagated by the size of the matrix used to calculate the propagation, if the wave is propagated too far the beam will be larger than the physical size represented by the matrix and will no longer give an accurate calculation of the propagated wave. The sampling criteria for ASM is that the sampling rate in the angular spectrum must be at least twice the maximum spatial frequency in the field. The sampling rate used for ASM in this thesis was twice the maximum spatial frequency measurable by the detector. Using ASM to transform between the aperture and the object plane allows for parameters of the system to be recovered and imaging of the aperture. The distance that the probe has propagated from the aperture can be found by performing ASM on the probe and propagating a range of distances that the aperture is believed to be between. In this thesis, the aperture to object propagation distance was found by using the distance at which the aperture was in focus. This information can then be used in later reconstructions to refine the probe further. This is possible as the reconstructive code can propagate the probe back to the aperture plane, and values outside of the known aperture size are reduced to zero. Using backpropagation of the probe to the aperture allows us to investigate and confirm

the shape of the aperture, and see if the aperture has been damaged in any way. The reason (D) does not have the classic shape of a double slit diffraction pattern is because at a distance of 141 μm the Fresnel number is 1.48 and is in the near-field regime, and the Rayleigh length of that system is 655 μm. It can seen from (E) that objects on the aperture can be reconstructed, and more importantly, can alter the shape of the probe. It is also important to note that since the aperture is positioned at the CLC the phase has a saddle shape, and this can be seen in 5.1 (A), (C), and (E) across the circular aperture and double slit aperture.

Since the probe used in reconstruction needs to be coherent, when using a double slit both of the slits need to have light that is coherent with one another. When light propagates through a double slit, if the light is coherent between both slits, you get the classic double slit diffraction pattern. When using light that is incoherent between the two slits the diffraction pattern becomes the sum of two individual slits.

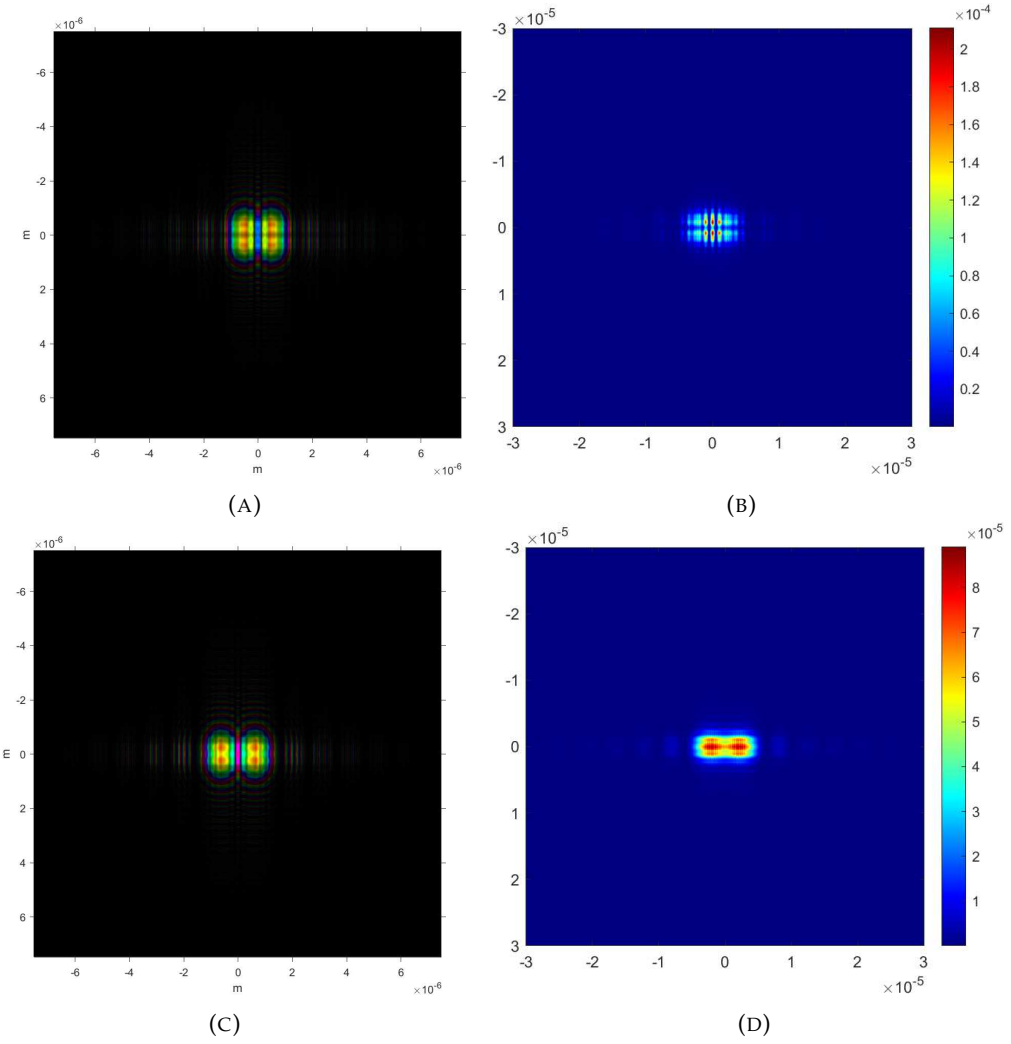

FIGURE 5.2: Images comparing a coherent and incoherent beam at the CLC for a double slit aperture (5x1 μm slits spaced 4 μm from centres) using simulated data. (A) is the amplitude and phase of a propagated beam from the double slit aperture 141 μm away using a coherent beam. (B) is the intensity of a propagated beam from the double slit aperture 3.69 cm away using a coherent beam. (C) is the amplitude and phase of a propagated beam from the double slit aperture 141 μm away using an incoherent beam. (D) is the intensity of a propagated beam from the double slit aperture 3.69 cm away using an incoherent beam.

As can be seen from figure 5.2 we don't get the classical diffraction patterns for a coherent and an incoherent beam, this is due to the saddle-shaped phase at the aperture. (A) and (C) look similar as the beam has not propagated far and in the coherent case of (A) not much distance for the beam through both slits to interfere. The difference between the coherent and incoherent cases of (B) and (D) is much more pronounced.

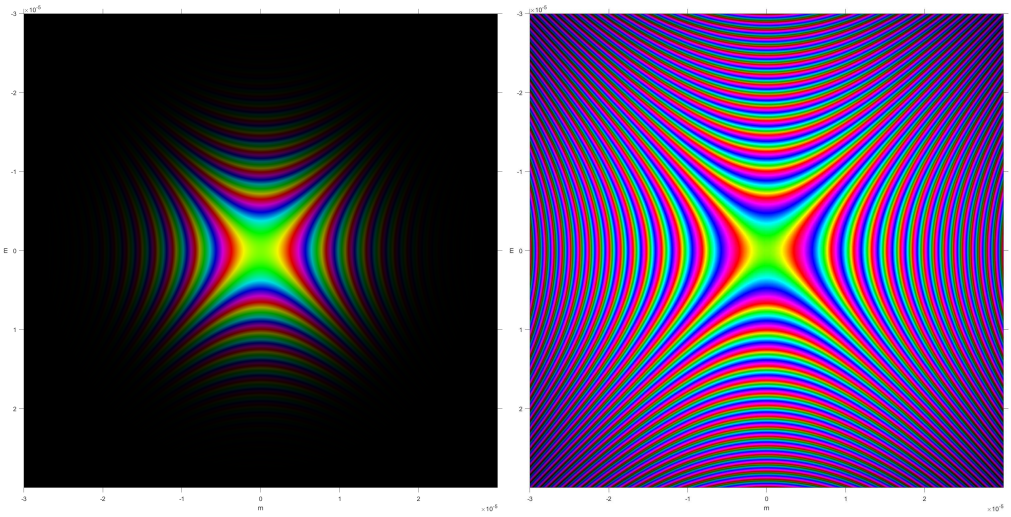

(A) (B)

FIGURE 5.3: Images comparing the beam at the aperture for two different M^2 values using simulated data. (A) is the beam at the aperture with an M^2 value of 3, the value used for all other simulated data throughout this thesis. (B) is the beam at the aperture with an M^2 value of 10.

From figure 5.3 it can be seen that increasing the M^2 value of the beam at the aperture only increases the extent of the amplitude of the beam, and that the phase variation of the beam remains constant. Since the probe illumination of the beam remains constant the shape of the probe also remains constant.

When reconstructing the data from ptychography, the reconstructed probe recovered did not appear to come from a perfectly circular aperture as expected; when the probe was back-propagated to the plane of the aperture, the image of polystyrene spheres could be seen around the edge of the aperture. The presence of the spheres had changed the probe at the sample from what a circular aperture's probe would have been, indicating something had happened to the aperture. The effect on the changes to the probe led to investigating reconstructions using different apertures and their effect on the resolution of reconstructed objects. When reconstructing an object using the double slit, the double slit had a higher resolution than the circular aperture when comparing the Fourier Ring Correlation (FRC) of each, so a series of experiments and simulations were performed in order to refine what makes a 'good' probe.

Not much research has been conducted into what makes a good probe. Guizar-Sicairos *et al.* (96) investigated the effect of the spatial frequency of the probe's spectrum on the

resolution of reconstructions, and concluded that a wider spread in reciprocal space is beneficial.

When analysing the scatter patterns from the circular and double slits, the double slits' scatter pattern had a greater angular spread. The Fourier transforms of natural objects have a decaying power spectrum, where higher spatial frequencies have a lower power (97). The scatter pattern measured is the Fourier transform of the product of the probe and object, thus the scatter pattern is the convolution of the Fourier transform of the object and the Fourier transform of the probe. A probe with a higher angular spread will cause the higher spatial frequency components of the spectrum to have a higher signal-to-noise ratio. This increase in the signal-to-noise ratio at the higher spatial frequencies will increase the resolution at which the object can be reconstructed.

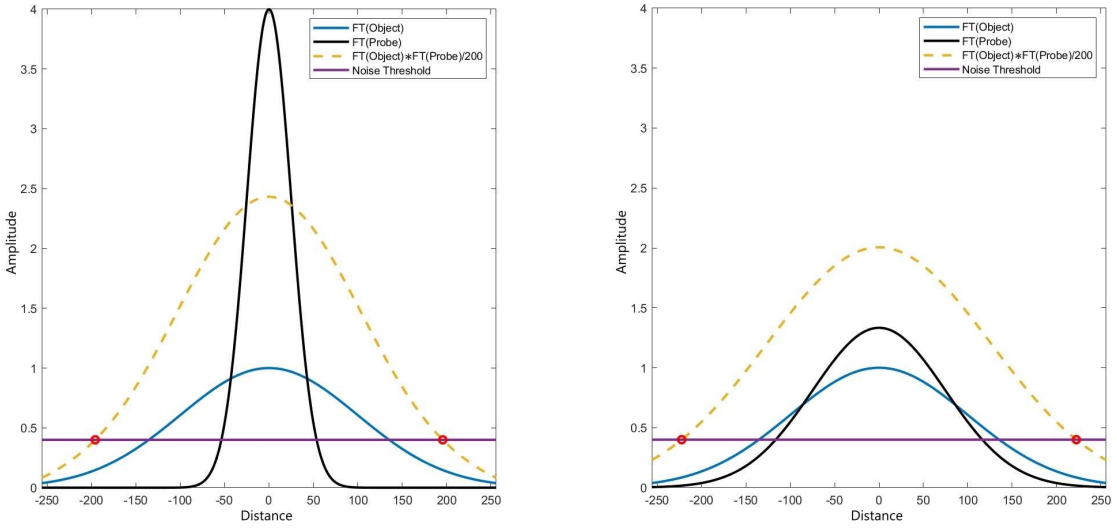

FIGURE 5.4: The cross-sections of the power spectrums of the Fourier transform of a Gaussian object, two probes, the convolution of object and individual probes, (A) the low angular spread probe, and (B) the high angular spread probe, with the power spectrum of the object's Fourier transform (blue line), the Fourier transform of the probe (black line), the convolution of the object and the probe (yellow dashed line), the noise level (purple line), and the intercept of a noise threshold and the convolution of the object and the probe (red circles).

In figure 5.4, it is shown that a probe of lower maximum intensity and higher angular spread has more of the convolution of the object and the probe above the noise threshold. The low angular spread probe intercepts the noise level at 196 units from the centre, and the high angular spread probe intercepts the noise threshold at 222 units from the centre. The noise level in figure 5.4 represents the amount of fluctuation in the noise, as the readout noise from the CCD has a defined average value; if the noise

was a constant value it could be removed. The CCD used for experimental work has a readout noise of 2 counts, but 0.4 was used here for clarity of the figure. Convolution theorem states the Fourier transform of the convolution of two arbitrary functions f and g is equal to the product of the Fourier transforms of f and g (98). This can be expressed as:

$$\mathcal{F}[f * g] = \mathcal{F}[f] \cdot \mathcal{F}[g] = \mathbf{F} \cdot \mathbf{G} \tag{5.1}$$

where $\mathbf{F}$ is the Fourier transform of f, and $\mathbf{G}$ is the Fourier transform of g. Equation (5.1) can be written alternately as:

$$\mathcal{F}[f \cdot g] = \mathcal{F}[f] * \mathcal{F}[g] = \mathbf{F} * \mathbf{G}. \tag{5.2}$$

From equation (5.2), if the object is the function f and the probe is function g, and if the angular spread of the probe is larger, the convolution of the Fourier transforms will have larger spatial frequency amplitudes for higher spatial frequencies. The concept is that the object is fixed, but the angular spread of the probe can be changed; therefore, the scatter pattern measured can contain higher spatial frequencies of a greater intensity, unlocking the ability to reconstruct objects with higher resolution without increasing flux.

By using a simulation that replicates an experimental setup to test multiple apertures to give different probes and calculating the angular spread for different probes, the probes with a greater angular spread should yield a reconstruction with higher resolution, then a value to predict the probe's quality can be assigned. Other parameters will be characterised to attempt to determine what makes a good probe.

It is possible to increase the angular spread of a probe by reducing the size of the aperture; however, this will reduce the transmitted flux, the probe size at the object, and the probe's complexity.

5.2 Fourier Ring Correlation

Defining resolution as a single number, by using a method such as knife-edge resolution, is a simplification. FRCs were developed by Saxton and Baumeister in 1982 to give a more accurate measure of resolution (99). The accuracy of a reconstruction varies depending on spatial frequency, where the reconstruction of lower spatial frequencies, which correspond to larger features of the object, are usually more accurate, this can be due to the Fourier transforms of natural objects having a decaying power spectrum mentioned earlier (97). An FRC calculates the correlation between the summation of values at different spatial frequencies for two Fourier transforms of reconstructions of an object. The FRC is defined as (100):

$$FRC(r) = \frac{\sum_{r \epsilon r_i} F_1(r) \cdot F_2(r)^*}{\sqrt{\sum_{r \epsilon r_i} F_1^2(r) \cdot \sum_{r \epsilon r_i} F_2^2(r)}} \tag{5.3}$$

where F_1 is the Fourier transform of the first object, F_2 is the Fourier transform of the second object, and r_i is the individual element at radius r. The one-bit and half-bit criteria were introduced to determine a value where the information in a pixel in Fourier space has dropped below a threshold, where the one-bit criterion is defined by:

$$T_{1-bit}(r_i) = \frac{0.5 + 2.4142 \cdot 1/\sqrt{n(r_i)}}{1.5 + 1.4142 \cdot 1/\sqrt{n(r_i)}} \tag{5.4}$$

and the half-bit criteria defined by:

$$T_{1/2-bit}(r_i) = \frac{0.2071 + 1.9102 \cdot 1/\sqrt{n(r_i)}}{1.2071 + 0.9102 \cdot 1/\sqrt{n(r_i)}} \tag{5.5}$$

where $\mathrm{n}(r_i)$ for both are the number of elements in the ring for each spatial frequency. The one-bit and half-bit criteria are thresholds in which the signal-to-noise ratio (SNR) has reached a certain level. The one-bit criterion is when the signal is equal to the noise, and the half-bit criterion is when the signal is twice the noise. For (5.4) and (5.5), when the FRC curve intercepts the criteria, the average information contained per pixel at that spatial frequency will be one bit or half a bit, hence the names of the criterion. The one-bit criterion is a more stringent criterion when defining an image's resolution. To

produce a resolution that agrees with previous X-ray crystallography criteria, the half-bit criterion was introduced for cryo-EM experiments. This led to the half-bit criteria being widely used as the standard resolution measurement for FRCs. An FRC that doesn't intercept the chosen criterion shows the object is at the maximum resolution of the system (100).

When calculating the FRC, two independent images reconstructed from different data of the same object are usually required as an FRC with the same object would result in a correlation of 1 for all spatial frequencies. If the objects are not aligned, they need to be spatially shifted to perform the FRC. Recently in 2019 it has been shown by Koho that only one image is required for Fourier correlations (101). This is achieved b dividing a single image into two image pairs, where the first image pair uses all pixels with even row and column indices for the first image, and all pixels with odd row and column indices for the second image. The second image pair is created by using all even row and odd column indices for the first image, and by using all odd row and even column indices for the second image. An FRC can be calculated from a single image pair, but averaging the two image pairs gives a better result.

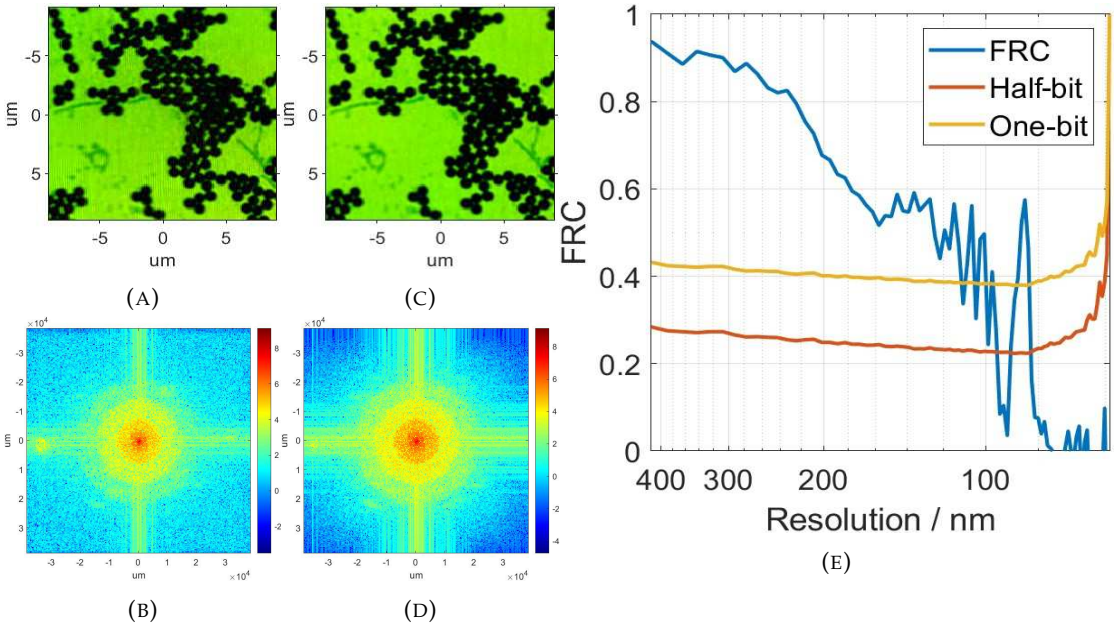

FIGURE 5.5: FRC calculation of experimental datathat I took. (A) and (C) are cropped images of reconstructions from unique data of 945 nm polystyrene spheres using a double slit (5x1 μm slits spaced 4 μm from centres) positioned 140 μm before the object at the CLC of 29 nm soft X-ray beam. (B) and (D) are the Fourier transforms of (A) and (C) respectively. (E) is the FRC against the ratio of spatial frequency and Nyquist frequency (blue) with the one-bit criterion (yellow) and the half-bit criterion (orange).

Figure 5.5 shows two aligned reconstructed images of the same object, their Fourier transforms, and the resultant FRC. The correlation between the Fourier transforms first intercepts the half-bit criterion at a spatial frequency corresponding to 95 nm but then shows a strong correlation between 89 nm and 82 nm. The features from 82 to 89 nm may arise from the way the Fourier transforms were windowed. The resolution at the Nyquist limit of the detector is 82 nm, where the Nyquist limit is the maximum spatial frequency measurable by the detector; a higher Nyquist limit is achieved by increasing the size of the detector or reducing the distance to the object. The Nyquist limit is defined by:

$$\text{Nyquist limit} = \frac{\lambda}{2\text{NA}} \tag{5.6}$$

where λ is the wavelength being measured at the detector, and NA is the numerical aperture of the detector. The resolution for figure 5.5 would be defined as 95 nm even though features between 89 nm and 82 nm are resolvable, which is the main issue of reducing the resolution to a single value.

5.2.1 Two-axis Fourier Line Correlation

The probe of a circular aperture is radially symmetric in shape; the scatter pattern will then be radially symmetric, if nothing such as an object interrupts the wave. The double slit probe is not radially symmetric, and has greater angular spread along the x-axis, compared with circular aperture of the equivalent diameter. The FRC is the average correlation of spatial frequencies along all directions, this does not matter for a radially symmetric probe as the Fourier correlation is the same in all directions. Non-radially symmetric probes do not necessarily have the same Fourier correlation in a particular direction as the FRC value. Instead of a ring at increasing spatial frequencies, the Fourier correlations can be taken at increasing spatial frequencies along the x and y-axes. To test this, the same principles from FRCs will be used, comparing the flux between the two Fourier transforms of reconstructions from repeat experiments of the same object using displacement in the x and y-axes instead of the magnitude of distance

r, where the Fourier Line Correlation (FLC) in x is defined by:

$$FLC(x) = \frac{\sum_{x \epsilon x_i} F_1(x) \cdot F_2(x)^*}{\sqrt{\sum_{x \epsilon x_i} F_1^2(x) \cdot \sum_{x \epsilon x_i} F_2^2(x)}} \tag{5.7}$$

where x is the distance from the centre along the x-axis. The FLC in y is defined by:

$$FLC(y) = \frac{\sum_{y \epsilon y_i} F_1(y) \cdot F_2(y)^*}{\sqrt{\sum_{y \epsilon y_i} F_1^2(y) \cdot \sum_{y \epsilon y_i} F_2^2(y)}} \tag{5.8}$$

where y is the distance from the centre along the y-axis.

Before comparing FLCs of a non-radially symmetric probe, it would be prudent to investigate a radially symmetric probe to investigate if using FLCs are a good measure of directional resolution.

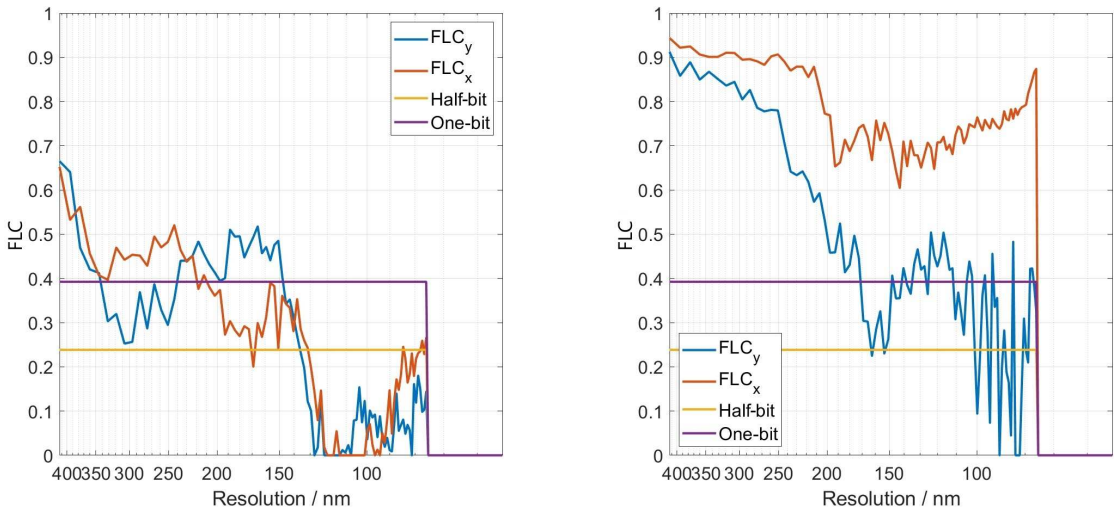

(A) (B)

FIGURE 5.6: FLC calculations of experimental data. (A) is the FLC for reconstructed data from a 7 μm circular aperture, (B) is the FLC for the data used in figure 5.5, reconstructed data from a double slit aperture (5x1 μm slits spaced 4 μm from centres, with the slit diffraction along the x-axis), to compare FLC_x (orange) and FLC_y (blue), and containing the one-bit criterion (purple) and the half-bit criterion (yellow).

From figure 5.6, it is clearly shown that a nearly radially symmetric probe has nearly equal FLCs in both the x and y directions. The double slit probe has greater angular spread on the x-axis, leading to two different FLCs in x and y. Figure 5.6 continues to 55 nm as this is the resolution in the corners of the detector as calculated by using equation (5.6) using the numerical aperture of the corners of the detector; however,

FRC_x and FRC_y only reach the resolution at the Nyquist limit of the detector of 82 nm. The double slit's resolution along the x-axis is 82 nm and resolution along the y-axis is 162 nm.

5.2.2 Complete Fourier Line Correlation

Building upon Fourier correlation in two directions, an FLC can be measured at all angles between the x and y-axis. An FLC for all directions is needed to explore the best possible aperture. It is possible to take the Fourier line correlation further by expanding it from two directions to all directions by using the equation:

$$FLC(\theta) = \frac{\sum_{u \epsilon u_i} F_1(u) \cdot F_2(u)^*}{\sqrt{\sum_{u \epsilon u_i} F_1^2(u) \cdot \sum_{u \epsilon u_i} F_2^2(u)}} \tag{5.9}$$

where θ is the angle of the line from the y-axis, and u is the distance from the line from the origin. Equations (5.7) and (5.8) are specific forms of this equation (5.9) for $\theta = 0°$ and $\theta = 90°$ respectively.

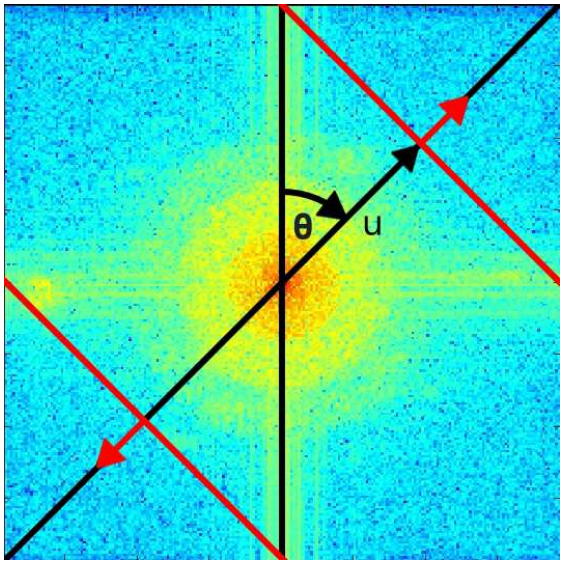

FIGURE 5.7: A diagram showing how the Fourier correlations for FLCs are calculated for an angle θ at a distance u where the red lines without arrows are the regions being compared between the two Fourier transforms of the two reconstructions of the same object.

Figure 5.7 shows how one Fourier correlation for an angle θ at a distance is calculated. All Fourier correlations would be calculated for all distances of u at each angle of θ to calculate the full FLC.

With (5.9) multiple FLCs of varying angles of θ can be calculated.

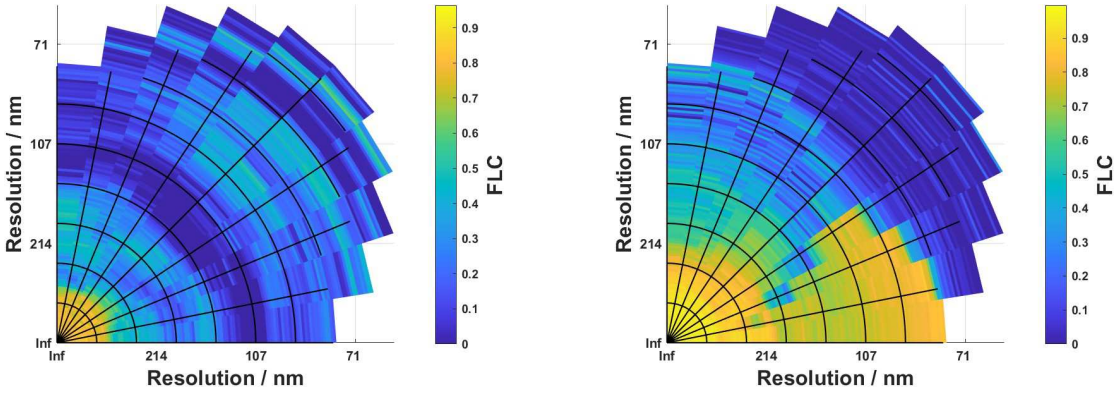

(A) (B)

FIGURE 5.8: FLC calculations of experimental data that I took. (A) is the FLC for reconstructed data from a 7 μm circular aperture, (B) is the FLC for the data used in figure 5.5, reconstructed data from a double slit aperture (5x1 μm slits spaced 4 μm from centres).

The polar plots from figure 5.8 give a more complete picture of the resolution and a deeper understanding of the probe's shape on the effect of reconstruction quality. As shown by figure 5.8 (A), the radial symmetry of the 7 μm circular aperture leads to a nearly symmetric FLC; this is not perfectly symmetrical as the aperture is at the CLC, causing a slightly non-symmetrical probe. From figure 5.8 (B) the resolution is the greatest in the direction that the double slit has the highest angular spread, and where the double slit scatter pattern is very weak in the corners of the CCD the FLC is also at its lowest.

From figure 5.8 looking at (B) there is a sharp change in resolution, this is due to how the directional resolution is being calculated using FLC. The double slit scatter pattern has a high amplitude along the x-axis and y-axis, and at certain angles when calculating the FLC these high amplitude regions contribute to the FLC value for longer than compared to neighbouring angles. This causes the FLC value to be dominated by the smaller high amplitude region compared to the larger noisy region, therefore, when comparing neighbouring angles in the double slit case a sharp change in FLC value can be seen. The sharp change in FLC value is also due to the number of angles used in

the FLC calculations, and by increasing the number of angles the sharp changes in FLC values are smoothed out.

In the field of cryo-EM, directional Fourier shell correlations (FSC) were developed in 2021 (102). The directional FSC calculates the Fourier correlation from cones; the technique was developed in response to the different resolutions of proteins angled differently. FLCs were developed separately and were not intended to show the effect of the object on directional resolution but instead the effect of the probe's angular spread on the directional resolution; however, FLCs would also be affected by the object with directional resolution.

5.3 Methodology

It has been shown in the previous section that a higher angular spread in a direction leads to a greater Fourier correlation in that direction. Fabricating new apertures to test new probes is time-consuming; therefore, a simulation will dramatically speed up the rate at which apertures can be tested. An accurate simulation can be developed by comparing experiment results with the simulation at every step from the beam to the reconstructed objects and FLCs. An accurate simulation can test the resolution of reconstruction for different apertures of varying angular spreads in varying directions. The simulation will also allow other fundamentals of the experiment to be investigated, such as the impact of flux on the resolution of reconstructed objects.

5.4 Simulation

Here is a detailed description of the simulation that allowed a more rapid data collection than obtaining data from an experiment. The simulation needed to allow for all parameters of the experiment to be varied. This simulation can then be used to investigate the effect of all parameters on the resolution of the reconstructed object. This simulation has been developed by myself over the last couple of years with its continuous refinement during my studies. Due to the time spent creating this simulation, it has become easy to test hypotheses regarding how to improve the resolution of ptychography and how experimental parameters affect the reconstruction, by simply adjusting

variables. Where it would take up to four hours to collect data and hours after to get the best reconstruction, it now takes minutes. With the speed of the simulation, it is possible to reduce a month of data acquisition down to a day.

5.4.1 Initialisation

The parameters of the simulation are defined. The parameters here have been set to replicate an experimental setup and can be changed later to investigate their effects on reconstruction resolution.

Aperture		
Parameter	**Value**	**Description**
dire	C:****\	Code location
apertureFile	Test_Apertures\star.png	Default aperture to use
aperFile	DoubleSlit	Aperture file identifier
aperSize	7.00E-06	Size of the aperture matrix in µm
aperPixels	720	Number of pixels in the aperture
a	4.00E-06	Aperture radius (5e-6 for clover)
apertureNo	1	Index of aperture used (1 is circular)
Object		
Parameter	**Value**	**Description**
objectFile	Test_Objects\NeuronImage.mat	Default object to use
thickness	0.25	Thickness of the object
polyAttenuation	-0.06	Attenuation of polystyrene for 29 nm
polyRIndex	(1-0.10329546) - (1i*0.037276342)	Refractive index of polystyrene for 29 nm
objFile	PolysphereObject5	Object file name
objPixScale	10e-6/720	Object pixel scale
BeamInstab(1)	2	Position instability
BeamInstab(2)	0.17	Power oscillations instability
BeamInstab(3)	0.1	Power amplitude instability
objPad	0.5	Padding multiplier for the object
CLC		
Parameter	**Value**	**Description**
L	1.51	Distance from source to mirror
R	0.5	Mirror radius
th_deg	5	Angle of the mirror (degrees)
l0	7.90E-07	Wavelength of the parent beam
harmonic	27	Which harmonic
W0	1.00E-05	spot size
M2	3	M^2 (beam quality factor, normally 3)
z	0.24999	Distance from the gas cell
fluxScaleSelect	1	Factor to change the flux of the beam
extent	6.00E-05	Extent (120e-6 is normal)
fluxFudge	4	factor to match flux count(1 for 120, 4 for 60)

TABLE 5.1: First half of the initialisation parameters for the simulation, their default values, and a brief description of each parameter.

Aperture		
Parameter	**Value**	**Description**
dire	C:****\	Code location
apertureFile	Test_Apertures\star.png	Default aperture to use
aperFile	DoubleSlit	Aperture file identifier
aperSize	7.00E-06	Size of the aperture matrix in µm
aperPixels	720	Number of pixels in the aperture
a	4.00E-06	Aperture radius (5e-6 for clover)
apertureNo	1	Index of aperture used (1 is circular)
Object		
Parameter	**Value**	**Description**
objectFile	Test_Objects\NeuronImage.mat	Default object to use
thickness	0.25	Thickness of the object
polyAttenuation	-0.06	Attenuation of polystyrene for 29 nm
polyRIndex	(1-0.10329546) - (1i*0.037276342)	Refractive index of polystyrene for 29 nm
objFile	PolysphereObject5	Object file name
objPixScale	10e-6/720	Object pixel scale
BeamInstab(1)	2	Position instability
BeamInstab(2)	0.17	Power oscillations instability
BeamInstab(3)	0.1	Power amplitude instability
objPad	0.5	Padding multiplier for the object
CLC		
Parameter	**Value**	**Description**
L	1.51	Distance from source to mirror
R	0.5	Mirror radius
th_deg	5	Angle of the mirror (degrees)
l0	7.90E-07	Wavelength of the parent beam
harmonic	27	Which harmonic
W0	1.00E-05	spot size
M2	3	M^2 (beam quality factor, normally 3)
z	0.24999	Distance from the gas cell
fluxScaleSelect	1	Factor to change the flux of the beam
extent	6.00E-05	Extent (120e-6 is normal)
fluxFudge	4	factor to match flux count(1 for 120, 4 for 60)

TABLE 5.2: Second half of the initialisation parameters for the simulation, their default values, and a brief description of each parameter.

5.4.2 The Gaussian Beam

First, code is used to simulate the propagation of the XUV beam using ABCD matrices after a spherical mirror. The beam width in the x and y-axis are calculated for the beam at the CLC using (3.42) and (3.43). Then, the complex beam parameters, the q values, are calculated to generate the beam wavefront. Finally, the x and y components are combined with meshgrid to form the beam at the CLC.

Using the desired extent as the size of the beam and object, then dividing by the desired number of pixels the difference between adjacent pixels is the pixel size. The extent should be large enough to fully encapsulate the beam and object; the number of pixels should be large for a more accurate simulation, or smaller for a faster simulation.

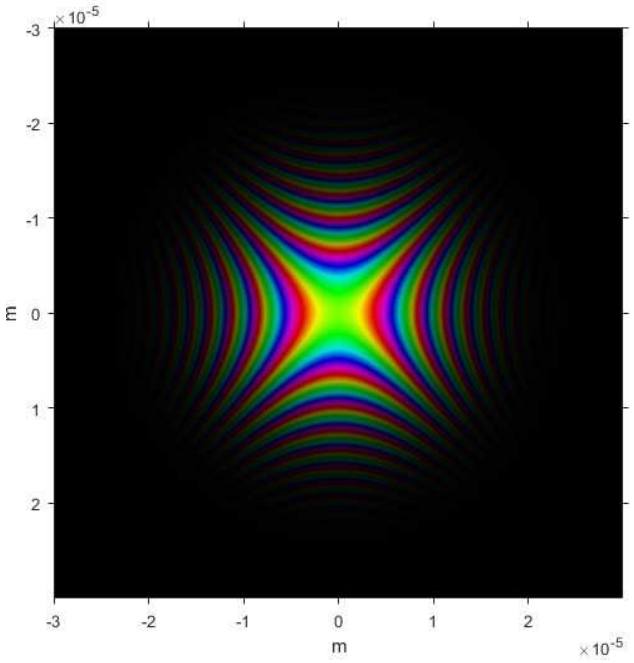

FIGURE 5.9: The electric field of the beam just before the aperture and at the CLC used in the simulations.

5.4.3 The Aperture and Probe

A mask is used to simulate the aperture. Real values define how much the aperture transmits at that pixel, where 0 is no transmission and 1 is full transmission. Imaginary values define the phase shift induced by the aperture. Complex values corresponding to phase shifts have not been used in any simulation in this thesis as we have no fabrication facilities for a phase mask at present; the benefits of using a phase mask would be that more flux of the beam could pass through the aperture, and it could allow for apertures that are impossible to fabricate with just transmission masks due to the structure not connecting. The beam at the aperture is generated by multiplying the mask and the beam. The beam at the aperture is propagated using ASM to calculate the probe at the object.

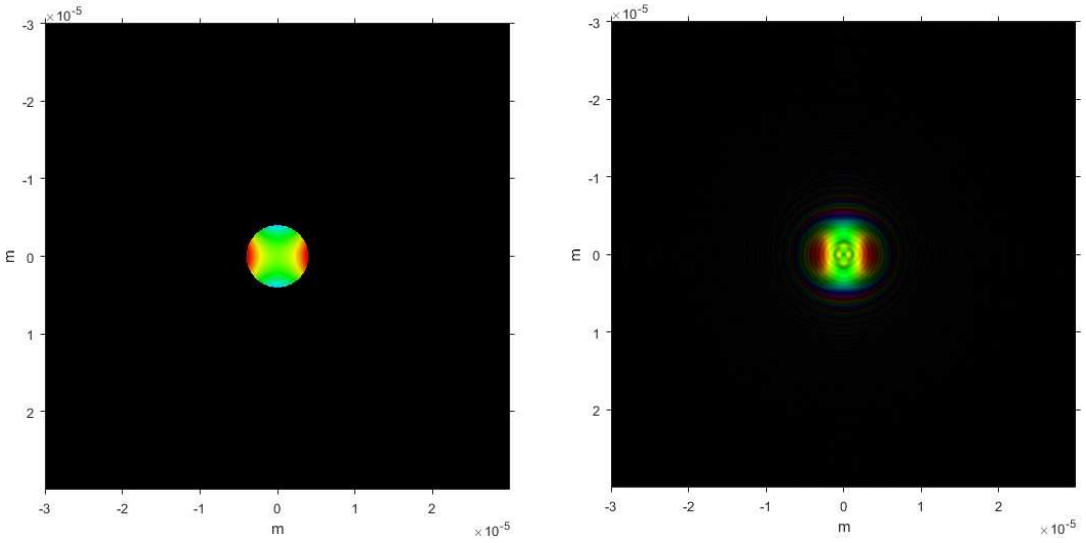

FIGURE 5.10: (A) the beam at a circular aperture (8 μm diameter), and (B) the probe after the beam propagated 141 μm from the aperture to the plane of the object.

From figure 5.10 it can seen that the phase is nearly flat, but the inversion of the saddle-shape phase can be seen at the edges of the circular aperture along the x-axis and y-axis. Boundary diffractive wave effects have not been accounted for here, ASM was used to propagate the beam which does not account for these effects.

5.4.4 The Object and Scanning Pattern

A reconstruction of neurons has been chosen as the object to be imaged within the simulation; this allows for a closer comparison with actual data and will make the simulation more accurate as the neurons are an actual object. The experimental data used are neurons imaged using a circular aperture (10 μm diameter). This had the issue that the reconstructed object didn't have detail greater than what was reconstructed, so the object was defined to be half the size and then tiled to create a larger object with smaller features. This would allow the reconstructed object to have features half the size, and the simulation wouldn't be limited by feature resolution.

When performing ptychography, positions of a scanning pattern are needed, allowing for overlap between points and covering the desired size. Though almost any scanning pattern with overlap can be used to perform ptychography, a Fermat spiral was used, as the Fermat spiral has low symmetry. High symmetry in a scanning pattern can lead to

"raster grid pathology", page 340 (103), which can cause artefacts in the reconstructed image (104). The first ring has seven scanning positions to remove any periodicity when taking a cross-section of the scatter pattern.

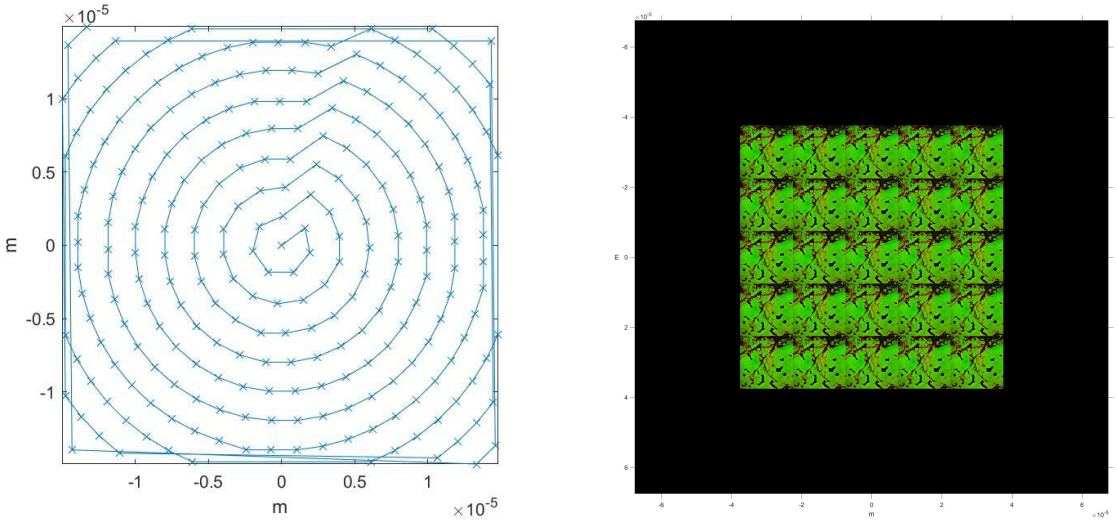

(A) (B)

FIGURE 5.11: (A) The scanning positions and order of a 30 μm by 30 μm scan area with a step size of 2 μm, resulting in 251 scanning positions, and (B) the object used in the simulation, where it has been created from an actual experimental reconstruction of neurons, then reduced in size and tiled.

5.4.5 The Scatter Pattern

The probe and the object are multiplied at the scanning position, then Fraunhofer propagation is used to calculate the far-field scatter pattern, as the Fresnel number is 0.024, which is far below 1. Then the scatter pattern is binned to simulate the pixels on the detector.

CCD Detectors have a saturation limit where flux counts can only be measured up to this value. If a scatter pattern were measured by a detector with no adjustments, the high spatial frequency components would have a low signal-to-noise. A high dynamic range (HDR) technique can remove this problem. A HDR image starts by taking a long exposure image, then if any pixels are saturated a shorter exposure image is taken, and this is repeated until an image is taken with no saturation. The images then can be divided by the time and combined. The code recreates this effect by taking the scatter pattern, dividing the value of the saturated pixels by ten, and repeating this until there are no pixels with a value above the saturation limit. Then, the readout and Poisson

noise are added. Afterwards, the values of the pixels are multiplied by the amount they were originally divided by to give the final scatter pattern.

The beam has spatial and power instability. The spatial instability is modelled by shifting the probe with a normal distribution from the intended scan position in the form of:

$$(x_{new}, y_{new}) = (x_{old}, y_{old}) + (g(0,d), g(0,d)) \tag{5.10}$$

where x is the x position of the scan position, y is the y position of the scan position, and g is a random Gaussian distribution about 0 with a standard deviation of d, where d was 50 nm for the simulation by default. The beam's power instability is modelled by a sine function, where the sine function's amplitude affects the instability's amplitude, and the frequency affects the rate at which the power fluctuates. This instability was in the form of:

$$P_{new} = P_{old}(1 - \frac{\text{instability}_{\text{amp}}}{2}) + \text{instability}_{\text{amp}} \sin(n \cdot \text{instability}_{\text{freq}}) \tag{5.11}$$

where P is the probe function, $\text{instability}_{\text{amp}}$ is the instability in the amplitude of the probe function, $\text{instability}_{\text{freq}}$ is the frequency of the instability, and n is the scan position index.

To reduce the thermal noise when measuring scatter patterns, the CCD chip is cooled to -40°. Due to the residual water content of the vacuum chamber, ice will begin to form on the CCD chip. The XUV beam is heavily attenuated by any ice that forms. The ice layer will grow if the CCD temperature is below 0°; this results in CCD measuring a lower-intensity scatter pattern as data are collected. This is simulated by increasing the size of the ice on the CCD at a constant rate per scan and attenuating the beam using the amount of ice calculated. The default amount of ice each scan added was 50 μm, which would result in about 50% transmission after 251 scans.

5.4.6 Reconstruction

PtychoShelves (35) from PSI is code used to reconstruct the object from the scatter patterns. To get high-resolution reconstructed objects, many settings must be optimised

per data set. To ensure the reconstructions do not fail with the simulated data, the settings have been changed to perform robust reconstructions. The main settings that were changed to perform robust reconstructions were using a loaded probe as the initial guess for the probe, and performing DM first to get a good estimation of the object before using MLs. PtychoShelves also performs well when given a good estimate of the probe, such as using a previous reconstruction of the probe. Here the actual probe used in the simulated data has been used to minimise failed reconstructions (35). Using the actual probe used for creating the simulated data removes one unknown for the reconstruction allowing for a better convergence for the reconstruction of the object. This is representative of our experiments.

5.4.7 The Error Calculation

To calculate the error of the reconstructed simulated object, two reconstructions of different data sets of the same object are required to perform an FRC. The resolution is defined as the first intercept of the FRC and half-bit criterion. This doesn't consider the FRC rising above the half-bit criterion line again; however, this is a widely accepted value for resolution and simplifies the results.

5.5 Variation of Simulation

In the following section it is helpful to know the variation of the FRC values of the simulation for the same initialisation values, where only the noise is varying. By running the simulation 24 times with the same input parameters the variation of reconstruction quality can be measured by the resulting FRC values.

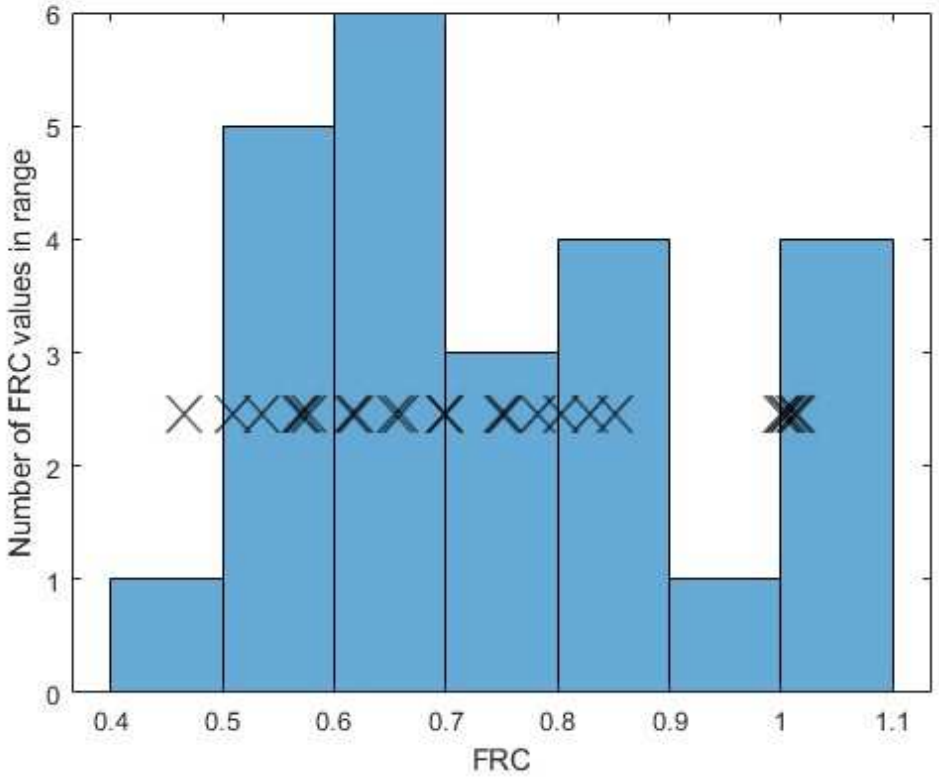

FIGURE 5.12: A histogram and scatter plot 24 runs of the simulation with same initialisation values. The histogram shows groups of FRC values in 0.1 ranges (blue bars). The scatter plot shows the exact FRC values for the 24 simulation runs (black crosses).

From figure 5.12 the variation of the FRC for the same initial parameters can be seen, with a near gaussian-shape except for the peak around 1. With the data for this graph, the mean of 0.7413 and standard deviation of 0.1734 can be calculated.

5.6 Flux

The double slit aperture's probe has half the flux of the circular aperture (7 μm diameter), yet reconstructions using the double slit aperture had a higher FRC first intercept of the half-bit criterion of 1 compared to 0.6. This shows that higher flux does not necessarily result in a higher resolution. Higher flux would increase the signal-to-noise ratio, so the resolution might be expected to improve with higher flux for the same aperture.

To investigate the effect of flux on the resolution of the reconstructed object the simulation would be used to calculate the FRC first intercept of the half-bit criterion for

varying amounts of flux. The amount of flux for a circular aperture (8 μm diameter) was measured to be $2{\cdot}10^7$ countswhen using initial parameters that match the experimental setup; a range from $1{\cdot}10^5$ to $2{\cdot}10^{13}$ was used in the simulation. While an 8 μm circular aperture was simulated in this section, only experimental data for the flux count of a 7 μm circular aperture were available to match to. In this section an 8 μm circular aperture was simulated as it balances the flux count and angular spread of the probe to attempt to achieve the highest resolution during the simulations.

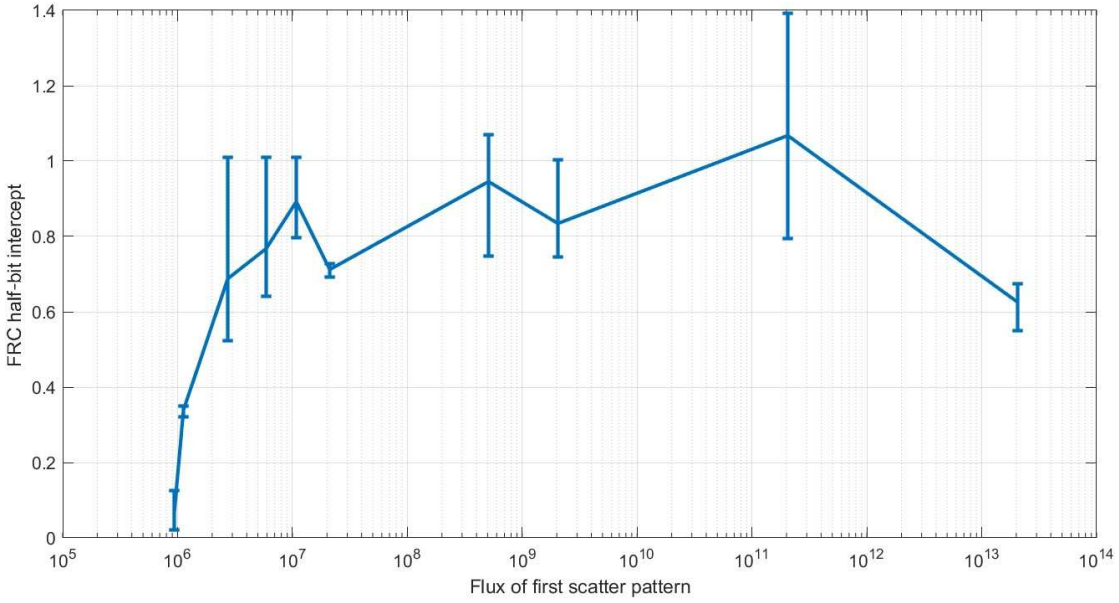

FIGURE 5.13: FRC half-bit intercept of simulated data with varying levels of flux. The FRC half-bit intercept (blue line) for simulated data using a circular aperture (8 μm diameter) with a reconstructed object of neurons for flux counts from 1% to $1 \cdot 10^8$% of a flux count measured from a circular aperture (7 μm diameter).

From figure 5.13, it is shown that the FRC first intercept of the half-bit criterion rises quickly when increasing the flux of the reconstruction, and then plateaus when reaching an FRC first intercept of the half-bit criterion of the detector's Nyquist limit, where in this thesis a detector's Nyquist limit refers to maximum spatial frequency recorded by the detector at the edge of its x or y-axis. The cause of a decrease in the FRC first intercept of the half-bit criterion for the final data point could be due to the reconstruction algorithms' inability to handle high flux counts over the whole scatter pattern. The second-to-last point's FRC first intercept of the half-bit criterion having a maximum of 1.4 is also unusual, but it is possible to have two independent reconstructions that are that similar.

This implies once the flux is high enough to reach the maximum resolution for a given probe, the reconstructed object's resolution cannot be improved by increasing the flux.

5.7 CCD Distance

When measuring the scatter pattern from the combination of the probe and object, the further from the centre of the scatter pattern, the greater the spatial frequency. The CCD, however, is a set size; without changing the aperture or beam, the CCD must be moved perpendicular to the beam to change the spatial components measured. By reducing the distance of the CCD to the object, the Nyquist limit of the CCD will increase. With higher spatial frequencies when reconstructing, the resolution of the reconstruction should increase.

Using the simulation to reconstruct two unique data sets of the same parameters over eleven object to CCD distances averaged over three runs, it is possible to investigate the effect of object to CCD distance on resolution. If the signal-to-noise is high enough at higher spatial frequencies, the FRC first half-bit intercept should reach 1 for all object to CCD distances.

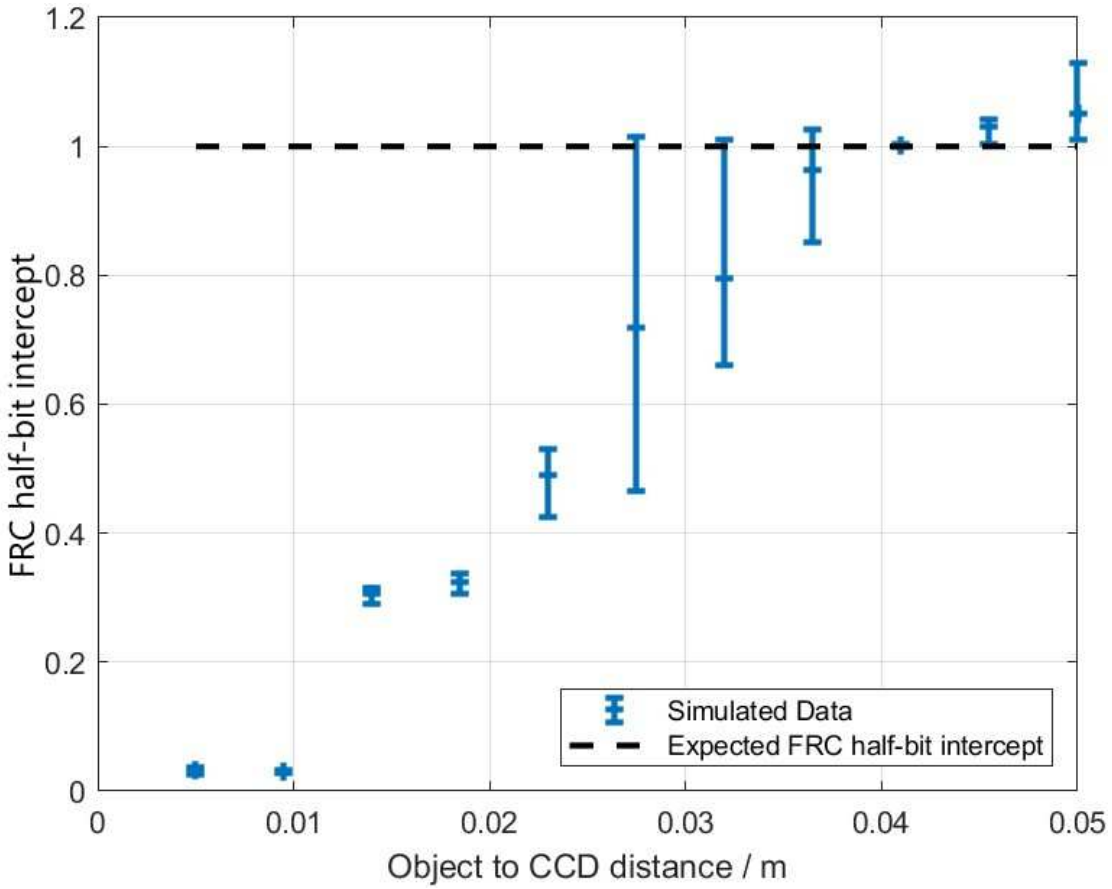

FIGURE 5.14: FRC half-bit intercept of simulated data with varying object to CCD distances. The average FRC half-bit intercept compared to the Nyquist of the CCD (blue line) against the object to CCD distance, and error bars are the maximum and minimum of the three FRC half-bit intercept values.

When comparing the FRC half-bit intercept value against the Nyquist limit of the CCD at those distances from figure 5.14, 0.5 cm to 5 cm object to CCD distance, it is clearly shown that FRC half-bit intercept value increases with distance, this does not strictly mean the reconstructions are worse as the Nyquist limit of the CCD corresponds to higher spatial frequencies for shorter object to CCD distances. Figure 5.14 shows that the signal-to-noise is not great enough at higher spatial frequencies as the FRC first half-bit intercept increases with object to CCD distance.

By converting the Nyquist limit of the CCD to the smallest resolvable feature, it can be shown that there is a limit to the resolution for the circular aperture (7 μm diameter). Even though the signal-to-noise for higher spatial frequencies is not great enough, we would expect the resolution to improve as the object to CCD distance decreases as the higher spatial frequencies can be measured by the CCD.

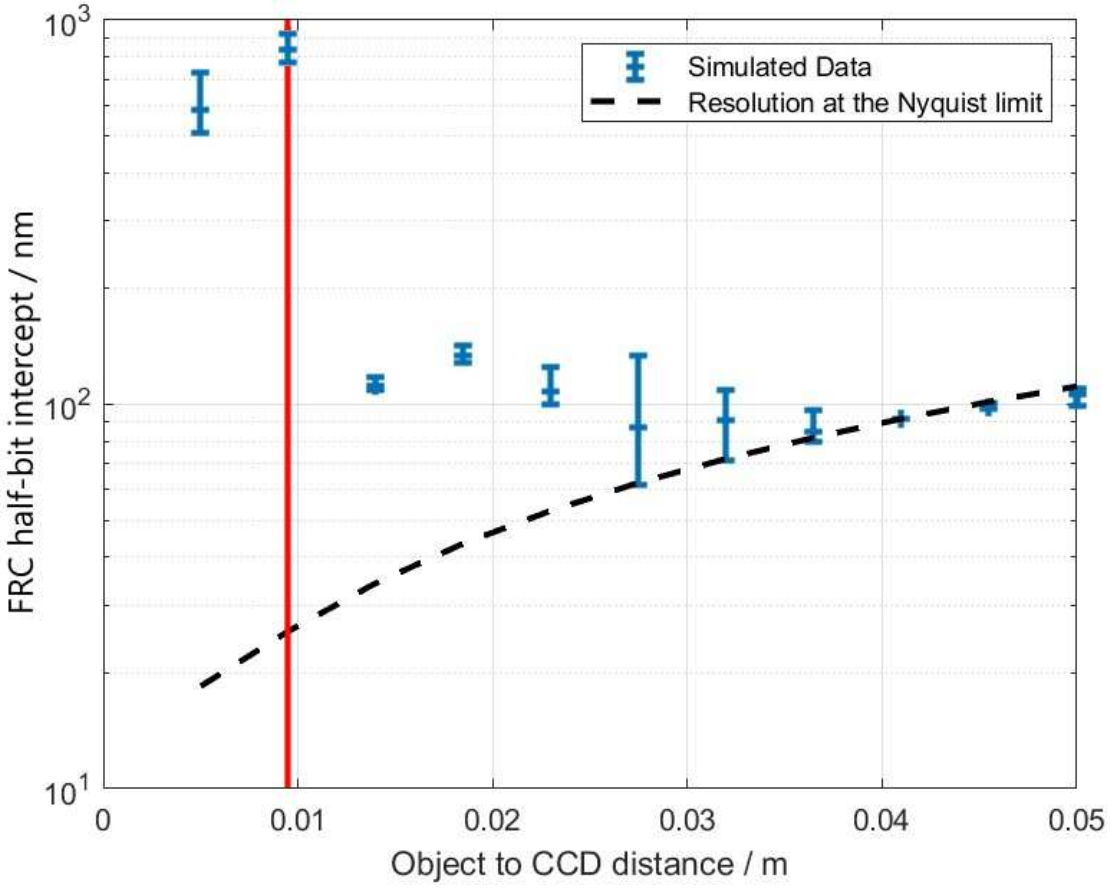

FIGURE 5.15: FRC half-bit intercept of simulated data with varying object to CCD distances. The average FRC half-bit intercept as the smallest resolvable feature (blue line) against the object to CCD distance, and error bars are the maximum and minimum of the three FRC half-bit intercept values. Where reconstructions at distances equal to and lower than object to CCD distances at the red line are not valid due to approximations.

From figure 5.15, it can been seen that the FRC first half-bit intercept decreases initially as the object to CCD distance decreases, showing an improvement in the resolution. Then, the resolution plateaus and no longer reaches the resolution at the Nyquist limit of the CCD. When the object to CCD distance is too low the resolution suddenly becomes much worse. This shows that there is a limit to the resolution to be gained by just decreasing the CCD to object distance. This sudden increase in the FRC first half-bit intercept is due to the small angle approximation used when converting the distances of the CCD pixels to angles. At 3.69 cm the actual angle at the edge of the CCD is 0.1785 rad and the approximation is 0.1804 rad, with a percentage difference of 1.0%, whereas at 1 cm the actual angle at the edge of the CCD is 0.5873 rad and the approximation is 0.6656 rad, with a percentage difference of 12.5%. The small angle approximation becomes less valid around 0.26 rad, which would be an object to CCD distance of 2.5 cm.

Also as the object to CCD distance decreases the Fresnel number increases, reducing the accuracy of Fraunhofer propagation, where at 3.69 cm away the Fresnel number for an 8 μm circular aperture is 0.015, for 1 cm away the Fresnel number is 0.055. This could be fixed by integrating software such as COMSOM to more accurately calculate the propagated beam, this is especially becoming more viable as computers improve, keeping reconstruction times low. This was however not used due to time constraints in integrating these methods into the workflow used throughout this thesis.

The object to CCD distance can be converted to the numerical aperture to find the limit of this CCD in terms of the numerical aperture.

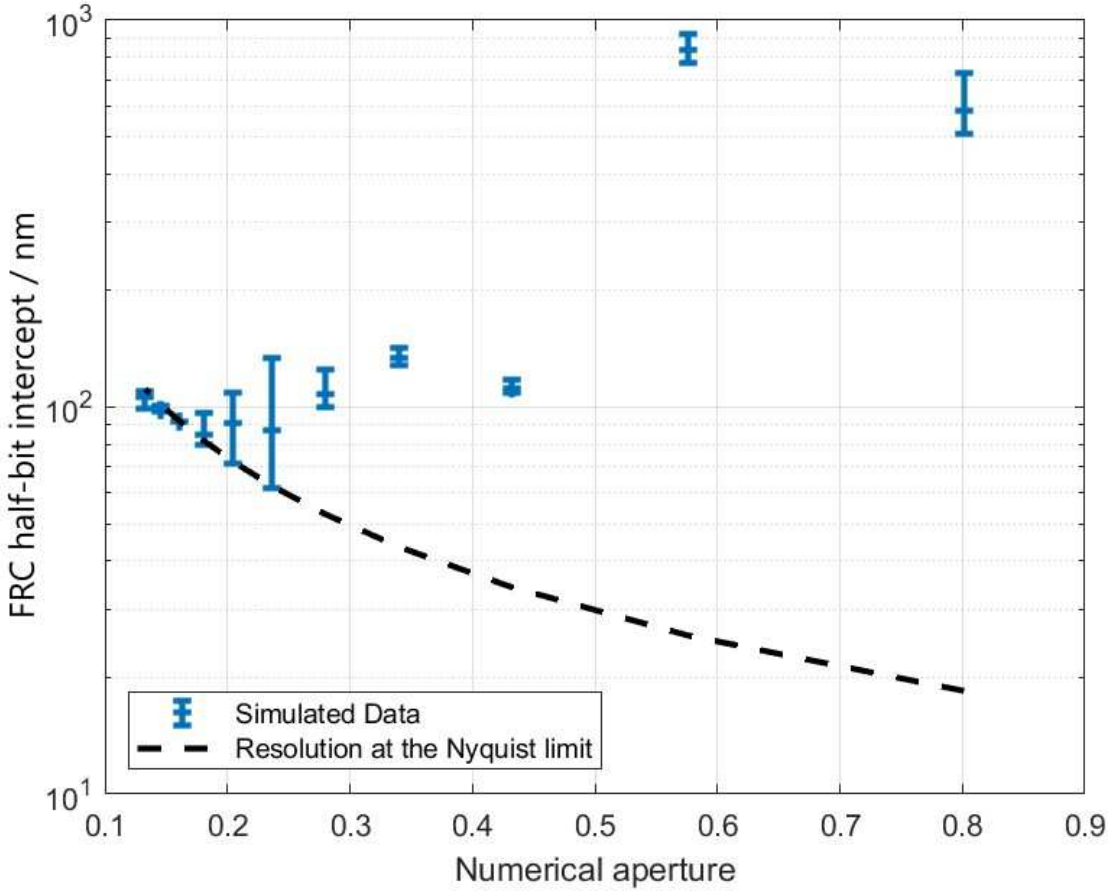

FIGURE 5.16: FRC half-bit intercept of simulated data with varying object to CCD distances. The average FRC half-bit intercept as the smallest resolvable feature (blue line) against the numerical aperture, and error bars are the maximum and minimum of the three FRC half-bit intercept values.

From figure 5.16 the quality of reconstruction drastically decreases after a numerical aperture of 0.45, which is far beyond when the small angle approximation breaks down, showing the robustness of the reconstruction algorithms and simulation.

From figure 5.15 and figure 5.16, the plateau in resolution suggests that an aperture has determined maximum resolution for a given flux. This can be explained by the higher spatial frequency components of the scatter patterns, which have a lower intensity, are below the noise threshold no matter the object to detector distance.

To predict the FRC first intercept of the half-bit criterion value for a given aperture at any distance and the maximum resolution, a function of the scatter pattern's characteristics that varies with distance would be desired. The beam width is a good initial estimate as the beam width increases with distance, and so does the FRC first intercept of the half-bit criterion.

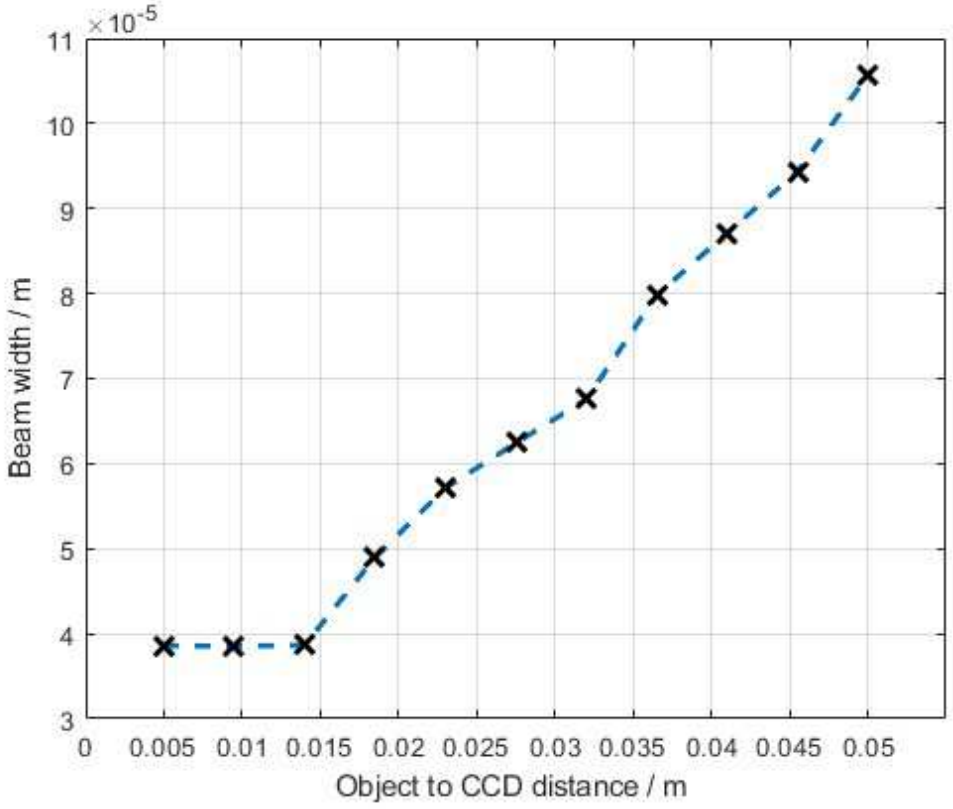

FIGURE 5.17: The beam widths (black crosses) of a circular aperture (8 μm diameter) for multiple object to CCD propagation distances.

From figure 5.17, it is shown that initially, the beam width does not increase, and neither does the FRC first half-bit intercept from figure 5.14. The beam width then begins to increase, and so does the FRC first half-bit intercept; however, the beam width continues to increase, whereas the FRC first half-bit intercept begins to plateau as it reaches

the Nyquist limit. This shows beam width alone does not predict the resolution; however, it could contribute to the estimate of the resolution achievable from an aperture for a given distance.

5.8 Probe Complexity

The probe is not just determined by the beam at the aperture and the aperture itself, but also by the distance the beam propagates from the aperture to the object. In the far-field, the probe's shape remains constant, but the size increases with longer propagation distances; this can be compensated for by changing the step size of the probe positions. This is not to be confused with the M^2 of the beam; this increase in the beam width is due to the beam propagating and not due to the M^2 of the beam increasing. In the near-field, the probe's profile changes shape, which could change the resolution of the reconstruction as the probe's complexity can improve. The probe's complexity is not fully understood and may not be able to be parameterised. This possible inability to parameterise the complexity of the probe is due to probe complexity not having a definition, but when observing two probes there is intuition of which is the more complex.

When trying to parameterise how complicated the probe is, one approach is to use the normalised value of the average summation of the absolute gradients of the probe within the beam width. This will give a value of how much the probe changes within the beam width. This is defined by:

$$Complexity = \frac{\sum_i |dx_i| + |dy_i|}{n_i} \tag{5.12}$$

where dx is the gradient in x for each element i, dy is the gradient in y for each element i, and n is the number of elements. Using equation (5.12) the complexity value for an 8 μm circular aperture at the aperture is 6.35×10^{-4}. The complexity value for a beam 3.69 cm after an 8 μm circular aperture is 292. The complexity value for a beam 141 μm after a double slit (5x1 μm slits spaced 4 μm from centres) is 5.12×10^{-4}. The complexity value for a beam 3.69 cm after a double slit (5x1 μm slits spaced 4 μm from centres) is 59.

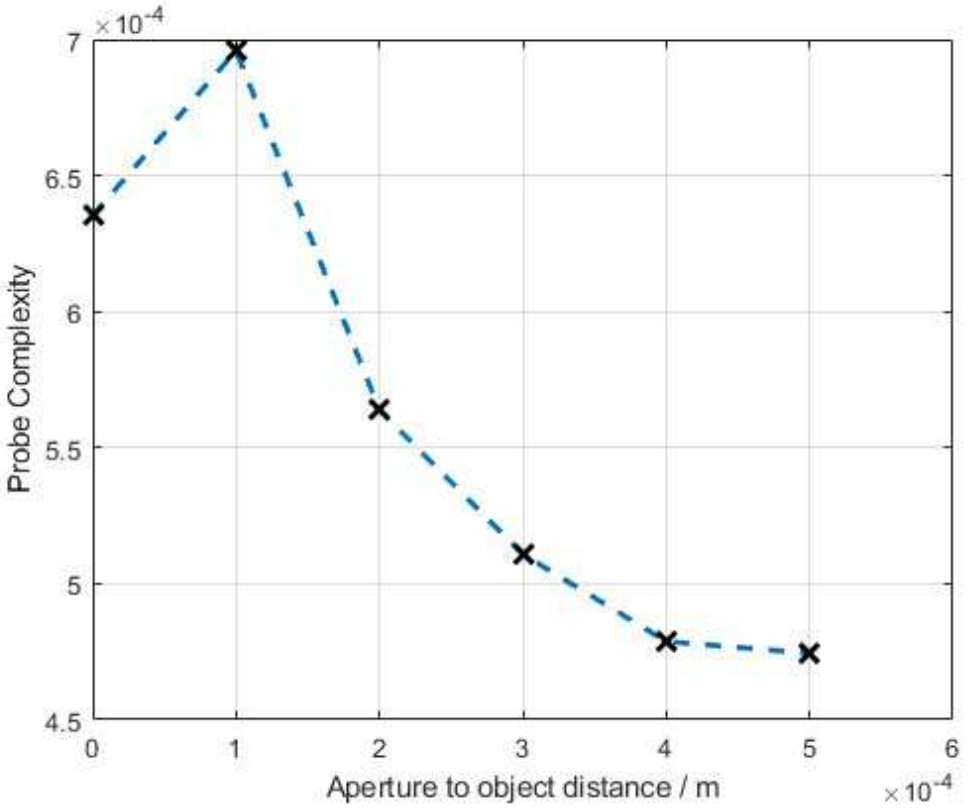

FIGURE 5.18: The probe complexity of a circular aperture (8 μm diameter) for multiple aperture to object propagation distances.

From figure 5.18, it can be seen that for this method of calculating probe complexity, the 100 μm aperture to object propagation distance should result in the best quality of reconstruction; after 100 μm aperture to object propagation distance the resolution of reconstruction should decrease.

When comparing probes from the same aperture with different aperture to object propagation distances, it is hard to make this perfectly fair, as the beam width varies. For a circular aperture (8 μm diameter), the beam width is roughly 4 μm for all propagation distances. Adjusting the step size would change the number of scatter patterns collected, or changing the scan area would change the object being imaged; therefore, the step size is unchanged throughout this simulation.

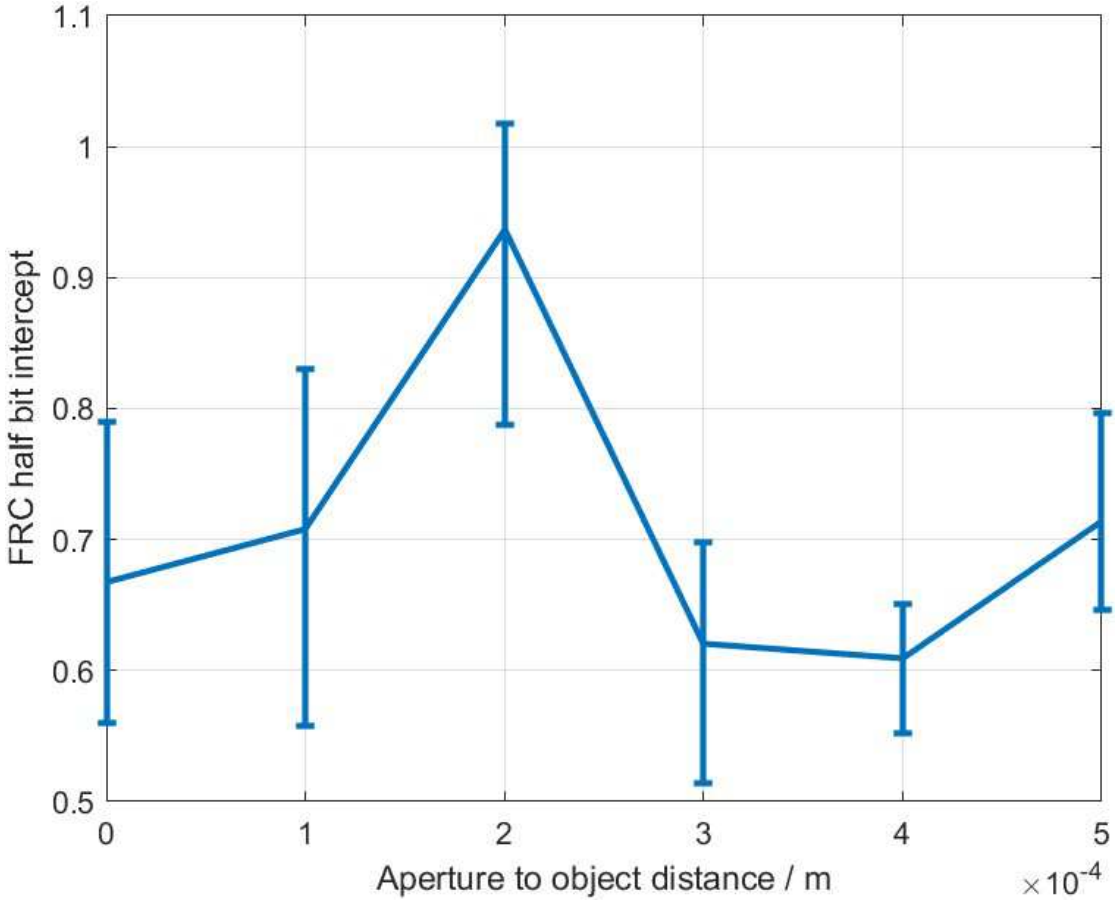

FIGURE 5.19: The FRC first intercept of the half-bit criterion of a circular aperture (8 μm diameter) for multiple aperture to object propagation distances.

From figure 5.19, it can be seen that 200 μm has the highest quality of reconstruction, which is not as predicted from the method of defining probe complexity in (5.12). Figure 5.18 and figure 5.19 both increase and then decrease; however, figure 5.19 has the highest FRC first intercept of the half-bit criteria at a longer object to detector distance. Although figure 5.19 may not show any correlation between aperture to object distance and resolution, it does show that the probe from 200 μm aperture to object distance results in the highest resolution from these distances. This means the chosen method of calculating complexity does not predict the point of the highest resolution. Therefore, in the future, another parameter will be required to predict the resolution of reconstruction from different probes from the same aperture. Figure 5.19 still shows that selecting the best aperture to object distance for a given aperture is important in getting the highest resolution possible for an aperture as there is a relation between complexity and resolution, however, the correct parametrisation for complexity was not found.

5.9 Probe Overlap

When discussing probe overlap in ptychography, what is usually meant is linear overlap. Linear overlap compares the overlapping area of the same probe separated by a distance. Linear overlap is defined by:

$$O = 1 - \frac{d}{2r} \tag{5.13}$$

where d is the distance the two probes are separated by, and r is the beam width of the probe. When using simple circular probes, this overlap is easy to define. When using more complex probes with significant amplitude variation across the probe, a different measure of effective radius is needed. The probe beam width in the thesis is defined by the point that the radial integral of the probe crosses the threshold $1/e^2$ of the maximum value of the probe. The radial integral is calculated by taking the average value of the beam's amplitude at discrete ranges of distance from the beam centre. This measurement is a good representation of how the probes overlap when discussing radially symmetric probes, such as the circular aperture's probe. Using the linear overlap for a circular aperture, it was reported that a linear overlap of 70% to 90% was optimal (95). However, issues emerge when not using a radially symmetric probe, as the overlap is dependent on the relative orientation of the two probes.

When comparing a double slit aperture (5x1 μm slits spaced 4 μm from centres) and circular aperture (8 μm diameter), the value that the radial integral of the probe crosses the threshold $\frac{1}{e^2}$ are nearly equal. Hence, the linear overlap of these two probes is nearly equal, though the actual overlap is different when considering overlap in any direction.

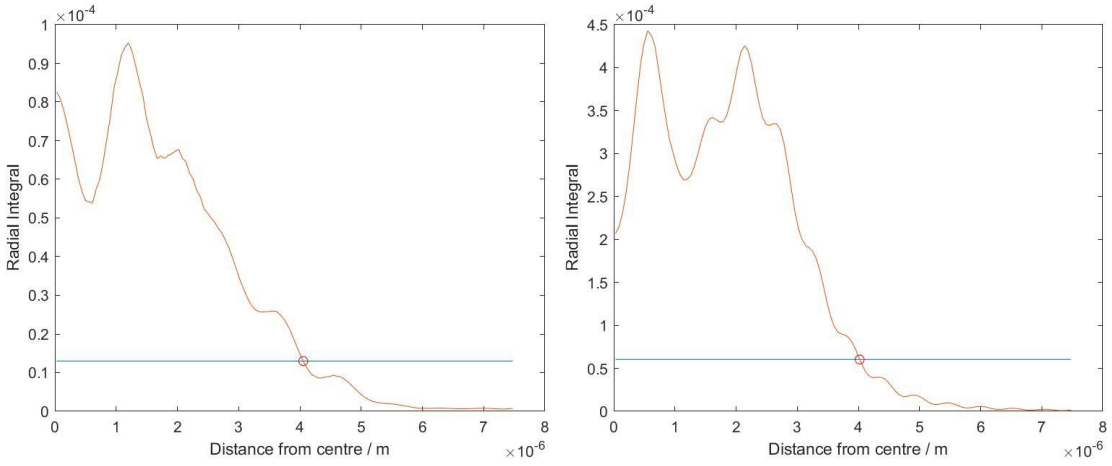

(A) (B)

FIGURE 5.20: Radial integrals of probes for (A) a double slit aperture (5x1 μm slits spaced 4 μm from centres), and (B) a circular aperture (8μm diameter). Both with an aperture to object propagation distance of 141 μm.

It is seen from figure 5.20 that the probe radius of both is nearly equal with a radius of approximately 4 μm. With a step size of 2 μm, the linear overlap would therefore be 75%. This could lead some to believe that the intensity distribution of the probes over the object are closely related for both the apertures; however, due to the asymmetrical nature of the double slit, the double slit's probe extent is greater in the x direction. This leads to asymmetric overlap between probes; in these cases, interesting patterns emerge when examining the intensity distribution of the double slit's probe compared to the circular aperture's probe.

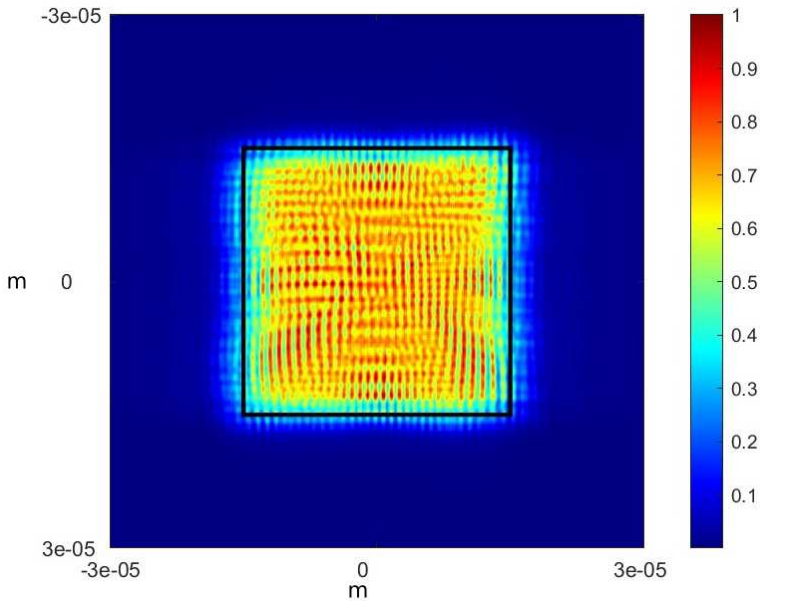

(A)

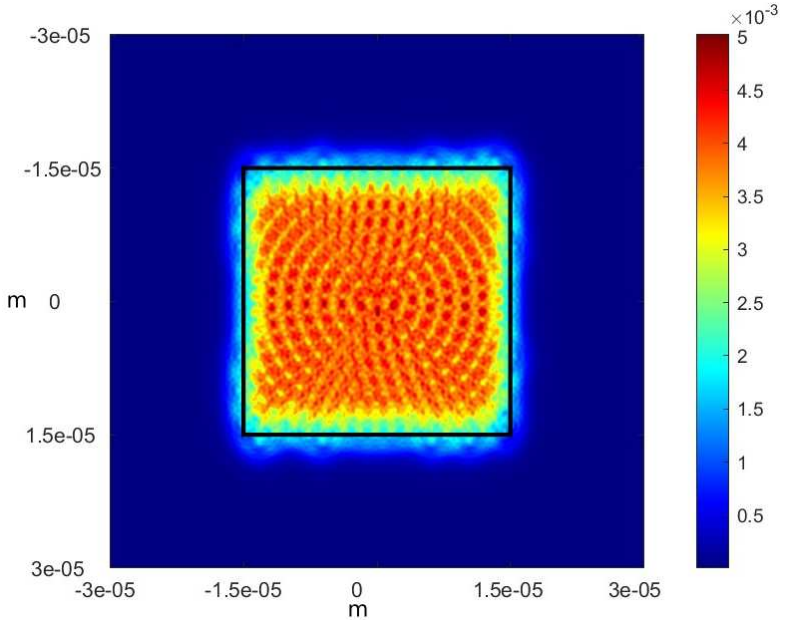

(B)

FIGURE 5.21: The total intensity distribution for simulated data of all probes over an object over a scan area of 30 μm by 30 μm with 251 scans for (A) a double slit aperture (5x1 μm slits spaced 4 μm from centres), and (B) a circular aperture (8 μm diameter). Both with an aperture to object propagation distance of 141 μm.

From figure 5.21, two interesting developments can be observed: the patterns that emerge in the reconstructions from the two probes, and the extent the double slit's probe extends in the x direction. When reconstructing objects with a double slit, the reconstruction contains vertical lines throughout the reconstruction. When reconstructing with the circular aperture, rings can appear in the reconstructed object. Given the

double slit's probe intensity distribution, the vertical lines of higher intensity distribution are clearly visible; less obvious, but easier to see at the edges of the intensity distribution of the circular apertures are rings. Following the paper that discussed optimal linear overlap for the best resolution of reconstruction at a macro level, where the macro level is the resolution over the whole object (95), it would make sense that the resolution of reconstruction would vary at a micro level, small regions of the object, where different levels of overlap over the object are experienced. This variation in resolution would explain the vertical lines found in reconstruction using the double slit and ring patterns observed in reconstructions using the circular aperture.

While it is harder to see the extent of the probe's intensity distribution from figure 5.21, if the values of intensity are converted to multiples of the intensity of the beam at the beam width, it is much clearer to see the extent of the probe's intensity distribution.

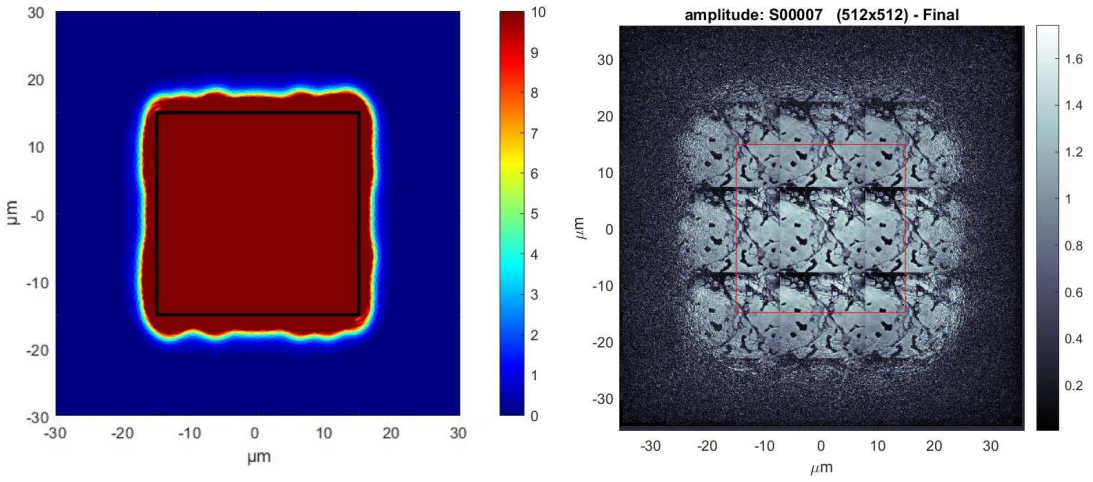

(A) (B)

FIGURE 5.22: (A) The multiples of intensity at the beam width of all probes over an object over a scan area of 30 μm by 30 μm with 251 scans for a circular aperture (8 μm diameter), and (B) the reconstructed object. The black square of (A) is the same region as the red square of (B).

From figure 5.22 it can been seen that the region of the reconstructed object that is of higher quality in (B) matches the region of high values of overlap in (A). It also shows that the lower quality regions are close to the scan area where the circular probe does not spread far; this region is also nearly equidistant around the scan area as the circular probe is nearly radially symmetric.

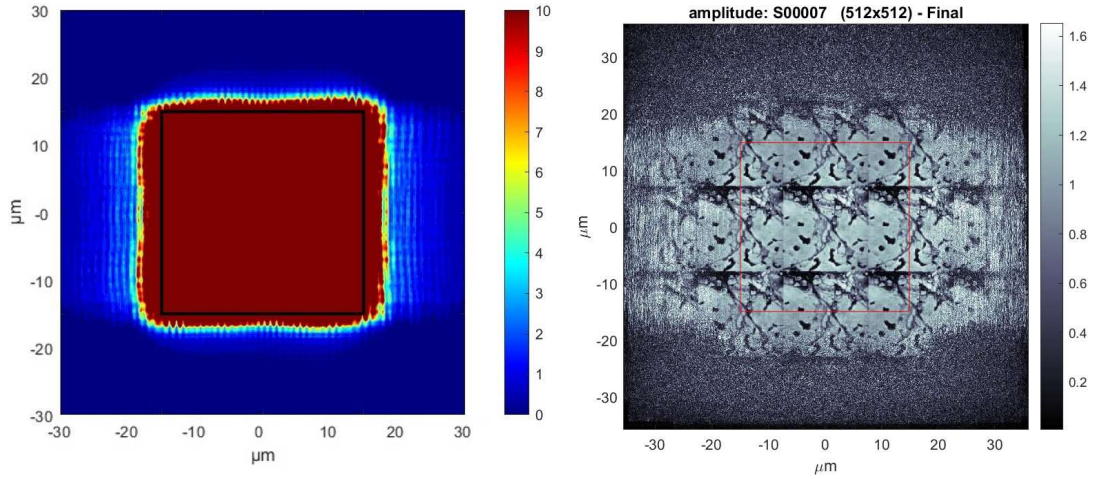

(A) (B)

FIGURE 5.23: (A) The multiples of intensity at the beam width of all probes over an object over a scan area of 30 μm by 30 μm with 251 scans for a double slit aperture (5x1 μm slits spaced 4 μm from centres), and (B) the reconstructed object. The black square of (A) is the same region as the red square of (B).

Figure 5.23 (B) shows the reconstruction using the double slit can reconstruct the object further in the x-axis, albeit at a reduced quality. With the large spread of the double slit's probe along the x-axis, the object that is reconstructed goes far beyond the scan area, and this can be seen from the values of overlap from (A).

While the reconstructed object in that region is noisy and low resolution, this additional information can be useful. Many systems either use destructive levels of flux, or are imaging delicate samples; combining this with the low levels of flux the double slit probe deposits on the object, an image larger than the scan area could be taken to orientate an object in an environment that is not accessible, such as a vacuum chamber.

While 75% is a good linear overlap for determining the step size required for a double slit and circular aperture, it does not work for all apertures. When using the radial integral, using an increasing radius to calculate the radial integral, to calculate the probe width, a non-uniform star aperture's probe has a narrower beam width than the double slit and circular aperture's probes. The star aperture is a non-uniformly star-shaped aperture with an approximate height and width of 4 μm.

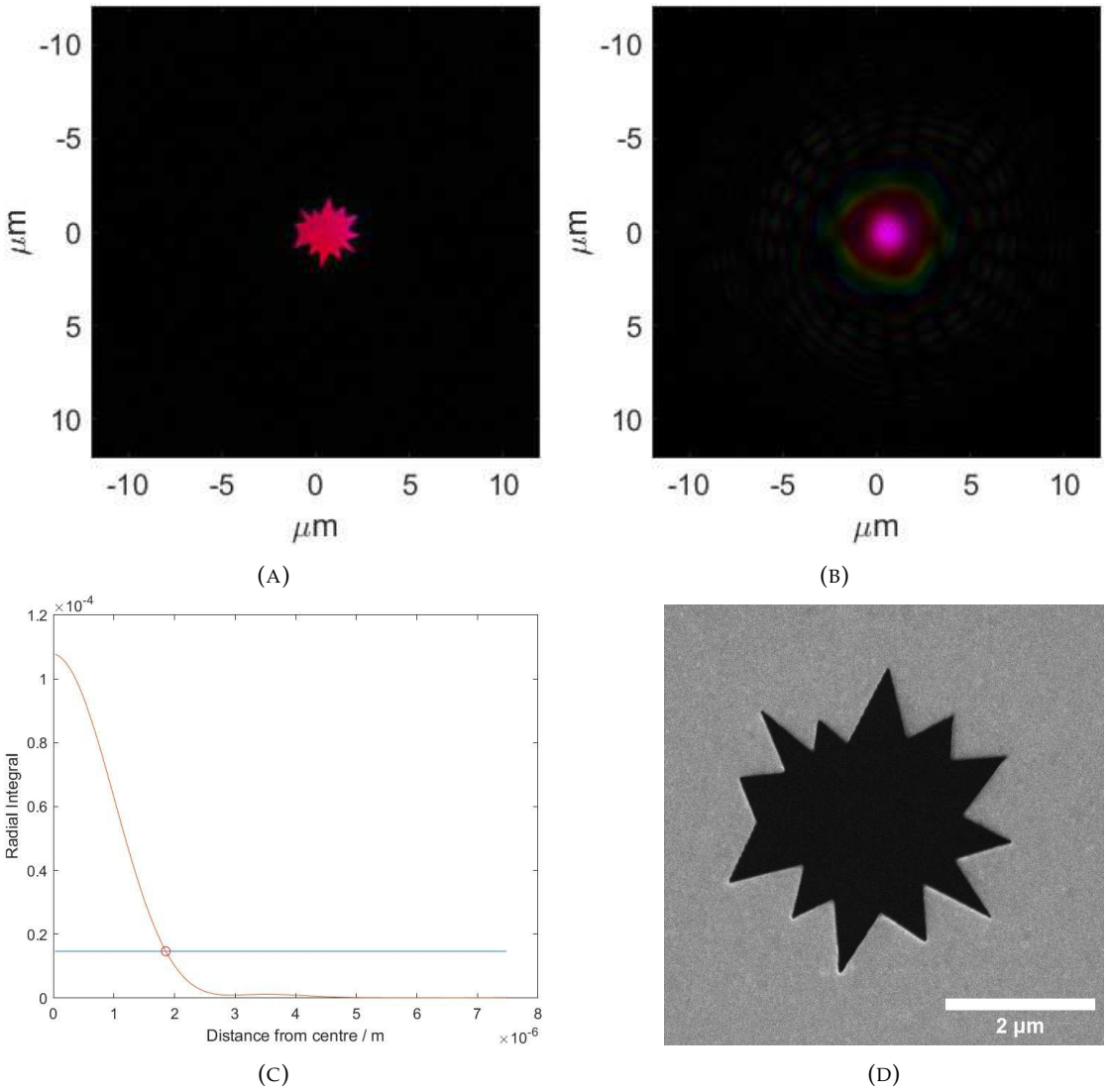

FIGURE 5.24: (A) Beam at the star aperture, (B) beam after propagating 141 μm from the star aperture, and (C) the radial integral of the beam after propagating 141 μm from the non-uniform star aperture. (D) shows a scanning electron microscope image of the star aperture.

From figure 5.24 it is shown that the probe $1/e^2$ width is 1.86 μm after propagating 141 μm. This leads to a linear overlap of 46%, which is far from optimal; however, this should be improved by adjusting the linear overlap.

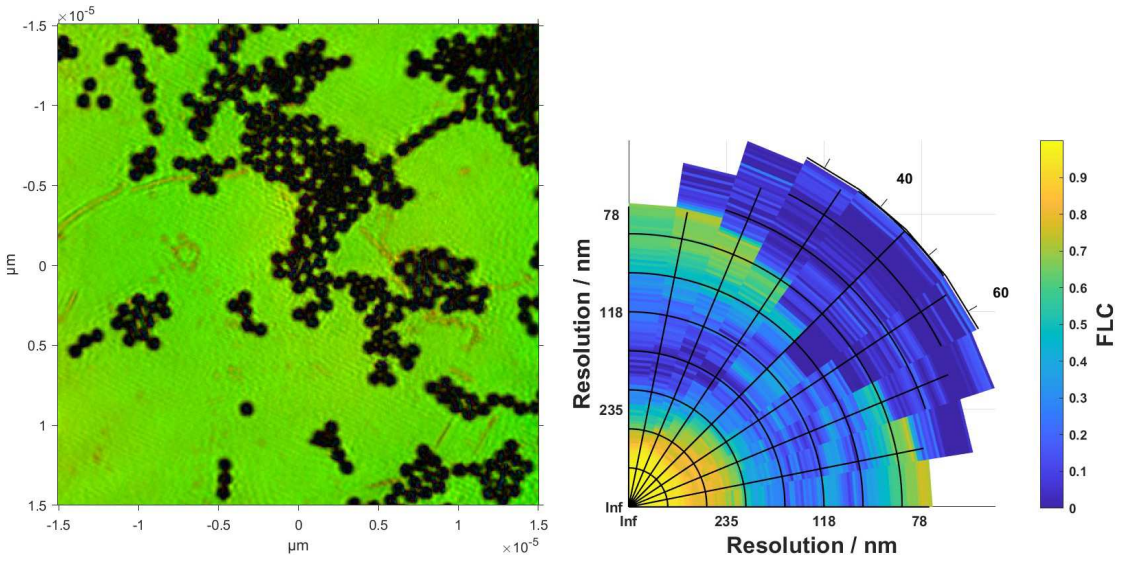

(A) (B)

FIGURE 5.25: (A) Reconstructed object of a non-uniform star aperture, with an aperture to object propagation distance of 141 μm and object to CCD distance of 3.69 cm, using 100 iterations of DM and then 500 iterations of MLs for reconstruction, and a binning of 2. The resolution at the Nyquist limit is 82 nm. The linear overlap is 50%. (B) is the FLC of the reconstructed object.

From figure 5.25, it can be seen that the star aperture has a low resolution from the FLCs, where the FLC is high for low and high frequencies, but low for the middle resolutions. The point in which the FRC intercepts the half-bit criteria results in a resolution of 164 nm. To match the linear overlap of 75% of the double slit and circular aperture's probe at 141 μm propagation, from equation (5.13) either the step size between scanning positions, d, needs to be decreased and or the propagation distance from the aperture to the object needs to be increased, to increase the probe radius, r. The polystyrene sphere sample was prepared by myself, and the code used to analyse the FLCs was also written and developed by myself.

Changing the step size to 1 μm would result in a linear overlap of 75%, if the propagation distance from the aperture to the object is unchanged. This will result in a smaller scan area to make the number of scan positions constant.

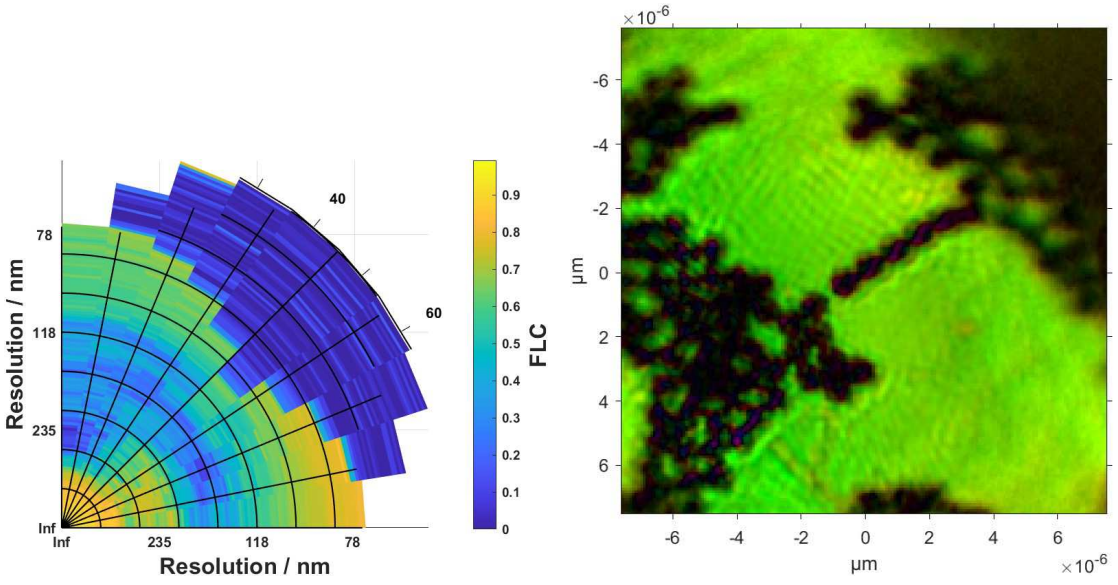

(A) (B)

FIGURE 5.26: (A) Reconstructed object of a non-uniform star aperture, with an aperture to object propagation distance of 141 μm and object to CCD distance of 3.69 cm, using 100 iterations of DM and then 500 iterations of MLs for reconstruction, and a binning of 2. The resolution at the Nyquist limit is 82 nm. The linear overlap is 75%. (B) is the FLC of the reconstructed object.

From figure 5.26 it can be seen that the FLC is worse than from figure 5.25 at lower resolutions, but is better at higher resolutions. Higher correlation at higher resolutions is typically considered better; however, this is not the improvement expected from changing the linear overlap to the optimal range of values. The size of the object image has been reduced, and the flux deposited onto the object has been concentrated. Therefore, attempting to match the linear overlap to the optimal range of linear overlap values is not a direct improvement.

The other method of matching the linear overlap is to increase the propagation distance of the probe from the aperture to the object, as this will increase the spread of the probe. An object to CCD propagation distance of 700 μm will result in a probe of 8 μm beam width, and a linear overlap of 75% for a step size of 2 μm.

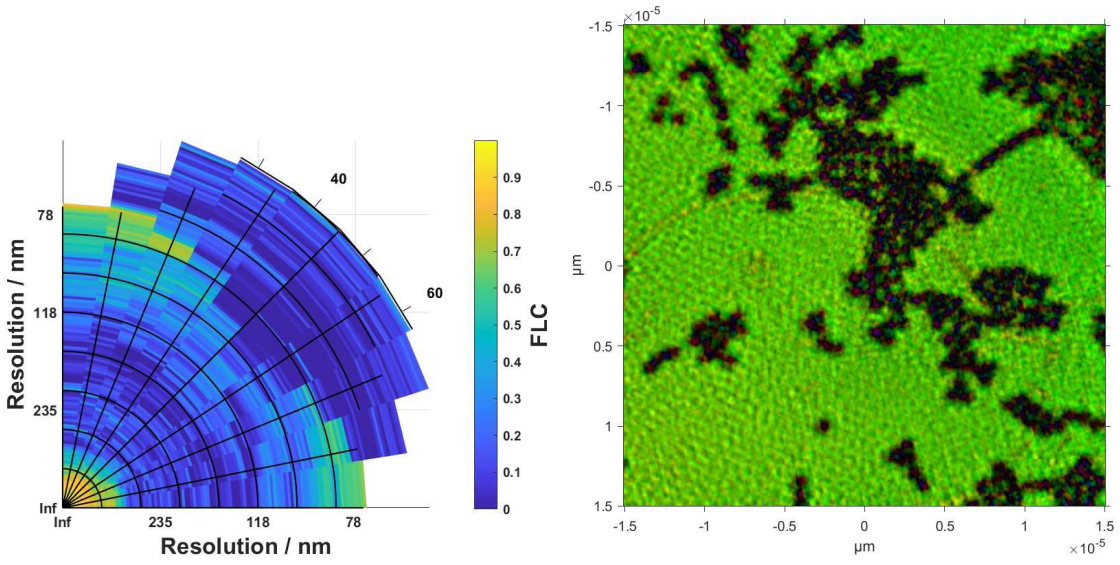

(A) (B)

FIGURE 5.27: (A) Reconstructed object of a non-uniform star aperture, with an aperture to object propagation distance of 700 μm and object to CCD distance of 3.69 cm, using 100 iterations of DM and then 500 iterations of MLs for reconstruction, and a binning of 2. The resolution at the Nyquist limit is 82 nm. The linear overlap is 75%. (B) is the FLC of the reconstructed object.

From figure 5.27 the FLC is worse compared to figure 5.25. The scan area is the same; however, when examining the reconstructed object, artefacts can be seen in regions of maximum transmission.

While not tested in this thesis, it has been proved that the scanning pattern also matters (104). When performing all reconstructions within this thesis, a pattern similar to the Fermat spiral has been used, and therefore we can be confident in the scanning position pattern not reducing the resolution of the reconstructions.

Using the linear overlap is a great method to find the correct step size when performing ptychography with the probe from a simple circular aperture; however, linear overlap does have limitations, where it doesn't fully explain the overlap experienced across the object. Two probes with the same linear overlap can have different intensity distributions across the object.

5.10 Binning

Binning is the act of averaging nearby groups of pixels when the CCD is measuring the intensity of the scatter pattern; where a binning of 1 is measuring each pixel individually, a binning of 2 is grouping the pixels into unique squares of 2 by 2 and averaging the count, and this process can keep increasing to the size of the CCD. The CCD readout time is much faster if binning is performed during the readout, typically with an n^2 improvement in readout speed. While it may feel like binning loses detail in the scatter pattern, it only reduces the extent of the probe array being reconstructed. The extent of the probe array in the object plane depends on the pixel size in the detector plane. A binning of 2 will reduce the extent of the probe array in the object plane by 2 when reconstructing. This can reduce the overlap during reconstruction between probes if the probe intensity extends to the edges of the probe array, if too high a binning is used. In this section, it will be shown that reducing the amount of binning for higher angular spread probes will increase the resolution of the reconstructed images.

This can easily be visualised using the cross-sections of two probes, represented by top-hat functions, and limiting the probe array extent in the object plane due to the pixel size resulting from binning.

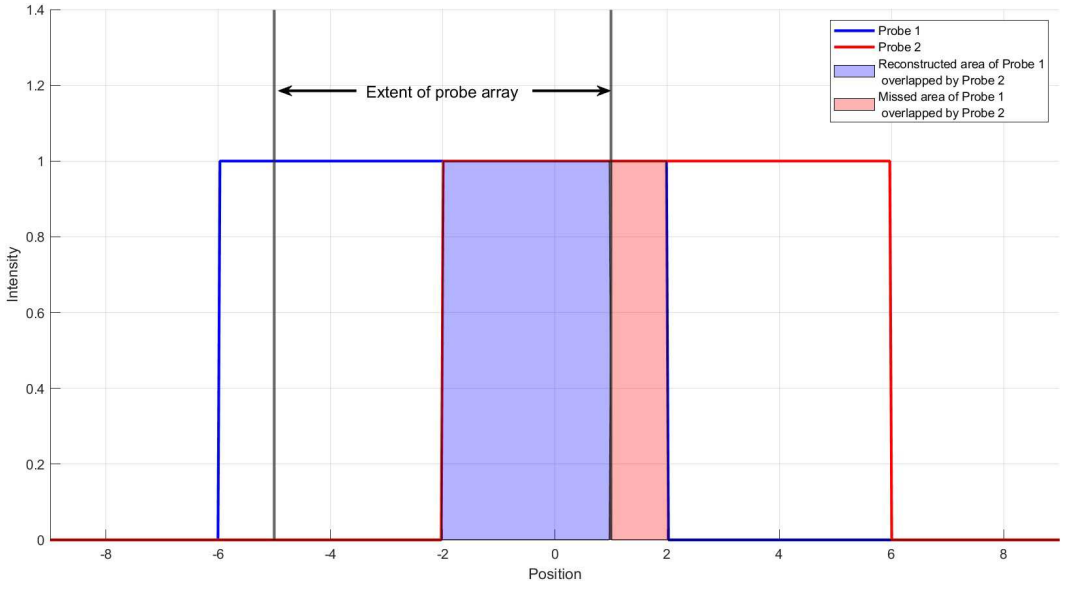

FIGURE 5.28: The cross-section of two overlapping probes with a binning of 2. The Probe at position 1 (blue line), and the probe at position 2 (red line), the extent of the probe array 1 (grey vertical line). The region of overlap between the two probes within the extent of the probe array (blue area), and the region of overlap missed due to binning (red area).

Figure 5.28 shows the cross-section of two probes represented as top-hat functions, and the regions of overlap within the extent of the probe array and outside of the extent of the probe array.

From figure 5.28 it can be seen that the blue area representing the overlapped region of the probe array does not extend to the full overlap between the two probes. Here the extent of the probe array is limited by the detector pixel size, and a substantial amount of overlap between the two probes is lost.

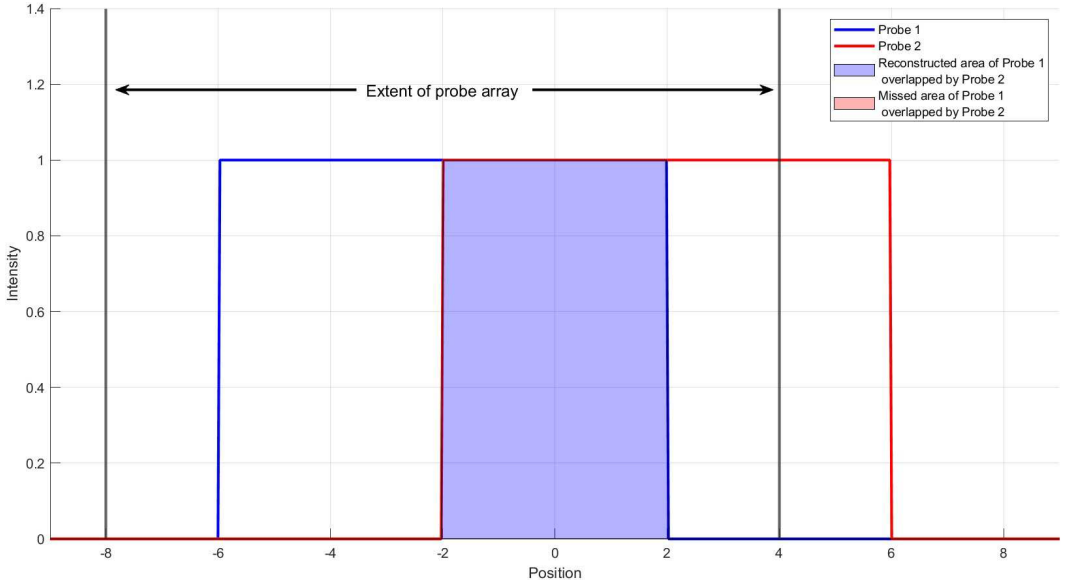

FIGURE 5.29: The cross-section of two overlapping probes with no binning. The Probe at position 1 (blue line), and the probe at position 2 (red line), the extent of the probe array 1 (grey vertical line). The region of overlap between the two probes within the extent of the probe array (blue area), and the region of overlap missed due to binning (red area).

Figure 5.29 shows the cross-section of two probes represented as top-hat functions where the probe array extent is double that of figure 5.28, and the region of overlap within the extent of the probe array now covers all the overlap between probes.

From figure 5.29 it can be seen that the full region of overlap between the two probes is within the extent of the probe array; therefore, no overlap is being lost due to binning.

With an 8 μm diameter circular aperture, the angular spread is low, and when reconstructing the probe, there is not much intensity at the edge of the probe array.

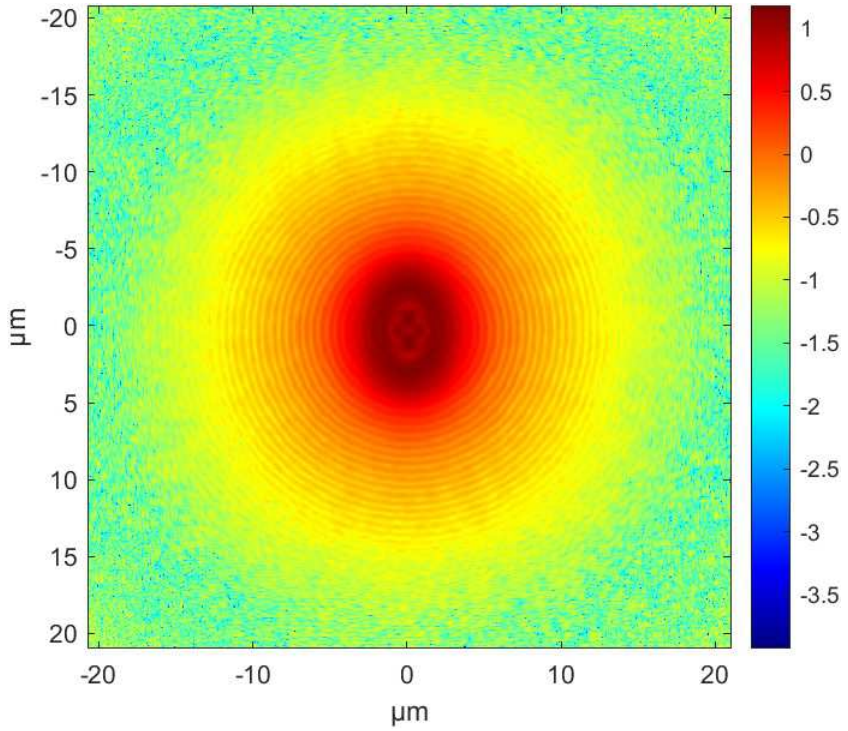

FIGURE 5.30: log10 of the amplitude a reconstructed probe of an 8 μm diameter circular aperture that has propagated 141 μm with a binning of 2. This image was reconstructed by PtychoShelves from data that I took.

From figure 5.30, it can be seen that the probe from a circular aperture (8 μm diameter) has an amplitude at the edge of the probe array of two orders of magnitude lower than the centre. Therefore, reducing the binning should not improve the overlap when reconstructing by a substantial amount. Figure 5.30 shows that the extent of the probe during reconstruction does not appear to be limited by the reduced field of view of the probe.

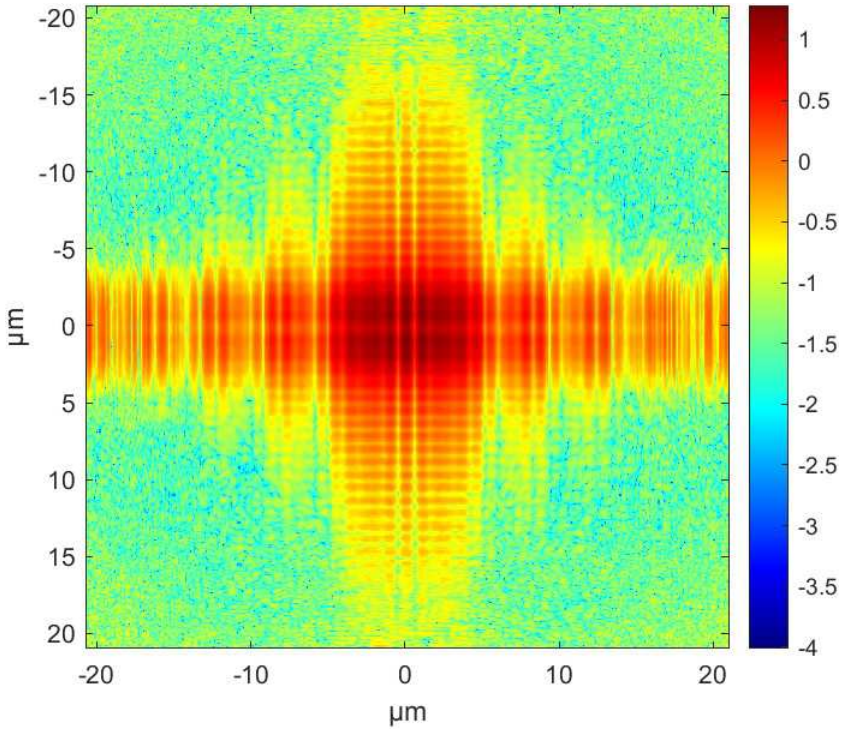

FIGURE 5.31: log10 of the amplitude a reconstructed probe of a double slit aperture (5x1 μm slits spaced 4 μm from centres) that has propagated 141 μm with a binning of 2. This image was reconstructed by PtychoShelves from data that I took.

Figure 5.31 clearly shows that the probe amplitude at the edge of the CCD of a double slit aperture (5x1 μm slits spaced 4 μm from centres) has high amplitude towards the edges of the extent of the probe array. Here, a reduction in binning would increase the size of the probe array during reconstruction and increase the overlap between probes by a substantial amount.

To investigate the effect of binning on reconstruction resolution, two FRCs can be calculated, one where the data are not binned and one where the data are binned by 2.

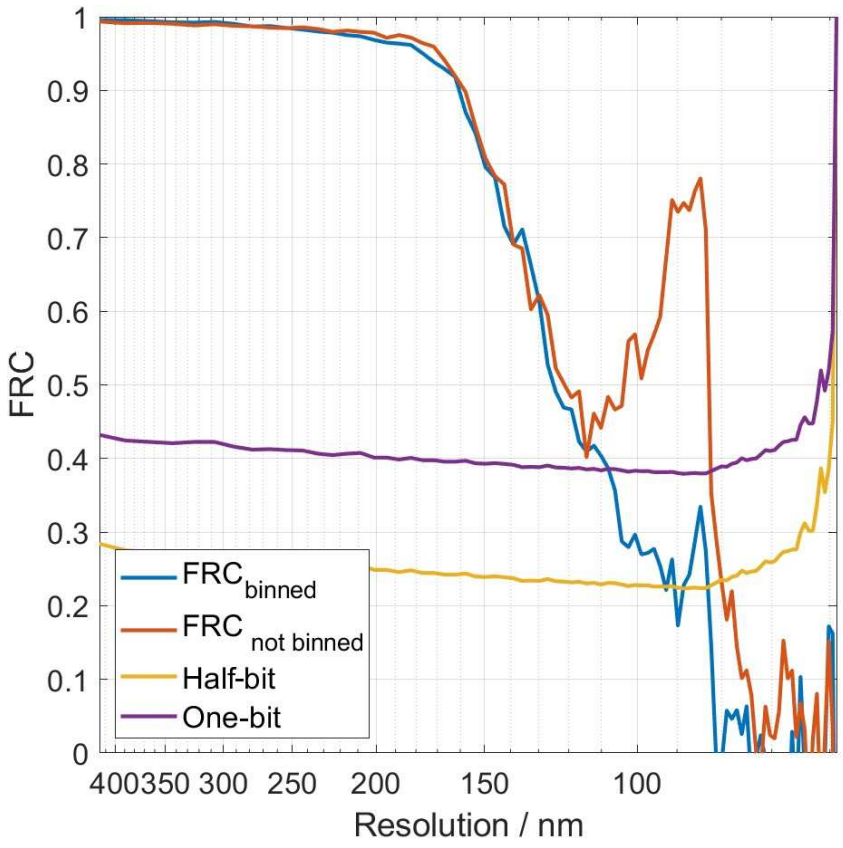

FIGURE 5.32: The FRC for different amounts of binning for an 8 μm circular aperture using 100 iterations of DM followed by 100 iterations of MLs with an aperture to object distance of 141 μm and an object to detector distance of 3.69 cm, where a not binned reconstruction (orange line) and binning of 2 reconstruction (blue line) are compared against the one-bit criterion (purple line) and the half-bit criterion (yellow line).

From figure 5.32 it can be seen that the FRC of the unbinned data are much better for the higher frequencies. It can also been seen that the first FRC intercept of the half-bit criterion is at 79 nm, which is beyond the resolution at the Nyquist limit of the CCD of 82 nm. Even though the probe of the circular aperture (8 μm diameter) has low angular spread, not binning has still improved the resolution of reconstruction. This understanding of the effects of binning on reconstructing objects is very impactful, as trying to push for better quality reconstructions is typically limited by the higher resolution components falling below the half-bit threshold criterion.

5.11 Beam Instability Effects

Beam instability is expected when performing experiments, and much time and effort is applied to reduce the amount experienced by the system. Still, there is instability,

and the reconstruction algorithms have to be able to compensate for this. Otherwise, with power instability, the reconstructed object would appear more or less transmissive than the actual object, with varying levels of resolution. With position instability, the reconstructed object would be shifted incorrectly compared to the actual object. With position instability, the reconstructive algorithms can compensate for small movements of the beam compared to where the data believes the beam is, and if this is working, there shouldn't be a difference in the quality of the reconstructed object. Using the simulation, the normal distribution of position error of the beam has been varied. A normal distribution of position error of two pixels is the measured amount from experiments, averaging all the beam positions over 251 scan positions took 3 hours. Here will be an investigation of reconstruction resolution with varying levels of instability, and how robust the algorithms are to beam instability.

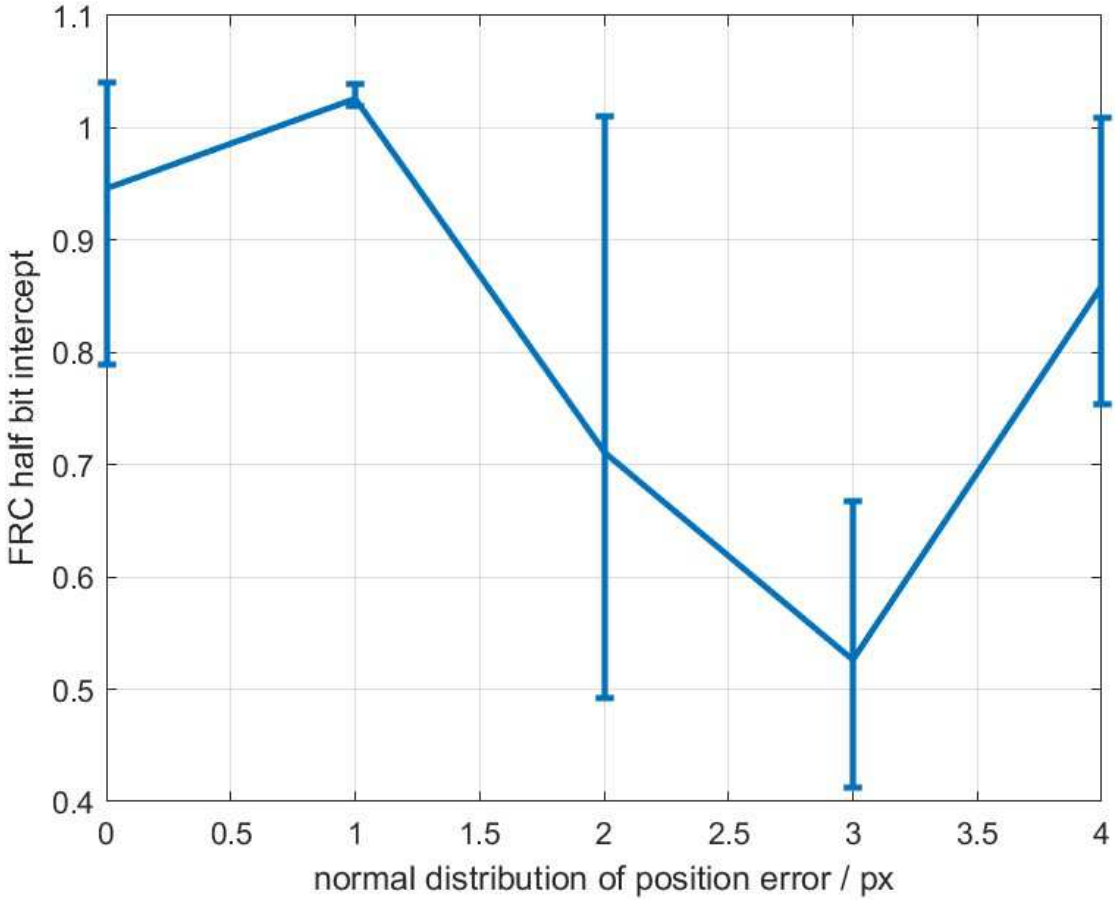

FIGURE 5.33: The first FRC intercepts of the half-bit criterion for varying levels of normal distribution of the position error for an 8 μm circular aperture using 100 iterations of DM followed by 100 iterations of MLs with an aperture to object distance of 141 μm and an object to detector distance of 3.69 cm, with the average FRC intercepts of the half-bit criterion (blue line), the maximum and minimum FRC intercepts of the half-bit criterion (error bars).

From figure 5.33 there is a no relation between position error and the FRC first intercept of the half-bit criterion, which was not expected; however, the best reconstructions of each value of the normal distribution of position error is similar. Therefore, the reconstructive algorithm's ability to compensate for position error is robust and not a limiting factor in the resolution of reconstructions for these levels of position error. Although a normal distribution of 4 pixels appears to be better for reconstruction than 3 pixels. It is possible that the 3 runs of 3 pixel normal distribution happened to be on the lower end of its achievable reconstruction quality, and the 4 pixel normal distribution runs happened to be good, where figure 5.12 this is possible.

Power instability can result from two factors: the rate at which the power oscillates, and the amount by which the power oscillates. Firstly, the rate at which the power oscillates will be investigated. The measured number of power oscillations of scatter patterns over two hours is around seven; however, experimental power oscillations are more complex than the sinusoidal oscillations used in the simulation.

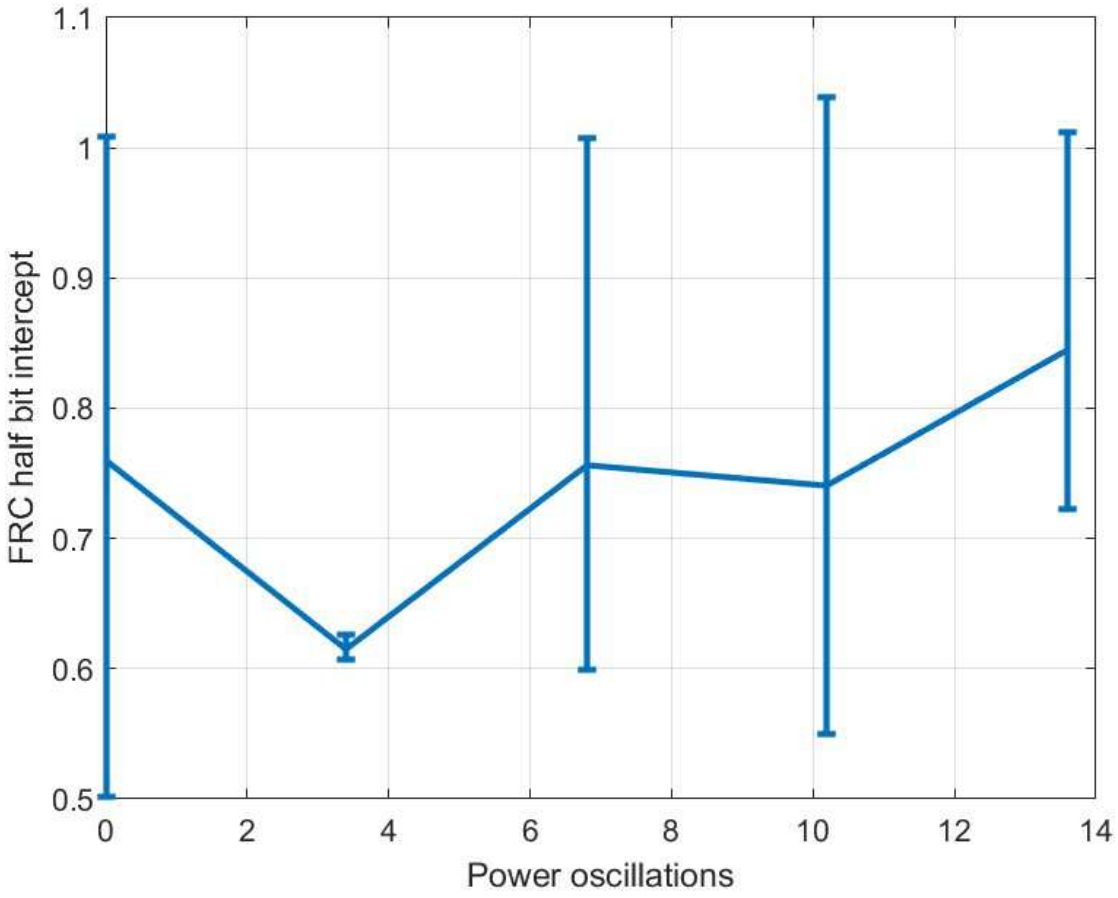

FIGURE 5.34: The first FRC intercepts of the half-bit criterion for varying levels of power oscillations of the position error for an 8 μm circular aperture using 100 iterations of DM followed by 100 iterations of MLs with an aperture to object distance of 141 μm and an object to detector distance of 3.69 cm, with the average FRC intercepts of the half-bit criterion (blue line), the maximum and minimum FRC intercepts of the half-bit criterion (error bars).

From figure 5.34, there is no correlation between the number of oscillations of the power and the FRC first intercept of the half-bit criterion, which was not expected as this would cause greater variations in the intensity of scatter patterns measured; however, the best reconstructions for each value of oscillations of power are similar, yet again proving the robustness of the reconstructive algorithm's ability to compensate for unexpected variations in the beam.

The other type of power instability is the amount by which the beam's power oscillates. Here, the maximum and minimum values of the beam's power will be more extreme, leading to higher maximums and lower minimums, which could lead to better reconstructions due to higher flux, improving the FRC first intercept of the half-bit criterion. Equally, lower fluxes decrease the FRC first intercept of the half-bit criterion more than

higher fluxes improve it, which should cause the reconstructions to be worse. However, the reconstructive algorithms have proved their robustness to instability and may still perform well.

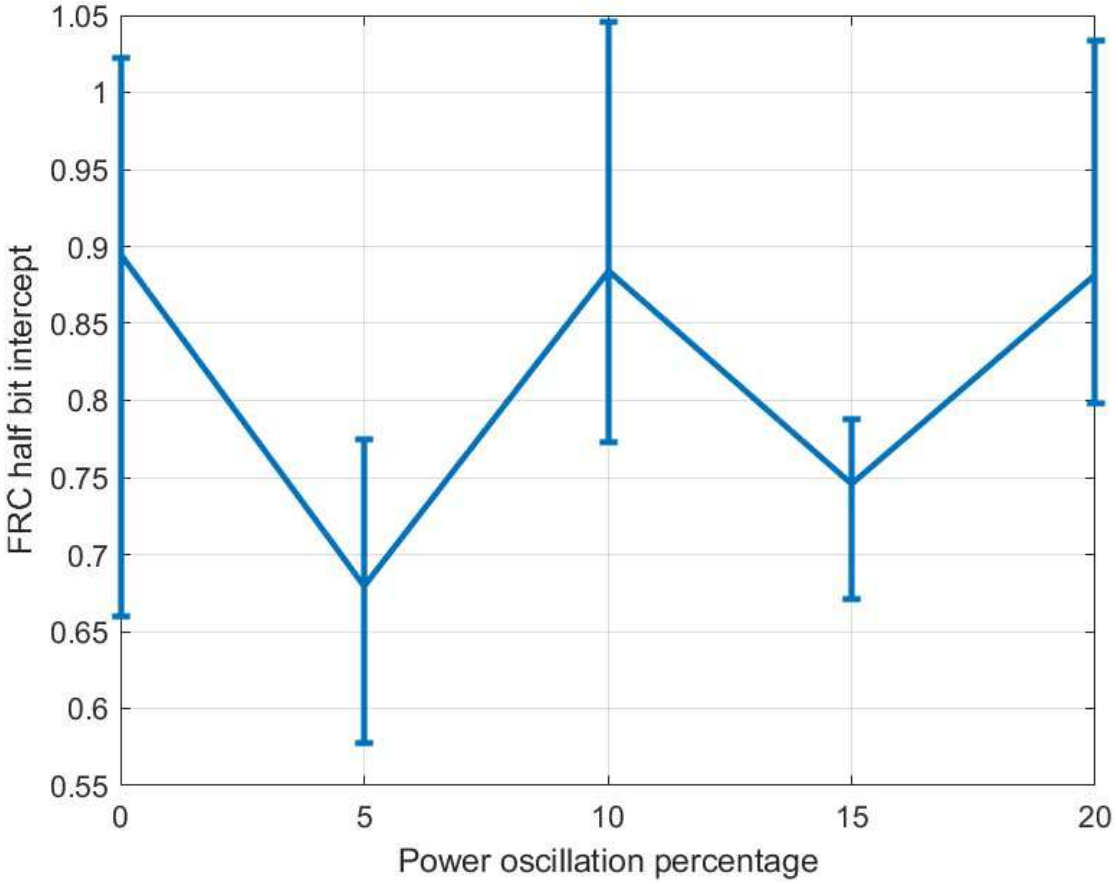

FIGURE 5.35: The first FRC intercepts of the half-bit criterion for varying levels of power oscillations of the position error for an 8 μm circular aperture using 100 iterations of DM followed by 100 iterations of MLs with an aperture to object distance of 141 μm and an object to detector distance of 3.69 cm, with the average FRC intercepts of the half-bit criterion (blue line), the maximum and minimum FRC intercepts of the half-bit criterion (error bars).

From figure 5.35, it appears that the resolution of reconstruction oscillates with the amount the beam's power oscillates, but overall, there appears to be no trend. This is most likely due to the higher flux regions compensating for the lower flux regions.

5.12 Ice Formation

Where the CCD chip is at -40°, and there is water in the vacuum chamber, ice will form on the CCD chip. Ice attenuates the XUV beam, and the ice layer on the CCD chip

will increase in thickness as the experiment progresses. Due to the size of the vacuum chamber used in experiments for data collection for ptychography and the inability of the current experimental setup to change samples without opening the chamber, much water enters the vacuum chamber regularly. In the future it would be possible to reduce this with a smaller chamber that is easier to remove water content from, or use methods such as a cold finger to trap the water elsewhere. This causes the intensity of the measured scatter patterns to be reduced by an increasing amount as data are collected.

To investigate the effect of ice formation on the detector FRCs will be calculated for different parts of the reconstructed object over a 31 by 31 grid, where the results will be linearly interpolated to match the size of the reconstructed object. The rate of ice formation will range from 0 μm to 8 μm per scatter pattern, where the two middle values match rates of ice formation previously recorded. Previous ice formation rates have resulted in 20% and 90% flux lost for the final scatter pattern measurements. This section assumes linear ice growth over the CCD, in reality, the ice would form crystalline structures. This assumption is because this section investigates the general effect of ice thickness on reconstruction and therefore simplifies the ice formation.

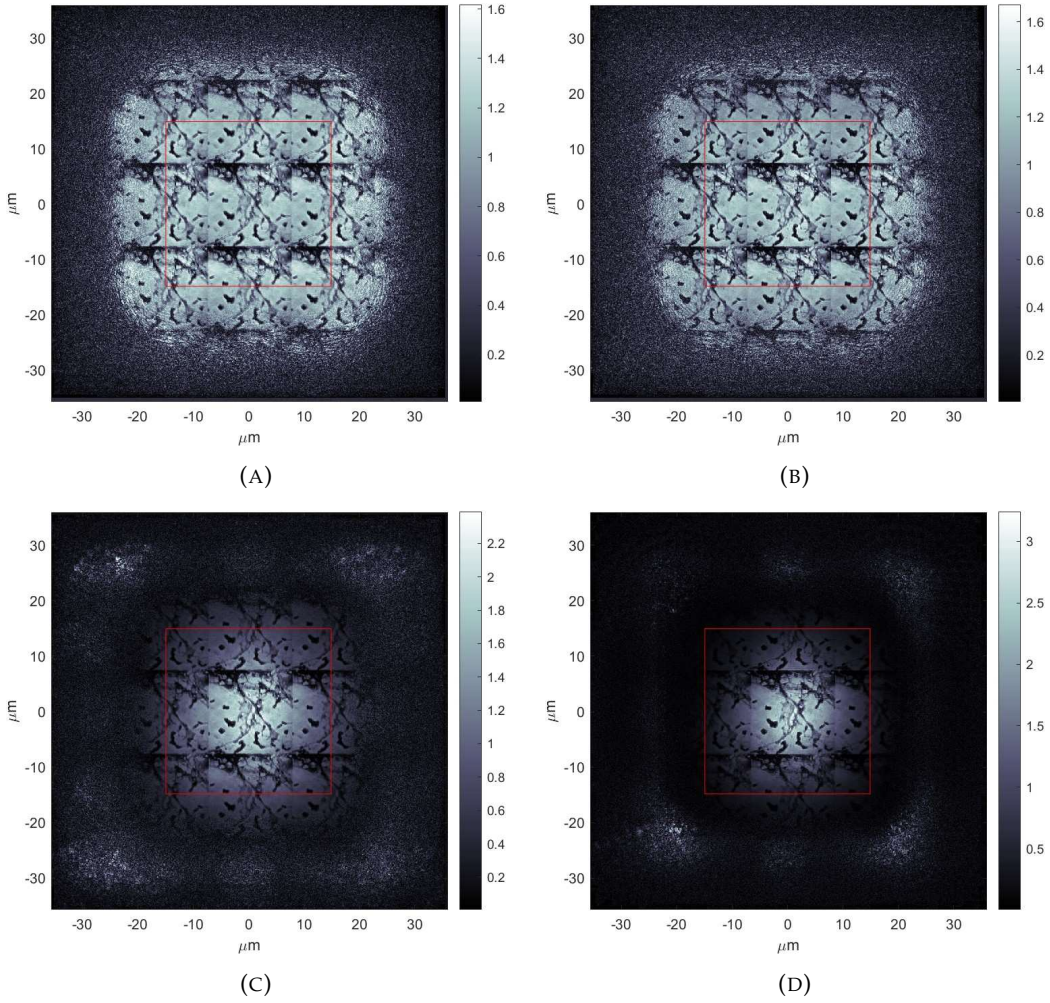

FIGURE 5.36: The reconstructed objects for varying levels of rate of ice formation on the detector at different regions of the reconstructed object for an 8 μm circular aperture using 100 iterations of DM followed by 100 iterations of MLs with an aperture to object distance of 141 μm and an object to detector distance of 3.69 cm, (A) 0 intensity lost to ice for final scatter pattern, (B) 20% intensity lost to ice for final scatter pattern, (C) 90% intensity lost to ice for final scatter pattern, (D) 95% intensity lost to ice for final scatter pattern.

From figure 5.36 the effect of lower flux for the later scatter patterns is most pronounced in (D) where the edges are reconstructed as nearly opaque, where the ice thickness is so large that little flux is measured by the detector. The higher amount of ice formation has led to the outer regions of the reconstructed objects to have a lower intensity. Calculating FRCs for multiple regions of the reconstructed objects is now possible.

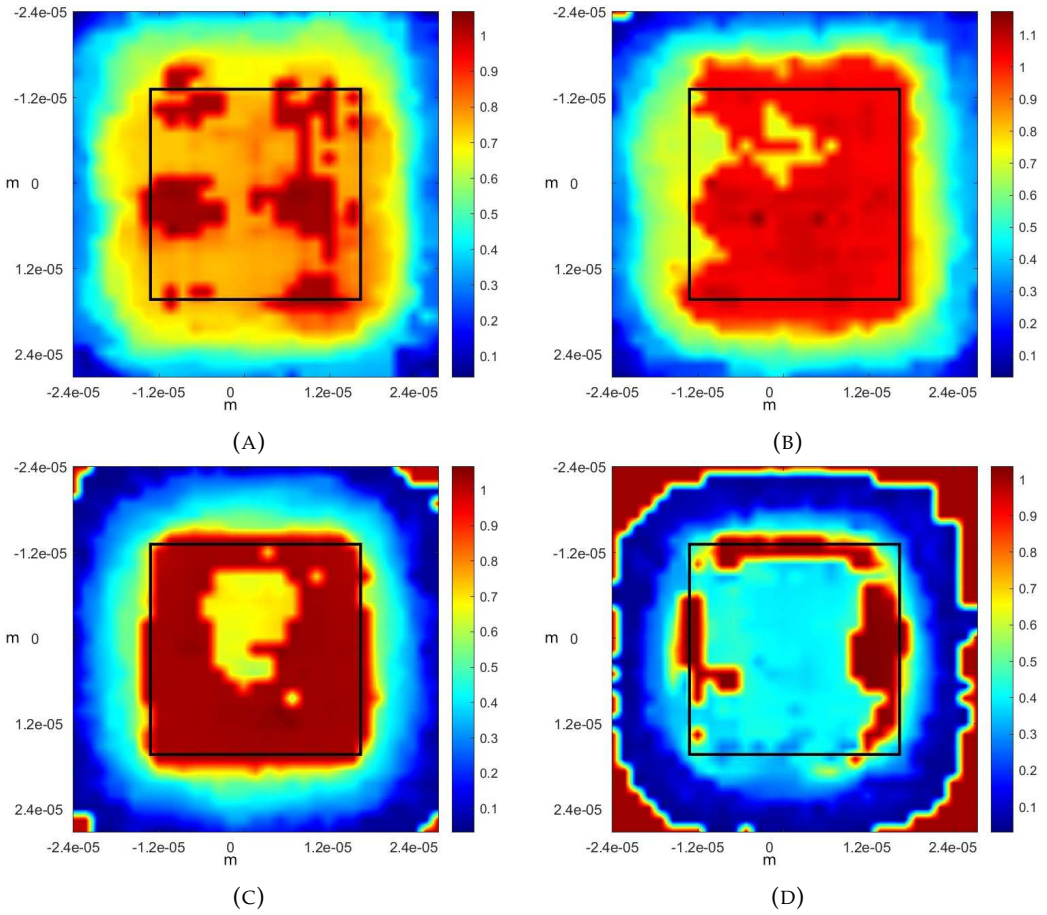

FIGURE 5.37: The first FRC intercept of the half-bit criterion for varying levels of rate of ice formation on the detector at different regions of the reconstructed object for an 8 μm circular aperture using 100 iterations of DM followed by 100 iterations of MLs with an aperture to object distance of 141 μm and an object to detector distance of 3.69 cm, (A) 0 intensity lost to ice for final scatter pattern, (B) 20% intensity lost to ice for final scatter pattern, (C) 90% intensity lost to ice for final scatter pattern, (D) 95% intensity lost to ice for final scatter pattern.

From figure 5.37, it can be seen that the first FRC intercept of the half-bit criterion improves in the later scatter pattern measurements with higher ice formation. This is the opposite of what was expected, as the amount of flux for the later scatter patterns is much lower. The first FRC intercepts of the half-bit criterion of the central regions are worse, where there is less intensity for the scatter patterns in the outer regions.

The reason for the improvement in the first FRC intercepts of the half-bit criterion in regions of the later scatter pattern measurements can be seen in figure 5.36 where the regions of higher FRCs correspond to the regions of low intensity. This shows that care must be taken when performing FRCs on samples of low intensity as the reconstructed object does not resemble the sample.

5.13 Super Resolution

Super-resolution for ptychography was introduced by Maiden *et al.* in 2011, where it was shown that there was much unused information in non-super-resolution ptychography (105). Because the scatter pattern is the convolution of the Fourier transform of the probe and Fourier transform of the object, there is information about scattered light beyond the limit of the detector encoded within the scatter pattern measured by the detector (106).

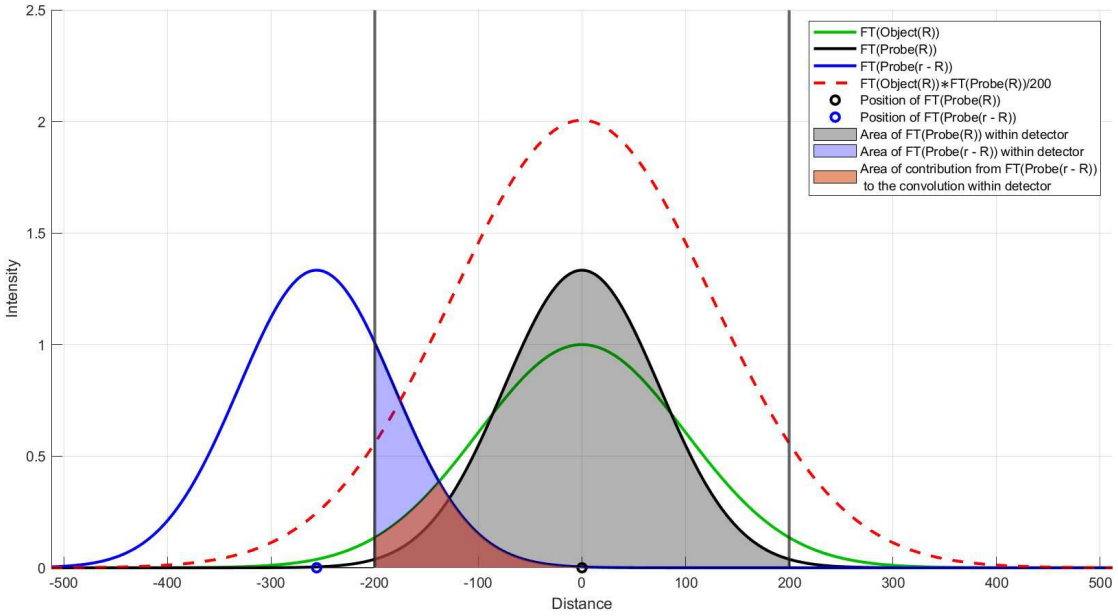

FIGURE 5.38: The contribution of the Fourier transform of a probe on the convolution for two positions, at the centre of the detector (black line) and outside the detector (blue line). Within the detector (grey verticals) is the area of the Fourier transform of the probe at the centre of the detector (black area) and the area of the Fourier transform of the probe outside the detector (blue). The amount of contribution to the convolution of the Fourier transform of the probe at the outside position is shown under the Fourier transform of the object and the Fourier transform of the probe (red area).

From figure 5.38, it is shown that information about a position outside the detector is encoded in the convolution of the Fourier transforms of the object and probe within the detector. This is why a working super-resolution technique is important, as not all the information measured is being used, and higher-resolution reconstructions are possible.

With the high angular spread of the double slit's probe this means there is much-unused information about the pixels beyond the CCD in the x-axis.

To test if super-resolution is possible for XUV HHG ptychography, a mask around the edge of the data taken by the CCD can be used. The mask is a matrix of values that are 0 or 1, where 0 is the data that are not used in reconstruction, and 1 is the data that are used. The reconstructive algorithm will then reconstruct the data as if the CCD size has not changed and not use the data that has a value of 0 in the masked region. If the reconstruction with the masked data has the same resolution as without masking, this will prove that super-resolution is possible with XUV HHG ptychography.

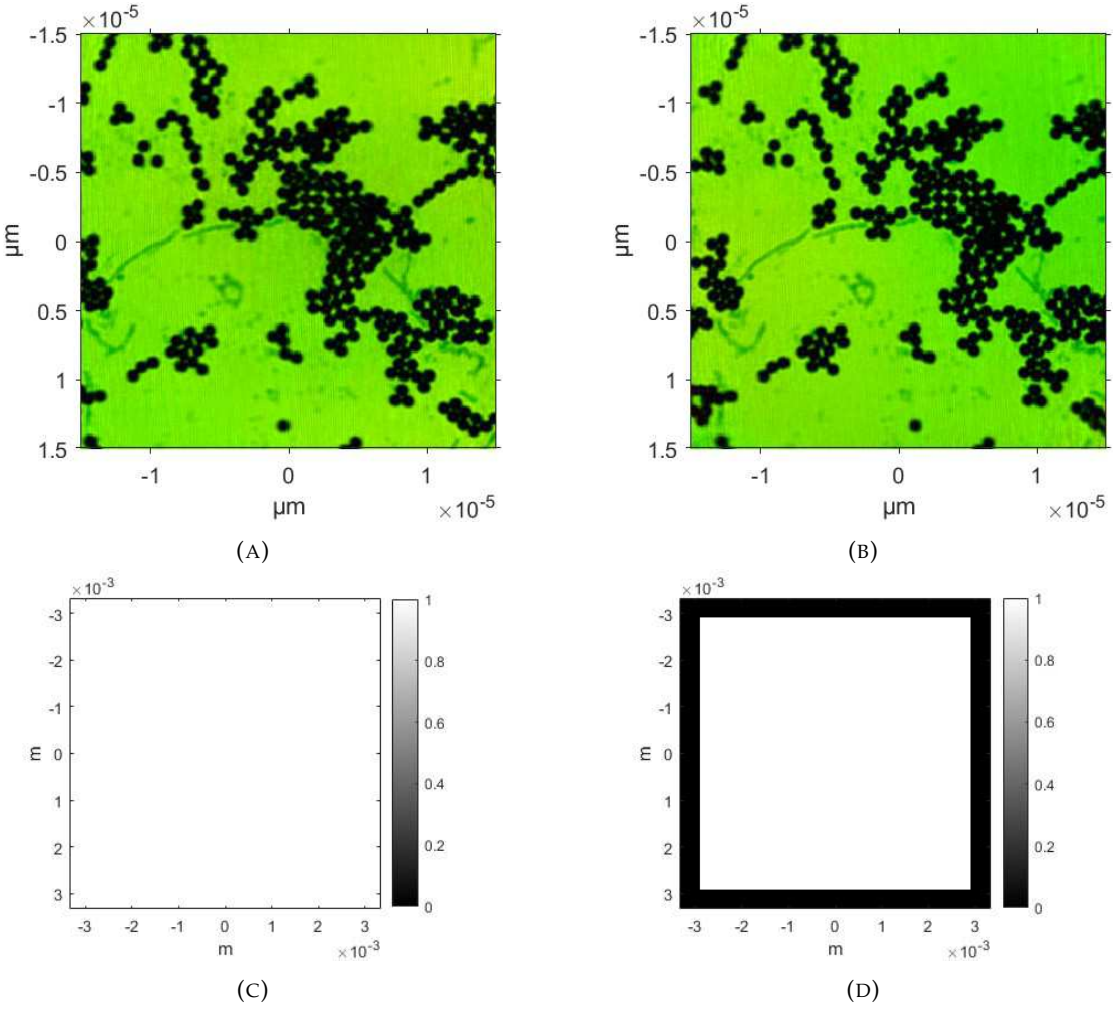

FIGURE 5.39: Reconstructed 945 nm diameter polystyrene spheres where no mask (A) and a 32-pixel inward mask (B) has been applied on the data, using a double slit aperture (5x1 μm slits spaced 4 μm from centres) 141 μm before the object and detector 3.69 cm away from the object, using 100 iterations of DM and 500 iterations of MLs. Where (A) and (B) are two different data sets of the same object. (C) and (D) are the masks for what data were used in the reconstruction of (A) and (B) respectively, where 1 is the data are used and 0 is the data were not used. (C) is the mask where all the data are used, and (D) is the 32-pixel inward mask where the black border is where the data were not used.

From figure 5.39 it is shown that the reconstructive algorithms are still able to reconstruct the object with no noticeable issues. To determine if the reconstruction is comparable to the non-masked reconstruction, FRCs and FLCs can be performed. When reducing the detector size the resolution at the Nyquist limit of the CCD would be 93.5 nm, but if super-resolution is performed the reconstructions should be able to achieve a resolution of 82 nm.

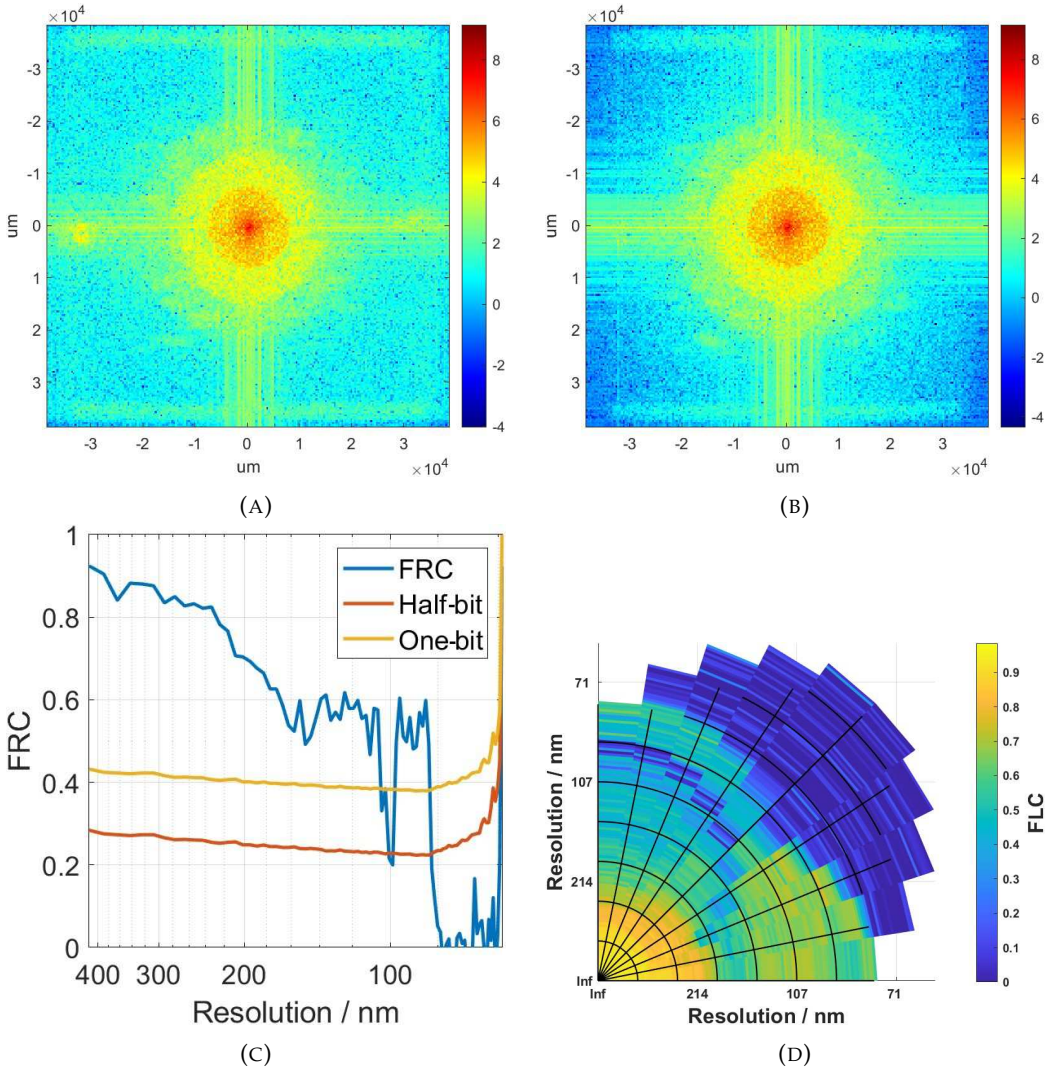

FIGURE 5.40: (A) and (B) are the Fourier transforms of a central region from figure 5.39 respectively, (C) is the FRC of (A) and (B), and (D) is the FLC of (A) and (B). The resolution at the Nyquist limit for this is 82 nm.

From figure 5.40, it can be seen that the FRC is as good as figure 5.5 and has an FLC as expected from a reconstruction using a double slit; however, the Fourier transforms of the object in figure 5.40 have a sudden increase in value towards the edge of the y-axis. For natural objects, the intensity of the Fourier transform decreases (97), and this is a

clear increase in the y-direction, and the x-direction does not have this issue. This can be explained by the shape of the double slit scatter pattern spreading further in the x-direction, where more information beyond the CCD is encoded into pixels on the CCD. The spread is not as great in the y-axis and, therefore, fails to reconstruct the object correctly along the y-axis. Here, the mask would lead to the reduced CCD size to have a resolution at the Nyquist limit of 93.5 nm; however, the reconstructed objects' FRCs reach the mask size resolution at the Nyquist limit of 83 nm, the same as the unaltered CCD. The reason the central region of the reconstructed object is used for FRCs is that it is the region of greatest overlap between probes and is least affected by the reduced flux from the ice thickness.

With super-resolution being possible, even if only along the x-axis for a double slit, the data and mask can have a border of 32 pixels of zeros added. This will allow the code to reconstruct the data beyond the size of the CCD. The resolution at the Nyquist limit of the increased CCD size will be 74 nm. While actin have diameters around 7 nm and microtubules have diameters around 25 nm, super-resolution with this setup does not reach this resolution. For future setups, an increase in resolution of 12.5% could reach these resolutions, and it is important to have such a technique available.

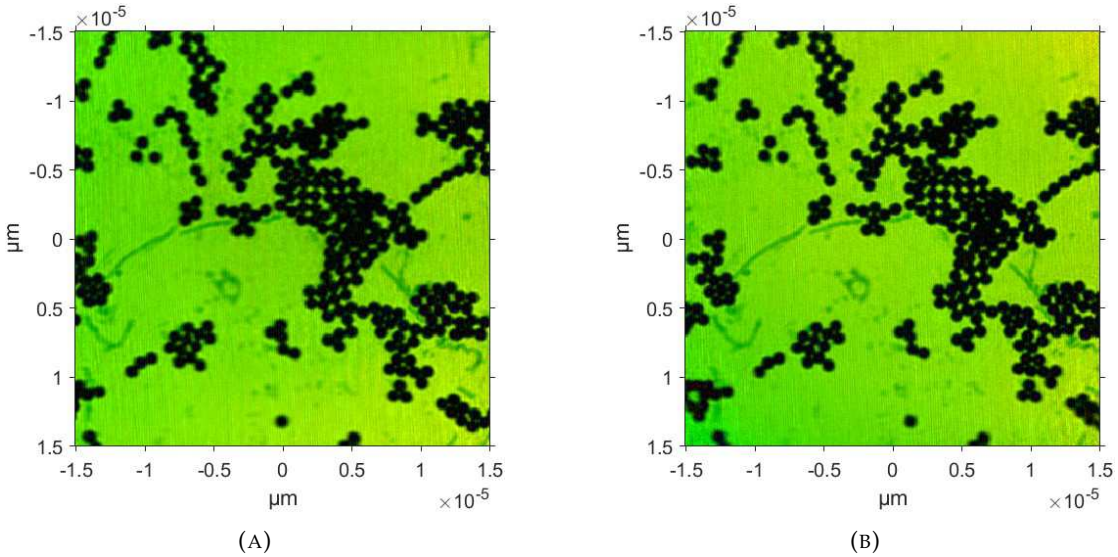

FIGURE 5.41: Reconstructed 945 nm diameter polystyrene spheres where a 32-pixel outward mask has been applied on the data, using a double slit aperture (5x1 μm slits spaced 4 μm from centres) 141 μm before the object and detector 3.69 cm away from the object, using 100 iterations of DM and 500 iterations of MLs. Where (A) and (B) are two different data sets of the same object.

In figure 5.41, it is shown that the reconstructive algorithms can reconstruct the object

with a mask and data with a border of 32 pixels; however, the vertical artefacts found in reconstructions that use a double slit are more pronounced. To calculate if super-resolution has been achieved with increased data and mask size, first FRCs and FLCs need to be calculated.

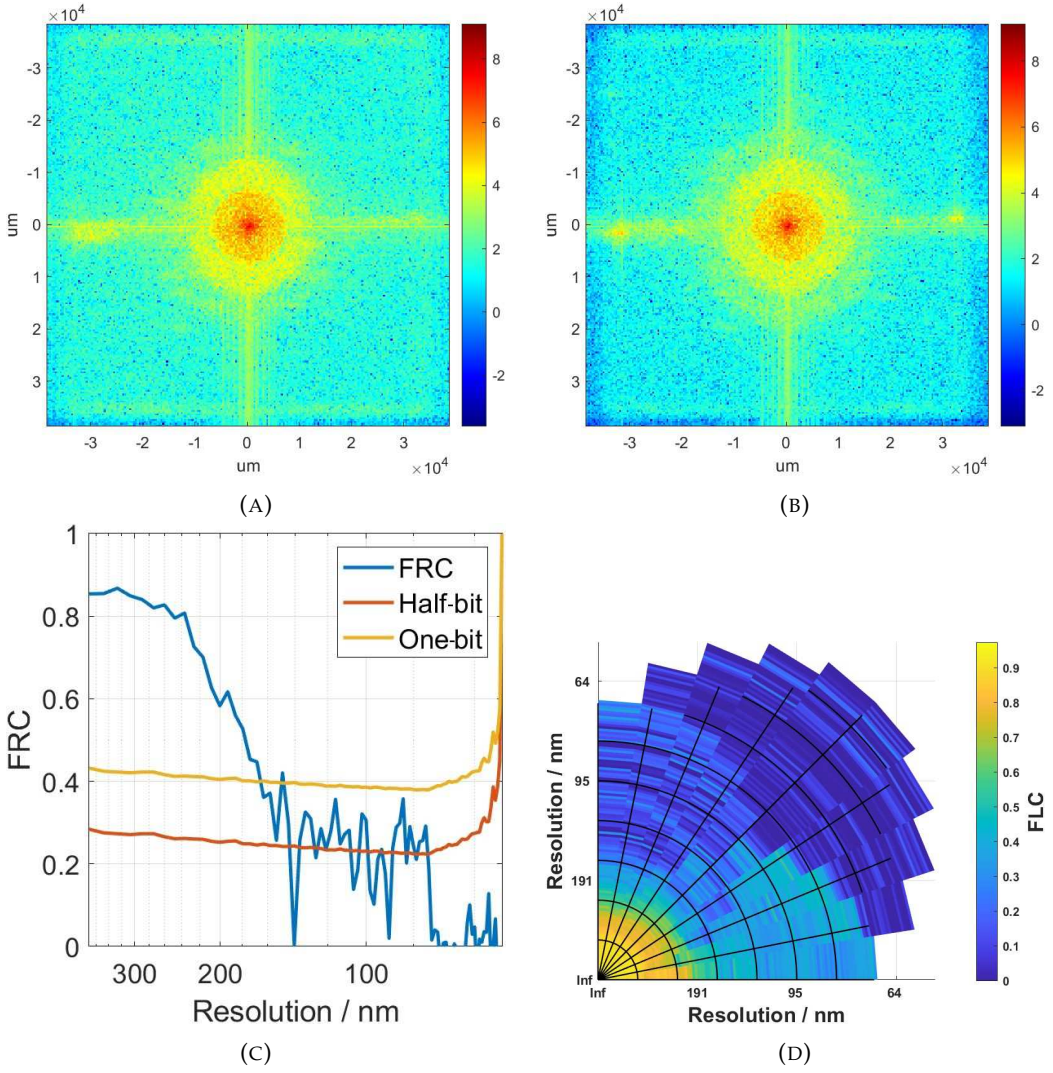

FIGURE 5.42: (A) and (B) are the Fourier transforms of a central region from figure 5.41 respectively, (C) is the FRC of (A) and (B), and (D) is the FLC of (A) and (B). The resolution at the Nyquist limit for this is 74 nm.

From figure 5.42, it can be seen that the FRC first intercepts the half-bit criterion at 145 nm, which is much worse than figure 5.40; however, the FLC in the x-axis reaches the Nyquist limit of the increased CCD size, as shown by the x-axis of (D) from figure 5.42. Here the resolution at the Nyquist limit of the increased size CCD is 74 nm.

The reason the inward mask reconstruction attempt may have worked where the outward mask failed is that the scatter pattern becomes weaker further from the centre.

This would lead to less information encoded in the scatter pattern from the convolution of the probe and object, and this was not enough for the reconstructive algorithms to correctly reconstruct the object.

From figure 5.42 it can be seen in (A) & (B) that the intensity of the Fourier transform of the object increases at the edges of the y-axis, which is wrong as the Fourier transform of a natural image decays with spatial frequency (97). This shows the super-resolution did not work along the y-axis, where the angular spread of the double slit's probe is lower. The x-axis does not have this increase in the intensity of the Fourier transform of the object and shows that super-resolution can work if the angular spread of the probe is great enough.

The problem of the irregular Fourier transforms could be explained by observing what happens to figure 5.38 when the detector size is increased.

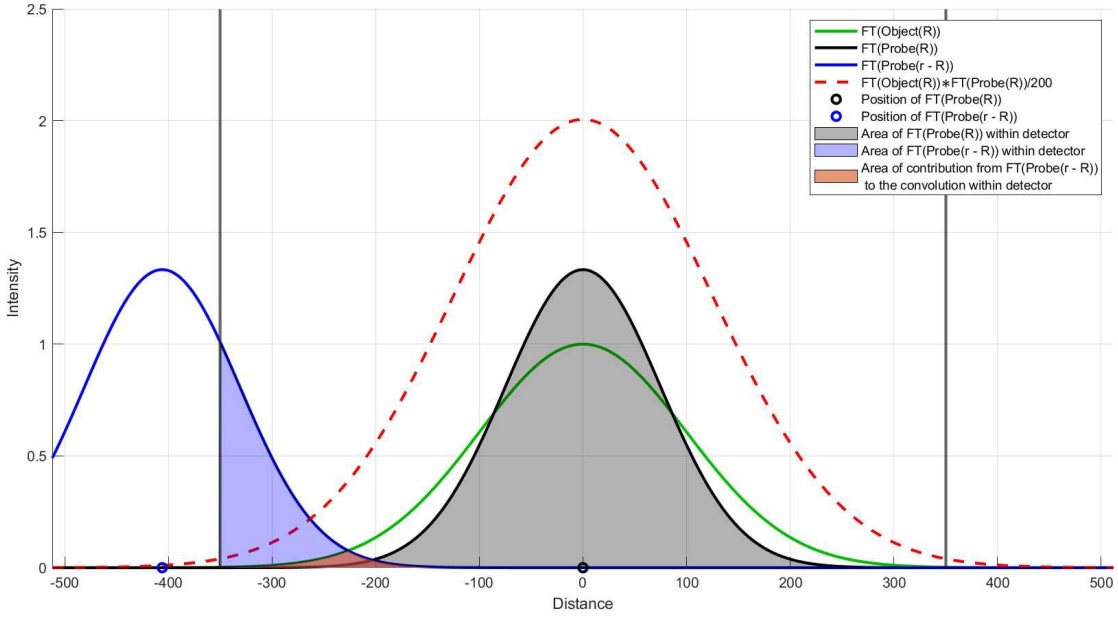

FIGURE 5.43: The contribution of the Fourier transform of a probe on the convolution for two positions, at the centre of the detector (black line) and outside the detector (blue line). Within the detector (grey verticals) is the area of the Fourier transform of the probe at the centre of the detector (black area) and the area of the Fourier transform of the probe outside the detector (blue). The amount of contribution to the convolution of the Fourier transform of the probe at the outside position is shown under the Fourier transform of the object and the Fourier transform of the probe (red area).

From figure 5.43 it can be seen that the Fourier transform of a probe at a position the same distance from the edge of the detector as in figure 5.38 has the same amount of area within the detector; however, the contribution to the convolution is much smaller.

This would explain why super-resolution worked when the CCD size was decreased, as the contribution to the convolution at the edges was much higher, and there was enough information encoded about positions outside of the detector to perform super-resolution. When the CCD size was increased, the encoded information about positions outside of the CCD was lower. This implies there is a required amount of encoded information from Fourier transforms of probe positions outside the detector to perform super-resolution.

It would be possible to increase the convolution at the edge of the detector by using a probe of higher flux. This would allow for super-resolution on positions further out from the probe.

While an interesting idea to wobble the CCD is to increase resolution, it would be too difficult due to the lack of optics and problems from moving a water-cooled CCD in a vacuum chamber.

5.14 Angular Spread

It has been shown that the angular spread in a direction improves the resolution of a reconstruction in that direction. Research also shows angular spread improves reconstruction resolution. Here will be an attempt to parameterise the improvement in resolution gained by the angular spread.

By comparing five apertures of increasing angular spread, the FRC first half-bit intercept can be compared. The areas of apertures were only considered to make sure enough flux passed through each aperture for successful reconstruction, as a thin circle would have a high angular spread but low flux passing through. With the different shapes of apertures it would be difficult to define a fair area for each aperture to have, as different regions of the beam can pass through the different apertures. This section was to help find a better aperture to use for ptychography. Before selecting the following apertures multiple apertures were briefly tested to investigate their performance, to see if they warranted further investigation.

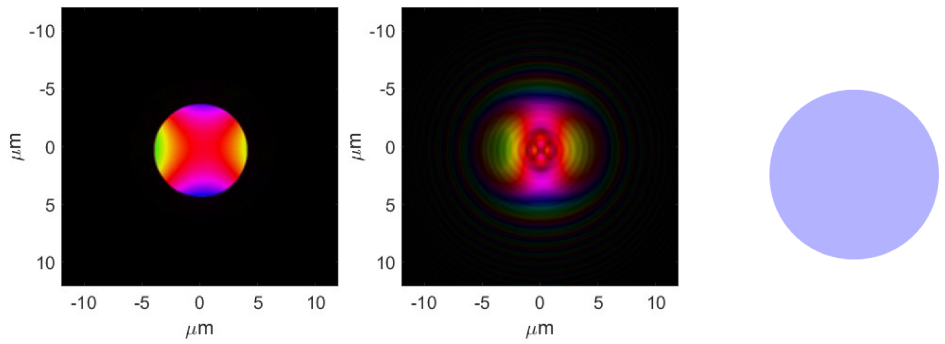

(A) (B) (C)

FIGURE 5.44: The beam at the aperture (A) and probe after propagating 141 μm (B) of the circular aperture (8 μm diameter). (C) will be the symbol for the circular aperture (8 μm diameter).

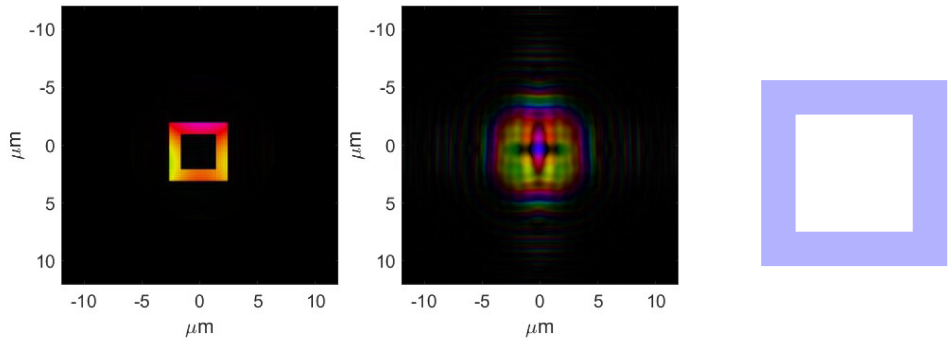

(A) (B) (C)

FIGURE 5.45: The beam at the aperture (A) and probe after propagating 141 μm (B) of the double-double slit aperture (5 μm square outside height and width and 4 μm inside height and width). (C) will be the symbol for the double-double slit aperture (5 μm square outside height and width and 4 μm inside height and width).

It is important to note that the aperture in figure 5.45 would either need supports to manufacture or use solid materials that alter the phase of the beam, but not block the beam, passing through the aperture.

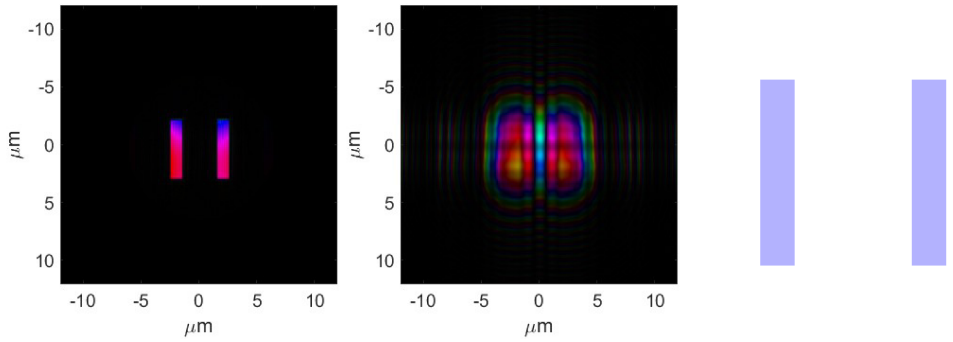

(A) (B) (C)

FIGURE 5.46: The beam at the aperture (A) and probe after propagating 141 μm (B) of the double slit aperture (5x1 μm slits spaced 4 μm from centres). (C) will be the symbol for the double slit aperture (5x1 μm slits spaced 4 μm from centres).

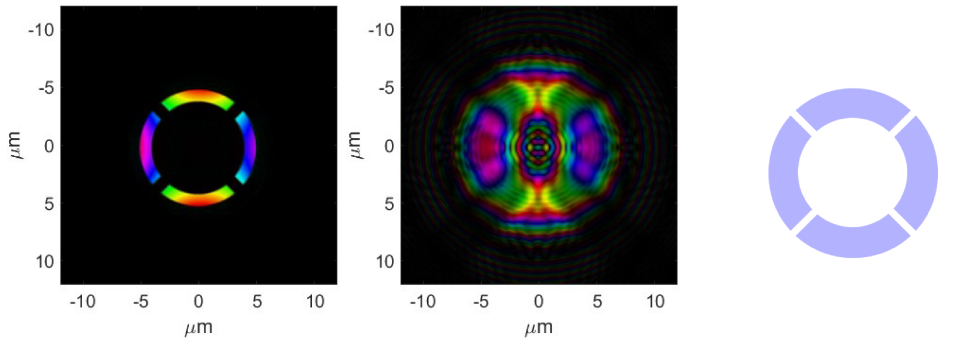

(A) (B) (C)

FIGURE 5.47: The beam at the aperture (A) and probe after propagating 141 μm (B) of the ring aperture (10 μm outside diameter and 9 μm inside diameter). (C) will be the symbol for the ring aperture (10 μm outside diameter and 9 μm inside diameter).

The aperture in figure 5.47 is not a full ring, as that would not be possible to fabricate as a transmission mask. In the brief trialling of multiple apertures, it was a full ring, but appeared to be performing the best and the gaps in the ring were added to see if a ring aperture that could be fabricated still performed the best.

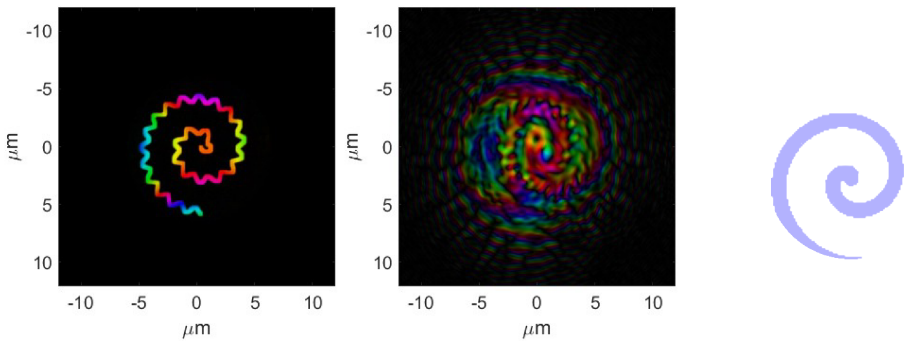

(A) (B) (C)

FIGURE 5.48: The beam at the aperture (A) and probe after propagating 141 μm (B) of the deformed spiral (10 μm outside diameter and 0.5 μm thickness). (C) will be the symbol for the deformed spiral (10 μm outside diameter and 0.5 μm thickness).

It is important to note that the beam propagation from all the apertures used Fraunhofer propagation, and may omit the effects of boundary diffractive waves. If this was an issue it would be most pronounced in the spiral aperture with its small features. This could be improved in future analysis with more rigorous propagation methods.

The circular aperture was chosen as it is a commonly used aperture and the aperture my group previously used. The double slit was chosen as it was the aperture with the highest angular spread that I had access to. The double-double slit was chosen as it should have high angular spread in both x and y directions. The ring aperture was chosen as it has high angular spread in most directions. The spiral aperture was chosen as it has been used by the Jena group for XUV ptychography (107). A double ring aperture was considered when trialling multiple apertures to see which warranted further investigation, and it did not appear to perform better than the singular ring aperture, but in the future, further investigation could be undertaken into testing the viability of the double ring aperture.

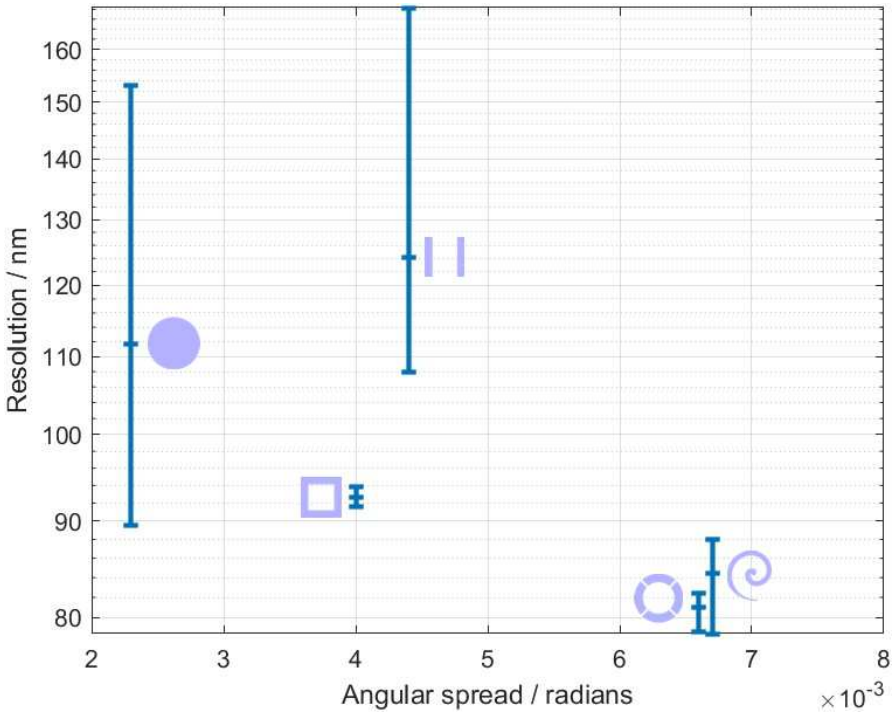

FIGURE 5.49: The average FRC first intercept of the half-bit criterion of three runs for a circular aperture (8 μm diameter), double-double slit aperture (5 μm square outside height and width and 4 μm inside height and width), double slit aperture (5x1 μm slits spaced 4 μm from centres), ring aperture (10 μm outside diameter and 9 μm inside diameter), deformed spiral (10 μm outside diameter and 0.5 μm thickness) respectively (blue line), with lowest resolution FRC first intercept of the half-bit criterion (top error bar), and highest resolution FRC first intercept of the half-bit criterion (bottom error bar).

From figure 5.49, there is a slight trend towards higher angular spread probes having higher resolution; however, it can clearly be seen that the probes with the greater angular spread do not always have a better resolution of the reconstructed object. Where the resolution at the Nyquist limit for reconstruction was 82 nm, it can be seen that many probes reach this limit, and some surpass it.

All the probes have the same beam power at the aperture, but different-shaped apertures will have different flux amounts transmitted. The flux counts of the first scatter pattern were measured to ensure that the higher angular spread probes did not have a higher resolution just due to a higher flux. The initial beam was kept the same, and therefore different amounts of flux were measured by the detector, because this section of the chapter was also to find the best aperture for a given beam, as flux can always be increased in future experiments, and increasing the flux count the scatter patterns would be affected by the high dynamic range calculations.

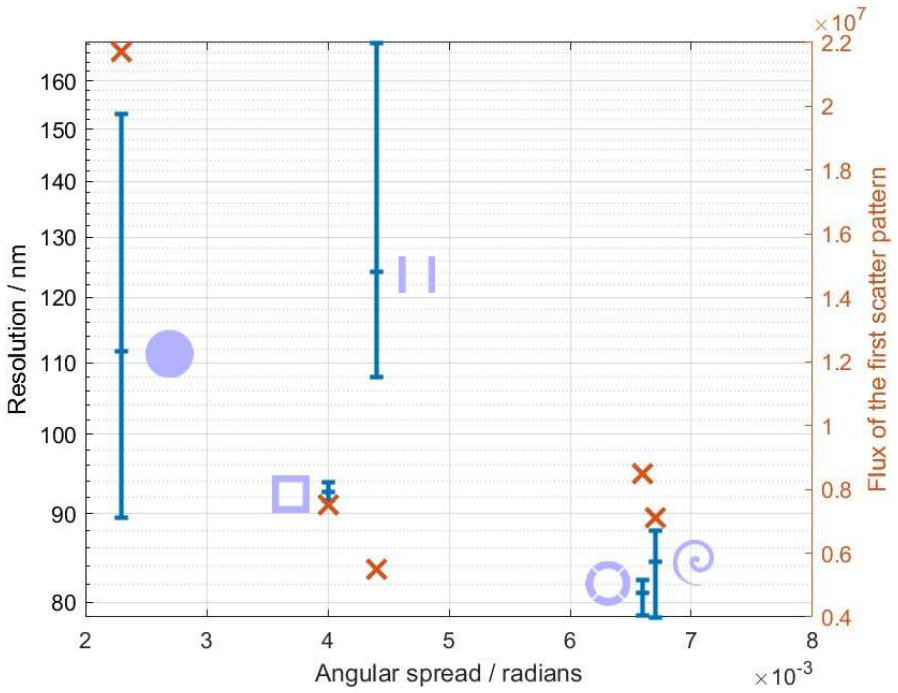

FIGURE 5.50: On the right axis, the flux of the first scatter pattern for a circular aperture (8 μm diameter), double-double slit aperture (5 μm square outside height and width and 4 μm inside height and width), double slit aperture (5x1 μm slits spaced 4 μm from centres), ring aperture (10 μm outside diameter and 9 μm inside diameter), deformed spiral (10 μm outside diameter and 0.5 μm thickness) respectively (orange crosses). This figure also contains figure 5.49 on the left axis.

As shown by figure 5.50, the circular probe (8 μm diameter), which had the highest flux count, performed worse, and the remaining four probes had a similar flux count. This shows that transmitted flux is not a good measure of probe quality and that flux does not need to be heavily considered during this experiment. Flux still influences the results, but this section was to find the best aperture for a given system.

To compare the limits of the best probes from figure 5.49, the double-double slit, the ring aperture, and the spiral aperture, will be simulated at a short object to CCD distance. A shorter object to CCD distance is required to increase the resolution at the Nyquist limit of the CCD. These probes will then be compared again with a higher resolution possible.

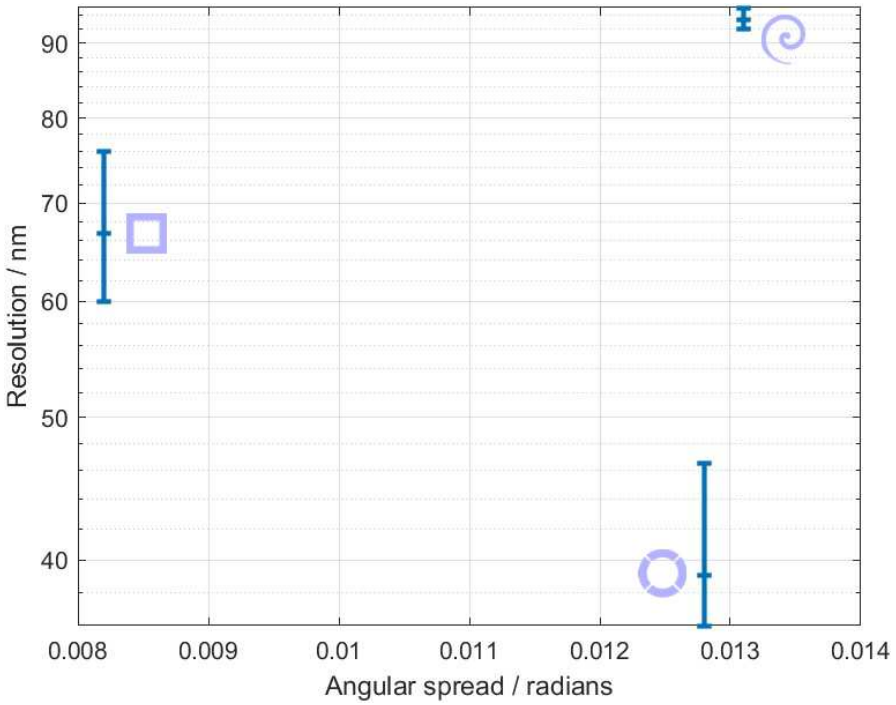

FIGURE 5.51: The average FRC first intercept of the half-bit criterion of three runs for a double-double slit aperture (5 μm square outside height and width and 4 μm inside height and width), ring aperture (10 μm outside diameter and 9 μm inside diameter), deformed spiral (10 μm outside diameter and 0.5 μm thickness) respectively (blue line), with lowest resolution FRC first intercept of the half-bit criterion (top error bar), and highest resolution FRC first intercept of the half-bit criterion (bottom error bar).

From figure 5.51, it is shown that the ring aperture is the best aperture for higher resolution of reconstructed objects. With this increased resolution at the Nyquist limit, it can be seen that higher angular spread probes are not always better. While high angular spread is important for high resolution of reconstructed objects, there appear to be other characteristics that impact the resolution of reconstructed objects.

5.15 Best aperture

Throughout this chapter, certain characteristics have been shown to enhance the reconstruction. The double slit aperture's probe had a high angular spread of the scatter pattern; however, the double slit aperture suffered from vertical lines in the reconstructions owing to its scatter pattern mostly spreading along the x-axis. The circular apertures did not suffer from these vertical lines as their FLCs were more radially symmetric.

Knowing that the characteristics of high angular spread and uniform FLCs are what make a good probe, this combination of the circular aperture and double slit would make a good probe. The combination would make a ring, which also performed the best out of all the apertures in the previous section.

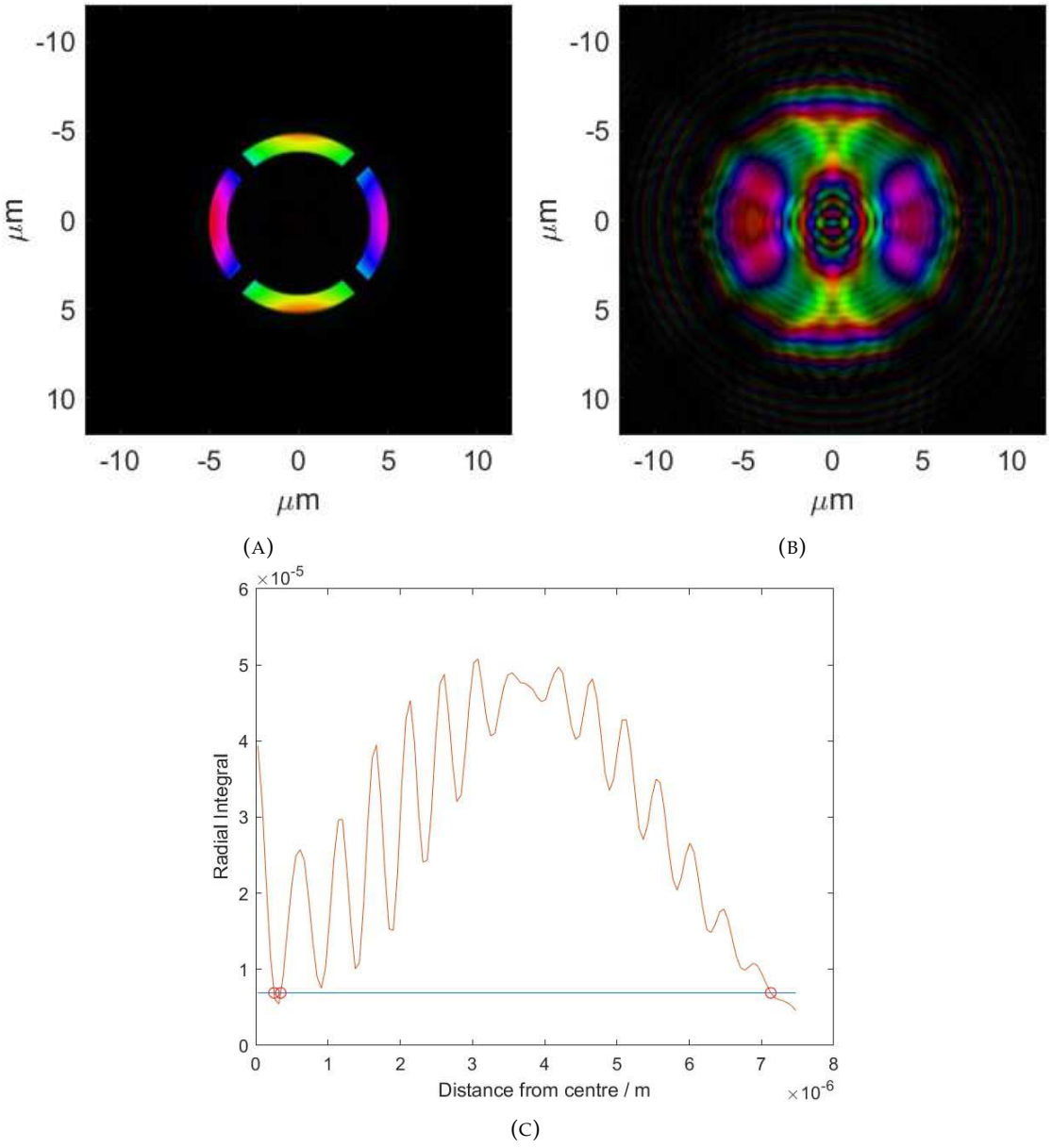

FIGURE 5.52: (A) Beam at the ring aperture, (B) beam after propagating 141 μm from the ring aperture, and (C) the radial integral of the beam after propagating 141 μm from the ring aperture.

From figure 5.52 it can be seen in (C) the ring aperture (10 μm outside diameter and 9 μm inside diameter) that the probe after propagating 141 μm has a beam width of 14 μm. In (A) is it shown that the probe in nearly radially symmetric. This probe also has

a total flux count comparable to the double slit aperture, which is a quarter of that of the 10 μm diameter circular aperture.

The high angular spread of this aperture and near radial symmetry should lead to high-quality reconstruction, as higher frequency components will have a good signal-to-noise in all directions.

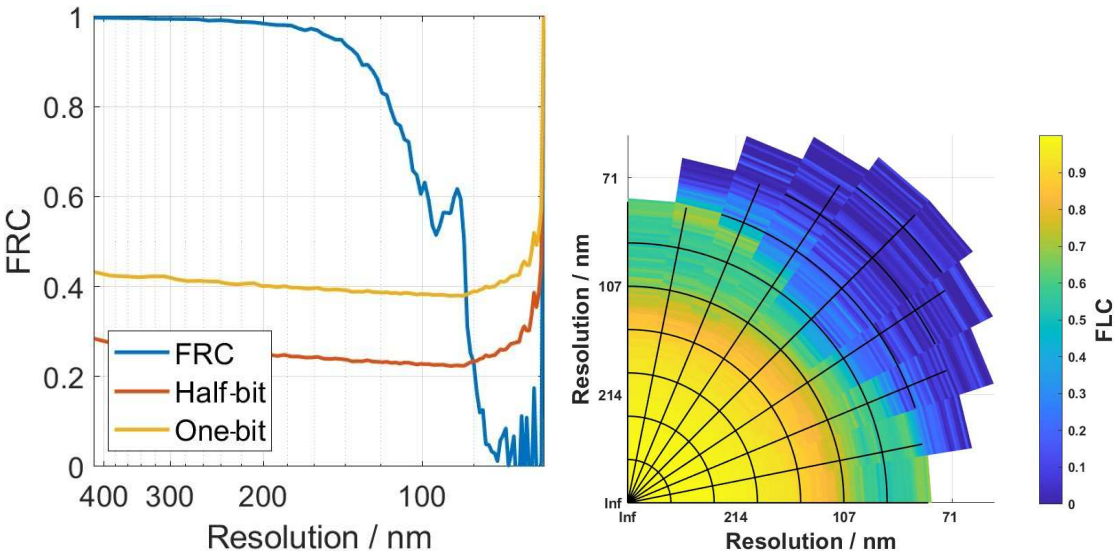

(A) (B)

FIGURE 5.53: Fourier correlations for the ring aperture (10 μm outside diameter and 9 μm inside diameter), with an aperture to object propagation distance of 141 μm and object to CCD distance of 3.69 cm, using 100 iterations of DM and then 100 iterations of MLs for reconstruction, and a binning of 2. The resolution at the Nyquist limit is 82 nm.

From figure 5.53 it can be seen that FRC is high for all resolutions up to the resolution at the Nyquist limit of the CCD; even going beyond and intercepting the half-bit threshold criterion at 79 nm, where the resolution at the Nyquist limit of the CCD of 82 nm. Figure 5.53 also shows a near radially symmetric FLC, meaning this aperture has good resolution in all directions. The FLC is slightly worse towards the corners of the CCD, though this is most likely due to the non-transmissive corners of the aperture limiting the spread of the beam in these directions.

With this aperture performing so well, its limits need to be investigated. This was done firstly by reducing the object to CCD distance, increasing the resolution at the Nyquist limit of the CCD. No binning was performed to improve the resolution for higher-frequency components, as shown by figure 5.32, and due to the high angular spread of the ring aperture's probe.

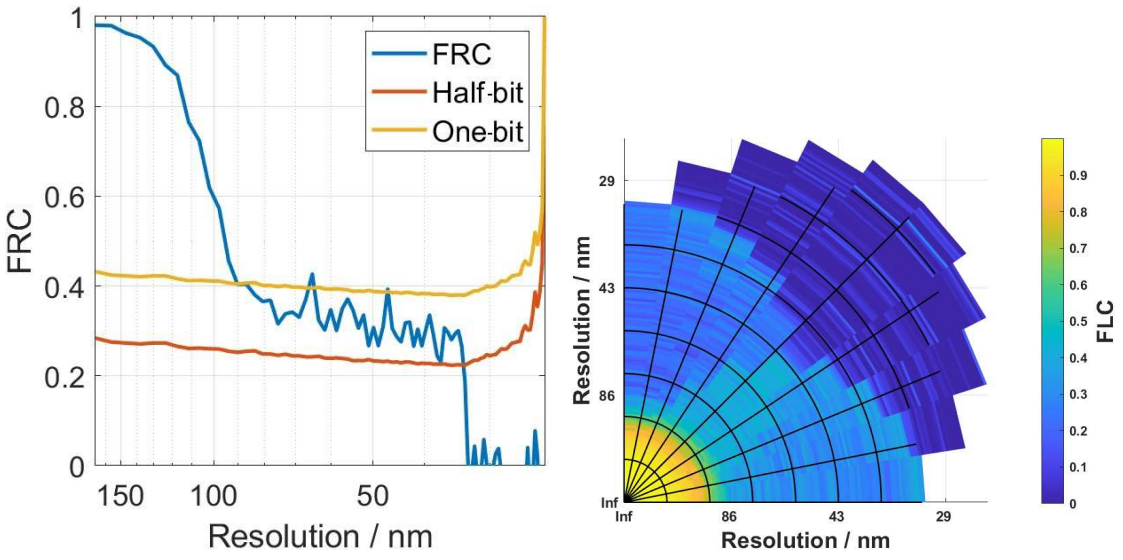

(A) (B)

FIGURE 5.54: Fourier correlations for the ring aperture (10 μm outside diameter and 9 μm inside diameter), with an aperture to object propagation distance of 141 μm and object to CCD distance of 1.35 cm, using 100 iterations of DM and then 100 iterations of MLs for reconstruction, and a binning of 1. The resolution at the Nyquist limit is 33 nm.

From figure 5.54, the limit of this aperture, with current methods, can be found to reconstruct objects with a resolution of 33 nm. With binning, the aperture fails to reconstruct the object at this object to CCD propagation distance, due to the reconstruction algorithm requiring the increased size of the probe gained from not binning. With a resolution of 33 nm this aperture would make this technique comparable to STORM, one of the highest resolution techniques for imaging neurons.

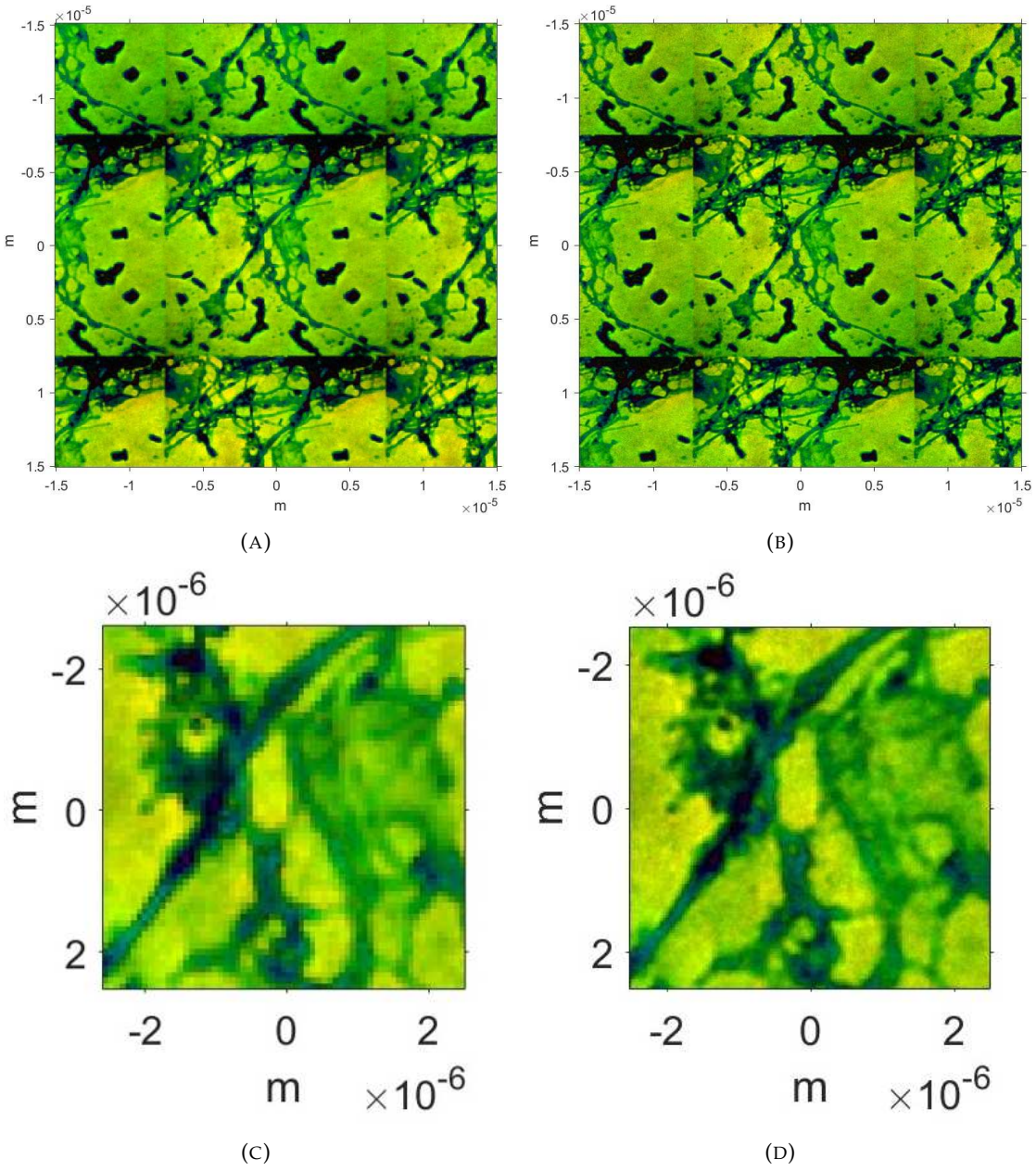

FIGURE 5.55: A simulated reconstruction of neurons, using a ring aperture (10 μm outside diameter and 9 μm inside diameter) 141 μm before the object and detector. (A) had an object to CCD distance of 3.69 cm, and (B) had an object to CCD distance of 1.35 cm, using 100 iterations of DM and 100 iterations of MLs. (A) had a resolution at the Nyqusit limit of 82 nm, and (B) had a resolution at the Nyquist limit of 33 nm. (C) and (D) are the same zoomed-in region of (A) and (B) respectively.

When comparing the reconstructions from figure 5.53 & 5.54 in figure 5.55 it can clearly be seen that the reconstructed object from the closer CCD position is much sharper.

With the probe being much larger than previously used probes, the intensity distribution goes beyond the scan area much further with a lower resolution object being reconstructed as before.

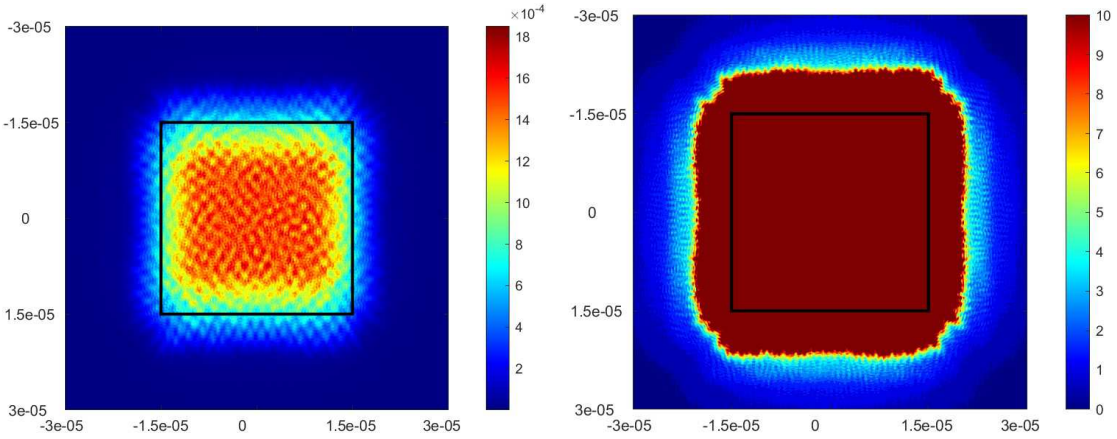

(A) (B)

FIGURE 5.56: (A) The total intensity distribution of all probes over an object over a scan area of 30 μm by 30 μm with 62 scans for ring aperture (10 μm outside diameter and 9 μm inside diameter). (B) The multiples of intensity at the beam width of all probes over an object. With an aperture to object propagation distance of 141 μm.

Figure 5.56 shows how far the probe overlap extends beyond the scan area. With this larger probe, it is possible to image the same scan area in fewer scanning positions.

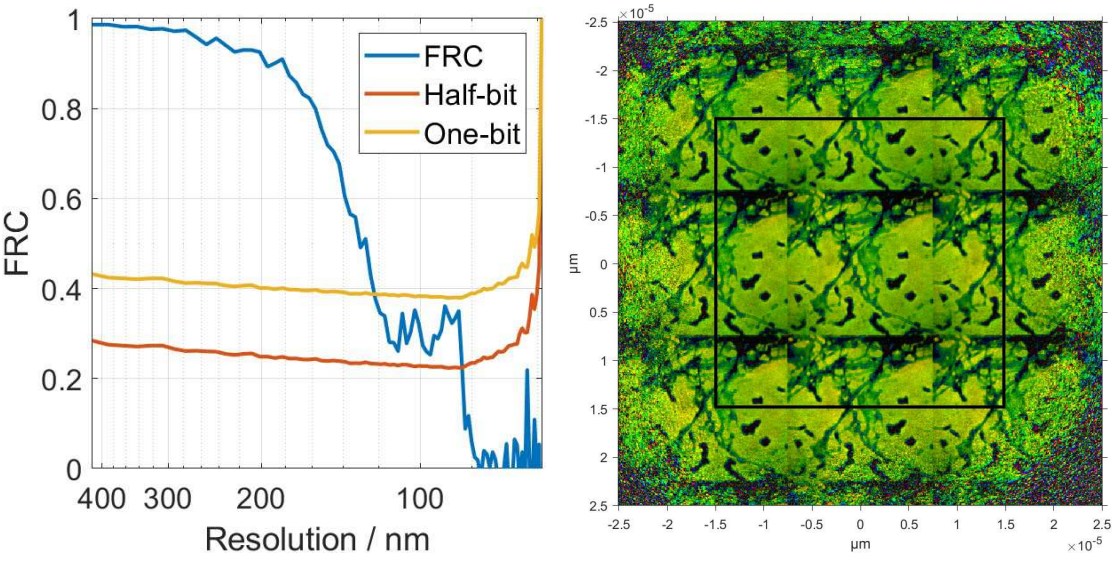

(A) (B)

FIGURE 5.57: (A) The FRC and (B) one of the corresponding simulated reconstruction of neurons. (B) was using a ring aperture (10 μm outside diameter and 9 μm inside diameter), with an aperture to object propagation distance of 141 μm and object to CCD distance of 3.69 cm, using 100 iterations of DM and then 100 iterations of MLs for reconstruction, and a binning of 2. The resolution at the Nyquist limit is 82 nm. This reconstruction used 62 scan positions with a step size between scan positions of 4 μm.

The reconstruction in figure 5.57 used a step size of 4 μm, which leads to only 62 scanning positions for the full scan area compared to the usual 251 scanning positions, as used in figure 5.53. The ability to image with lower flux while maintaining maximum resolution is incredibly impactful, as it improves the speed at which data are taken and minimises damage to the sample.

To investigate if these results are only valid for reconstructions of a neuron, the previous setup will be used on a simulation using a reconstruction of polystyrene spheres from experimental data, that I collected and reconstructed. The object is of 0.5 μm diameter polystyrene spheres.

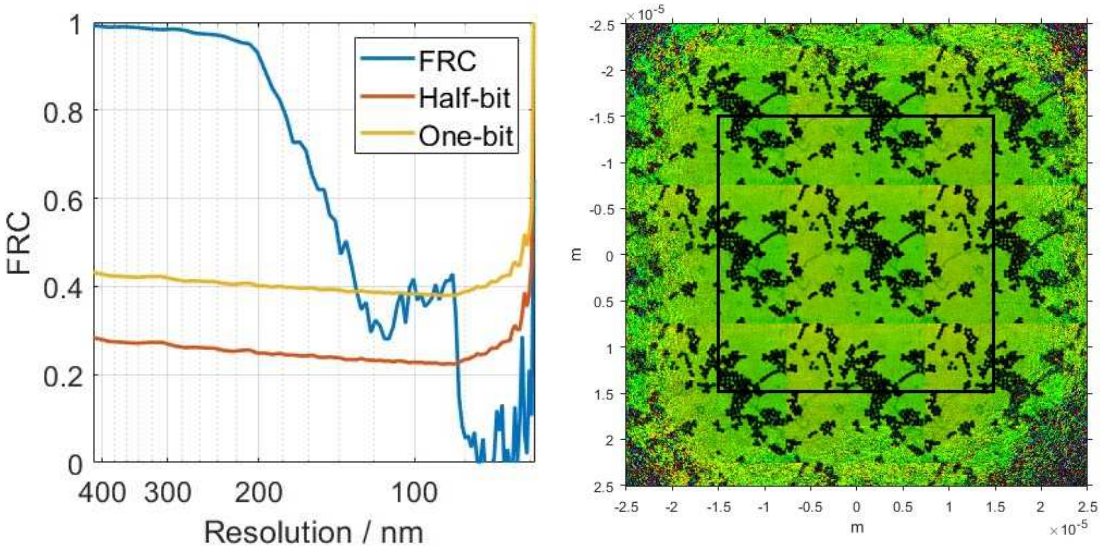

(A) (B)

FIGURE 5.58: (A) The FRC and (B) one of the corresponding simulated reconstruction of polystyrene spheres. (B) was using a ring aperture (10 μm outside diameter and 9 μm inside diameter), with an aperture to object propagation distance of 141 μm and object to CCD distance of 3.69 cm, using 100 iterations of DM and then 100 iterations of MLs for reconstruction, and a binning of 2. The resolution at the Nyquist limit is 82 nm. This reconstruction used 62 scan positions with a step size between scan positions of 4 μm.

Figure 5.58 shows that this setup still achieves the resolution at the Nyquist limit of 82 nm, as did the reconstruction from figure 5.57. This adds to the robustness of the data for the ring aperture and the resolutions achieved. This only shows that the aperture works for neurons and polystyrene spheres, but these are the most common objects imaged by my group.

5.16 Summary

Using the new method of FLCs to quantify the resolution of a reconstruction in all directions gave a more detailed insight into the quality of a reconstruction, improving upon the well-established method of FRCs that gave the quality of the overall reconstruction. Using FLCs, it was possible to analyse why the double slit aperture's probe had high-quality reconstructions even with lower flux compared to the typically used circular apertures. Using this information, we were able to predict a probe from a ring aperture that could give resolutions of 33 nm, improving upon the 82 nm resolution of reconstructions of the circular aperture (10 μm diameter).

Increasing the flux through an aperture will increase the resolution of the reconstructed object, up to the resolution at the Nyquist limit of the detector, with diminishing returns afterwards. This allows for more flux-sensitive samples to be imaged at lower amounts of flux if the FRC first intercept of the half-bit criterion is at the resolution at the Nyquist limit of the detector.

We have found that while linear overlap is a good measure of determining the step size required while imaging, it does not explain the intensity distribution of the probe over the object. When calculating the intensity distribution of the probe on the object, it is possible to find artefacts that will be reconstructed in the sample and regions beyond the scan area that will be reconstructed at a lower resolution.

While investigating the robustness of the reconstructive algorithms, it has been found that the code is very robust to experimental imperfections, such as beam instability and ice formation. This informs us that these effects have not impeded the reconstruction resolution and are not cause for concern.

Chapter 6

Correlative Imaging

When imaging samples, the ability to identify the composition of the sample allows for a greater understanding beyond simply the structure of the object. SIM, STORM, and Lightning are techniques with a similar resolution to XUV ptychography and use fluorophores to image the sample. These fluorophores mark different components, such as actin and tubulin, and allow for identification once imaged. This chapter will compare these techniques on similar samples and provide a more in-depth explanation of their preparation and application. When performing correlative imaging with fluorescence-based techniques, the composition of the cell will be imaged. It can be compared with XUV ptychography, which will image the structure of the cell. This will grant a greater insight into the sample. However, there are challenges involved in getting these techniques to work in tandem, as each technique has different requirements to perform optimally, and these will also be discussed. This section is not about comparing the different techniques, but trying to image the same region with techniques that recover different information about the sample and then combine to improve the overall information about the sample.

It has been discovered that fluorescence-based techniques do not image all of the sample's structure when imaging (108). When attaching the fluorophores to the sample, they are designed to attach to specific proteins; however, they do not always attach to every specific protein. Therefore, images from the fluorescence-based techniques

measure all the fluorophores but not always the whole sample. Performing correlative imaging with fluorescence-based techniques and XUV ptychography will show if reconstructed objects from XUV ptychography can identify these missed regions.

6.1 Sample preparation

The correlative imaging will be performed on a sample of neurons. Neurons are well suited for being imaged by the four techniques, as the fluorescent-based techniques can mark the actin and tubulin, and the neurons do not attenuate the XUV beam too much to prevent imaging. Neurons also have interesting features at sizes at the resolution of the techniques.

When imaging with SIM, STORM, and Lightning, the sample can be prepared the same way to begin with. A group in the School of Biological Sciences at the University of Southampton created the samples. I did not do any preparation involving the development of the embryo or neuron collection, though I observed the whole process. Creating the samples used in this chapter starts with a fifteen-to-eighteen-day-old mouse embryo. The embryo is dissected, and the neurons are extracted and transferred to a nutrient-rich agar medium; this is a liquid, and cells grow on poly-d-lysine coated surfaces in this liquid, called Neurobasal medium, supplemented with B27, a neuronal culture supplement, all from Gibco. In the agar is a silicon nitride membrane for the cells to grow on, and after two weeks the cells are mature. Once the cells are mature they are fixed using formaldehyde; formaldehyde is a compound made up of many long and thin molecules that crosslink the proteins, stopping cellular processes. This stops the cells from developing so that they can be imaged at a specific growth stage.

At this point of preparation, the cell membranes are impermeable, so a low-concentration detergent is used to form holes in the cell membrane to make it permeable. Goat serum is then used as a blocking agent to cover the charged organic molecules within the cell; this suppresses the molecule's charge so that the antibodies will only bind to their specific epitopes. Otherwise, the antibodies would attach to the whole sample.

The next antibodies can be attached since they will now only attach to the actin and tubulin. First, phalloidin conjugated to Alexa-647 is added to the cells; phalloidin is a fungal toxin that binds directly to the cell and is very specific in binding to actin.

The phalloidin is conjugated to Alexa-647 as Alexa-647 is excited by a wavelength of 647 nm, which is what will be imaged. To attach to tubulin, monocloncal rabbit anti-tubulin clone 5-1-2 is first added as the primary, the primary being the first antibody that is bound, and this binds to the tubulin. Then goat anti rabbit H&L IgG conjugated to Alexa-488 is the second antibody used, and is referred to as the secondary, and will attach to the primary. Alexa-488 is excited by a wavelength of 488 nm, which is what will be imaged. This causes linkage error, which is the error incurred by imaging the fluorophore and not the object, where the fluorophore is offset from the object by the size of the link between the fluorophore and the object. Each of these antibodies is 10-15 nm in size (109), so when imaging with these fluorophores there is a 20-30 nm linkage error on each side of the cell's components; therefore, the total linkage error is 40-60 nm.

After this preparation, the sample consists of neurons on a silicon nitride membrane that have been fixed and have the fluorophores attached to the epitopes actin and tubulin. The silicon nitride membrane the neurons were grown on does not affect the fluorescence-based imaging as the laser does not propagate through the silicon nitride, since the neurons are closer to the laser.

6.2 Resolution of Techniques

When calculating the resolution of the four techniques, the resolution stated is from the methods used by the communities that use their respective imaging techniques. Fourier correlations were not possible with the fluorescence-based techniques because the fluorophores become bleached when imaging and a second image would be worse than the first. This means the resolution for the fluorescence-based techniques was based on the components of the one image and it could not analysed if the components were artefacts of that image or actual components of the object. If a Fourier correlation had been used, it would have been possible to identify if the image from the fluorescence-based techniques was accurate at all spatial frequencies. The smallest full-width half-maximum measurable would be the object's and probe's convolution. The resolution, up to the maximum possible value, is determined by the smallest feature in the sample. When determining the resolution of STORM, the accuracy of the

central position of the fluorophore is used. The error of the central position of the fluorophore is the full-width half-maximum of the amplitude spectrum of a fluorophore. A Gaussian curve applied to the full-width half-maximum would be able to perfectly find the central position; however, noise prevents accurately calculating the position of the Gaussian curve and, therefore, the central position of the fluorophore.

6.3 Structured Illumination Microscopy

SIM was previously discussed in chapter 2, and this section will explain how to implement SIM for imaging. A few system optimisations are required to image with SIM: the solution in which the sample is suspended, the refractive index of the immersion oil, and the correction on the objective correction collar. The solution in which the sample is suspended is required to match the NA of the glass slip that contains the sample for the best imaging. Typically, when imaging with SIM on the system at the University of Southampton, glycerol is used as the solution in which the sample is suspended, as it has a refractive index of 1.46, which closely matches the refractive index of the glass that the sample is on, of around 1.5. However, glycerol would cause polymerisation, and the result of polymerisation could be imaged with XUV ptychography. Phosphate Buffer Solution (PBS) was therefore used instead, as this solution was not destructive to the sample, though PBS's refractive index of 1.335 does not match the refractive index of the glass. Other fluids were not used due to the logistical constraints of aligning beam time and sample preparation time with other time constraints. This was a limiting factor for this attempt at imaging with SIM.

Immersion oil is used to remove air between the objective and glass slip, and the objective correction collar is used to adjust the refractive index of the objective. To optimise the immersion oil refractive index and objective collar correction requires imaging with SIM. Three immersion oils with refractive indices 1.5, 1.51, and 1.52 were tested, with the highest-quality images being from the immersion oil with a refractive index of 1.51. Then, multiple images were taken while varying the objective collar by adding a refractive index correction of 0.013 to 0.019. The highest-quality images from these tests were acquired when the correction collar was set to 0.017, giving a total refractive index of 1.517.

Images were then collected at focuses for seven equally spaced heights over a range of 0.6 μm to be able to focus on the sample, where manual refocusing was not required between each image. Unfortunately, the optical transfer function used in SIM reconstruction was designed for a refractive index of 1.51, limiting the quality of the reconstruction. This is the first challenge of correlative imaging between the four techniques; imaging with SIM was possible, but the images are not of the highest resolution that SIM can produce.

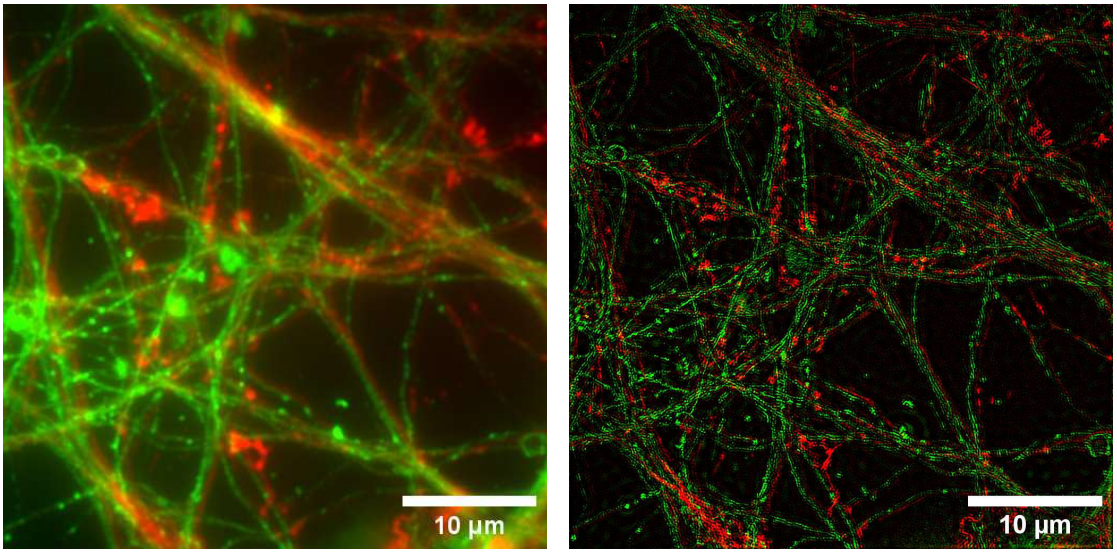

(A) (B)

FIGURE 6.1: Comparison of raw data collected for SIM (A), and the reconstructed image of the mouse neurons (B), with tubulin stained with Alexa-488 (green) and actin stained with Alexa-647 (red).

These images were taken by myself after being given instructions on how to use the SIM system from Dr Mark Willett. From figure 6.1 it can be seen that the use of SIM improves the raw data collected. Though the sample has not been optimised for the SIM imaging, it has still produced a super-resolution image. The tool called SIMCheck was developed by Ball *et al.* in 2015 (110). I then used this tool for the following analysis to calculate the resolution and quality of the SIM images in figure 6.1. The resolution is defined by the edge of second-order information; quality is determined by high levels of modulated contrast-to-noise, and a low rate of change in the intensities through different z-heights for the three moiré patterns.

When analysing regions of super-resolution the modulation contrast-to-noise ratio is used to measure the quality. The modulation contrast-to-noise ratio is the ratio of the

modulation transfer function and the noise power spectrum, where the modulation transfer function is a measure of the quality of the contrast. Regions of higher modulation contrast-to-noise ratio correlate to a region of higher quality.

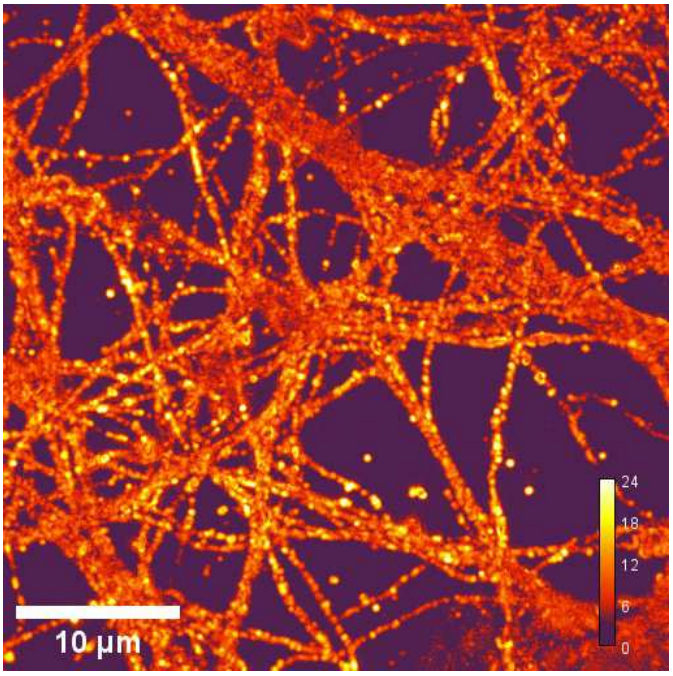

FIGURE 6.2: Heat map of modulation contrast-to-noise ratio for the reconstructed image (B) from figure 6.1.

From figure 6.2, it is shown that the reconstructed image has high levels of modulation contrast-to-noise, resulting in a high-quality reconstruction. The regions of low modulation contrast-to-noise are where there were no fluorophores.

Another check for the reconstruction quality is the moiré patterns' angles. This check is to make sure the moiré patterns' angles are calibrated well, and do not change when imaging at different z-heights. When imaging with SIM, multiple images are taken at different z-height to find where the image is in focus. To find if the moiré patterns' angles have been calibrated correctly, the rate in change of mean intensity through the different z-heights should be similar for the three moiré patterns' angles. The three moiré patterns' angles can be found by the three regions of similar intensity.

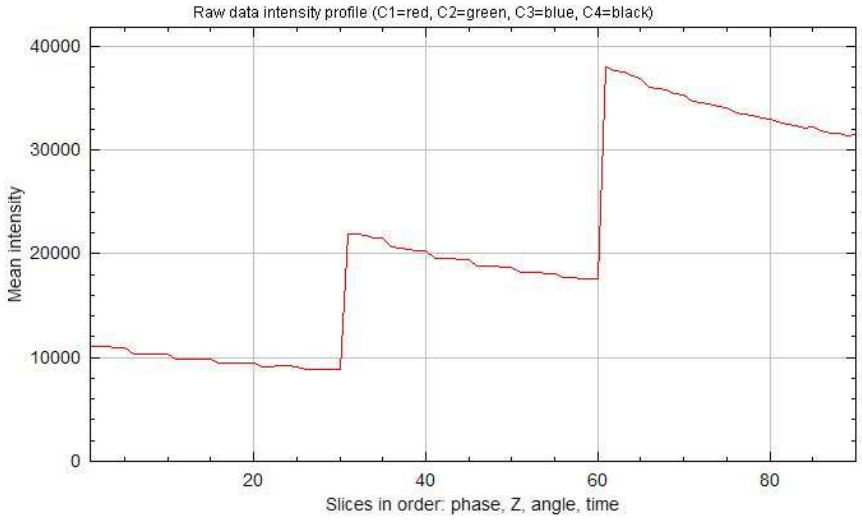

FIGURE 6.3: The mean intensity of each data slice taken used in the reconstruction of the image (B) in figure 6.1

From figure 6.3, the three angles of the moiré patterns can be seen at scans 1-30, 31-60, and 61-90. The rate of change in intensity through different z-heights for the three moiré patterns' angles are similar, and therefore, the system's calibration can be considered successful. If the rate in change of mean intensity through the different z-heights for the three angles of the moiré patterns were not nearly equal, the system would have to be recalibrated. The data are ordered in the axis by their phase, Z, angle, and then time. The data are first ordered by their phase of the illumination pattern, then by the Z-height in which those data were taken, then the angle of the illumination pattern, and then finally by the time the data were taken (110).

To quantify the resolution of the image reconstructed with SIM, the Fourier transform of the reconstructed object is used. When performing a Fourier transform on SIM data a 'flower' pattern emerges, and the edge of the outer 'petals' denotes the maximum of the second-order components (110). The second-order information is higher frequency information gained from the moiré patterns.

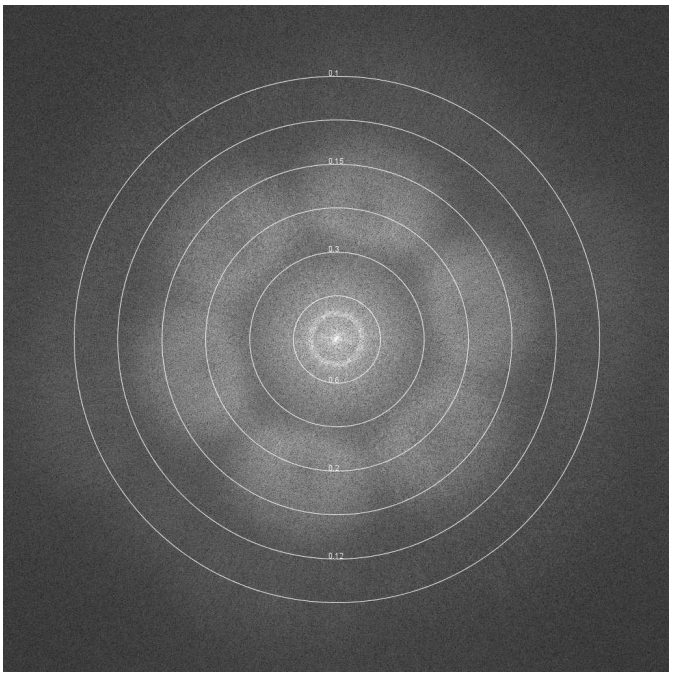

FIGURE 6.4: The Fourier transforms of the reconstructed image (B) from figure 6.1, with concentric rings denoting the spatial frequency in mm.

From figure 6.4, a 'resolution' of 130 nm can be measured as defined by the software, as this is the edge of the second-order information. To find the maximum possible resolution of this system, the Rayleigh criterion is used; the Rayleigh criterion is defined by:

$$d = \frac{0.61\lambda}{NA} \tag{6.1}$$

where λ is the wavelength of light, and NA is the numerical aperture defined by (2.1). Where SIM uses second-order information, half of d is the maximum resolution, leading to a maximum resolution of this system of 120 nm, using a wavelength for 488 nm and an NA of 0.125. Therefore, while not optimal, the image (B) in figure 6.1 is not far from the best image achievable.

6.4 Lightning

Lightning is the Leica-specific form of deconvolution, which is a development of confocal imaging discussed in Chapter 2. This chapter will explain the implementation of

Lightning for imaging. Restricting the size of the pinhole used in confocal microscopy during the scanning process of the sample results in a sharper PSF (111). Deconvolution can be used to further sharpen the image; in normal deconvolution, the regularisation is based on the Richardson-lucy procedure(112). Lightning uses an improved form of deconvolution called adaptive deconvolution that uses local image properties to adapt the deconvolution approach (113).

Lightning is the simplest to use of the three fluorescent-based techniques here. While Lightning can be performed with the sample in any solution as the reconstruction can account for this, one close to the glass's refractive index will minimise the refractive index mismatch. It is possible to use the confocal microscope of the system to image the entire sample initially, then a region of interest can be selected and Lightning performed.

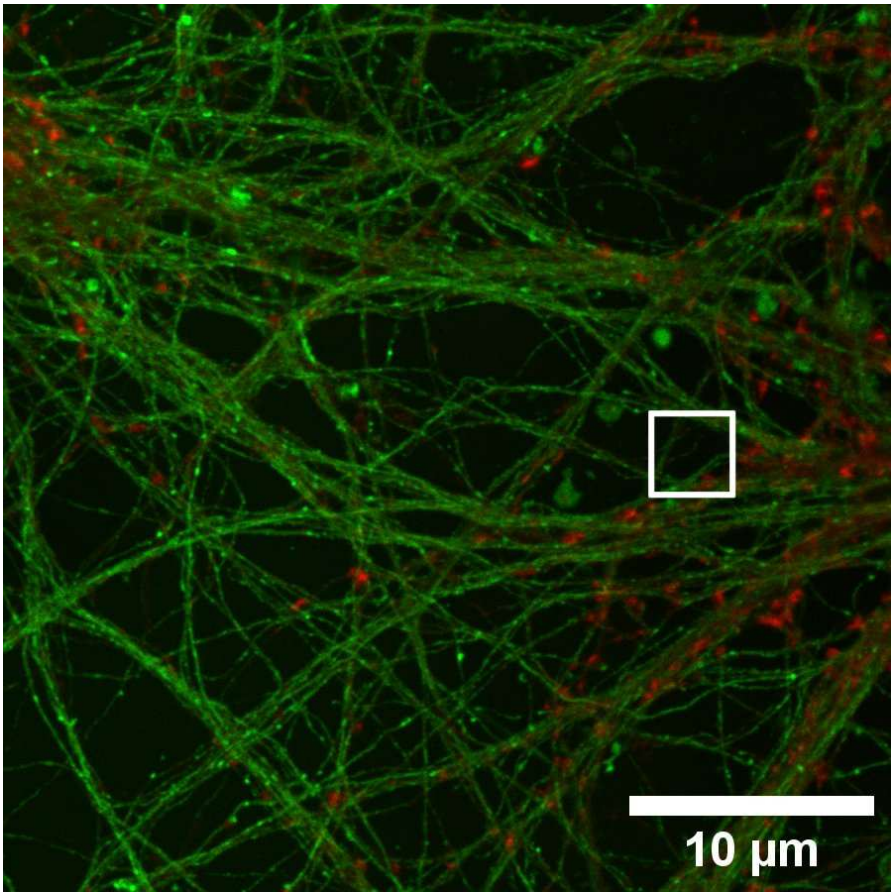

FIGURE 6.5: The deconvolved image of mouse neurons (B), with tubulin stained with Alexa-488 (green) and actin stained with Alexa-647 (red). The white square indicates the area used for figure 6.6.

Figure 6.5 shows the deconvolved image reconstructed from the Lightning imaging

technique. When determining the 'resolution' of an image reconstructed by Lightning as defined by the Laica software, the full-width half-maximum of the smallest feature is typically used. First, the smallest feature needs to be identified.

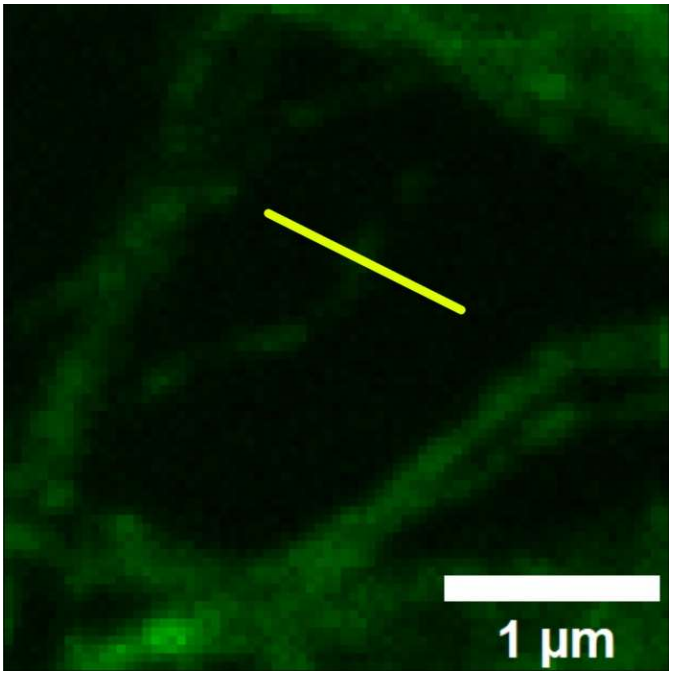

FIGURE 6.6: A zoomed-in region of figure 6.5, a deconvolved image of mouse neurons (B), with tubulin stained with Alexa-488 (green) and actin stained with Alexa-647 (red). The yellow line indicates the cross-section used for figure 6.7.

Figure 6.6 shows a zoomed-in region of figure 6.5 where a small feature has been identified, by analysing the full-width half-maximum of many features. From here, the cross-section is taken to calculate the resolution.

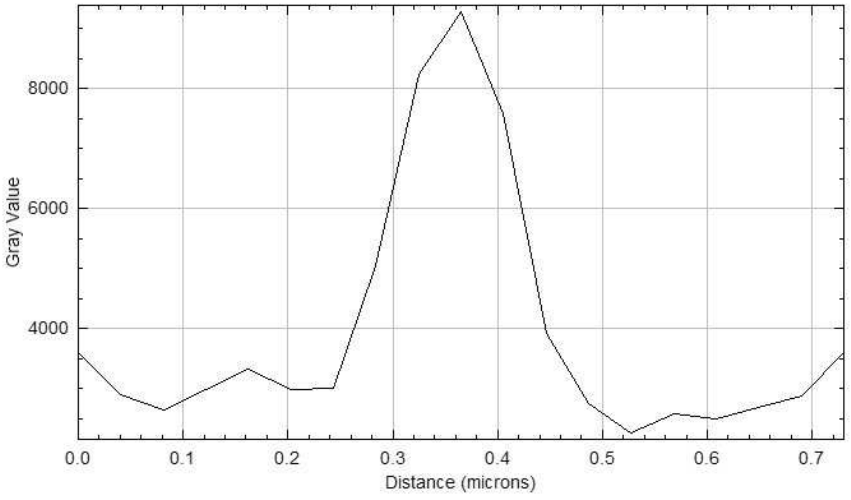

FIGURE 6.7: The full-width half-maximum of the smallest feature from figure 6.6.

From figure 6.7, the full-width half-maximum is calculated to be 130 nm using the fit function in MATLAB using a fit type of 'gauss2' (114). Leica states that Lightning can reach resolutions of 120 nm (113), so again, this is not the best the technique can reach; however, this sample was not optimised for Lightning and is a good image given the limitations.

6.5 STORM

STORM was previously discussed in chapter 2, and this section will explain how to implement STORM for imaging. When performing STORM a buffer is required, and is used to keep the fluorophores in the triplet state for longer. The buffer consists of two parts: the reducing agent, and the oxygen scavengers. STORM necessitates inducing the electrons of the fluorophores into a triplet state to stop their fluorescence, where the triplet state is a long-lived dark state. Electrons have a low probability of entering the triplet state instead of the singlet state when excited; the reducing agent can make the electron enter the triplet state through radical anion states (115). This increases the time in which the fluorophore is in the dark state. To maintain the radical anion states, the removal of oxygen is required. The oxygen scavengers are therefore used to minimise oxygen concentration when performing STORM to extend the duration of the triplet state (116).

With the powers of the lasers and the time involved in performing STORM, the region of the sample being imaged will typically become photobleached. This is an issue that can affect the repeatability. STORM was not possible on the system at the University of Southampton, however, and was therefore performed with a different sample, made by the same group that made the previous sample with the same method, on a system at Rutherford Appleton Laboratories.

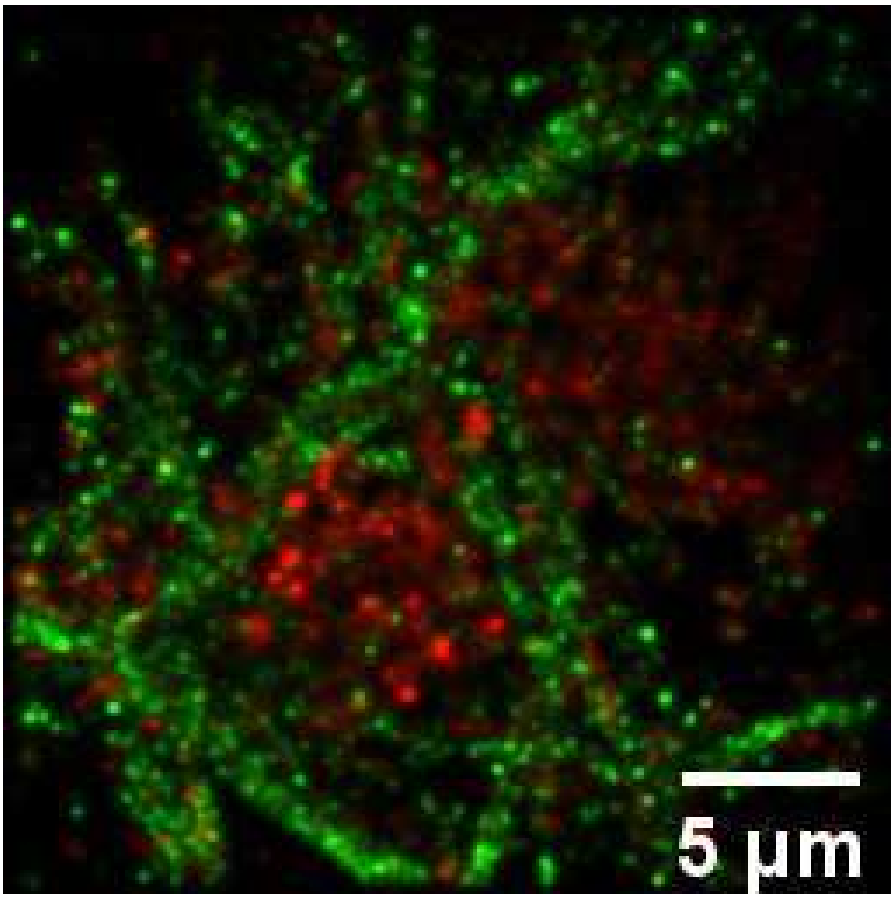

FIGURE 6.8: The STORM image of mouse neurons (B), with tubulin stained with Alexa-488 (green) and actin stained with Alexa-647 (red).

This image was taken by Dr Charles Pooley and myself. Figure 6.8 shows STORM's ability to resolve individual fluorophores with a high signal-to-noise ratio. To find the resolution of figure 6.8, the cross-seciton of an imaged fluorophore can be used to calculate the PSF of the fluorophore. STORM's resolution is defined by the accuracy of the central position of the PSF.

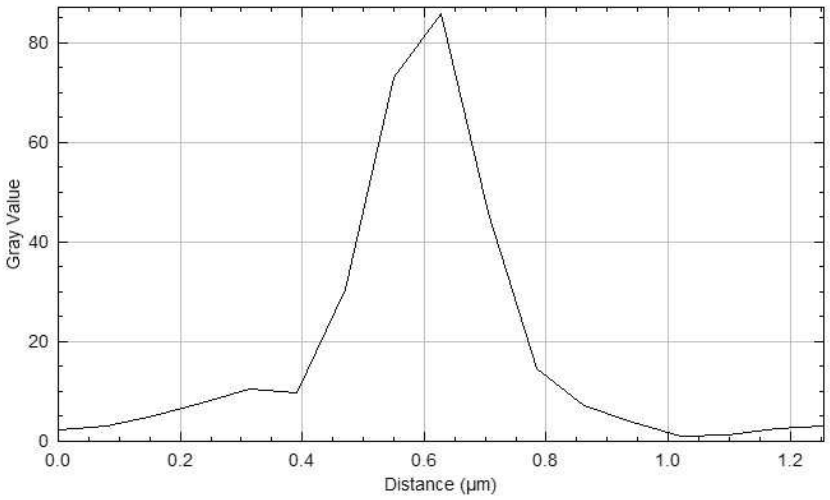

FIGURE 6.9: The full-with half-maximum of the smallest feature in figure 6.8.

Figure 6.9 shows how a resolution of 50 nm can be recovered, where this is the range in which the centre of the PSF is located. This is not ideal compared to the maximum resolution of STORM being around 20 nm. This highlights the difficulty of imaging with STORM where careful optimisation is required to reconstruct high-quality images.

6.6 Comparison

When attempting this correlative imaging, certain issues arose preventing a true comparison of the techniques. These issues were the refractive mismatch incurred from the solution the sample was submerged in, incorrect OTF leading to sub-optimal reconstructions from SIM, the STORM laser not working, and damage incurred to the membrane during transportation. Only the combination of SIM and Lightning required the sample in the same conditions for maximum resolution when imaging; therefore, three different conditions are required to do correlative imaging with neurons. These conditions can be changed between imaging techniques and are not an intrinsic issue of correlative imaging.

Imaging the same region of the sample was prevented by technical and physical limitations. The technical limitations for imaging the same region were with SIM and STORM, where finding the same regions would have caused much photobleaching, thus reducing the resolution of future imaging. Lightning also causes photobleaching, but using a confocal microscope to map the whole sample minimises this effect.

The physical limitation was that the sample is fragile and became damaged between the four imaging techniques, though a different region with similar structures was imaged. The optimal solution to image the sample for SIM and Lightning would leave the sample marked, so increased refractive mismatch had to be endured to avoid this. If the samples were marked there would be polymerisation and this would be imaged with XUV ptychography. The STORM buffer is toxic to the sample if left for a prolonged time, damaging the sample, which would have been a factor when imaging with XUV ptychography. Despite these factors, it was still possible to image similar regions with the four techniques.

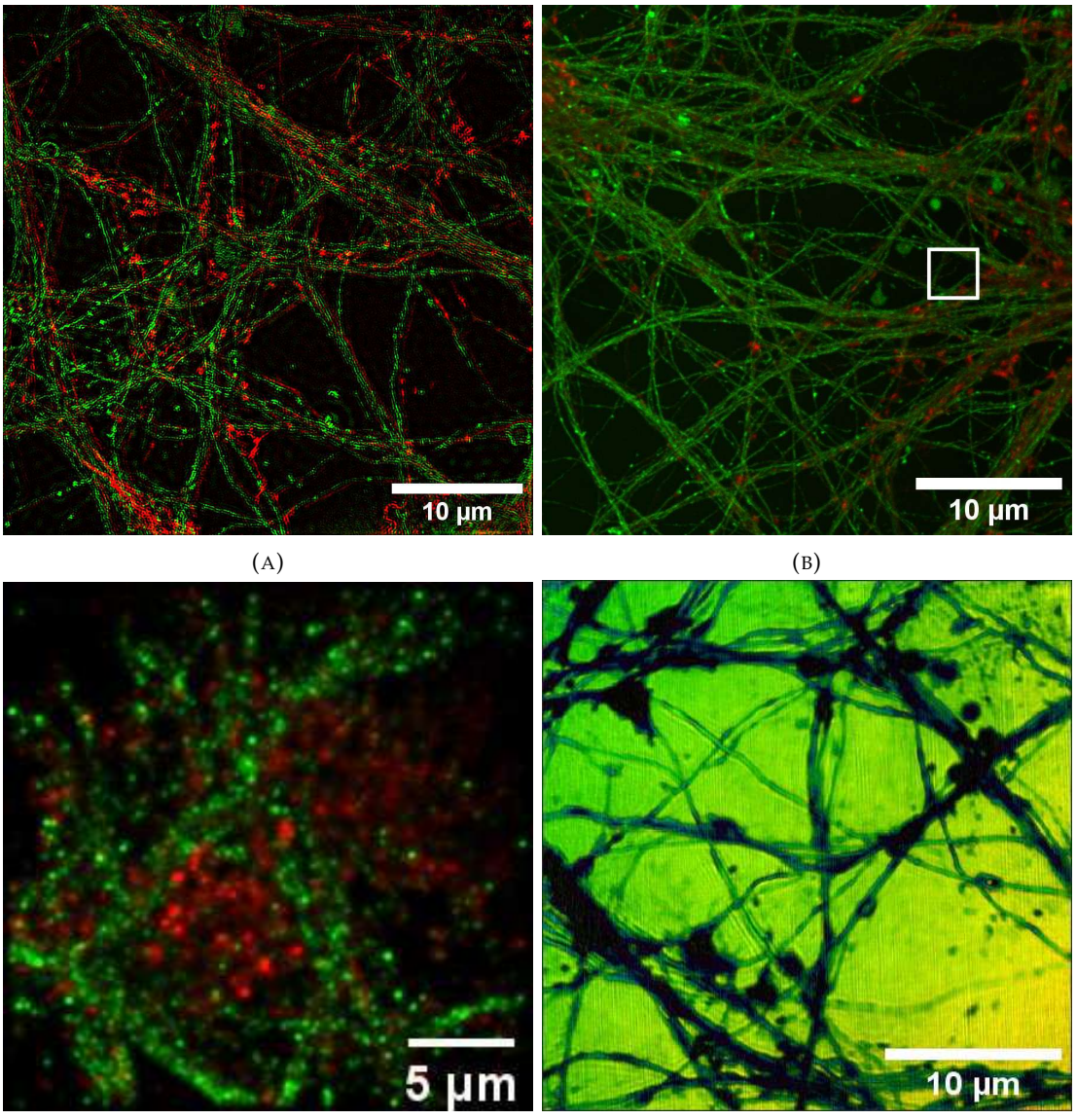

(A) (B)

(C) (D)

FIGURE 6.10: A comparison of images from the four techniques: (A) is the reconstructed SIM object from figure 6.1, (B) is the reconstructed Lightning object from figure 6.5, (C) is the reconstructed STORM object from figure 2.26, (D) is the reconstructed object of mouse neurons using a double slit aperture (5x1 μm slits spaced 4 μm from centres).

All of these images were taken by myself, with collaboration with Dr Charles Pooley for (C). There is only one image of each technique in the comparison due to the difficulties of attempting to image the same sample with four different techniques. From figure 6.10, it is shown that STORM had the highest resolution, but all of the fluorescent-based imaging techniques could discern the actin from the tubulin. XUV ptychography can not differentiate between tubulin and actin as their refractive indices are too similar to

use the retrieved phase to identify them. XUV ptychography of neurons had a resolution of 80 nm (117); however, the smallest features suffer from the low y-axis resolution of the double slit aperture, and XUV ptychography cannot differentiate the tubulin and actin from each other.

6.7 Summary

Throughout this chapter, the techniques of SIM, Lightning, and STORM have been discussed in further detail, giving a greater understanding of what is required to perform the three techniques. The individual methods used for calculating the resolution of these techniques have also been discussed, showing that SIM and Lightning nearly achieved maximum resolution, and STORM achieved less than half its maximum resolution.

For this correlative imaging to work, additional steps and preparation would need to be taken. When discussing with the head of microscopy for the University of Southampton Biology Sciences it was suggested that an indexable stage insert could be used to position the sample during SIM and STORM such that the same region would be imaged as with Lightning and XUV ptychography. This positioning could then be refined with fiducial markers, such as gold nanoparticles, facilitating clarification of the region of the imaged sample.

Another optical transfer function for SIM would have to be created for the use of Phosphate Buffer Solution (PBS) to give optimal reconstructions. A new microscope is currently being delivered to the University of Southampton that would allow for the future use of STORM. This is important as the samples are fragile, and transporting them between faraway locations would be to the detriment of the samples' structural integrity, as even transporting them between buildings on the same campus caused damage.

Different methods of calculating resolution were discussed; if a Fourier correlation were used, it would have been possible to identify if all spatial frequencies from the image of fluorescence-based techniques were accurately represented. This lack of correlation could have led to inflated resolutions where spatial frequency components may not be accurately represented for the object imaged.

If the resolution of the actin and tubulin positions does not need to be less than 120 nm, then Lightning and XUV ptychography would be the simplest method of correlative imaging. Using the confocal microscope to image the entire sample and then choosing multiple regions to perform Lightning with, XUV ptychography can find the same regions with a transmission intensity scan; however, if less than 120 nm resolution is desired for the actin and tubulin positions, then SIM or STORM would need to be used.

Chapter 7

XUV damage

Damage caused to the sample is a major problem with hard X-ray techniques, as this damage can result in the small features of the sample being lost, limiting the resolution and repeatability of the experiment. In this chapter, an investigation into the limits of XUV damage thresholds is explored, with comparisons between a 42 eV beam from XUV ptychography and a 7.3 keV beam from a synchrotron. 7.3 keV was used as this is above the K-edge of iron of 7.11 keV, and the beam was tuned to detect iron in a previous experiment. During this experiment is when the damage to the sample was observed. First, the dose of radiation that a sample experiences is defined to compare the amount of radiation each technique deposits. Then, the mechanism behind the believed cause of damage from hard X-ray techniques is discussed, and why XUV imaging is unaffected. Finally, an attempt will be made to quantify the damage threshold of XUV ptychography.

7.1 Radiation dose unit: Gray

Grays (Gy) are the SI unit used to quantify the radiation dose an object is exposed to, where a higher amount of Grays means more radiation is being deposited on the sample. The radiation dose in Grays is defined as:

$$D = \frac{E}{m} \tag{7.1}$$

where E is the energy of the radiation absorbed, and m is the mass of the object being dosed by the radiation. Grays can therefore be expressed as $J \cdot kg^{-1}$ or in SI units as $m^2 \cdot s^{-2}$. The energy of radiation absorbed when performing ptychography can be defined by a formula derived from Howells *et al.* (118) and used by previous members of my group Pete Baksh *et al.*(119) is:

$$D = \frac{N_0 h\nu}{L_a n S} \tag{7.2}$$

where N_0 is the number of photons incident on the sample in the area S, $h\nu$ is the photon energy, L_a is the attenuation length, and n is the average density of the sample.

For a 10 μm circular aperture using 251 scans with a scan area of 40 μm^2, the total photons would be $9.0{\cdot}10^9$ with an energy of 42.5 eV, the attenuation length is 0.03 μm (1), and the density of brain white/grey matter is 1060 kg/m^3 (120), the Grays would $4.8{\cdot}10^6$.

7.2 Damage mechanism

It was found through previous research from Pete Baksh *et al.* in 2017 (119) that high-energy photon, 7.3 keV, imaging techniques cause damage to the sample, and low-energy photon, 42 eV, imaging techniques do not from a single data set. The damage caused is where the smallest features of the sample are destroyed and, therefore, are not there when imaged. The radiation dose of the 7.3 keV technique deposited $4{\cdot}10^5$ Gy on the sample, compared to the $4.4{\cdot}10^7$ Gy of the 42 eV technique (119). This implied that the amount of radiation deposited did not drive the damage caused by a technique, but instead the photon's energy caused the damage (119).

High and low energy photons are both ionising radiation for carbon atoms, a common element in biological samples. In 1972 Kanaya and Okayama introduced the following equation to calculate the electron penetration depth into a solid material (121):

$$R = \frac{0.0276 \times A}{Z^{0.889} \times \rho} \times E^{1.67} \tag{7.3}$$

where A is the atomic weight of the material, Z is the atomic number of the material, ρ is the density of the material, and E is the incident electron energy. A photon energy of 42 eV has enough energy to interact with the first two outer shells of carbon; therefore, the photoelectrons produced are of low energy and the damage caused will be minimal as the penetration depth is around 5 nm (122). Whereas, 7.3eV greatly surpasses the inner-shell's ionisation energy of 283 eV, allowing the 7.3 keV photon to eject the inner-shell's electron. When the inner-shell electron is ejected, an electron from a higher energy level may fill the vacancy and release energy that is usually transferred to a valence electron, causing the valence electron also to be ejected; this is the Auger effect (123). Due to the high energy of the 7.3 keV photons, the primary and secondary ejected photoelectrons have a penetration depth beyond 100 nm (122), and this penetration depth also leads to greater radiation damage of the sample.

Where the synchrotron radiation pulse length was on the scale of nanoseconds, and the XUV ptychography was on the scale of femtoseconds, the damage may also be related to the temporal nature of the radiation. The short pulse duration of the XUV ptychography radiation may be too short for the neuron's atoms to respond, preventing the damage from being incurred; however, this is speculation.

7.3 Attempted XUV damage of Neurons

Even though high-energy photons cause the mechanism related to damage, ionisation is still being caused by 42 eV photons. To investigate the damage threshold when imaging with XUV ptychography, two images of reconstructed objects are required with an attempt at damage in between. The object being imaged was a neuron sample; this sample was prepared by the same group in the Biological Sciences at the University of Southampton that prepared the samples in Chapter 5. Creating the sample used in this chapter started with a fifteen-to-eighteen-day-old mouse embryo. The embryo was dissected, and the neurons were extracted and transferred to a nutrient-rich agar medium.

First, a 40 μm by 40 μm region of neurons was imaged using a circular aperture (10 μm diameter) over 197 scan positions with a step size of 3 μm over three exposures for a total exposure time of 11.1 s; this deposited $9.4{\cdot}10^5$ Gy over the entire sample. The

object was then reconstructed to clarify that the region imaged had small features so that if the sample were to be damaged in the next step, the small features would be removed via the damage incurred. Next, the imaging routine was used to deposit an increased dose of radiation on a scan area of 10 μm by 10 μm over 197 scan positions with a step size of 0.75 μm over three exposures for a total exposure time of 33.3 s; this deposited $4.5{\cdot}10^7$ Gy over the reduce scan area, this dose was forty-eight times higher than the previous imaging deposited. The forty-eight times higher radiation dose was chosen for multiple reasons: if tomography were to be performed in the future, this would require imaging over fifty angles, and if the sample were damaged at forty-eight, then tomography would not be possible. Another amount of Grays, such as forty-nine times the normal dosage, was not chosen because a number in the region of fifty was needed and forty-eight times worked well with our data acquisition methods. When imaging with ptychography a sample would not be imaged a thousand times and forty-eight times was a reasonable number of times a single sample would be imaged. If the sample were to be damaged at a thousand times this would not give much insight into the damage threshold of XUV ptychography on neurons, as this would only give the information damage happens somewhere between two and a thousand times. COVID prevented further investigation into the damage threshold beyond forty-eight times. Finally, the same 40 μm by 40 μm region of neurons was imaged again using a circular aperture (10 μm diameter) over 197 scan positions with a step size of 3 μm over three exposures for a total exposure time of 11.1 s; this deposited $9.4{\cdot}10^5$ Gy over the entire sample. Finally, the object was reconstructed to investigate whether the small features were damaged.

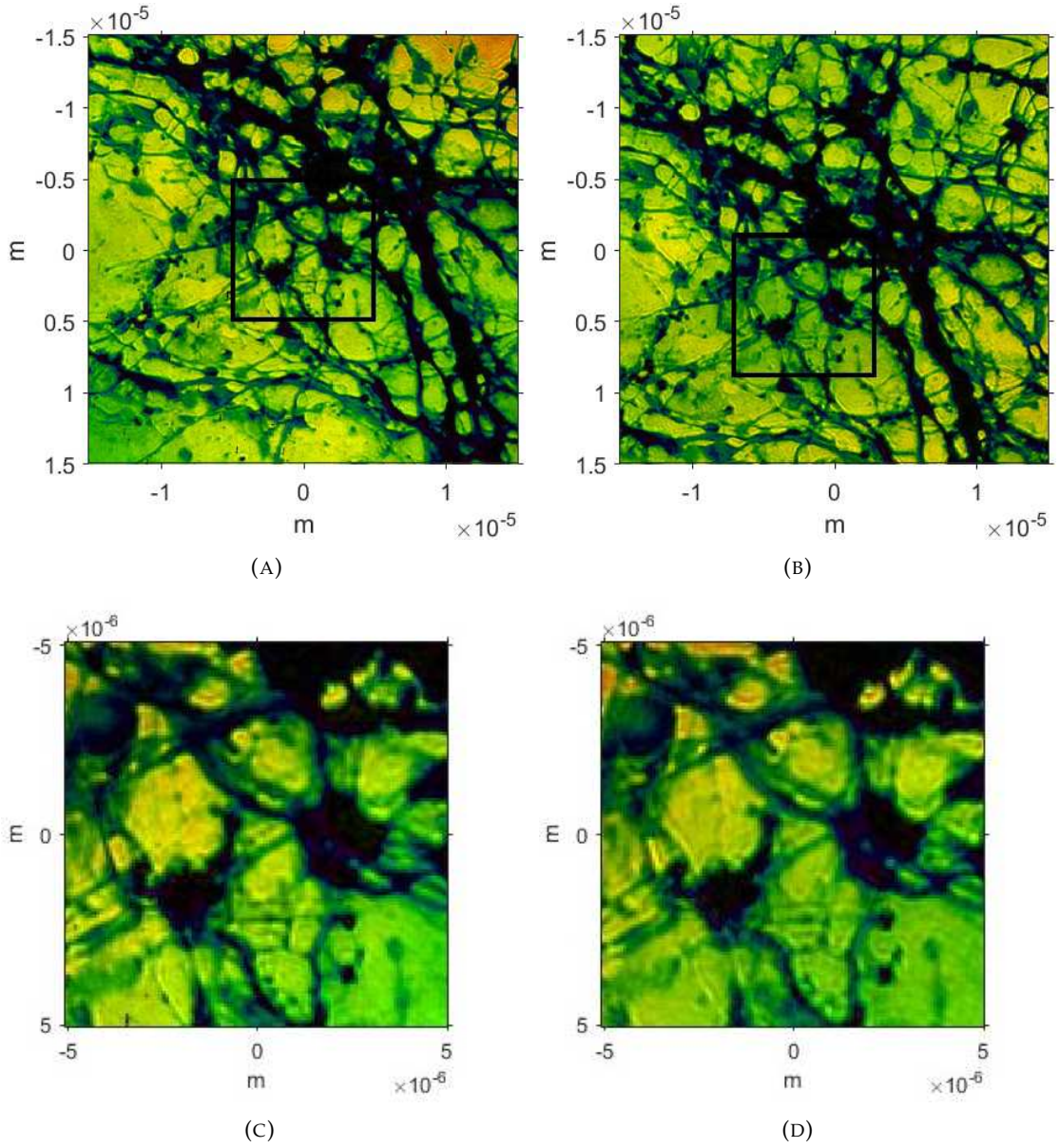

FIGURE 7.1: Reconstructed objects of a 40 μm by 40 μm region using a circular aperture (10 μm diameter) with 197 scan positions with a step size of 3 μm, (A) reconstructed object of the sample before attempted damage, (B) reconstructed object of the sample after attempted damage, and region of attempted damage (black box). (C) and (D) show the regions in the black boxes from (A) and (B) respectively.

From figure 7.1, there is no visible damage in the region where the increased dose of $4.5{\cdot}10^7$ Gy was deposited. To discover if the smallest features have been damaged, an FRC and FLC can be taken to analyse the resolution at higher spatial frequencies, where the removal of small features due to the damage would correspond to a worse correlation at higher resolutions.

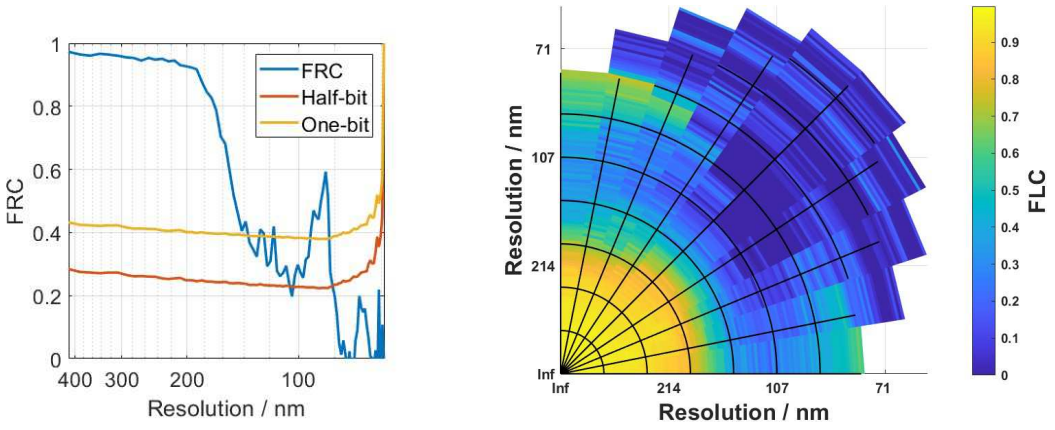

(A) (B)

FIGURE 7.2: (A) the FRC of the two reconstructed objects in figure 7.1, and (B) the FLC of the two reconstructed objects in figure 7.1.

From figure 7.2, it is clear that the reconstructed object after the attempted damage still contains the small features and that they have not been damaged as the FRC reaches the resolution at the Nyquist limit of the CCD. Although there is a low correlation between 104 nm and 106 nm, if the sample had been damaged, smaller features would have also been affected. The FLC does show a low resolution at 45°; however, the resolution is still high along the x-axis and y-axis, which would also be low if damage had occurred. This shows that XUV radiation, when performing ptychography, the sample is not damaged within a reasonable amount of imaging, forty-eight times higher than required for a single image of the reconstructed object.

7.4 Summary

This chapter discussed the amount of radiation absorbed by hard X-rays and XUV beams, with XUV being found to deposit more radiation onto the sample. The cause of damage instead is due to the energy of the photons in each technique, where higher energy photons can ionise the inner-shell electron and cause the Auger effect, with the inner-shell electron ejection causing another electron to be ejected. The penetration depth of the hard X-rays is over 100 nm compared to the XUV beam, only causing a penetration depth of 5 nm. Both of these effects cause hard X-rays to cause much more radiation damage than XUV beams.

The damage threshold for XUV imaging on neurons was not found; therefore, radiation damage does not currently need to be addressed. The low levels of ionisation caused by XUV are not enough to damage the sample within a reasonable amount of imaging, where the same region can be imaged fifty times with no discernible damage to the sample.

Chapter 8

Conclusion and Future Work

8.1 Conclusions

8.1.1 What Makes a Good Probe?

Chapter 4 introduced a directional resolution with the FLC, which is a more detailed approach than an FRC. FRC is the average Fourier correlation of all directions, and an FLC is the Fourier correlation of a specific direction. As part of this research, the FLCs of experimental data were calculated for different apertures, and the importance of the probe's angular spread in a direction was linked to the improved Fourier correlation in that direction.

Chapter 4 would not have been possible without the accurate simulation of an XUV ptychography system, as all facets of the system could be changed almost instantaneously. This has led to a greater understanding of the robustness of the reconstructive algorithms when applied to real-life conditions. With the simulation, the lack of importance of flux beyond the flux required to reach the resolution at the Nyquist limit was discovered, and with diminishing returns afterwards.

With the discoveries throughout chapter 4, it was decided that the ring aperture would result in a probe capable of high resolutions of reconstructed objects. This would combine the radial symmetry of the circular aperture to have an equal resolution in all directions, and the double slit aperture, which has a large angular spread. The ring aperture proved to excel with reconstructions, reaching 33 nm resolution, which can

image neurons to greater resolution than currently possible with our XUV ptychography system. This increased resolution will allow samples to be imaged with a higher resolution and allow smaller features that may have not been reconstructed to be reconstructed.

8.1.2 Correlative Imaging

In chapter 5, correlative imaging between SIM, STORM, Lightning, and XUV ptychography was attempted. With non-optimal parameters, SIM and Lightning were nearly able to achieve the maximum expected resolution, both with 130 nm resolution and a maximum resolution of 120 nm. STORM was not possible on the same sample, and a previously taken STORM image had a resolution of 50 nm, far from the maximum resolution STORM can achieve of 20 nm. When using XUV ptychography, the same region could not be imaged, but a resolution of around 100 nm was achieved.

Chapter 5 showed the difficulties of not only correlative imaging with the four techniques, but the difficulty of imaging with SIM and STORM. The solutions to the issues presented by correlative imaging were also discussed. If these issues can not be resolved, then the use of Lightning and XUV ptychography could be used for correlative imaging, which will show the composition and the structure of the neurons. If the issues are resolved, the higher-resolution fluorescence-based technique of STORM could be used.

8.1.3 XUV Damage

This chapter discussed the mechanism believed to cause damage to the sample in high-energy photon techniques, such as 7.3 keV. The high-energy photons cause ionisation of the inner-shell electron, also causing the Auger effect. Low-energy photon techniques of 42eV only ionised the two outer shell electrons, leading to minimal damage. The unit for the radiation deposited on the sample, the Gray, was also discussed; however, the does in Grays was higher for the measurement at 42 eV, showing that dose amount alone is not a suitable parameter to describe damage.

When attempting to damage the sample with XUV ptychography, a region was exposed to a dose fifty times higher than normal. When imaged again, there was no discernible

damage. The damage threshold of XUV ptychography using a photon energy of 42eV was not found; it can, therefore, be assumed that the threshold is far above a reasonable amount that the sample would ever be imaged with and would not limit future experiments, such as tomography, which require many images.

8.2 Future Work

8.2.1 Ring Aperture

With the potential shown by the ring aperture, the fabrication of the aperture and experimental adjustment would be required. Fabrication would only take time as the required material has already been acquired. The mounts for the samples are currently too large to allow the detector to be as close as 1.35 cm from the sample. Imaging at a 1.35 cm sample to detector distance requires no binning; this would cause the imaging to take four times as long. This would total eight hours; the CCD can only currently image for three consecutive hours without breaking.

If this aperture were to be created and the ptychography imaging system improved, higher resolution images could be taken. This will unlock small features within the reconstructed objects lost due to the lower resolution of the circular apertures.

8.2.2 Super Resolution

While initial attempts at super-resolution proved unsuccessful, adjustments to the reconstructive algorithms or the inputted data would allow for increased resolution in both new and old data.

8.2.3 Correlative Imaging

Preparations can be undertaken with a greater understanding of what is required to perform correlative imaging between SIM, STORM, Lightning, and XUV ptychography. An indexable stage and fiducial markers can be used to reliably locate the same region of the sample. An optical transfer function for PBS for SIM and a powerful laser for STORM are required.

It would be possible to image with just Lightning and XUV ptychography to perform correlative imaging. This would allow the identification of actin and tubulin within the neurons on a reconstructed object from XUV ptychography with images from Lightning.

8.2.4 Sample in Water Vapour

I performed work towards imaging a sample at atmosphere, as discussed in chapter 4. This would involve encasing the sample between two membranes with water vapour inside. By 3-D printing a 50 μm thick square that is used to space two membranes apart, it is possible to keep the sample at atmosphere while in the vacuum chamber. This will have the issue of greater beam attenuation, but will allow the sample to be imaged without being exposed to the vacuum and minimising damage. Imaging samples at atmosphere will give a more accurate image of what the neurons are meant to look like before drying or being fixed, as these processes will alter the samples.

References

[1] B.L. Henke, E.M. Gullikson, and J.C. Davis. X-ray interactions: Photoabsorption, scattering, transmission, and reflection at e = 50-30,000 ev, z = 1-92. *Atomic Data and Nuclear Data Tables*, 54:181–342, 7 1993.

[2] A. L'Huillier, D. Descamps, A. Johansson, J. Norin, J. Mauritsson, and C.-G. Wahlstrm. Applications of high-order harmonics. *The European Physical Journal D - Atomic, Molecular and Optical Physics*, 26:91–98, 9 2003.

[3] PA Franken, Alan E Hill, CW el Peters, and Gabriel Weinreich. Generation of optical harmonics. *Physical review letters*, 7(4):118, 1961.

[4] NH Burnett, HA Baldis, MC Richardson, and GD Enright. Harmonic generation in co laser target interaction. *Applied Physics Letters*, 31(3):172–174, 1977.

[5] B. Dromey, S. Kar, C. Bellei, D. C. Carroll, R. J. Clarke, J. S. Green, S. Kneip, K. Markey, S. R. Nagel, P. T. Simpson, L. Willingale, P. McKenna, D. Neely, Z. Najmudin, K. Krushelnick, P. A. Norreys, and M. Zepf. Bright multi-kev harmonic generation from relativistically oscillating plasma surfaces. *Physical Review Letters*, 99:085001, 8 2007.

[6] Zenghu Chang. Enhancing kev high harmonic signals generated by long-wave infrared lasers. *OSA Continuum*, 2(7):2131–2136, 2019.

[7] Michael W Davidson. Pioneers in optics: Zacharias janssen and johannes kepler. *Microscopy Today*, 17(6):44–47, 2009.

[8] Mingshu Liang and Changhuei Yang. Implementation of free-space fourier ptychography with near maximum system numerical aperture. *Optics Express*, 30(12):20321–20332, 2022.

[9] C.D. McGillem and G.R. Cooper. *Continuous and Discrete Signal and System Analysis*. Oxford series in electrical and computer engineering. Oxford University Press, 1991.

[10] Joseph W Goodman. *Introduction to Fourier optics*. Roberts and Company publishers, 2005.

[11] W H Bragg, W L Bragg Apr, By W H Bragg, and Cavendish Professor of Physics. The reflection of x-rays by crystals. *Proceedings of the Royal Society of London. Series A, Containing Papers of a Mathematical and Physical Character*, 88:428–438, 7 1913.

[12] WL Bragg, JJ Thomson, and Herren Friedrich. Mr bragg, diffraction of short electromagnetic waves, etc. 43. In *Proceedings of the Cambridge Philosophical Society: Mathematical and physical sciences*, volume 17, page 43, 1914.

[13] D. Sayre. Some implications of a theorem due to shannon. *Acta Crystallographica*, 5:843–843, 11 1952.

[14] James R Fienup. Reconstruction of an object from the modulus of its fourier transform. *Optics letters*, 3(1):27–29, 1978.

[15] RHT Bates. Fourier phase problems are uniquely solvable in more than one dimension. i: Underlying theory. 1982.

[16] Jianwei Miao, David Sayre, and HN Chapman. Phase retrieval from the magnitude of the fourier transforms of nonperiodic objects. *JOSA A*, 15(6):1662–1669, 1998.

[17] J. C.H. Spence, U. Weierstall, and M. Howells. Coherence and sampling requirements for diffractive imaging. *Ultramicroscopy*, 101:149–152, 11 2004.

[18] James R Fienup. Phase retrieval algorithms: a comparison. *Applied optics*, 21(15):2758–2769, 1982.

[19] JR Fienup and CC Wackerman. Phase-retrieval stagnation problems and solutions. *JOSA A*, 3(11):1897–1907, 1986.

[20] S. Marchesini, H. He, N. Chapman, P. Hau-Riege, A. Noy, R. Howells, U. Weierstall, and H. Spence. X-ray image reconstruction from a diffraction pattern alone. *Physical Review B - Condensed Matter and Materials Physics*, 68, 2003.

[21] W Hoppe. Diffraction in inhomogeneous primary wave fields. 1. principle of phase determination from electron diffraction interference. *Acta Crystallogr. A*, 25:495–501, 1969.

[22] W Hoppe and G Strube. Diffraction in inhomogeneous primary wave fields. 2. optical experiments for phase determination of lattice interferences. *Acta Crystallogr. A*, 25:502–507, 1969.

[23] W Hoppe. Diffraction in inhomogeneous primary wave fields. 3. amplitude and phase determination for nonperiodic objects. *Acta Crystallographica Section a-Crystal Physics Diffraction Theoretical and General Crystallography*, page 508, 1969.

[24] Henry N Chapman. Phase-retrieval x-ray microscopy by wigner-distribution deconvolution. *Ultramicroscopy*, 66(3-4):153–172, 1996.

[25] John M Rodenburg, AC Hurst, Anthony G Cullis, Barry R Dobson, Franz Pfeiffer, Oliver Bunk, Christian David, K Jefimovs, and I Johnson. Hard-x-ray lensless imaging of extended objects. *Physical review letters*, 98(3):034801, 2007.

[26] Matthew D Seaberg, Bosheng Zhang, Dennis F Gardner, Elisabeth R Shanblatt, Margaret M Murnane, Henry C Kapteyn, and Daniel E Adams. Tabletop nanometer extreme ultraviolet imaging in an extended reflection mode using coherent fresnel ptychography. *Optica*, 1(1):39–44, 2014.

[27] John M Rodenburg. Ptychography and related diffractive imaging methods. *Advances in imaging and electron physics*, 150:87–184, 2008.

[28] Zhuoqun Zhang and Andrew M. Maiden. A comparison of ptychographic phase retrieval algorithms. page 30. SPIE-Intl Soc Optical Eng, 3 2019.

[29] Veit Elser. Phase retrieval by iterated projections. *JOSA A*, 20(1):40–55, 2003.

[30] Pierre Thibault, Martin Dierolf, Andreas Menzel, Oliver Bunk, Christian David, and Franz Pfeiffer. High-resolution scanning x-ray diffraction microscopy. *Science*, 321:379–382, 7 2008.

[31] J. M. Rodenburg and H. M.L. Faulkner. A phase retrieval algorithm for shifting illumination. *Applied Physics Letters*, 85:4795–4797, 11 2004.

[32] Andrew M. Maiden and John M. Rodenburg. An improved ptychographical phase retrieval algorithm for diffractive imaging. *Ultramicroscopy*, 109:1256–1262, 9 2009.

[33] Charles Pooley. *Efficient high harmonic generation sources for applications in X-Ray imaging*. PhD thesis, University of Southampton, 2021.

[34] Michal Odstrčil, Andreas Menzel, and Manuel Guizar-Sicairos. Iterative least-squares solver for generalized maximum-likelihood ptychography. *Optics Express*, 26:3108, 2 2018.

[35] Klaus Wakonig, H-C Stadler, Michal Odstrčil, Esther HR Tsai, Ana Diaz, Mirko Holler, Ivan Usov, Jörg Raabe, Andreas Menzel, and Manuel Guizar-Sicairos. Ptychoshelves, a versatile high-level framework for high-performance analysis of ptychographic data. *Journal of applied crystallography*, 53(2):574–586, 2020.

[36] Harwell Campus, Stephen Kill Spindloe, and Monty Rakusen. Clf annual report 2016-2017.

[37] Michael Tanksalvala, Dennis F Gardner, Giulia F Mancini, Elisabeth R Shanblatt, Xiaoshi Zhang, Benjamin R Galloway, Christina R Porter, Robert Karl, Charles Bevis, Margaret M Murnane, et al. Coherent ptychographic imaging microscope with 17.5 nm spatial resolution employing 13.5 nm high harmonic light. *Microscopy and Microanalysis*, 22(S3):88–89, 2016.

[38] Dennis Gabor. A new microscopic principle. 1948.

[39] Guanhai Li, Brendan P Clarke, Jin-Kyu So, Kevin F MacDonald, and Nikolay I Zheludev. Holographic free-electron light source. *Nature communications*, 7(1):1–6, 2016.

[40] Simonetta Grilli, Pietro Ferraro, Sergio De Nicola, A Finizio, G Pierattini, and R Meucci. Whole optical wavefields reconstruction by digital holography. *Optics Express*, 9(6):294–302, 2001.

[41] Toshiaki Tanigaki, Tetsuya Akashi, Takaho Yoshida, Ken Harada, Kazuo Ishizuka, Masahiko Ichimura, Kazutaka Mitsuishi, Yasuhide Tomioka, Xiuzhen Yu, Daisuke Shindo, et al. Electron holography observation of individual ferrimagnetic lattice planes. *Nature*, 631(8021):521–525, 2024.

[42] Xiangyu Ou, Xian Qin, Bolong Huang, Jie Zan, Qinxia Wu, Zhongzhu Hong, Lili Xie, Hongyu Bian, Zhigao Yi, Xiaofeng Chen, et al. High-resolution x-ray luminescence extension imaging. *Nature*, 590(7846):410–415, 2021.

[43] S. W. Wilkins, T. E. Gureyev, D. Gao, A. Pogany, and A. W. Stevenson. Phase-contrast imaging using polychromatic hard x-rays. *Nature*, 384:335–338, 11 1996.

[44] Franz Pfeiffer, Timm Weitkamp, Oliver Bunk, and Christian David. Phase retrieval and differential phase-contrast imaging with low-brilliance x-ray sources. *Nature Physics*, 2:258–261, 2006.

[45] Christoph Rau, Ulrich Wagner, Zoran Pešić, and Alberto De Fanis. Coherent imaging at the diamond beamline i13. *physica status solidi (a)*, 208(11):2522–2525, 2011.

[46] I M Ternov. Synchrotron radiation. *Physics-Uspekhi*, 38:409–434, 4 1995.

[47] Albert V Baez. Fresnel zone plate for optical image formation using extreme ultraviolet and soft x radiation. *JOSA*, 51(4):405–412, 1961.

[48] Zhiyu Zhang, Chengli Guo, Ruoqiu Wang, Haixiang Hu, Xiaoguang Zhou, Tao Liu, Donglin Xue, Xing Zhang, Feng Zhang, and Xuejun Zhang. Hybrid-level fresnel zone plate for diffraction efficiency enhancement. *Optics Express*, 25(26):33676–33687, 2017.

[49] B. Niemann, D. Rudolph, and G. Schmahl. X-ray microscopy with synchrotron radiation. *Applied Optics*, 15:1883, 8 1976.

[50] Weilun Chao, Bruce D. Harteneck, J. Alexander Liddle, Erik H. Anderson, and David T. Attwood. Soft x-ray microscopy at a spatial resolution better than 15 nm. *Nature*, 435:1210–1213, 6 2005.

[51] John H Kinney and Monte C Nichols. X-ray tomographic microscopy (xtm) using synchrotron radiation. *Annual review of materials science*, 22(1):121–152, 1992.

[52] P. R. Shearing, R. S. Bradley, J. Gelb, S. N. Lee, A. Atkinson, P. J. Withers, and N. P. Brandon. Using synchrotron x-ray nano-CT to characterize SOFC electrode microstructures in three-dimensions at operating temperature. *Electrochemical and Solid-State Letters*, 14(10):B117, 2011.

[53] Zhirong Huang and Kwang-Je Kim. Review of x-ray free-electron laser theory. *Physical Review Special Topics-Accelerators and Beams*, 10(3):034801, 2007.

[54] Tetsuya Ishikawa, Hideki Aoyagi, Takao Asaka, Yoshihiro Asano, Noriyoshi Azumi, Teruhiko Bizen, Hiroyasu Ego, Kenji Fukami, Toru Fukui, Yukito Furukawa, Shunji Goto, Hirofumi Hanaki, Toru Hara, Teruaki Hasegawa, Takaki Hatsui, Atsushi Higashiya, Toko Hirono, Naoyasu Hosoda, Miho Ishii, Takahiro Inagaki, Yuichi Inubushi, Toshiro Itoga, Yasumasa Joti, Masahiro Kago, Takashi Kameshima, Hiroaki Kimura, Yoichi Kirihara, Akio Kiyomichi, Toshiaki Kobayashi, Chikara Kondo, Togo Kudo, Hirokazu Maesaka, Xavier M. Maréchal, Takemasa Masuda, Shinichi Matsubara, Takahiro Matsumoto, Tomohiro Matsushita, Sakuo Matsui, Mitsuru Nagasono, Nobuteru Nariyama, Haruhiko Ohashi, Toru Ohata, Takashi Ohshima, Shun Ono, Yuji Otake, Choji Saji, Tatsuyuki Sakurai, Takahiro Sato, Kei Sawada, Takamitsu Seike, Katsutoshi Shirasawa, Takashi Sugimoto, Shinsuke Suzuki, Sunao Takahashi, Hideki Takebe, Kunikazu Takeshita, Kenji Tamasaku, Hitoshi Tanaka, Ryotaro Tanaka, Takashi Tanaka, Tadashi Togashi, Kazuaki Togawa, Atsushi Tokuhisa, Hiromitsu Tomizawa, Kensuke Tono, Shukui Wu, Makina Yabashi, Mitsuhiro Yamaga, Akihiro Yamashita, Kenichi Yanagida, Chao Zhang, Tsumoru Shintake, Hideo Kitamura, and Noritaka Kumagai. A compact x-ray free-electron laser emitting in the sub-ångström region. *Nature Photonics*, 6:540–544, 8 2012.

[55] J. Amann, W. Berg, V. Blank, F. J. Decker, Y. Ding, P. Emma, Y. Feng, J. Frisch, D. Fritz, J. Hastings, Z. Huang, J. Krzywinski, R. Lindberg, H. Loos, A. Lutman, H. D. Nuhn, D. Ratner, J. Rzepiela, D. Shu, Yu Shvyd'Ko, S. Spampinati, S. Stoupin, S. Terentyev, E. Trakhtenberg, D. Walz, J. Welch, J. Wu, A. Zholents, and D. Zhu. Demonstration of self-seeding in a hard-x-ray free-electron laser. *Nature Photonics*, 6:693–698, 10 2012.

[56] DA Peterson. Confocal microscopy, encyclopedia of movement disorders, 2010.

[57] Britta Schürmann, Daniel P Bermingham, Katherine J Kopeikina, Kristoffer Myczek, Sehyoun Yoon, Katherine E Horan, and Crystle J Kelly. Structured illumination microscopy (sim) imaging of bin1 colocalization with trafficking markers in cultured rat cortical neurons. *Molecular Psychiatry*, 25(9):1905–1906, 2020.

[58] E. Hesper Rego, Lin Shao, John J. Macklin, Lukman Winoto, Göran A. Johansson, Nicholas Kamps-Hughes, Michael W. Davidson, and Mats G. L. Gustafsson. Nonlinear structured-illumination microscopy with a photoswitchable protein reveals cellular structures at 50-nm resolution. *Proceedings of the National Academy of Sciences*, 109, 1 2012.

[59] W. E. Moerner. Single-molecule mountains yield nanoscale cell images. *Nature Methods*, 3:781–782, 10 2006.

[60] Mark Bates, Sara A Jones, and Xiaowei Zhuang. Stochastic optical reconstruction microscopy (storm): a method for superresolution fluorescence imaging. *Cold Spring Harbor Protocols*, 2013(6):pdb–top075143, 2013.

[61] Michael J. Rust, Mark Bates, and Xiaowei Zhuang. Sub-diffraction-limit imaging by stochastic optical reconstruction microscopy (storm). *Nature Methods*, 3:793–795, 10 2006.

[62] Stefan W Hell and Jan Wichmann. Breaking the diffraction resolution limit by stimulated emission: stimulated-emission-depletion fluorescence microscopy. *Optics letters*, 19(11):780–782, 1994.

[63] Michael Remmel, Lukas Scheiderer, Alexey N Butkevich, Mariano L Bossi, and Stefan W Hell. Accelerated minflux nanoscopy, through spontaneously fast-blinking fluorophores. *Small*, 19(12):2206026, 2023.

[64] David B. Williams and C. Barry Carter. *The Transmission Electron Microscope*. Springer US, 1996.

[65] K C A Smith and C W Oatley. The scanning electron microscope and its fields of application. *British Journal of Applied Physics*, 6:391–399, 11 1955.

[66] Francesca Santoro, Wenting Zhao, Lydia Marie Joubert, Liting Duan, Jan Schnitker, Yoeri Van De Burgt, Hsin Ya Lou, Bofei Liu, Alberto Salleo, Lifeng Cui, Yi Cui, and Bianxiao Cui. Revealing the cell-material interface with nanometer resolution by focused ion beam/scanning electron microscopy. *ACS Nano*, 11:8320–8328, 8 2017.

[67] B. W. Ward, John A. Notte, and N. P. Economou. Helium ion microscope: A new tool for nanoscale microscopy and metrology. *Journal of Vacuum Science Technology B: Microelectronics and Nanometer Structures Processing, Measurement, and Phenomena*, 24:2871–2874, 11 2006.

[68] Jerry Tersoff and Donald R Hamann. Theory of the scanning tunneling microscope. *Physical Review B*, 31(2):805, 1985.

[69] Franz J. Giessibl. Advances in atomic force microscopy. *Reviews of Modern Physics*, 75:949–983, 7 2003.

[70] Guanghui Yuan, Katrine S. Rogers, Edward T.F. Rogers, and Nikolay I. Zheludev. Far-field superoscillatory metamaterial superlens. *Physical Review Applied*, 11, 6 2019.

[71] Tanchao Pu, Jun Yu Ou, Vassili Savinov, Guanghui Yuan, Nikitas Papasimakis, and Nikolay I. Zheludev. Unlabeled far-field deeply subwavelength topological microscopy (dstm). *Advanced Science*, 8, 1 2021.

[72] Edward TF Rogers, Jari Lindberg, Tapashree Roy, Salvatore Savo, John E Chad, Mark R Dennis, and Nikolay I Zheludev. A super-oscillatory lens optical microscope for subwavelength imaging. *Nature materials*, 11(5):432–435, 2012.

[73] Carsten Winterfeldt, Christian Spielmann, and Gustav Gerber. Colloquium: Optimal control of high-harmonic generation. *Reviews of Modern Physics*, 80(1):117, 2008.

[74] Paul B Corkum. Plasma perspective on strong field multiphoton ionization. *Physical review letters*, 71(13):1994, 1993.

[75] M Lewenstein, Ph Balcou, 't Anne L'huillier M Yu Ivanov, P B Corkum, and Lawrence Livermore. Theory of high-harmonic generation by low-frequency laser fields, 1994.

[76] CR McDonald, G Orlando, G Vampa, and T Brabec. Tunneling time, what is its meaning? In *Journal of Physics: Conference Series*, volume 594, page 012019. IOP Publishing, 2015.

[77] Amelle Zair, M Holler, A Guandalini, F Schapper, J Biegert, Lukas Gallmann, Ursula Keller, AS Wyatt, A Monmayrant, IA Walmsley, et al. Quantum path interferences in high-order harmonic generation. *Physical review letters*, 100(14):143902, 2008.

[78] Andrew D Shiner, Carlos Trallero-Herrero, Nathaniel Kajumba, H-C Bandulet, Daniel Comtois, François Légaré, Mathieu Giguère, Jean-Claude Kieffer, Paul B Corkum, and DM Villeneuve. Wavelength scaling of high harmonic generation efficiency. *Physical Review Letters*, 103(7):073902, 2009.

[79] M. Hohenleutner, F. Langer, O. Schubert, M. Knorr, U. Huttner, S. W. Koch, M. Kira, and R. Huber. Real-time observation of interfering crystal electrons in high-harmonic generation. *Nature*, 523:572–575, 7 2015.

[80] Thomas Brabec and Ferenc Krausz. Intense few-cycle laser fields: Frontiers of nonlinear optics. *Reviews of Modern Physics*, 72:545–591, 4 2000.

[81] Philippe Balcou, Pascal Salieres, Anne L'Huillier, and Maciej Lewenstein. Generalized phase-matching conditions for high harmonics: The role of field-gradient forces. *Physical Review A*, 55(4):3204, 1997.

[82] Xiaoshi Zhang, Amy L. Lytle, Tenio Popmintchev, Xibin Zhou, Henry C. Kapteyn, Margaret M. Murnane, and Oren Cohen. Quasi-phase-matching and quantum-path control of high-harmonic generation using counterpropagating light. *Nature Physics*, 3:270–275, 4 2007.

[83] Tenio Popmintchev, Ming-Chang Chen, Alon Bahabad, Michael Gerrity, Pavel Sidorenko, Oren Cohen, Ivan P. Christov, Margaret M. Murnane, and Henry C. Kapteyn. Phase matching of high harmonic generation in the soft and hard x-ray regions of the spectrum. *Proceedings of the National Academy of Sciences*, 106:10516–10521, 6 2009.

[84] Soeren Lichtenberg, Christian Heinisch, Victor Petrov, Juergen Petter, and Theo Tschudi. Refractive-index measurement of gases with a phase-shift keyed interferometer. *Applied optics*, 44(22):4659–4665, 2005.

[85] Peter Baksh. *Ptychographic imaging of real biological samples using a high harmonic and synchrotron source*. PhD thesis, University of Southampton, 2016.

[86] H.A. Haus. Mode-locking of lasers. *IEEE Journal of Selected Topics in Quantum Electronics*, 6:1173–1185, 11 2000.

[87] Sterling Backus, Charles G. Durfee, Margaret M. Murnane, and Henry C. Kapteyn. High power ultrafast lasers, 1998.

[88] Melvin Lax. The franck-condon principle and its application to crystals. *The Journal of chemical physics*, 20(11):1752–1760, 1952.

[89] Donna Strickland and Gerard Mourou. Compression of amplified chirped optical pulses. *Optics communications*, 55(6):447–449, 1985.

[90] P. Maine, D. Strickland, P. Bado, M. Pessot, and G. Mourou. Generation of ultrahigh peak power pulses by chirped pulse amplification. *IEEE Journal of Quantum Electronics*, 24:398–403, 2 1988.

[91] A. Mathis, F. Courvoisier, L. Froehly, L. Furfaro, M. Jacquot, P. A. Lacourt, and J. M. Dudley. Micromachining along a curve: Femtosecond laser micromachining of curved profiles in diamond and silicon using accelerating beams. *Applied Physics Letters*, 101, 8 2012.

[92] AE Siegman. Abcd-matrix elements for a curved diffraction grating. *JOSA A*, 2(10):1793–1793, 1985.

[93] B. Mills, E. T. F. Rogers, J. Grant-Jacob, S. L. Stebbings, M. Praeger, A. M. de Paula, C. A. Froud, R. T. Chapman, T. J. Butcher, W. S. Brocklesby, and J. G. Frey. Euv off-axis focusing using a high harmonic source. volume 7360, page 736003. SPIE, 5 2009.

[94] Dave Litwiller. Ccd vs. cmos. *Photonics spectra*, 35(1):154–158, 2001.

[95] Oliver Bunk, Martin Dierolf, Søren Kynde, Ian Johnson, Othmar Marti, and Franz Pfeiffer. Influence of the overlap parameter on the convergence of the ptychographical iterative engine. *Ultramicroscopy*, 108:481–487, 4 2008.

[96] Manuel Guizar-Sicairos, Mirko Holler, Ana Diaz, Joan Vila-Comamala, Oliver Bunk, and Andreas Menzel. Role of the illumination spatial-frequency spectrum for ptychography. *Physical Review B*, 86(10):100103, 2012.

[97] Daniel L Ruderman. The statistics of natural images. *Network: computation in neural systems*, 5(4):517, 1994.

[98] George B Arfken, Hans J Weber, and Frank E Harris. *Mathematical methods for physicists: a comprehensive guide*. Academic press, 2011.

[99] WO Saxton and W Baumeister. The correlation averaging of a regularly arranged bacterial cell envelope protein. *Journal of microscopy*, 127(2):127–138, 1982.

[100] Marin Van Heel and Michael Schatz. Fourier shell correlation threshold criteria. *Journal of Structural Biology*, 151:250–262, 9 2005.

[101] Sami Koho, Giorgio Tortarolo, Marco Castello, Takahiro Deguchi, Alberto Diaspro, and Giuseppe Vicidomini. Fourier ring correlation simplifies image restoration in fluorescence microscopy. *Nature communications*, 10(1):3103, 2019.

[102] Sriram Aiyer, Cheng Zhang, Philp R Baldwin, and Dmitry Lyumkis. Evaluating local and directional resolution of cryo-em density maps. *cryoEM: Methods and Protocols*, pages 161–187, 2021.

[103] Pierre Thibault, Martin Dierolf, Oliver Bunk, Andreas Menzel, and Franz Pfeiffer. Probe retrieval in ptychographic coherent diffractive imaging. *Ultramicroscopy*, 109(4):338–343, 2009.

[104] Xiaojing Huang, Hanfei Yan, Ross Harder, Yeukuang Hwu, Ian K. Robinson, and Yong S. Chu. Optimization of overlap uniformness for ptychography. *Optics Express*, 22:12634, 5 2014.

[105] Andrew M Maiden, Martin J Humphry, Fucai Zhang, and John M Rodenburg. Superresolution imaging via ptychography. *JOSA A*, 28(4):604–612, 2011.

[106] XingChen Pan, Suhas P Veetil, Baosheng Wang, Cheng Liu, and Jianqiang Zhu. Ptychographical imaging with partially saturated diffraction patterns. *Journal of Modern Optics*, 62(15):1270–1277, 2015.

[107] Wilhelm Eschen, Chang Liu, Daniel S Penagos Molina, Robert Klas, Jens Limpert, and Jan Rothhardt. High-speed and wide-field nanoscale table-top ptychographic euv imaging and beam characterization with a scmos detector. *Optics Express*, 31(9):14212–14224, 2023.

[108] Michela Cosentino, Claudio Canale, Paolo Bianchini, and Alberto Diaspro. Afm-sted correlative nanoscopy reveals a dark side in fluorescence microscopy imaging. *Science advances*, 5(6):eaav8062, 2019.

[109] Susanna M Fruh, Ulf Matti, Philipp R Spycher, Marina Rubini, Sebastian Lickert, Thomas Schlichthaerle, Ralf Jungmann, Viola Vogel, Jonas Ries, and Ingmar Schoen. Site-specifically-labeled antibodies for super-resolution microscopy reveal in situ linkage errors. *ACS nano*, 15(7):12161–12170, 2021.

[110] Graeme Ball, Justin Demmerle, Rainer Kaufmann, Ilan Davis, Ian M. Dobbie, and Lothar Schermelleh. Simcheck: A toolbox for successful super-resolution structured illumination microscopy. *Scientific Reports*, 5, 11 2015.

[111] David A Agard. Optical sectioning microscopy: cellular architecture in three dimensions. *Annual review of biophysics and bioengineering*, 13(1):191–219, 1984.

[112] Nicolas Dey, Laure Blanc-Feraud, Christophe Zimmer, Pascal Roux, Zvi Kam, Jean Christophe Olivo-Marin, and Josiane Zerubia. Richardson-lucy algorithm with total variation regularization for 3d confocal microscope deconvolution. *Microscopy Research and Technique*, 69:260–266, 2006.

[113] ADAPTIVE DECONVOLUTION. Lightning. 2018.

[114] The MathWorks Inc. Statistics and machine learning toolbox, 2022.

[115] Jan Vogelsang, Thorben Cordes, Carsten Forthmann, Christian Steinhauer, and Philip Tinnefeld. Controlling the fluorescence of ordinary oxazine dyes for single-molecule switching and superresolution microscopy, 2009.

[116] Colin Echeverría Aitken, R. Andrew Marshall, and Joseph D. Puglisi. An oxygen scavenging system for improvement of dye stability in single-molecule fluorescence experiments. *Biophysical Journal*, 94:1826–1835, 3 2008.

[117] Peter D Baksh, Michal Ostrčil, Magdalena Miszczak, Charles Pooley, Richard T Chapman, Adam S Wyatt, Emma Springate, John E Chad, Katrin Deinhardt, Jeremy G Frey, and William S Brocklesby. Quantitative and correlative extreme ultraviolet coherent imaging of mouse hippocampal neurons at high resolution. *Science advances*, 6(18):eaaz3025, 2020.

[118] M.R. Howells, T. Beetz, H.N. Chapman, C. Cui, J.M. Holton, C.J. Jacobsen, J. Kirz, E. Lima, S. Marchesini, H. Miao, D. Sayre, D.A. Shapiro, J.C.H. Spence, and D. Starodub. An assessment of the resolution limitation due to radiation-damage in x-ray diffraction microscopy. *Journal of Electron Spectroscopy and Related Phenomena*, 170(1):4–12, 2009. Radiation Damage.

[119] Peter Baksh, Michal Odstrcil, Aaron Parsons, Jo Bailey, Katrin Deinhardt, John E. Chad, William S. Brocklesby, and Jeremy G. Frey. Quantitative evaluation of hard x-ray damage to biological samples using euv ptychography. volume 849. Institute of Physics Publishing, 6 2017.

[120] J H Hubbell and S M Seltzer. Tables of x-ray mass attenuation coefficients and mass energy-absorption coefficients 1 kev to 20 mev for elements z = 1 to 92 and 48 additional substances of dosimetric interest.

[121] KA Kanaya and S Okayama. Penetration and energy-loss theory of electrons in solid targets. *Journal of Physics D: Applied Physics*, 5(1):43, 1972.

[122] Ruth Signorell and Bernd Winter. Photoionization of the aqueous phase: clusters, droplets and liquid jets. *Physical Chemistry Chemical Physics*, 24(22):13438–13460, 2022.

[123] P Auger. The auger effect. *Surface Science*, 48(1):1–8, 1975.